Design and Study of Gallium Arsenide Optical Modulators Exploiting Quantum Well Excitonic Quenching

Craig Tombling.

Submitted to University of London for the degree of Ph.D.

Department of Electronic and Electrical Engineering,
University College London.

December 1989.

To Melissa

Abstract

The thesis describes the development of a gallium arsenide (GaAs) optical waveguide modulator suitable for the external or remote modulation of a laser source. Design techniques, fabrication, measurement tools and assessment are detailed and the device application is discussed.

In short, the device is a waveguide quantum well absorption modulator using the quenching of the excitonic resonance by an electron gas as the mechanism. A *p-n* or Schottky junction in the structure allows a small reverse bias to influence the electron density in a single quantum well, hence enabling controlled recovery of the excitonic absorption. Many devices have been developed which take advantage of quantum well excitonic absorption which is enhanced above that of the bulk material. This device contrasts most quantum well modulators by using the excitonic quenching mechanism rather than the conventional Stark shift of the excitonic peak.

The epitaxial GaAs structures are fabricated into two device types, one allowing photocurrent to be measured and the second enabling optical waveguiding. These measurements, performed on several samples, form the bulk of the experimental assessment and demonstrate the desired excitonic quenching. Low temperature measurements show an enhanced modulation depth but more importantly highlight the features of the absorption spectrum. A model of the electrical characteristics of the device is developed and successfully acts as a design and analysis tool in conjunction with measured capacitance-voltage doping profiles. The limitations to the achievable modulation depth are discussed in view of the experimental data and projections of the performance are made. The ultimate limit to the absorption change at the band edge is investigated by modelling the subband absorption taking into account the anticipated bandedge shifts associated with the large carrier densities in the quantum well. A critical assessment of the state of the art monolithic optoelectronic integrated circuits is made and the duality of the modulation mechanism with that of a heterostructure FET is discussed in this context.

Contents

Acknowledgements

The work presented in this thesis could not have been completed without invaluable contributions from numerous individuals and several institutions.

I would firstly like to thank Dr. Margaret Stallard for her excellent supervision throughout my course of research and Professor Gareth Parry for the unenviable task of nurturing me through the last 6 months. Their guidance and enthusiasm has inspired both the contents and completion of this thesis.

The Digital Optics Group (DOG) at UCL, under the guidance of Professor John Midwinter, thrives on strong communication, both organised and informal. In this climate my fellow doctoral students have always been a source of stimulating discussion. Peter Stevens has literally been at my side for three years and has devoted many hours to discussing forgotten rudiments and complex fundamentals. Mark Whitehead is a human compendium of printed literature and consequently an endless source of both scientific fact and non scientific trivia. *Dr.* Piero Bradley must be thanked for discussions into the night, and secondly for proving that *it* can be done.

Other invaluable members of the DOG perform ridiculous feats to assist in student research. I am indebted to Tony Overbury for sharing his knowledge of Laser systems, and for providing backup in the laboratories. Mark Abbott succeeded in providing this Apple Laserwriter () output from an IBM with an identity crisis, and he has also tutored me through my struggle to learn sensible programming languages. Tony Rivers' clean room fabrication skills have been more than useful.

Of the institutions, Sheffield University and particularly, John Roberts, Peter Robson and Chris Button, have been the major source of III-V epitaxial layers used in this thesis. Amoco Research Center have also provided help in this respect, particulary Ricardo Sussmann and Frank Chambers. The funding for this studentship was a grant from the Science and Engineering Research Council, supplemented by a Case Award with Plessey Research Caswell. The staff and my former colleagues at Plessey, Andy Moseley, Ian Bennion, Rob Walker, Dave Robbins have always been ready to help.

Finally I must thank my family and friends simply for putting up with me, especially Melissa who used every means to bring this thesis to a prompt conclusion.

Preface

The modulation of light is of paramount importance for a wide variety of optical communication systems. The III-V semiconductor quantum well modulator is expected to fulfill a role in future systems due to the excellent modulation characteristics and the material compatibility with the most common light source, the semiconductor laser. Optical modulation, in quantum well material, was first observed by Wood et al in 1984, and this was later extended to give modulation in an optical waveguide [Wood et al 1985]. The waveguide device of Wood et al [1985] was the first to reach the 10dB barrier by achieving an on/off ratio of 10:1, whilst it was not until 1989 that Whitehead et al [1989] exceeded this using a modified normal incidence or *transverse* structure.

My proposed course of study was the analysis of optical modulation in undoped InGaAs/InAlAs/InP quantum well material at wavelengths suitable for communications purposes in fibre systems. This was embarked upon at the start of this work in 1986 and the initial goals were the observation of the required modulation phenomena before subsequent investigation and development of waveguide modulators. Device fabrication techniques were developed, as were optical assessment systems, one of which included a method for the generation of tunable (1.4 - 1.65μm) laser light [Cotter]. The required quality of InGaAs/InP material proved difficult to obtain in practice and structures exhibiting good operation of the quantum well modulation mechanism did not become available. These materials have been studied by several authors and a high optical modulation contrast of 30:1 was reported for an InGaAs/InP waveguide device by Wakita et al late in 1986.

Other groups have recently studied further optical phenomena in quantum well material. In particular the carrier density dependence of the quantum well optical absorption strength has been investigated both by means of photon generated carrier populations, and through the use of doped structures. The former case provides the means of producing a low power optical nonlinearity where saturation of the quantum well *excitonic* absorption is the underlying mechanism: this was demonstrated by Miller et al in 1982 and was of interest for all optical processing. In the latter case a gated doped structure, similar to many of the SDHFETs under development [Inoue and Sakaki], enables the continuous transition from a high to low carrier concentration in the quantum well. This is of much interest from a physical point of view as a means of studying the carrier density dependent absorption spectra and the structure is an excellent test ground for the experimental confirmation of many body interaction theory [Delalande et al]. This latter phenomena was studied by Chemla et al in 1987 by probing the conduction channel of a InGaAs quantum well FET: it was proposed that the room temperature quenching of the exciton which was found, was similar in nature to that observed in the case of the optical nonlinearity, and could be used as a modulation mechanism. At the same time Sakaki et al and Kastalsky et al proposed devices with this FET-like structure within the core of a waveguide.

The obvious inference is that this alternative quantum well modulation mechanism offers the advantage of a dual capability as both optical modulator and FET, hence this structure is a simple approach to realising very high performance optoelectronic integrated circuits (OEICs). OEICs represent combinations of both optoelectronic and electronic devices on the same chip and this monolithic integration, as it is termed, exhibits advantages in performance, functionality, cost and reliability [Wada et al 1988].

At the time, waveguide phase modulation was being studied in undoped quantum well material at UCL [Piero Bradley] and the results of waveguide *absorption* modulation, seen by Wood et al[1985], were clearly reproducible in these GaAs/AlGaAs structures. I performed a study of excitonic saturation data from the literature [Sakaki et al] and showed that indeed this *alternative* mechanism in doped structures would also be capable of providing a large optical modulation in a waveguide device. From this, the work expanded into the development of a GaAs/AlGaAs waveguide modulator, named the quantum well field effect modulator (QW-FEM), and the preliminary results illustrating the functionality of the mechanism were published at the European Conference on Optical Communications in 1988. The first waveguide study was performed a couple of months later and presented at the Institute of Electrical Engineers. Further waveguide data was published at the OSA Topical Meeting on Quantum Wells for Optics and Optoelectronic in 1989.

In describing the theoretical and experimental implementation of the QW-FEM, this thesis takes on the following form. The basic concept of the quantum well and the physical advantages gained from its use are introduced in chapter 1. Typical devices are discussed and the more recent developments in the field are explored. The discussion then moves to introduce the basic idea of the QW-FEM which forms the bulk of the investigations in this thesis. A more detailed overview of the mechanism used in the QW-FEM is presented in chapter 2 along with a review of relevant topics from which data is extracted to assist in the initial device design. The epitaxial growth of these structures is then considered in chapter 3 with a view to illustrating the complexities related specifically to the QW-FEM. The full design of the device follows with the parameters of the growth process carefully taken into account: a model of the device electrical properties is used in conjunction with a second separate model of the optical waveguiding characteristics as a means of determining the specific epitaxial structure required. The fabrication and packaging of the variety of devices used in this thesis is discussed in chapter 4 along with details of the techniques used for measurement of the optical and electrical properties of QW-FEM devices. Chapter 5 unfolds the results obtained: initially a brief chronology is used which describes the progression of the optical properties of successive epitaxial structures through the simplest assessment method, that of photocurrent spectroscopy. More detailed analysis of the behaviour of the device follows with comparisons of the modelled and experimental bias dependent optical and electrical operation. The spectral chirp advantage gained from use of this device is outlined at this point. An assessment of the functionality of the modulation mechanism is made and experimental investigations suggest that the performance limit is beyond that found in this work. An optimisation of the waveguide design is also presented and performance of the re-designed structure is predicted using experimental data. An ultimate limit to the optical modulation attainable in the QW-FEM is anticipated due to the maximum saturation achievable. This can be predicted by modelling of the absorption spectra, using an extension to calculations derived for characterising the gain of quantum well lasers, and is described in chapter 6. A major advantage of the QW-FEM is the duality of the structure with that of a high performance SDHFET. The possibilities of monolithic integration are consequently exciting and chapter 7 discusses OEICs from their concept to the role of the QW-FEM in this context. Initial FET results are presented from a structure designed to realise the suggested duality.

Chapter 1

Introduction to III-V Materials and Devices

1.1 III-V Semiconductor Research

The device developed in this thesis is an optical modulator which is fabricated from III-V compound semiconductor material. The work presented here also has a broader scope in the context of optoelectronic integrated circuit (OEIC) research. With this in mind, it is useful to introduce this thesis from the viewpoints of III-V materials research and optoelectronic integration.

Research into III-V compound semiconductors has gained an ever greater momentum over the past three decades, fuelled by the fabrication of both optoelectronic and electronic devices. Current optical communication systems exist by virtue of the strong optical interactions exhibited in these materials. In electronics, transistors operate at bandwidths in excess of silicon devices due, at least in part, to the greater mobilities exhibited. Research into OEICs is a more recent development [Yariv] with the goal of combining optoelectronic devices and electronic circuits on a single chip both to increase overall performance and reduce fabrication costs.

The direct bandgap of the III-V semiconductor materials is the root of their success in optoelectronics. This leads to optical emission as carriers lying at the semiconductor band minima recombine. Both silicon and germanium have indirect bandgaps and the corresponding transition is very much weaker. This single fact enables the operation of semiconductor lasers and gives III-V detectors their high efficiencies. These materials also benefit from a fabrication technique which involves the crystalline growth of further semiconductor material on top of a semiconductor substrate. The advantage gained from this complex technique is that layers of dissimilar compounds, or material with dissimilar doping levels, can be grown consecutively. This allows both abrupt changes in the bandgap of the semiconductor and the formation of *p-n* junctions, resulting in very precise engineering of device properties.

Most III-V electronic and optoelectronic devices exploit the available tailoring of the semiconductor bandgap and currently the so called hetero-interface is used to develop speed advantages in both bipolar and field effect transistors. The heterojunction bipolar transistor (HBT) [Kroemer] has reduced junction capacitances and, consequently, an increased bandwidth by virtue of an emitter base heterojunction. The hetero-interface is used in sophisticated FETs to accumulate charge and form a conduction channel remote from the doped regions which supply the conducting carriers. This enables a high density of electrons to reside in pure undoped semiconductor away from the effects of donor related impurity scattering which reduce carrier mobilities and degrade device performance [Sakaki]. In optoelectronic devices the effects are equally dramatic. The heterojunction laser exploits material composition in two ways: firstly, the refractive index changes associated with the bandgap difference guides the light generated in the device, and secondly, the bandgap steps act to accumulate injected charge in a thin active region so that the population inversion required for lasing is more readily achieved. The use of hetero-interfaces to form *very* thin alternate layers of material of different bandgap introduces quantum confinement. These structures, named quantum wells, alter the optical and electronic properties of the semiconductor and have distinct advantages for use in the active layers of lasers and in the optical modulators described in this thesis.

The bandgap of the active region of an optoelectronic device relates directly to the operating wavelength and this can be tailored to cover a considerable range through the use of various compound semiconductor materials. The material used in this thesis is GaAs and the hetero-interfaces are formed by use of AlGaAs layers. This gives operation at a wavelength of approximately 850nm. The development of a second material system, that of InP, was led by the needs of the optical communications industry as lasers operating at the low loss window of optical fibres (1.55μm) can be fabricated.

The emitters and detectors formed in III-V materials are fundamental to optical communications systems and the increasing demands for low power consumption and high bandwidth has led to considerable work in this field. A broader future is envisaged for optical communication systems than the long haul links currently employed. These systems may have far reaching consequences in local communications on the scale of several kilometres down to perhaps a fraction of a centimetre. Tasks under investigation fall into the categories of local area networks at the "long" end, through high data rate computer networks and networking within computers themselves, to inter- and intra- chip communications at the "short" end.

The optical modulator is introduced into the communications equation at this point and there are many uses and consequently several breeds. In long haul systems for example, the limit to performance lies in the loss and dispersion within the optical fibre. By using the loss minima, greater transmission lengths are obtained revealing a dispersion limit. The directly modulated semiconductor laser has a wavelength shift associated with switch-on and switch-off (chirp) and this is directly related to the maximum data rate achievable [Linke 1984]. As this is approached, the spectrum of each bit becomes broadened and the fibre dispersion temporally spreads the pulse until it overlaps with its neighbours. This limits data rates and transmission distances but can be overcome by the use of external modulation [Koyama and Iga] which provides low chirp high bandwidth performance.

Other optical systems rely on the modulator in the fundamental design [Goodman et al]. Of those mentioned above the short range high data rate systems for back plane or inter/intra-chip interconnect is envisaged as a means of increasing data rates above that of electronic transmission lines. Typically, a reduction of the pinout required for a chip would be achieved, access to the centre of a chip could be gained, or the interconnections of the backplane could be reduced. Systems with a large number of high bandwidth modulators and very few laser sources are envisaged due to high power requirement of lasers from both the aspect of driving circuitry and the heat source they represent. These systems could be implemented through the use of free space or guided optics.

The optoelectronic integrated circuit (OEIC) has the potential to form the basis of many of these proposed systems and replace components in those which currently exist. The OEIC, based in III-V technology (or III-V on silicon), is any combination of the devices outlined above integrated on a single chip, to produce, for example, a laser with an integrated driving circuit. The basic advantages are that such chips should have lower parasitics than manually interconnected discrete devices and correspondingly higher bandwidths, reductions in overall dimensions, increased durability and ruggedness. The advantages to be exploited above all are the increased functionality and the feasibility of mass production. In the former, case signal analysis or switching functions can be anticipated with either a large electronic device involvement, or through a mainly optoelectronic function in a waveguide Photonic Integrated Circuit (PIC). In the latter case, mass production of reliable, rugged transmitters and receivers is expected to fuel the implementation of dense local area networks.

Two configurations of modulator are apparent for these systems. A waveguide device has heteroepitaxial layers which form an optical guide, in a manner similar to that of a laser, while the core is designed to be a controllable absorber at the desired operating wavelength. The second structure is the transverse modulator with light propagating normal to the semiconductor surface. Waveguide modulators find their uses as integrated modulators of semiconductor lasers, within planar PICs, and are generally suited to fibre systems. Transverse modulators on the other hand are suitable for use within systems based on free space propagation, are proposed for stackable inter-chip connections, but are also equally compatible with fibre systems.

A high speed (GHz) transverse modulator is basically unique to III-V quantum well materials, however the waveguide structure is common to another material. The electro-optic effect in $LiNbO_3$ is capable of giving both high bandwidth and high contrast modulation in a Mach-Zehnder interferometer arrangement. Speeds of up to 40GHz have been established at operating voltages of 7.5 volts [Dolfi et al]. However, the length of these devices and the poor reproducibility of the processing technology is a major disadvantage. Similar modulator schemes have used the electro-optic effect in GaAs to good effect [Walker]. However, the electroabsorption modulator is preferred as it offers both a size advantage and the feasibility of integration with semiconductor lasers. This topic has already been successfully addressed by Tarucha and Okamoto who used the same quantum well structure for the two devices.

1.2 Quantum Well Physics and Devices

This section briefly describes the physics of quantum well structures relevant to this thesis and then moves on to cite various devices which gain advantage from incorporation of quantum well layers.

The properties of quantum well materials differ from that of the bulk semiconductor due to confinement of the charge carrying particles, i.e. the electrons and holes. The effective mass of these particles is small in III-V materials resulting in readily observable quantum mechanical effects, which arise when the confining dimension approaches the de Broglie wavelength of the confined particle. The spectrum of energies which the confined particle can have ceases to be smooth continuum as quantisation of the states occurs. The quasi-two-dimensional behaviour required can be produced in structures where a thin layer of low band gap semiconductor (e.g. GaAs) is sandwiched between layers of a lattice matched semiconductor compound with a larger bandgap (e.g. GaAlAs) giving confinement of carriers in the low gap layer. The optical absorption and electrical conduction properties are altered if the low gap layer thickness is less than the order of several hundred angstroms. The resultant energy quantisation was first observed by Dingle et al in the optical absorption spectra of GaAs/AlGaAs material and the success of these early measurements owes much to the emergence at the time of the new thin film III-V growth technology, molecular beam epitaxy (MBE) [Gossard].

The quantisation of the energy levels in this quasi-two-dimensional fashion can be described by the simple particle in a box solution of the Schrödinger equation. This model operates within the effective mass approximation whereby the crystal structure can be can be removed from the calculation by definition of a renormalised mass of electrons and holes to account for the crystal behaviour. The energy levels in a quantum well are illustrated in figure 1.2.1 and the relationship of this diagram to a physical epitaxial structure can be understood by considering the three sections as planar crystalline layers. It is evident at this point that the confinement provides quantisation of the energy and momentum of a carrier perpendicular to the layers but the particle can have any in-plane component of momentum. Hence in the three

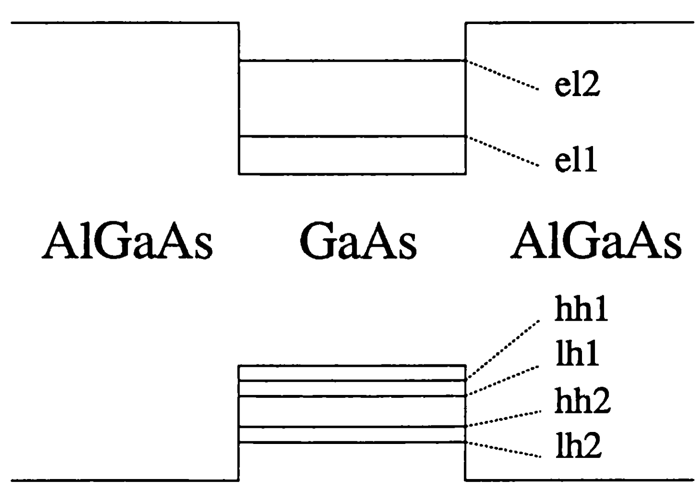

Figure 1.2.1 *Two dimensional quantum well and the associated energy levels which exist.*

dimensional physical structure the discrete energy levels represent subbands each of which contributes to the density of states. The result is summation of these bands giving a step like appearance to the density of states diagram (figure 1.2.2). Optical transitions involving absorption or emission of a photon may only occur between the quantised levels in the conduction and valence bands, and selection rules exist which imply that these transitions must comply to the condition $\Delta N = 0$, where N is the label for the energy level in the quantum well [Dingle et al]. This has the effect that the absorption spectra of such a sample closely represents the shape of the density of states diagram. The selection rules can be simply understood by consideration of the wavefunctions at each confined level, which, for zero penetration into the barrier, are sinusoidal and cosinusoidal and hence completely orthogonal. Some relaxation of these rules occurs experimentally as the barriers are finite, allowing penetration of the wavefunctions, hence breaking the orthogonality. This effect is also seen in the case of distortion of the quantum well due to applied fields when these forbidden features appear in the absorption spectra.

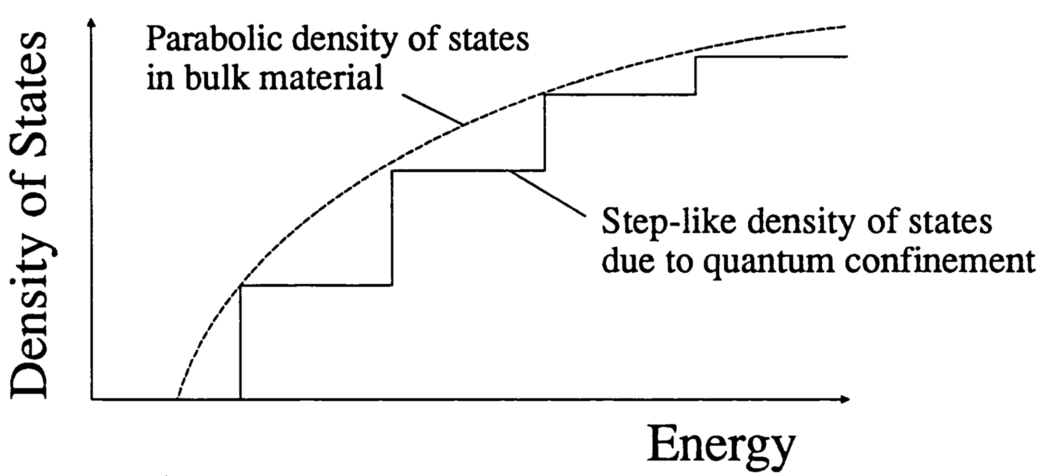

Figure 1.2.2 *Density of states diagram for a quantum well. The parabolic band of the bulk semiconductor is superimposed.*

The confinement of particles and the quantisation of their energy levels has an important effect on the formation of excitons. The exciton is a particle which consists of an electron and hole bound together in a manner similar to the electron and proton of a hydrogen atom. In bulk material related absorption features can be observed at low temperatures, but phonon densities at room temperature broaden the absorption peak and it cannot be resolved from the continuum. The forced proximity of the electron and hole of the quantum well exciton and its quasi-two-dimensional nature act to reduce the radius from that of a bulk material exciton and consequently the binding energy is increased. Also the exciton-phonon interaction is decreased by the quantum confinement reducing the broadening [Chemla et al 1984]. These two effects in combination make it possible to observe the excitonic resonance at room temperature.

The binding energy associated with the formation of an exciton means that absorption is observed to the gap side of each subband. The increased overlap of electron and hole wavefunctions compared to the bulk exciton also acts to enhance the absorption above that of the subband continua and consequently sharp excitonic peaks appear just below each of the step like edges. An absorption spectra showing the step structure and excitonic resonances is illustrated in figure 1.2.3. It is clear from this data that the excitonic peak is in fact split and these features represent two different effective masses of the

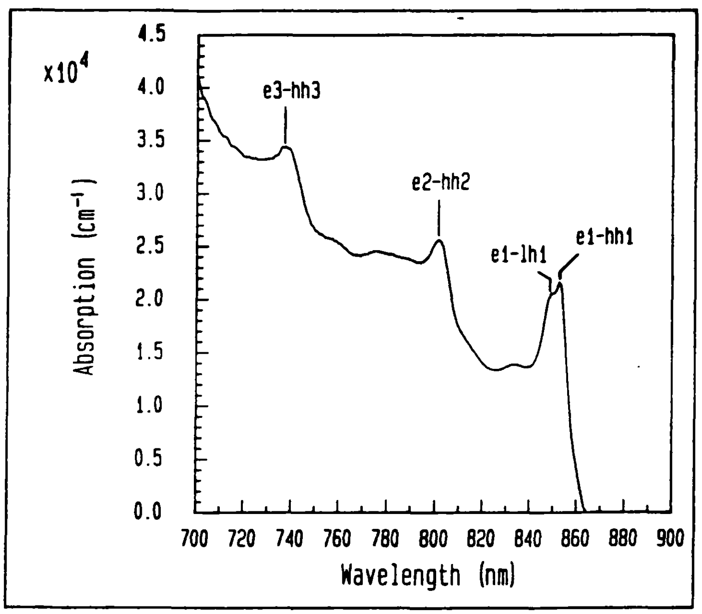

Figure 1.2.3 *Absorption spectra for GaAs/AlGaAs quantum well material with 100Å wells and barriers. Excitonic transitions between the electron (e) and the heavy (hh) and light (lh) hole subbands are labelled. Measurement by Mark Whitehead.*

holes. The quantum well lifts the degeneracy of the hole bands, which normally exists in the bulk material at k=0 [Weisbuch p13], and the light and heavy holes bands then exhibit different energies giving two sets of subbands and excitonic features. The wavelength position of the excitons in an absorption spectrum are heavily influenced by well width, barrier height, and temperature. Decreasing the well width forces the confined energy levels towards the top of the quantum well pushing the absorption features to shorter wavelength [Whitehead et al 1988]; a similar but less marked effect is seen as the barrier height is increased. The temperature dependence relates to the bulk material bandgaps which widen as the temperature falls [Adachi] with a corresponding shift of the features to short wavelength.

The properties of quantum wells outlined above are advantageous for several categories of device. The discussion which follows briefly outlines the specific advantage of incorporation of quantum well layers in a series of compound semiconductor structures. In introducing the quantum well modulator, the field dependent properties of quantum wells are first described before discussion of current performance figures.

Quantum Well Lasers

The change in the density of states of the semiconductor with the use of quantum wells, as outlined above, is of prime importance for the development of laser diodes. The square shape of the 2D density of states function increases the gain at low injection currents and the gain can also be expected to vary more rapidly with injection current [Tsang 1984]. The overall density of states is also reduced as compared to the bulk case and consequently a smaller current density is needed to produce the population inversion for laser action. This leads to low power, low threshold devices.

Enhanced Conduction Effects

Enhanced electron mobilities are found in quantum confined structures by virtue of a technique termed modulation doping. The underlying idea is that at equilibrium charge transfer occurs across a heterojunction to equalise the fermi level to both sides. Doping of the wide gap side of a GaAlAs/GaAs heterojunction serves to provide charge which transfers to form a population in the GaAs layer. This GaAs layer can either be a quantum well (<300Å) or a much larger channel. The advantage found with the use of a quantum well is an increase in the limit of the electron densities achievable [Inoue et al]. This charge transfer effect enables conduction electrons to exist in high purity material, separated from the mobility limiting donor impurities. Modulation doped structures have found application in very high performance FETs, often called the selectively doped heterostructure FET (SDHFET).

Optically Nonlinear Effects

The change in absorption or refraction with incident power in a medium is termed an optical nonlinearity. The nonlinearities found in quantum well materials are not only larger than comparable effects in other materials but they are seen at room temperature and at wavelengths and power levels compatible with semiconductor lasers. The quantum well material shows a saturation of the excitonic resonance at increased power levels which is direct result of a photo-induced carrier population which lies in the N=1 subband.

Electric Field Dependent Properties

The properties of quantum well absorption under applied electric field have been studied in considerable depth. The effect observed has been called the quantum confined Stark shift (QCSS) and was first examined and explained by Chemla et al [1983]. An electric field, perpendicular to the plane of the layers, tilts the quantum well and the energy levels are renormalised with respect to the centre of the well. The effect is illustrated in figure 1.2.4a and causes a shift of the features of the absorption spectra to longer wavelength (figure 1.2.4b). In modelling of this effect, the solutions to the Schrödinger equation are no longer as simple as for the zero field case and the energy levels are best determined by a tunnelling resonance calculation [Miller et al 1985]. This considers the tunnelling probability through a quantum well lying between two barriers of finite thickness and height as a function of incident electron energy. The probability reaches unity when this energy equals that of one of the confined levels. Excellent agreement of modelled and experimental data is found [Stevens et al]. There are several major effects on the absorption spectra (figure 1.2.4b) associated with the QCSS, the most notable of which is the reduction in oscillator strength with electric field. The electron and hole of the exciton become polarised to opposite sides of the quantum well and the overlap of their respective wavefunctions decreases. This has been reconciled with the reduction in oscillator strength observed [Miller et al 1986]. Other effects associated with the application of an electric field produce a broadening of the excitonic peaks and the individual components of this broadening have been successfully modelled by Stevens et al.

a)

b)

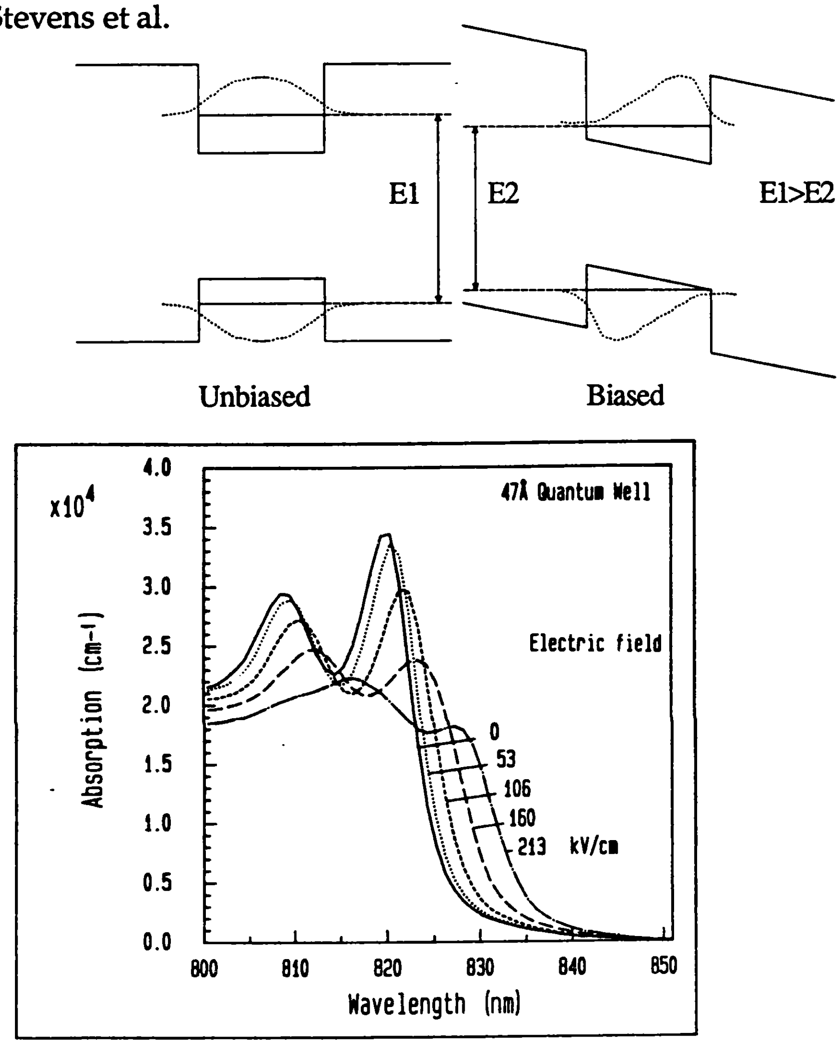

Figure 1.2.4 *The effects of electric field on a quantum well. The subband gap energy is reduced (a) giving a shift of the spectral features (b).*

Quantum Well Stark Shift Modulators

The quantum well Stark shift modulator was first proposed by Wood et al 1984. Two forms of the device exist, the first has light travelling parallel to the quantum well layers in an optical waveguide [Wood et al 1985], and the second operates with light incident normal to the epitaxial surface in a transverse structure. To increase the strength of the quantum well interaction with the incident light the optical path length is often increased by repeating the quantum well "sandwich" many times to produce a multiple quantum well (MQW) structure. Typically 50 quantum wells might be used in a transverse structure whereas only a few wells are required in a waveguide due to the interaction length already available. A uniform electric field must be applied across all of the wells to enable the Stark shift to be observed and hence they are placed in the intrinsic (undoped) region of a semiconductor junction. The doping level in this intrinsic region is vital to operation as the number of wells increases and the effects on the absorption spectra and operating characteristics of the transverse structures have been studied by Stevens et al. The limit to the modulation is a trade off between an increased number of quantum wells for greater modulation, and the decreased Stark shift resulting from the overall thickness reducing the electric field available. The maximum modulation which can be obtained in this manner for a transverse transmission device is of the order of 3.5dB and is insufficient for most conceivable practical purposes. However a recent development of a resonant device which uses an MQW structure within a Fabry-Perot cavity demonstrated >20dB modulation depth a low (5dB) insertion loss. The waveguide structure on the other hand has a long interaction length by design and the high modulation depths are readily attained at low voltages and often with low numbers of quantum wells. The table below (Table 1.2.1) illustrates the performance found in various III-V waveguide modulators. The best combined insertion/contrast figures for MQW structures are those of Wood et al [1985] and Koren et al. It must be noted that the insertion loss quoted in the latter case is low due to use of a multi-moded waveguide with a 4μm thick MQW intrinsic region and the application of anti-reflection (AR) coatings. None of the other experimental device results in table 1.2.1 have anti-reflection coatings applied and consequently the insertion loss figures can be expected to be reduced by approximately 3dB. The work of Noda et al serves to illustrate that high contrast modulation can be achieved without the use of quantum well material, however the device lengths tend to be longer increasing the device capacitance hence restricting the ultimate bandwidth. The data for the GaAs QW-FEM structure, described in this thesis, is also included in table 1.2.1 for comparison and indicates that similar performance is possible. The data from *this work* is derived from experimental data but extrapolated to an optimised structure and will be presented in full in chapter 5: coupling and reflection losses are not included in the overall insertion loss figure.

	Well width Å	No. of wells	Contrast ratio dB	Insertion loss dB	Drive volts V	Length µm
GaAs MQW						
Wood et al 1985	97	2	10	7.2	15	150
Taraucha et al	80	16	3	?	1.4	180
GaInAs MQW						
Wakita et al	67	10	8.86	13	1.8	140
Wakita et al	67	40	15	9	9	180
Koren et al	80	80	18.7	2.7*	20	375
Wood et al 1988	70	10	16/11.2	9.4	10	76
GaInAs Bulk						
Noda et al			20	9.6	11	470
GaAs QW-FEM						
Abeles et al	100	1	3.1	?	20	750
This work	50	1	10**	1.9**	6	160

**multimode operation*

***assumes AR coating, does not include coupling losses (chapter 5)*

Table 1.2.1 *Performance figures for waveguide absorption modulators.*

Wood et al 1985, Boyd et al and Wakita et al have independently demonstrated that MQW devices of waveguide or transverse form are capable of high speed operation and the limits reached in each case are related purely to the RC time constant. Charging the device capacitance through a 50Ω impedance has a fundamental time constant of $\tau = 2\pi RC$. For a 150μm long, 5μm wide waveguide device with a 1μm thick intrinsic region, the 75fF capacitance obtained relates to a bandwidth of 40GHz. The highest modulation bandwidths reported to date are 5.5GHz for a transverse structure [Boyd et al] and 10GHz for a waveguide structure [Wood et al 1985].

1.3 Introduction to the Quantum Well Field Effect Modulator

The device developed in this thesis differs from the undoped multiple quantum well optical modulators described above. The device has been named the Quantum Well Field Effect Modulator (QW-FEM) implying that it uses quantum well absorption, but the operation centres on the *field effect* control of a carrier density in a manner identical to a FET. The actual optical absorption modulation mechanism is an alternative to the quantum confined Stark shift (QCSS) and operates by quenching of the excitonic resonance. The effect is identical to that of quantum well optical nonlinearities, in that a carrier population saturates excitonic features in the absorption spectrum.

The sophisticated heterostructure FETs mentioned in the previous section use a quantum well as a channel and provide a sheet of electrons for conduction through the use of donor regions to one or both sides of the well. This type of FET has many names but is most frequently described as a selectively doped heterostructure field effect transistor (SDHFET). The sheet carrier densities achieved in these structures is very high [Sakaki] and is comparable or greater than those generated in MQW optically nonlinear experiments. The mechanism of excitonic quenching is detailed in section 2.2 of this thesis and essentially relies on the filling of states in the quantum well conduction band. With few states available the creation of excitons by photon absorption is inhibited and the peak in the absorption spectra diminishes giving rise to an optical modulation.

The field effect control of a carrier population is restricted to a single quantum well by virtue of the high densities required and the correspondingly large electric fields needed for their manipulation. The simple consequence of this is that the mechanism is suited to waveguide operation. As with the waveguide QCSS modulators the quantum well must be placed in the core of a heterostructure waveguide to enable the control of the optical absorption. The device consequently has the modified electrical format of a SDHFET buried within an optical waveguide.

The versatility of the design of this modulator is evident from this description. Both optical modulation and FET operation are available with potentially very high performance. The QW-FEM, as a consequence, is an excellent candidate for use in the design of OEICs through this duality of the device mechanism. Other functions can be anticipated from the structure. The possibility of lasing action is of great interest for the implementation of an OEIC circuit which might include laser, modulator and driving circuitry. Optical amplification is also possible, and in its absorbing state the QW-FEM waveguide acts as a high quantum efficiency photodetector. This considerable array of functions inherent in the structure echoes that of MQW devices, although with the excellent advantage of high performance FET operation. Chapter 7 of this thesis is devoted to discussion of monolithic integration for future systems use and places the QW-FEM in context within a framework of other monolithic designs.

In summary III-V compound semiconductors play a large role in optical communication systems through their optoelectronic properties. This role is expected to grow as more sophisticated communications networks evolve. The need for optical modulators has been established and this is currently persued through the use of ultra thin semiconductor layers in the form of quantum wells. The demanding requirements of future optical systems have provoked interest in the integration of optical and electrical devices to form high performance monolithic circuits. The QW-FEM, development of which is described in this thesis, is a possible candidate for OEIC use.

Chapter 2

Excitonic Quenching for Optical Modulation Applications

2.1 Introduction

The operation of the Quantum Well Field Effect Modulator (QW-FEM) is an intensity modulation of the excitonic absorption characteristic of quantum well material (section 1.2). A reduction in this excitonic absorption is achieved when carriers occupy the lower energy states in a quantum well, inhibiting the creation of excitons by incident optical photons. Electrically controlled absorption modulation is achieved by ensuring that the quantum well is filled with carriers when there is no bias across the device, providing excitonic quenching. An applied bias, producing a field in the well region, then sweeps the carriers from the quantum well restoring the excitonic feature.

This chapter primarily examines the operation of the QW-FEM by discussing in detail the mechanism of excitonic quenching, whereas the subsequent chapter examines the implementation of absorption control. As described in section 1.3 the quantum well excitonic saturation can be likened to that found in quantum well optical nonlinearities. However the differences are two fold: firstly the saturating carrier population of the QW-FEM is not generated optically but by regions of doped semiconductor; secondly the saturation is produced by only one carrier type as opposed to the equal electron and hole densities photogenerated in optical nonlinearities. Nevertheless the mechanism of excitonic quenching is identical and the study of MQW optical nonlinearites has lead to an excellent understanding of the processes involved in the QW-FEM: these are outlined below. Following this discussion the carrier density required in the quantum well can be anticipated from simple calculations and published work. Multiple quantum well structures using doping in the barrier layers have been demonstrated elsewhere [Sakaki et al] and serve to illustrate and quantify the desired excitonic quenching. High carrier density effects are expected in addition to the simple reduction in absorption at the excitonic feature and these are the decrease of the binding energy of the exciton and the renormalisation of the bandgap: their consequences for the operation of the modulator are highlighted. A further, but indirect consequence of the population of the quantum well which must be noted, is the introduction of internal fields and an associated quantum confined Stark shift of the exciton and subband energy. This is followed by a review of relevant work in the fields of optical nonlinearities and modulation doped quantum wells, with results discussed in the context of the potential operation of the QW-FEM.

2.2 Modulation Mechanism.

The underlying principle of modulation in the QW-FEM is quenching of excitonic absorption by occupation of subband states with an electron or hole plasma. High degrees of excitonic quenching by such plasmas have been observed in the investigation of both optical nonlinearities [Miller et al 1982] and modulation doped MQW structures [Sakaki et al], and have led to the development of comprehensive theoretical modelling by several authors [Schmitt-Rink et al, Sanders and Chang]. The strength of excitonic saturation has been demonstrated to be highly dependent upon the carrier density in the quantum well and consequently this leads to the lifetime of the plasma being a vital parameter for nonlinearity optimisation. The rate of recombination determines the steady state population achievable and varies with the quality of epitaxial growth. Lifetime ceases to be a problem in, for example, a *donor* modulation doped structure as it is only when both carrier types are present (an electron hole plasma) that the opportunity for recombination exists.

Optical Nonlinearities

Recent theoretical work regarding the effects of free electron or exciton gases on excitonic absorption [Schmitt-Rink et al, H.Haug and S.Schmitt-Rink] was motivated by the large optical nonlinearities seen in undoped MQW structures [Chemla et al 1984]. The work by Schmitt-Rink et al discusses a series of dynamic optical experiments by Knox et al which resulted in confirmation of a theory for the quenching of excitonic absorption. The results of this study are directly relevant to the understanding of the QW-FEM mechanism and the conclusions are outlined here.

Optical absorption at the exciton wavelength creates the stable excitonic state which, from temperature dependent linewidth considerations, has a short lifetime of approximately ΔT = 400fs [Chemla et al 1984]. Sub-picosecond absorption measurements at the excitonic wavelength were used to confirm the excitonic lifetime: they revealed that a large exciton quenching effect exists on the timescale of the excitonic decay [Knox et al]. This absorption saturation is the origin of a strong short lived optical nonlinearity, but more importantly for this present study it can confirm the relationship of the theoretical Bohr radius of the exciton to the exciton density in the quantum well: this is described below. Following the decay of the excitons to free electron hole (*e-h*) pairs, on the 400fs timescale, a second distinct exciton screening effect of much longer lifetime is observed. This is found to be approximately half as efficient per carrier pair as the bound excitonic state. This second quenching effect is of nanosecond duration, as governed by *e-h* recombination lifetimes, and is due to the occupation of the states in the subband inhibiting the creation of excitons essentially by band filling effects. This latter effect is the mechanism used in the QW-FEM.

The Pauli exclusion principle applies to the case of the excitonic state [Kittel]. A simple explanation of this is that when two atomic systems (excitons) approach each other there is a tendency for the electrons from one atom to part occupy the identical states of its neighbour, and vice versa. This multiple occupancy of an electronic state is forbidden by the Pauli exclusion principle and results in a strong repulsive force between identical atoms. As a consequence a restricted number of states must exist for excitons in the subband, by the use of a simple volume argument, and occupation of these in an ultrafast nonlinear experiment leads to the observed saturation. More difficult to grasp is the longer timescale interaction of the *e-h* free carrier plasma and the excitonic absorption, which is the vital mechanism for the work in this thesis. The electron can simply be considered to occupy a volume determined by its de-Broglie wavelength [Schmitt-Rink] and this suggests an approximately two fold increase in the density of states for electrons over the density of states for excitons, in reasonable agreement with the results of [Knox et al].

The effects of a free carrier plasma on the quantum well excitonic resonance can be explained from two different angles. Perhaps the most succinct explanation comes from noting that the excitonic state has a binding energy of approximately ≤10meV [Ekenberg and Altarelli] and hence lies to the long wavelength side of the subband edge. With the quasi-Fermi energy in the subband greater than this binding energy the states from which the excitons are "built" are occupied and the excitonic absorption collapses [Chemla et al 1988]. Obviously the sharpness of this cut off is determined by the large effect temperature has on a carrier Fermi distribution. This argument implies excitonic creation via an unbound *e-h* state [Chemla et al 1988].

To expand on this from a different viewpoint, we also note that the creation of *e-h* pairs by photon absorption produces a change in the single particle states of the quantum well resulting in a renormalisation of the subband gap [Kleinman and Miller]. However, the spectral position of the excitonic resonance does not shift significantly due to the neutrality of the bound state [Schmitt-Rink et-al]; i.e. the total effect of the *e-h* plasma on the electron of a bound pair is strongly compensated for by the corresponding effect on the companion hole. This implies that the binding energy of the exciton, relative to the renormalised bandgap, decreases as the carrier densities increase. The result is that the Bohr radius becomes enlarged and consequently absorption strength becomes diminished [Kleinman].

These parallel explanations are obviously related and this is confirmed by studying the basic interactions involved [H.Haug and S.Schmitt-Rink]. The blocking mechanism, inhibiting excitonic creation, is due to the exclusion principle (phase space filling (k-space)), and the changes in the exciton wavefunction are due to the modification of the *e-h* interaction by the presence of other carriers. The interaction with other carriers includes long range Coulomb screening effects and quantum mechanical fermion exchange effects (short range coulomb correlations), the latter of which are again a consequence of the exclusion principle. In fact, the screening of the long range coulomb interaction is diminished due to the 2D nature of the system and tends to be neglected, making the combined effects of the exclusion principle the origin of quenching effect.

Carrier Population Requirements

An exciton in a quantum well may be considered to have a radius in the plane of the well due to the hydrogenic nature of the bound state. Using this dimension (the 2D Bohr radius, a), the maximum achievable *sheet* exciton concentration in a 100Å well was found to be approximately $N_s=6.8\text{x}10^{11}\text{cm}^{-2}$ for a two-dimensional exciton radius of a=65Å [Knox et al]. This simple calculation uses the expression $N_s=1/2\sqrt{3}a^2$ which is the reciprocal of the area of the exciton in a close packed array and assumes simply that the excitons cannot overlap through the Pauli exclusion principle. This figure is in good agreement with the power density used in the short lived exciton-exciton screening experiment described above but is expected to under estimate the density of free electrons required in the QW-FEM. The reasons for this are two fold: firstly, the density of states for electrons is larger than the density of states for excitons as confirmed by the reduced quenching found after excitonic decay to an *e-h* plasma [Knox et al]. This work suggests the under-estimation is between a factor of 1.4 and 2 from incident power considerations. Secondly, the quenching effect in the QW-FEM may be altered by the use of only one carrier type which leads us to study and compare modulation doped structures reported in the literature.

A series of multiple quantum well structures grown by Sakaki et al [1987] have doped barrier layers with increasing doping levels. The doping is *n*-type and the work suggests that sheet carrier densities of approximately $5 \times 10^{11} cm^{-2}$ to $1 \times 10^{12} cm^{-2}$ are needed in the well for a large screening effect to be observed in a 90Å quantum well (figure 2.2.1). This is in good agreement with the

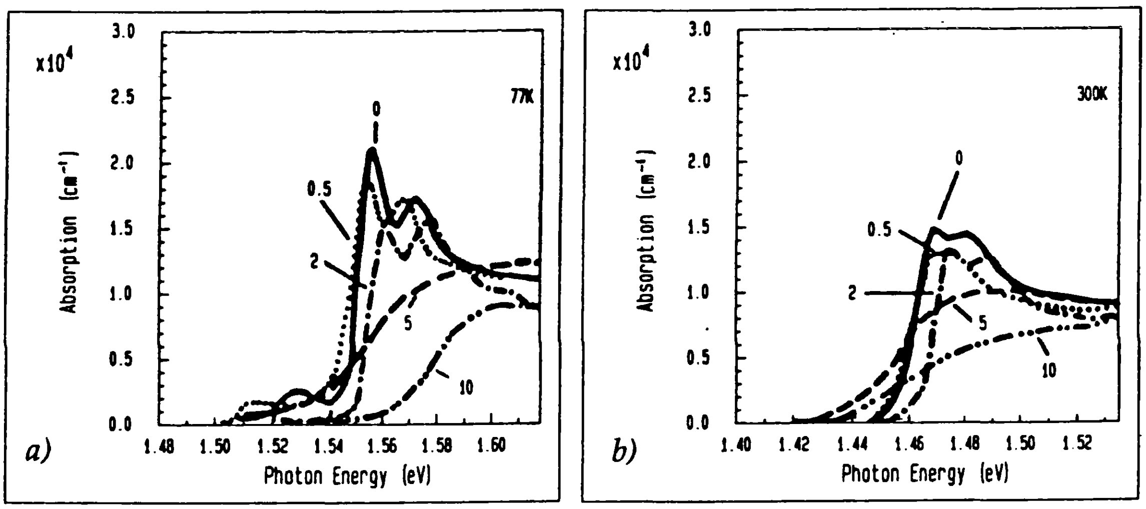

Figure 2.2.1 *Absorption spectra for modulation doped quantum well samples (after Sakaki et-al). The population densities are: 0, 0.5, 2, 5, 10* $x10^{11}cm^{-2}$ *with a well width of 90Å a) 77K b)300K.*

values suggested above from the simple consideration of the exciton radius. The quenching effect found by Sakaki et al is comparable to that seen in optical nonlinearities and would suggest that the the use of a single carrier type is certainly not detrimental to the quenching mechanism.

The modulation doped structure proposed for the QW-FEM is very similar to many Selectively Doped Heterostructure FETs (SDHFETs). These devices have a channel width in the order of that of a quantum well and have adjacent highly doped regions. The motivation behind this kind of structure was discussed in section 1.2 and is the ability to separate the conduction channel charge from the donors which have the detrimental effect of acting as scattering centres in a conventional FET reducing the mobility and transconductance of the device. Several authors have investigated the SDHFET and strived to optimise the performance through the increased population of the channel region. The largest sheet carrier concentrations measured to date [Inoue et al 1984] have values of $2x10^{12}cm^{-2}$ using a doping density of $8x10^{17}cm^{-3}$ in two 500Å regions 35Å to either side of the quantum well.

The sheet carrier density in quantum wells needs to be related to bulk donor levels to enable an estimation of the doping densities required to provide the plasma in the QW-FEM. As a rule of thumb, a doped region 100Å thick, with a doping density of $1x10^{18}cm^{-3}$, corresponds to a sheet donor density of $1x10^{12}cm^{-2}$.

Induced Spectral Shifts

When considering this mechanism for modulation there are three effects other than the quenching of the excitonic resonance which should be accounted for. These effects are all linked to the many body interactions brought about by the carrier population and have been studied in their own rights as the quantum well is a perfect test-ground for these theories.

As mentioned briefly above, the introduction of a large population of carriers into a quantum well changes considerably the bound *e-h* interaction. Simultaneously with the oscillator strength reduction the binding energy is expected to reduce, eventually falling to zero. This effect will quickly shift the excitonic resonance towards the subband edge under increasing electron density, while the oscillator strength diminishes at a smaller rate [Kleinman]. Almost contrary to this effect is the renormalisation of the subband gap. This is termed a Many Body Renormalisation (MBR) and corresponds to a red shift of the energy gap. The origin of this shift is in the effect that an *e-h* pair has on the existing free carrier plasma in the quantum well. The plasma, or "Fermi sea", is polarised by the introduction of photon generated charge through the Coulomb interaction. It is this *correlation* of the carriers which lowers the energy of the Fermi sea and gives rise to the observed bandgap shifts. The apparent rigid shift of *all* the subband gaps is due to the short range of this screened Couloumb interaction which samples a greater region of k-space than that occupied by the Fermi sea (figure 2.2.2a). This suggests that apparent bandgap shift occurs regardless of whether the created *e-h* pair lies to the bottom or the top of the Fermi distribution [Kleinman and Miller]. The work by Kleinman and Miller, also confirmed by others [Tarucha et al 1984] [Delalande et al], suggests that the gap moves with approximately a cube root dependence on the sheet carrier density in the quantum well.

A second and conflicting bandgap renormalisation effect is the Burstein-Moss shift (BMS). The mechanism is the filling of the subband leaving few states free below the Fermi level for an *e-h* pair to be created by photon absorption.

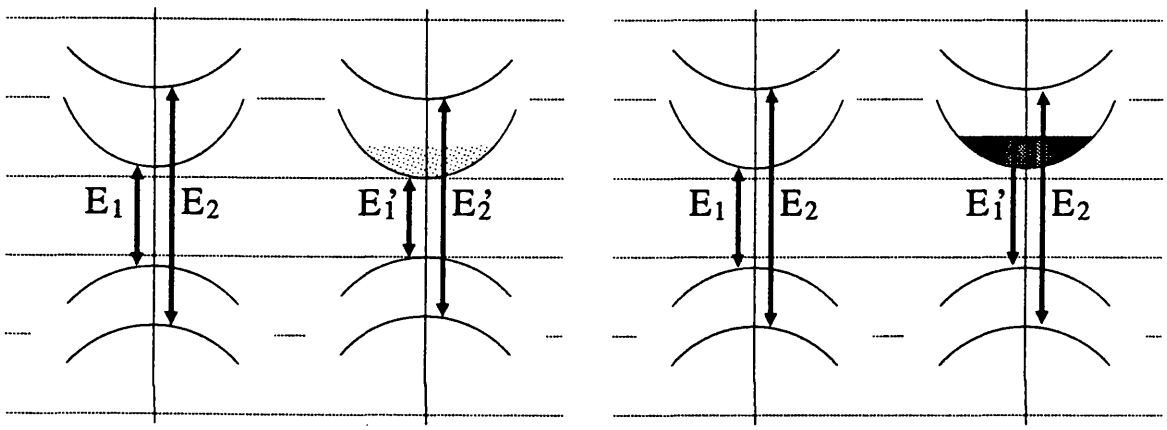

Figure 2.2.2 *Bandgap renormalisation effects a) Many Body Renormalisation showing a narrowing of all of the subband gaps b) Burstein-Moss renormalisation indicating the Fermi level in the n=1 electron subband and the transition available as a consequence.* E_1,E_2 *are the zero population energy levels and* E_1' *and* E_2' *indicate renormalised values*

This widens the gap of only the occupied subband and is distinct from the MBR in this respect (figure 2.2.2b). The BMS has a linear dependence upon the sheet carrier density [Sakaki et al] which causes it to dominate over the MBR at high carrier densities. This is seen to some extent in the low temperature data of Sakaki (figure 2.2.1) at a density of $1\text{x}10^{12}\text{cm}^{-1}$ but becomes a very broadened effect at room temperature where $kT \approx 25\text{meV}$ and is comparable with the Fermi level, leaving a considerable distribution of free states down to the original subband gap.

The effects of carrier induced MBR and oscillator strength reduction are opposites in terms of their effects on the spectral position of the n=1 excitonic resonance and the two shifts are seen to roughly cancel. More significant to the operation of the modulator is the spectral position of the subband edge which advances towards that of the *un-quenched* exciton. This is a likely cause of reduced modulation depth and/or increased insertion loss in the device: the anticipated operating wavelength lies at the absorbing un-quenched excitonic wavelength and in the opposite, transmitting, state the broad tail of the subband edge results (see figure 2.2.1 [Sakaki et al]). Further discussion and calculation of these effects appears in chapter 6 which is devoted to the modelling of the two states of absorption in the device.

A third effect on the spectral position of the excitonic resonance is the considerable band bending brought about by the method of introduction of free carriers to the quantum well. The carriers will typically lie to one side of the well and distort the potential even before any external influence is applied. This in itself is sufficient to change the energy levels in the well through the Quantum Confined Stark Shift (QCSS). The significance to the actual operation of the modulator is less than that of the combination of binding energy and MBR as all the excitonic and subband features of the spectrum will be shifted accordingly. The effective electric field is also less than that which will be applied to the well to instigate carrier removal.

To summarise, the modulation mechanism of excitonic quenching is complex but can be understood in fairly simple terms as a demonstration of the Pauli exclusion principle. Full excitonic quenching can be anticipated for carrier densities of the order of $1 \times 10^{12} cm^{-2}$ sheet concentration, or $1 \times 10^{18} cm^{-3}$ bulk concentration. These densities have been achieved in similar systems and have led to large quenching effects. On a cautionary note, I have indicated that there are several other effects associated with the required high electron populations which may lead to a degradation of the modulation effect.

2.3 Literature Review of Work to Date

Optical Nonlinearity Absorption Changes

The degree of quenching found in the investigation of optical nonlinearities varies from publication to publication but most can be reconciled against one another when the power densities are accounted for. Remaining inconsistencies are predominently due to the sample dependent recombination rates which affect the steady state population density and also variations in the well widths used. Some of the better data is that of Lee,H.C. et al for GaAs/AlGaAs quantum wells which, for the use of a pump beam providing 7.5kW/cm^2, achieves a change in the absorption coefficient of up to 65%. Like all of the data cited in this section, this value considers absorption change at the wavelength of the excitonic feature. This power level is in fact a modest value for use as a probe in optical nonlinearities. Drawing figures from the work of Miller et al [1982] a smaller absorption change (≈50%) is seen at a similar power level, but the use of greater ultimate power densities of up to 35kW/cm^2 gives a peak absorption change of ≥70%. An estimate of the carrier density in the quantum well was provided in this paper and is approximately 3.5x10^{11}/cm^2 for an incident power of 500W/cm^2. This carrier density has been adjusted to take into account accumulation of *e-h* pairs using a population decay time of 21ns, which is the measured recombination lifetime. The absorption change at this power figure corresponds to approximately 1/3 of the maximum seen, and hence a three fold increase in the sheet carrier density figure is a reasonable saturation value and brings this into line with the previous estimates.

Similar data for the "long wavelength" materials such as InGaAs/InP and InGaAs/AlInAs MQW structures also shows good quenching effects. A high absorption change of 86% was demonstrated by Tai et al at a power density of 150kW/cm^2. From the data provided, an estimated absorption change of 64% at 7.5kW/cm^2 can be assumed which shows considerable agreement with the values obtained for GaAs/AlGaAs quantum wells. This publication suggests a carrier density of 6x10^{10}cm^{-2} at 200W/cm^2 which again can be reconciled with anticipated population values as only a 5% absorption change is seen at this power level.

Complete saturation of the absorption at the excitonic wavelength has not been seen in the measurement of optical nonlinearities, but in the light of the discussion in the previous section, regarding the position of the renormalised bandedge, it is possible that complete *excitonic quenching* is being observed. However, it is noted that the very high power densities used to approach full saturation provide experimental difficulties in the form of considerable local heating effects in the sample leading to possible shifts of the spectral features and consequential experimental error.

Modulation Doped MQW Structures

Several authors have studied the effects of plasmas on the absorption of quantum well structures by doping the barrier regions in a MQW stack. This is a simple way to achieve high carrier densities without the experimental difficulties brought about by optical pumping or current injection. The obvious disadvantage to this technique is that the population is fixed in a given sample and carrier density comparisons must be made with other samples grown in a similar manner but in separate growth runs: this introduces experimental error due to growth fluctuations. The data of Sakaki et al (figure 2.2.1) is an excellent example of this approach and has been discussed previously with regard to absorption change and population densities. Several other authors have reported modulation doped MQW structures [Livescu et al][Huang et al][Kleinman and Miller] and discussed bandgap renormalisation and excitonic quenching. Unfortunately, the spectral data is restricted to low temperatures and cannot afford any further information for the potential operation of the QW-FEM, with the exception of the confirmation of bandgap renormalisation theories which are used in the device modelling of Chapter 6.

Selectively Doped SQW Heterostructures

The optical studies of a gated selectively doped quantum well structure were first performed by Skolnick et al in an InGaAs quantum well structure. The work predominently discusses the effect of the electron density on the photoluminescence of the sample but also illustrates photoconductivity as a function of bias. The collapse of the excitonic feature is clearly observed as the Schottky junction is pushed into slight forward bias, populating the quantum well.

Chemla et al [1987] have described absorption switching in the conduction channel of a FET which is in fact a structure nearly identical to that of Skolnick et al. The channel is probed by transmission through the semiconductor substrate and reflection off an oversized gate electrode. The double pass through the quantum well results in transmission change of approximately 2% and an absorption change of $\geq 10{,}000 cm^{-1}$ is calculated: total quenching of the excitonic resonance is inferred. A more complete analysis of the same device [Bar-Joseph et al] shows a larger absorption change of 4% at 10K which corresponds to a change in gate voltage from -0.2 to a forward bias of +1V. Considerable leakage-current-induced carrier heating effects are observed as a consequence and these are modelled, a bandgap renormalisation dependence assumed [Kleinman], and sheet carrier populations of ≈ $8x10^{11}$ derived for the maximum quenching condition. The photocurrent data from the same sample is published by Chemla et al [1988] and shows a large broadening of the bandedge when the exciton is quenched with a corresponding room temperature change in absorption at the excitonic wavelength of ≈70%. Photocurrent spectra published from the work described in this thesis [Tombling et al 1988a] similarly illustrates room temperature excitonic quenching and recovery in a modulation doped structure, but utilises the GaAs/AlGaAs material system.

The selectively doped quantum well structure has proven to be an excellent test ground for the confirmation of many body interaction theories. Photoluminescence (PL) and its related excitation spectrum (PLE) are very sensitive probes of the electronic states of the quantum well and have been used in the study of bandgap renormalisation and the investigation of the Fermi level dependences. Delalande et al have investigated the electron density dependence of the Stokes shift in a single modulation doped quantum well at low temperature. The Stokes shift is indicative of the degree of bandfilling and bandgap renormalisation and can clearly be seen to change from zero for the unpopulated well to 28meV for a density of $6x10^{11}cm^{-2}$. Similar PL and PLE data measured for modulation doped MQW structures [Kleinman and Miller][Livescu et al] has been reconciled directly with MBR bandgap renormalisation calculations and good agreement is found.

Waveguide Modulator Proposals

Devices using exciton quenching for the modulation of light were proposed recently by both Bell Communications Research [Kastalsky et al] and the University of Tokyo [Sakaki et al]. Both propose using the excitonic quenching mechanism in a SQW waveguide configuration with the possibility of dual operation as a FET. Kastalsky also suggests the use of the device as an optically switched FET which would have to operate at milliwatt power levels to satisfy electron density requirements. An important point to note is the mode of operation of the devices proposed by these two authors. To use the terminology of FETs, the use of *depletion mode* [Sakaki et al] [Tombling et al

1988b] may exhibit advantages over *enhancement mode* [Kastalsky et al] due to the removal of the carriers from the quantum well under a reverse bias and the ability to then apply further bias and invoke QCSS for greater modulator performance.

Published Waveguide Modulator Results

The first realisation of a modulator based on a waveguide geometry was demonstrated recently by Bell Communication Research [Abeles et al 1987]. Contrary to their proposed device structure [Kastalsky et al], depletion mode operation was used due to difficulties with the waveguide. Essentially the device attempted to put the core region, and consequently the quantum well, very close to the surface of the device for good electrical control via a Schottky gate electrode. Anticipated FET operation was found in this MEtal-Semiconductor FET (MESFET) configuration but to obtain waveguiding an extra oxide layer had to be added. This produced a Metal-Insulator-Semiconductor (MISFET) device and due to the required optical thickness of the insulating layer degraded the gate operation due to a lack of built-in-field in the semiconductor. High gate voltages $V_{gs} \leq -20V$ and depletion mode operation resulted, nevertheless, for a 750μm waveguide a contrast ratio of 3:1 was obtained: however no indication of the spectral position with respect to the excitonic peak was given. Initial waveguide results measured in this work [Tombling et al 1988b][Tombling et al 1989] illustrated for the first time the actual transmission spectra of the guide and clearly showed the excitonic quenching and recovery effects. A modest experimental contrast of 1.61:1 was reported at this stage but enabled the determination of absorption change at the *excitonic peak* of $8500cm^{-1}$ for a bias of -4V. The higher contrast ratio demonstrated by Abeles et al can be found away from the excitonic peak and at higher bias (section 5.5) but with a large increase in insertion loss penalty.

To conclude, the modulation mechanism of the QW-FEM, excitonic quenching, is understood through the comparison with the comprehensive studies of optical nonlinearities reported in the literature. Secondary effects also result from the large carrier populations required for quenching and these have been highlighted as possible degradations to modulation efficiency. The absorption changes reported in the literature for both doped structures and optically nonlinear experiments are found to be large and hence suitable for optical modulation. The large carrier densities needed for excitonic saturation in the QW-FEM are seen to be achievable by a comparison with FETs which will be expanded upon in the next chapter.

Chapter 3

Design, Epitaxial Growth and Performance Predictions of the QW-FEM

3.1 Introduction
Basic Design Criteria for the QW-FEM

3.2 Semiconductor Growth
Growth Techniques
Growth Parameters Relevant to QW-FEM Design

3.3 Electrical Design
Mode of Operation
Equilibrium Carrier Distribution
Semiconductor Junction Design

3.4 Optical Design of the QW-FEM
Optical Waveguides
Waveguide Model
Performance Prediction

3.1 **Introduction**

The waveguide and optoelectronic design of the QW-FEM is intimately linked with semiconductor growth parameters. This chapter introduces the basic criteria for QW-FEM operation, expands upon the boundary conditions introduced by semiconductor growth, and then proposes optical and electronic designs through the use of computer models.

Basic Design Criteria for the QW-FEM

The multiple quantum well doped barrier structures cited in section 2.2 [Sakaki et al 1987] have shown large exciton quenching effects using the unipolar exciton quenching mechanism but are unable to provide an optical modulation. With a high density of donors present in each of the barriers, sweeping the carriers from an entire MQW structure is impossible. Depletion through a highly doped region in a semiconductor device is generally limited by the breakdown field of the bulk crystal. This field is $4\text{x}10^5$V/cm in GaAs [Sze p103] and, to give an impression of the significance of this value, it is reached after depleting through only 500Å of 10^{18}cm^{-3} doped material. This has the consequence of restricting the design of the QW-FEM to use of a single quantum well. There are two good reasons for this restriction: firstly, the typical n^+ doped region thickness required for a high quantum well population is 100Å-300Å, making the depletion of even two wells difficult and undoubtedly non-uniform. Secondly, the control of the quantum well carrier density is achieved with greater ease and at lower bias, and restraints are lifted on the overall junction structure as described in the design sections below.

A series of design tools are needed to establish the effects of selective doping in quantum well structures, the available control of the carrier population, and the optical structure of the device. These calculations are centred around the basic requirements of QW-FEM as outlined here. A doped region neighbouring a quantum well is required to provide sufficient carriers to fill the N=1 subband. There must also be a junction within the device to enable an electric field to be applied in the region surrounding the well. The mode of operation of the device must then be selected and can either be *depletion* or *enhancement* mode as briefly discussed in section 2.3. For the work in this thesis depletion mode has been emphasised as improved performance can be expected: a justification of this choice is given in section 3.3. Design of the junction for depletion mode operation ensures that at zero bias the carriers reside in the quantum well and that the application of a bias provides a high enough electric field to sweep the carriers from the well. In addition, the quantum well region should form part of the core of an optical waveguide to achieve sufficient interaction length for high contrast optical modulation.

The following sections describe the epitaxial growth and its parameters vital to device design, and the tools used in producing layer specifications for the QW-FEM. These include: a simple description of the electric field in the well region due to the equilibrium distribution of carriers in the structure; a program which models the electric field in a multilayer pn or Schottky junction; a three layer slab model of the semiconductor waveguide; and calculations of the length of the waveguide for optimum modulation. The junction configuration and waveguide design are heavily restricted by the epitaxial growth, and hence this forms a large part of the discussion in this chapter.

3.2 Semiconductor Growth

Growth Techniques

There are two basic III-V epitaxial growth techniques commonly used for the growth of the $Al_xGa_{1-x}As$ quantum well materials. The techniques are those of Metal-Organic Chemical Vapour Deposition (MOCVD) and Molecular Beam Epitaxy (MBE), and although several variations on these techniques do exist their discussion is thought to be beyond the scope of this thesis. The goal of both of these techniques is to grow uniform epitaxial layers of controllable composition, thickness and doping on the surface of a commercially available GaAs wafer. The need for sharp interfaces and thin layers down the order of a few monolayers for quantum well and many other photonic and electronic devices has led to their development.

Possibly the most versatile from the design point of view is the technique of Molecular Beam Epitaxy (MBE) [Gossard]. The technique operates under ultra high vacuum and is an evaporation process using elemental sources. Like the evaporation of metals the flux of constituents adheres to any surface in its path and consequently, shutters can be employed to interrupt epitaxial growth. The substrate on which the growth occurs is heated to ≈550°C to allow surface migration which determines crystalinity. The growth rates in this system can be made sufficiently low that monolayer deposition on a 1s timescale is possible. Also, since the beams can be interrupted in less time than it takes to deposit a monolayer, the interfaces of material or alloy composition are very abrupt and the process is highly repeatable. MBE is a slow growth technique making it largely unsuitable for mass production, and often suffers from moderate to high densities of surface defects.

The technique of MOCVD [Roberts et al] is carried out in a quartz reactor tube and is performed at atmospheric pressure or in an intermediate vacuum of ≈10mTorr. The metal-organics, such as TriMethylGallium, are passed into the chamber with group III hydrides (eg AsH_3) and dopants (eg SiH_4) mixed with hydrogen as the carrier gas. The supply of these reagents is such that each can be switched on or off line very rapidly using a manifold in close proximity to the reaction chamber. These gasses then pass over a graphite substrate holder which is heated to temperatures of around 700°C by either induction or radiant heating. At the substrate, the compounds decompose and adhere at growth rates again with a typical minimum of 1 monolayer per second. The interfaces are abrupt, but since the reagent transit and switching time is not as quick as in MBE the interfaces are inferior. MOCVD growth can operate at rates very much greater than MBE and also has the advantage that large reactors can be formed which will enable many substrates to be prepared simultaneously.

Both growth systems depend upon the purity of the reagents or elements used for the quality of the end result. Typically minimum doping levels suffer from the introduction of contaminated sources. The MBE technique is less prone because of the elemental nature of the evaporants which are kept under ultra high vacuum. MOVPE on the other hand uses gaseous sources and a maze of pipe work and valves to deliver the gasses to the reaction chamber: contamination is unavoidable and compound sources (especially aluminium organics) are less pure leading to higher background doping levels.

When intentionally doping the semiconductor, the donor and acceptor interfaces are of vital importance to thin layered epitaxial structures. In addition to the consideration of the switching characteristics of the two systems mentioned above, the effects of diffusion must be included. The high temperatures of semiconductor growth allow donor or acceptor diffusion on the atomic scale, resulting in less abrupt interfaces. Frijlink et al suggest that this is better than 10nm for MOCVD material, whereas Inoue et al[1984] have found a value of $35<L_{diff}\leq 90$Å for material grown by MBE using silicon as a donor. The effect is thought to be due to segregation or diffusion, and is shown to be dependant on the growth temperatures and growth rates used.

Low dimensional heteroepitaxial structures can also suffer from the *Inverted Heterojunction Problem* [Morkoç et al]. This is a recognised problem related to the growth of GaAs on AlGaAs which is not seen with the reverse heterointerface. A marked reduction in crystalinity is found, and is most evident in the attempts to produce two dimensional gases in proximity to the interface (figure 3.2.1). Reductions in the mobilities occur and are attributed to an increased number of scattering centres at the interface. The problem has been largely overcome by several authors [Inoue et al 1984, Powell et al] as indicated by the excellent mobilities in *double* heterostructure FET channels.

Growth Parameters Relevant to QW-FEM Design

The points raised above indicate that the heterostructure FET, and consequently the QW-FEM, are very sensitive to the quality of epitaxial growth. There are two main parameters vital for the design of the QW-FEM. The first is the level of the unintentional doping in a layer of GaAs or AlGaAs and the second is the width of the spacer region required between the doping spike and the quantum well to avoid the segregation effects. The predominance of the use of MOCVD growth in this work has led to the basic design being centred around the restrictions imposed by this technique.

Low background (unintentional) doping in semiconductor growth is vital for the design of many devices. The parameter is difficult to control and the level achieved in the MOCVD material used in this thesis* is typically between 5×10^{14} and $5\times10^{15}cm^{-3}$ for GaAs, and has a compositional dependence which is an increasing function of x for $Al_xGa_{1-x}As$ [Roberts et al]**. The dependence of the acceptor level on the aluminium mole fraction is due to the carbon from the aluminium alkyl being incorporated as an impurity. The GaAs impurity level in the QW-FEM should be as low as possible, but is not as vital for this device as the MQW devices discussed in Chapter 1. More important, however,

* *Epitaxial growth at the University of Sheffield (J.S.Roberts et al)*

** *The GaAlAs MBE material supplied by Amoco Corporation has a very low background doping level ($<5\times10^{14}$) which is independent of Al mole fraction* is the unintentional doping in AlGaAs which forms both the barriers of the quantum well and the waveguiding structure of the device. The layers, with aluminium mole fractions between 20% and 45%, have an unintentional *p*-type doping which is typically in the region of 10^{16} - 10^{17}cm^{-3} [Roberts et al]. Low doped *n*-type material is consequently very difficult to produce due to the carefully adjusted "back-doping" which must be used. Knowledge of these doping values is vital to the combined design of the junction and waveguiding structure of the QW-FEM.

The second, and perhaps more important, parameter is that of the heterojunction and doping interfaces which are more likely to cause the catastrophic failure of the device (figure 3.2.1). The quantum well in the QW-FEM structure must remain undoped for effective operation and this is achieved in the manner used for SDHFETs. The n^+ doping which provides an electron population is separated from the quantum well by an undoped spacer layer. This region soaks up any donor diffusion which occurs during the growth process and was chosen as 100Å for the majority of the layer structures used. The *inverted* heterojunction interface on the other hand, has been shown to be of good quality by the work of Powell et al*. The effects this interface is reported to cause [Morkoç] are of lesser importance for the initial operation of the QW-FEM than for the SDHFET.

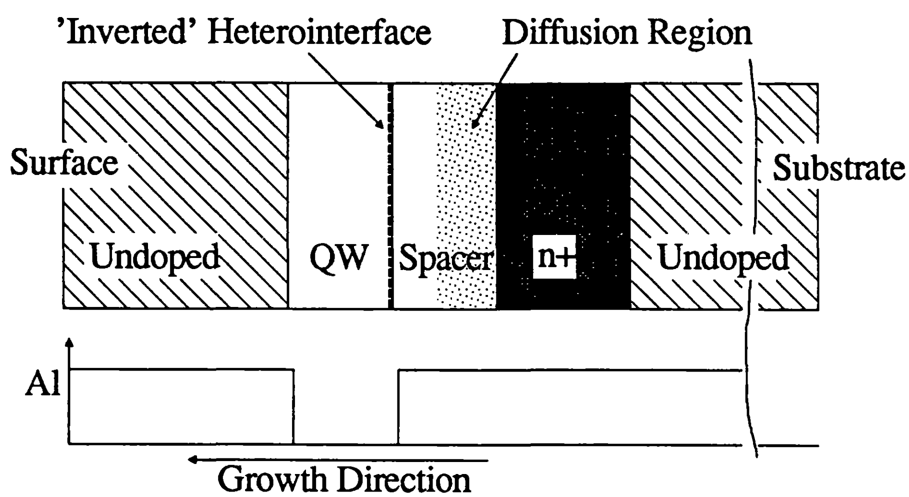

Figure 3.2.1 *The heteroepitaxy in the region of the quantum well illustrating the inverted heterojunction and donor segregation effects.*

* *Epitaxial growth at the University of Sheffield (J.S.Roberts et al)*

3.3 Electrical Design

Mode of Operation

The basic electrical requirements of the QW-FEM were outlined above and the preference for the depletion mode of operation was indicated. This choice introduces major advantages in terms of the flexibilty and tolerances in the design of the structure, and these will unfold in this and subsequent sections. There are three main arguments for the use of depletion mode operation:

1) FETs reported in the literature which achieve the highest sheet carrier densities tend to operate in depletion mode [Inoue and Sakaki]. The essential difference between the two modes is that an enhancement mode device must deplete the conduction channel at zero applied bias, i.e. using the internal field of the Schottky or *p-n* junction. As a consequence of this, the enhancement mode device suffers from being restricted in the thicknesses of the donor regions which can be used with the consequential limit on the population of the quantum well.

2) Forward bias must be used in an enhancement mode device to control the carrier density in the quantum well. This provides a limitation in that as the built in voltage of the junction is reached, corresponding to optimum population, injection commences causing large leakage currents. This heats the carriers in the quantum well [Chemla et al 1988], red-shifting the spectral features in a manner which is detrimental to high contrast modulation.

3) With the device in reverse biased operation (depletion mode), not only is the carrier density under greater control due to the extra field available, but following the removal of the carriers from the quantum well further applied bias will invoke the QCSS. This may lead to increased modulation depth in the device with no penalties to the operation of the device as a FET.

On balance, depletion mode operation requires higher peak electric fields in the quantum well to produce the control of carrier population. Low field conditions exist in the enhancement mode device hence it is favoured for the study of the physical effects of the continuous transition from high to low population on the excitonic absorption [Chemla et al 1988].

Equilibrium Carrier Distribution

The electric field associated with the removal of excitons from the quantum well subband is an important parameter when considering the carrier control aspects of the QW-FEM. A value for this field is determined by use of a simple model for the carrier distribution in the well region. An infinite doping spike separated from the quantum well by a spacer layer is considered. The quantum well is then assumed to have the n=1 subband full of carriers and consequently this level was assumed to line up with the Fermi level in the highly doped region. Figure 3.3.1 shows the equilibrium and applied external field conditions for the quantum well. The equilibrium state also assumes that the quantum well is not subject to an external field in the depletion region of a junction.

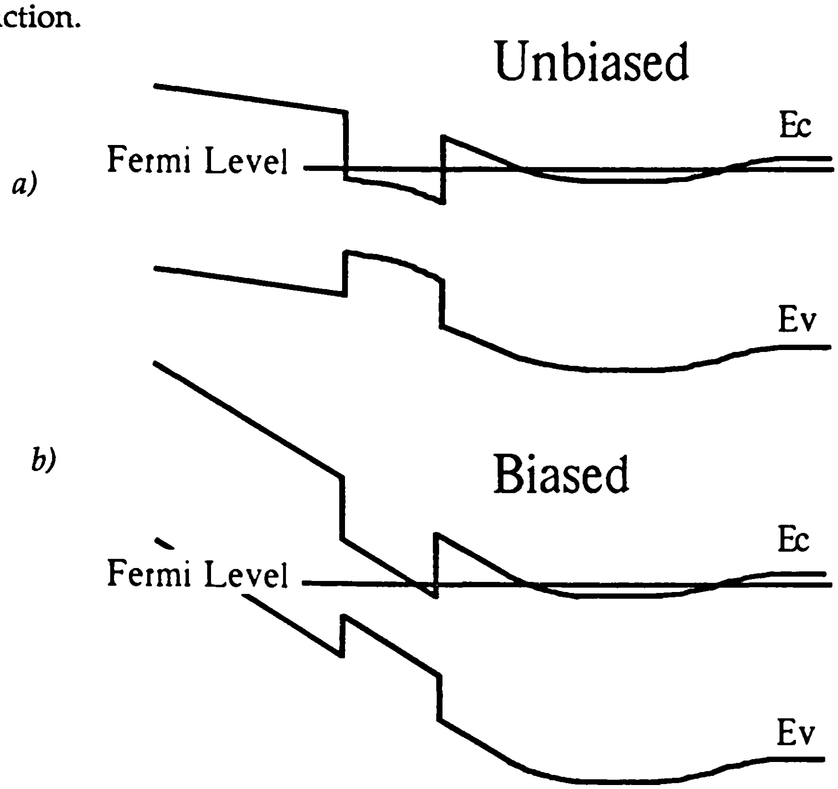

Figure 3.3.1 *The two states of the quantum well population. a) High population b) Zero population. The band bending signifies a changing population with distances and indicates electrons lying to one side of the full quantum well and a large field between the well and the doping spike. The straight bands in the empty quantum well indicate zero population by a similar argument and illustrate the equality of the in-built field and the applied field.*

Taking a value for the effective conduction band step, ΔE, at the barrier of a 100Å quantum well:

$$\Delta E = \Delta E_c - E_{el}^1 \cong 126\text{meV}$$

where ΔE_c is the conduction band offset [Duggan et al] and E_{el}^1 is the first electron subband level (section 6.2), a value for the electric field ξ can be determined from a mean *well-doping spike* separation of $\Delta x \cong 150$Å:

$$\xi = \Delta E/\Delta x \cong 84\text{kV/cm}$$

This corresponds to a built-in field across the undoped spacer region between the well and barrier which is a product of the equilibrium distribution of carriers. This simple calculation is confirmed by determining a sheet carrier density in the quantum well under these conditions (Q_{well}). Using Poisson's equation in one dimension:

$$\frac{d\xi}{dx} = \frac{\sigma(x)}{\varepsilon} \approx \frac{\Delta\xi}{\Delta x} = \frac{Q_{well}}{\varepsilon}$$

with the values of $\delta\xi$ and δx used above, Q_{well} was found to indicate a sheet density in the quantum well of approximately $6\text{x}10^{11}\text{cm}^{-2}$. This agrees well with the anticipated sheet carrier densities described earlier, confirming that this approximation gives a reasonable value for the electric field between the well and the doped region under equilibrium conditions. Similar values for both the field and carrier density are obtained with well widths down to 50Å.

To remove the electrons from the quantum well and provide the excitonic absorption recovery, an electric field of this strength must be applied across the quantum well. This zero population state is illustrated in figure 3.3.1b. Thus a field of $\approx 10^5$V/cm must be provided by a reversed bias junction in the vicinity of the well. The junction may be either a doped pn junction, Schottky contact or MOS structure, any of which can readily achieve the necessary electric field levels.

Semiconductor Junction Design

The basic QW-FEM electrical structure has been derived and this must now be moulded into a full epitaxial layer specification. As mentioned above, a rectifying junction must be formed so that an electric field can be applied across the quantum well region. To illustrate this the three schemes used in this work are shown in figure 3.3.2.

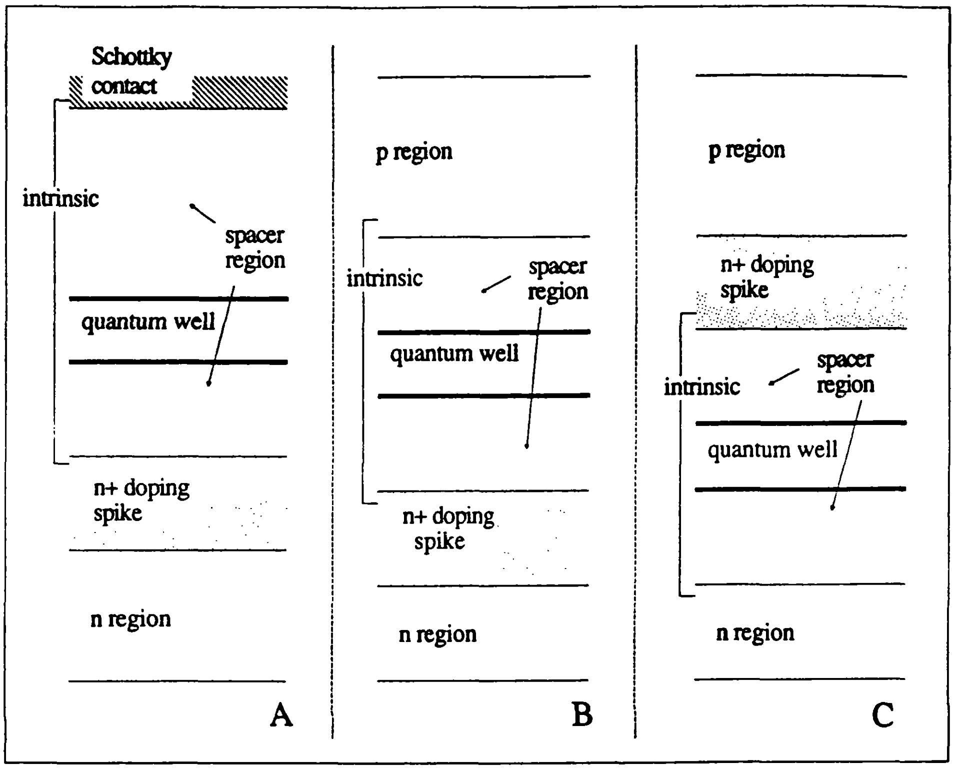

Figure 3.3.2 *The three basic junction configurations for the QW-FEM devices in this thesis. Type A is a Schottky device, Type B is a depletion mode p-n configuration and Type C is a p-n depletion/enhancement mode structure.*

The electric field in these diode structures was modelled as a *multilayer p-n*/Schottky junction with the thickness and doping of junction regions as input parameters. The field program does not take into account any heterojunctions within the device and is based on an abrupt junction approximation [Seymour]. The multilayer approach is necessary to take into account the depletion of combinations of intrinsic and highly doped regions, such as the quantum well and doping spike regions. The computational approach used to solve the problem is iterative by nature and it is the integral under the electric field curve which corresponds to the combination of applied and built-in junction bias. The electric field across a depletion region falls off at a rate dependent upon the impurity concentration so that field gradients can be found for each layer. From this information, and the obvious boundary condition of ξ-field continuity at each interface, the maximum electric field at the *p-n* junction is adjusted in an iterative loop to cause the integral of depletion region electric field to equal total voltage (applied and built-in). I developed the model on an IBM PC using the Pascal programming language and the graphical output plots a succession of field curves for different applied biases on an HP7475 plotter.

The voltage dependence of the electric field is illustrated in figure 3.3.3 for the three designs above. These plots show the position of the junction and the quantum well, with the discontinuities in the ξ-field gradient differentiating between the regions of differing doping. The field of typically $\geq 10^5$V/cm needed to remove carriers from the well is easily achieved in these structures and the reverse bias operating voltage can be inferred from the curves. This parameter is very useful when a comparison with experimental data is made.

The influence of the growth parameters on the layer structure design is strong (section 3.2) and the over-riding parameter for this section of the design is the minimum doping in the layers surrounding the quantum well. The intricacies of the full design unfold at this point: the need for provision of the waveguide configuration introduces undesirable doping levels due the material compositions which must be used and compromises the electric field control achievable within the junction. This is especially relevant to the Schottky diode which must deplete from the surface of the structure (figure 3.3.3a), through the high Al concentration cladding region, and into the core region in order to control carrier density in the quantum well. The limitation is the maximum electric field which GaAs can support: typical anticipated values are approximately $4\text{-}5 \times 10^5 \text{Vcm}^{-1}$ [Sze p103] and are reached with unfortunate ease. The waveguide optical profile will be discussed in the next section but the trade offs that are introduced need to be discussed here. Basically, for the Schottky device, the quantum well and waveguide core needs to be as close to the surface of the structure as possible for the population control to exist. Ordinarily, a FET would have only a 500Å separation of the conduction channel and surface Schottky contact, whereas a typical GaAs waveguide would have a peak optical field at a depth of the order of 1-2μm. Overlap of the optical field with the surface and its contacting metallisation is undesirable, consequently in narrowing the upper cladding region the Aluminium concentration must be increased to decrease the

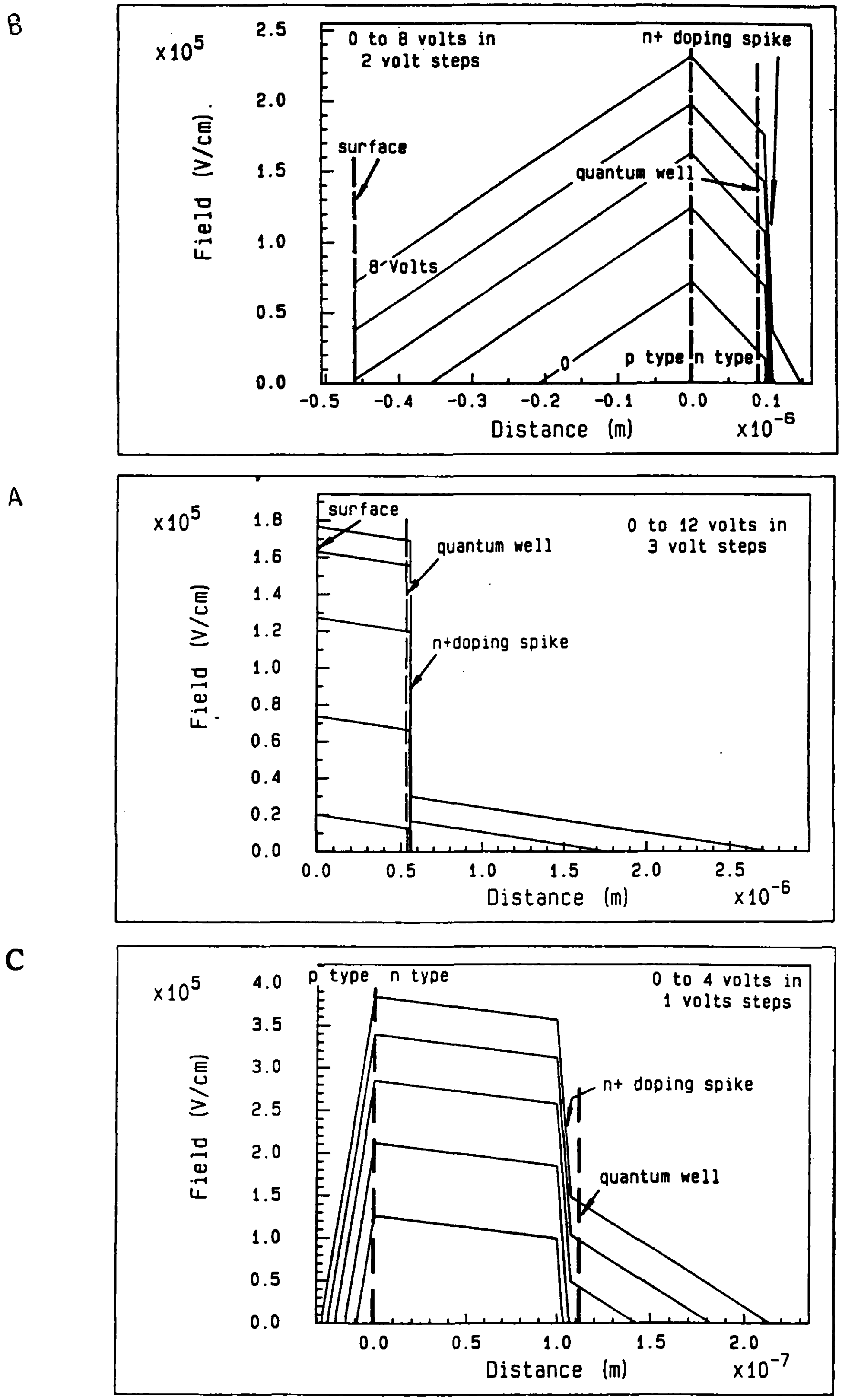

Figure 3.3.3 *Bias dependent electric field curves for the three basic design of the QW-FEM illustrated in figure 3.3.2*

refractive index and truncate the optical field. This has the undesirable consequence of introducing higher doping to this layer using the MOCVD growth technique, again reducing the depletion characteristics of the junction. This produces a seemingly endless loop which is in fact halted when back-doping becomes controllable, giving an approximate donor level of $\approx 5 \times 10^{16}$ in the upper cladding region.

For the *p-n* junction configuration, the emphasis again lies with the need for low doping levels in AlGaAs regions although many of the restrictions of the Schottky device are lifted. The electric field profiles of figure 3.3.3a,b show that the fields required at the quantum well ($>10^{5}$Vcm^{-1}) are more easily achieved, although again the breakdown field of GaAs comes into play at the interface between the *p* and *n* regions. Careful consideration of this is required as it restricts the level and thickness of the doping spikes which can be depleted. Nevertheless, when designing the structures, it was found that since the necessary field could be readily attained a judicial choice of the doping levels and layer thicknesses could relax those tolerances required from the growth process.

3.4 Optical Design of the QW-FEM

Optical Waveguides

An optical waveguide consists of a high refractive index core region surrounded by a low index cladding region [Hecht and Zajac]. Light is guided along such a waveguide core by the total internal reflection which results from this refractive index step. In the case of a semiconductor waveguide, a slab arrangement is used which provides optical confinement in the vertical direction only. Here, a high index core region is sandwiched between two low index cladding regions (figure 3.4.1a). Lateral confinement can be obtained by etching a rib into this structure (figure 3.4.1b) allowing air to provide a low index step. Varying refractive indices in GaAs/GaAlAs waveguides are obtained by altering the alloy composition, x ($0 \le x \le 1$): the refractive index decreases with increasing aluminium mole fraction.

The main optical requirement for high contrast modulation in the QW-FEM waveguide is that the absorbing quantum well region lies in the core region where a strong overlap with the optical field is found. This decreases the length of guide required for high contrast modulation and reduces the device insertion loss (see 'Performance Prediction' below). To use semiconductor laser terminology, the waveguide structure used is a separately confined heterostructure (SCH). For a MQW structure this typically implies that the optical confinement, which can be provided by the index change due to the quantum wells themselves, is increased by the use of alloy compositions higher than the well barriers in the waveguide cladding regions. In this way, the core width is not tailored by the number of wells and more control over the overlap of the optical field is achieved.

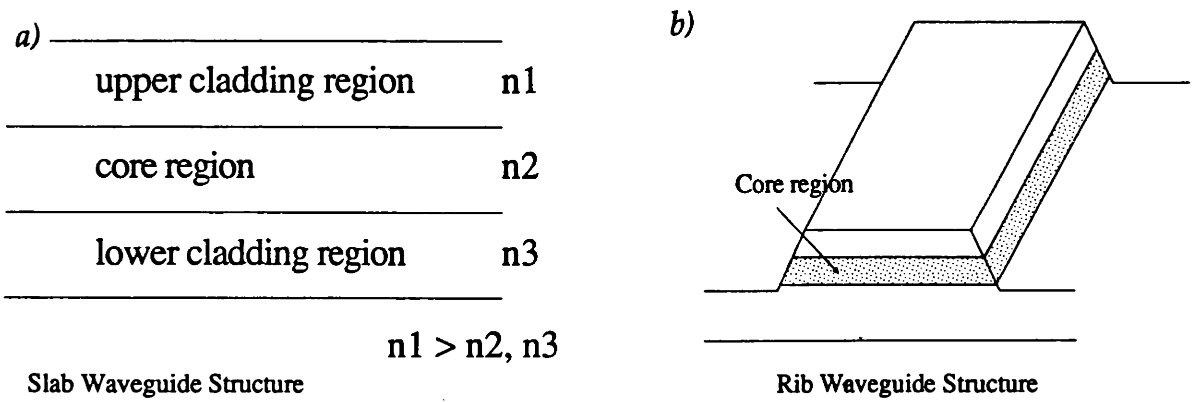

Figure 3.4.1 *Slab waveguide layer structure (a) and the implementation of lateral confinement (b)*

The design of the optical waveguide for the QW-FEM was largely influenced by the electrical structure. Foremost was the need for a quantum well in the core of the guide. This placed a restriction on the core alloy composition which must be high enough to give the conduction band step required to form a GaAs quantum well, but low enough to enable further alloy composition increases to give large index steps for implementation of the SCH structure. The influence of the doping levels in these AlGaAs layers has been noted above with the conclusion that the optical field must be brought towards the surface of the device without large overlap with the surface contact which would result in waveguide loss. The final design criteria is the need for the waveguide to support only a single optical mode.

Waveguide Model

The waveguide was modelled using a three layer slab waveguide approximation [Thompson] and a mode profile of the resulting waveguide design is illustrated in figure 3.4.2. The quantum well position and the three regions of the slab guide are indicated. This modelling was performed on an IBM PC using the Pascal programming language. The program takes aluminium mole fraction data and layer thickness as inputs and generates a graphical output of the supported mode profiles. As well as these profiles the waveguide

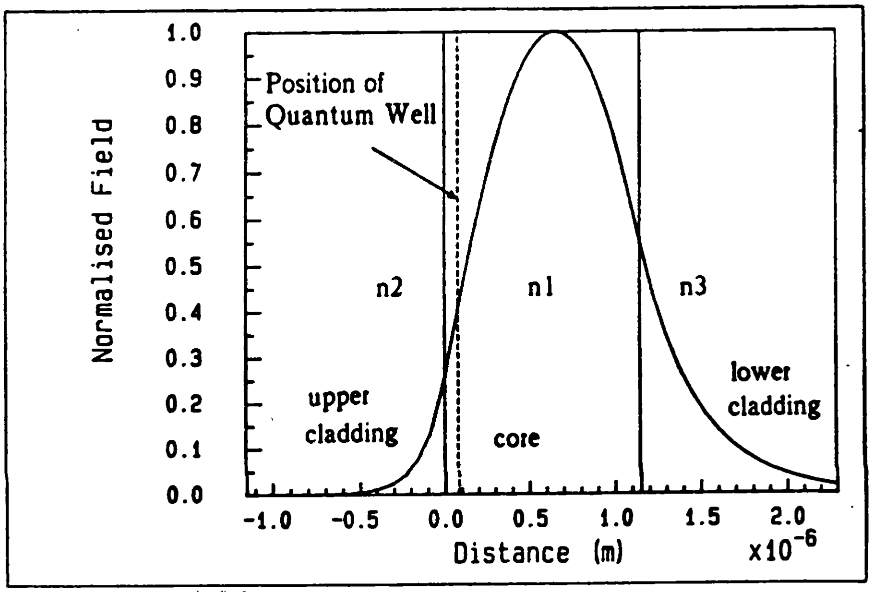

Figure 3.4.2 *Optical mode profile of the QW-FEM waveguide*

model also supplies the important parameter of optical field overlap with the quantum well Γ_{well} and an approximation of the same parameter for the surface metal $\Gamma_{surface}$. Reduction of the separation of the quantum well from the surface of the structure was achieved by using an asymmetric waveguide. The optical field has been minimised at the surface and the profile has been pushed towards the substrate by using a larger index step at the upper interface than at the lower interface: this enables a reasonable value for Γ_{well} to be maintained. The refractive indices used in the illustration (figure 3.4.2) correspond to GaAlAs alloy compositions of 0.2, 0.45 and 0.25 respectively. The calculation indicated that the guide only supports a zero order mode at the 850nm operating wavelength and the first order mode cut off lies at 790nm. The refractive index alloy composition dependence is given by the expression [Casey and Panish p45]:

$$n(x) = 3.590 - 0.710x + 0.091x^2$$

Performance Prediction

Using the design of the waveguide described above and data for excitonic quenching from the literature, the anticipated operation of the QW-FEM can be calculated. The change in absorption coefficient for the quantum well is derived from the data of Sakaki et al. (figure 2.2.1) and is seen to decrease from 15,000 to 5,500 cm^{-1}. These figures correspond to absorption in well material only, i.e. the well barrier ratio has been removed form the data. To outline the performance of the device and illustrate the calculation, a modulation contrast ratio of 10:1 was set as a target. Using the overlap of the optical field with the quantum well (100Å) in the waveguide of Γ_{well}=0.25%, the expression

$$\text{Modulation Ratio} = \exp(\Gamma_{well}\, \Delta\alpha\, L)$$

was used to determine the length (L) of waveguide required. For the absorption data above, a length of 970µm was found. This length could then be used to find the minimum absorption in the guide, representing the insertion loss under conditions of perfect coupling.

$$\text{Insertion loss (dB)} = 10 \text{ Log } (\exp(-\Gamma_{well}\, \alpha_{min}\, L))$$

For a modulation depth of 10dB, an anticipated insertion loss of -5.4 dB was found. The contribution to the absorption coefficient in the guide due to the well region alone is ($\Gamma_{well}\alpha_{min}$) 13.8$cm^{-1}$. The absorption due to free carriers in both the semiconductor and the metal contact can be expected to contribute up to a maximum of 2cm^{-1} [Casey and Panish] representing a further -0.8 dB loss. The values used in these calculations are representative of the waveguide design which has had to be adopted for the Schottky device. The absorption data of Sakaki et al was the only clear published spectral data available and shows only a 63% change in absorption at the excitonic peak. Larger values for the absorption change have been reported and were cited in section 2.3.

Further calculations of the performance of the QW-FEM using measured spectra and a scheme for further optimisation appear in the results section (Chapter 5).

Conclusions

The design of the QW-FEM centres around the structure of SDHFETs which have demonstrated the carrier densities needed for the QW-FEM. To use the terminology of FETs the *depletion mode* of operation has been argued to have advantages over *enhancement mode* devices, and hence this is the prefered design used in this work. The final semiconductor junction designs are highly interlinked with the waveguiding structure required to perform the function of optical modulation: it is the semiconductor growth parameters which make optical and electrical properties inseparable through the limits to the minimum doping levels which can be achieved. As a consequence of this, the waveguide design used is asymmetrical enabling reduction of the thickness of the upper layers of the epitaxial structures and hence greater electrical control of the absorption in the quantum well.

Chapter 4

Fabrication and Measurement Techniques

4.1 Introduction

The devices used for the studies described in this thesis were fabricated from semiconductor structures grown in the gallium-arsenide /gallium-aluminium-arsenide (GaAs/GaAlAs) material system at Sheffield University and Amoco Research Center. This chapter addresses the experimental fabrication steps and measurement techniques required for the variety of devices discussed elsewhere in this thesis.

Device Types

Typically, two types of device are fabricated from each epitaxial layer: 1. *Transverse Photodiodes* which enable rapid and accurate assessment of performance by means of photocurrent measurements under applied voltage; 2. *Waveguide Devices* which allow full biased transmission spectra to be measured. These two basic device types are illustrated in figure 4.1.1 with their modes of operation indicated by arrows showing the direction of incident light. The fabrication process steps differ for these device classifications (waveguide or transverse) and are also divided by the junction type (*p-n* or Schottky). The optical analysis methods which use either a monochromator or laser system are also divided by the device type, with the laser system being used for the waveguide structures due to the ease of optical coupling. The electrical measurement techniques used are restricted to current-voltage plots to check functionality of both device types, and

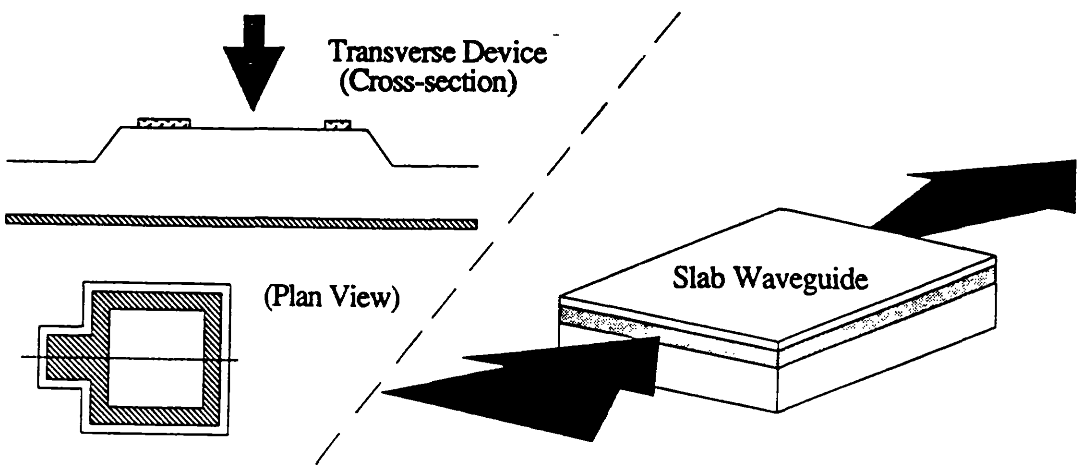

Figure 4.1.1 *Basic device types and modes of operation.*

capacitance-voltage doping profiles which are performed using the transverse photodiode.

4.2 GaAs Fabrication Techniques

Processing Steps

Three fabrication sequences are listed in table 4.2.1 and each has been refined to help with repeatedly producing successful devices. The first column represents the fabrication of a *p-n* or Schottky photodiode with the structure grown on an n^+ substrate. The second column is the sequence for producing a waveguide device from the same layer structure. The third column is the full fabrication process for devices having semi-insulating substrates. An

Device Type:	Transverse Photodiode	Slab Guide	Mesa on SI Substrate
Process			
Mount on Glass Slide	•	•	•
Substrate Thinning	•	•	•
n-Metal Deposition	•	•	
Demounted from Slide	•	•	•
Contact Alloying	•	•	
Mounted on Cover Slip	•	•	•
Photolith Step	•		•
Top Metal Deposition	•	•	•
Lift-off	•		•
Photolith Step	•		•
Mesa Etching	•		•
Photolith Step			•
n-Metal Deposition			•
Demounted from C/Slip	•	•	•
Cleaved to form W/Guides		•	

Table 4.2.1 *Fabrication procedures for various device types*

illustration of the fabrication process, which corresponds to the most complex situation of a mesa etched structure grown on a semi-insulating substrate, is shown in figure 4.2.1.

The fabrication of a transverse photodiode can be seen to involve more fabrication steps than that of a slab waveguide device due to the greater complexity of the mesa etched structure. Mesa etched devices require the use of photolithography and consequently the processing of these devices involves the use of clean room facilities. Slab waveguide geometry devices, however, can have very simple construction and neither mesa etching nor selective area metal deposition are required unless a semi-insulating substrate is used. The individual steps described in table 4.2.1 have been optimised for ease of fabrication and device performance, and are outlined in the sections below.

Substrate Thinning

To form individual devices the substrates have to be thinned to enable cleaving between mesas or to suitable sizes for slab waveguide devices. The need for thinning is greatest with the slab waveguides as the electrical, and to some extent, the optical characteristics of the device are determined by the quality of the cleaves. The substrates are generally thinned before any of the fabrication is performed which eliminates the chance of destroying fully fabricated devices. This has the disadvantage of increasing the difficulty of handling the samples during processing and consequently, the technique of mounting the samples on glass cover slips throughout was introduced. To perform the thinning operation, the sample is mounted on a glass slide with a low temperature wax and rough thinning of the substrate achieved manually using carborundum powder (1000 grit) mixed to form a smooth paste with deionised water. The substrate thickness was gauged by use of adhesive tape placed to either side of the sample which arrests the thinning when the sample and tape thicknesses are equal. No further polishing of the wafer is performed as the optical properties are of no importance and ohmic contacts are readily achieved on the rough surface.

Metallisations

Two forms of contact are commonly used on semiconductor devices [Sze Ch.5]. The first is an ohmic contact which relies on a very heavily doped surface region to give a low resistance and good ohmic behaviour. The second is a Schottky contact which generally requires a low doped surface region and large differences in work functions between the metal and the semiconductor to give rectifying behaviour.

For the variety of devices fabricated four metallisations schemes are used. The first contact applied to devices with n^+ substrates (Table 4.2.1) is the back contact. This is an ohmic metallisation formed from Sn (≈100Å) and Au (≈1200Å) which are evaporated sequentially in an Edwards 306 Vacuum Evaporator. The layer thicknesses are generally accurate to approximately ten percent through the use of a film thickness monitor (Edwards 3456). To give the contact its ohmic behaviour a short furnace alloying cycle is required (90s @420°C, nitrogen atmosphere) following deposition. Structures with *p-n* junctions then require a *p*-type ohmic contact on the surface layer. This is formed from Cr (≈50Å) and Au (≈1200Å) in a manner identical to that used for the SnAu contact. Neither of these metallisations are very sophisticated and, although ohmic, are generally quite resistive. This is not a major problem for the analysis of these structures and as long as the contacts have a resistance much less than that indicated by the anticipated reverse bias leakage current the expected behaviour of the device will be observed. In addition to these two basic metallisations a Schottky contact is required for the undoped structures. The Schottky contact must cover the optically active region without a window (used for the pn devices, figure 4.2.1) to enable bias to be applied within the structure. This requires the contact to be transparent for optical access. The metallisation is again formed from successive evaporation of Cr and Au but using extremely thin layers (≈5Å and ≈20Å respectively) and without the use of an alloying cycle [Rivers]. The final contact variety performs the special task discussed in section 7.4. A two dimensional electron gas exists in the quantum well and this can be contacted for the implementation of FETs. Mesa etching, discussed below, is used to strip the upper layers of the structure and approach the quantum well. A metallisation of In (≈50Å) Ge (≈100Å) Au (≈1200Å) is then deposited and alloyed in a nitrogen atmosphere for approximately 5 mins at 420°C to diffuse an *n*-type region down to the quantum well.

Photolithography

Standard photolithographic techniques were used for definition of metallisations and mesas during fabrication of the various devices. The photolithographic masks used for fabrication were designed using the GALIC computer aided design facility and were fabricated at Rutherford Appleton Laboratories.

The etching of a mesa is the most simple application of the photolithographic process. This is illustrated in part 2 of figure 4.2.1. Photoresist is applied, exposed to the mask and developed so that it covers the desired area; etching can then be performed by the method described below to produce the desired surface relief. A more demanding application of photolithography is the definition of the metallisation features. This is illustrated in parts 1 and 3 of figure 4.2.1. Gaps in the resist define where the metal will lie on the surface of the semiconductor, the deposition is then performed and unwanted metal is removed by dissolving the underlying resist. This relies on sharp definition of the resist edges and frequently the use of ultrasound is required to remove the waste metal when the photolithographic definition is substandard.

Photolithography on small samples is a difficult task. Resist build up at the edges of the samples stops good contact with the mask during resist exposure. This both reduces definition, which stops the formation of vertical resist edges needed for lift off of metallisations, and increases the difficulty of aligning successive masks to the features formed on the sample. The thinning of the substrates before lithography commences requires that samples are mounted on glass cover slips throughout processing to facilitate handling: this proves beneficial in reduction of resist build up as the coating spreads evenly across both sample and cover slip, and hence this vastly improves the lithographic process.

Mesa Etching

The purpose of mesa etching is to reveal layers of the semiconductor which lie below the surface of the *as-grown* structure. This can either be simply to form individual devices by providing isolation between each mesa, or to reveal a layer suitable for coating with a contact metallisation. GaAs mesa etching is performed using a fairly dilute ammonia peroxide etch giving a consistent etch rate of approximately 1 µm/min (H_2O : H_2O_2 : NH_4OH @ 20 : 1 : 1). Before etching the mesa, a 30s dip in silicon dioxide etch is used as an oxide removal and clean up stage (MIT Buffered HF [NH_2F : HF 7 : 1]).

The GaAs etch then produces smooth clean surfaces and good device breakdown voltages are generally achieved as a consequence.

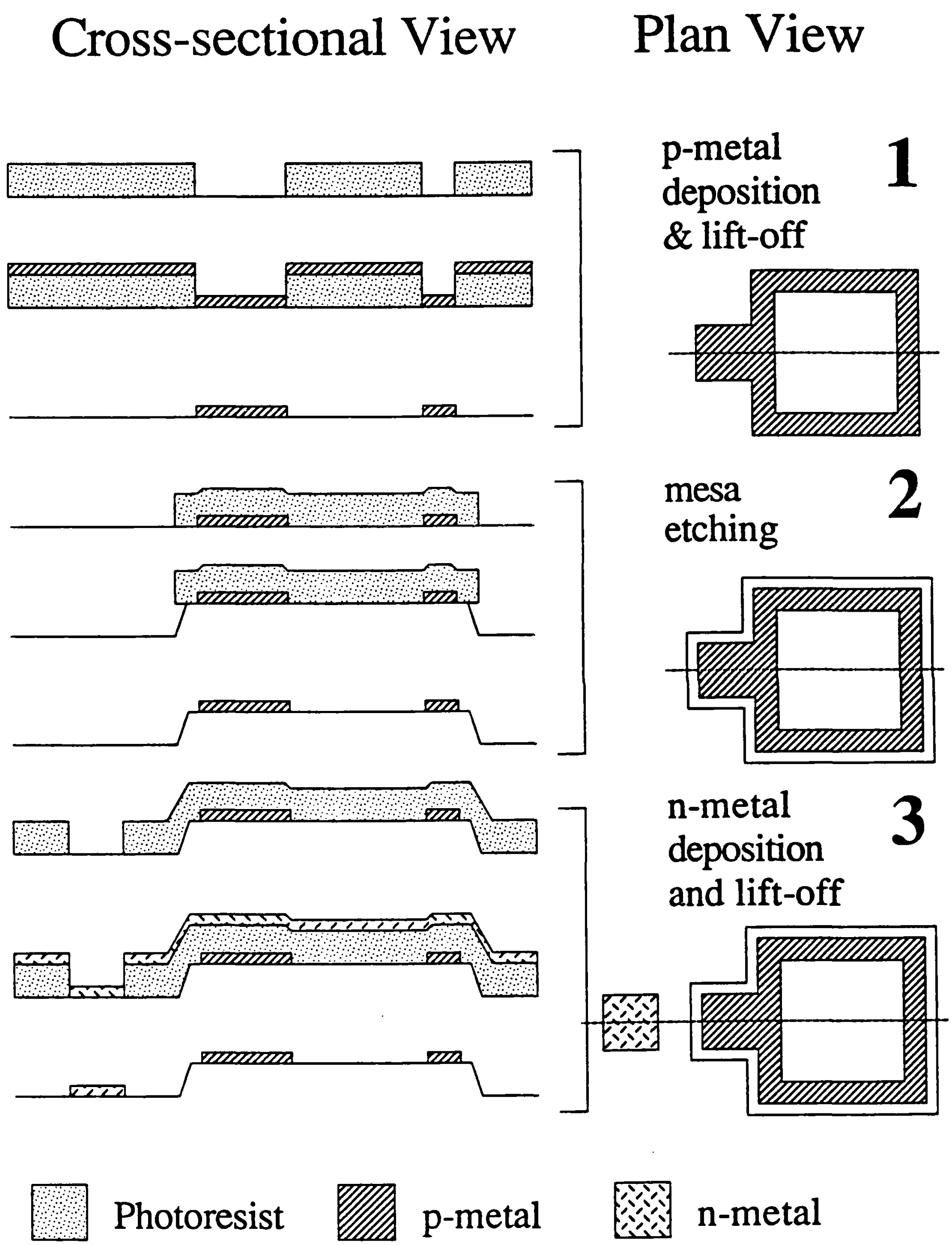

Figure 4.2.1 *Cross sectional and plan views of the fabrication steps for a mesa etched photodiode. The application of the n-metal is required if a back contact does not exist due to the use of a semi-insulating substrate*

Packaging

Fabricated mesa devices are mounted onto standard transistor packages. The packages used are of a T05 design and have three pins enabling each to carry two devices. A heat setting silver loaded conducting epoxy (Ablebond) was used to mount the devices onto the headers. The same epoxy was also used during hand bonding to attach gold bond wires to the device contact pad and header pins.

Slab waveguide devices are mounted on a specially devised package which is illustrated in figure 4.2.2. The package allows both electrical connection and unrestricted optical coupling into the waveguide. The core of a typical waveguide is approximately 1μm below the semiconductor surface and consequently light incident on the sample facet tends to scatter over the top of the sample. This can severely affect the accuracy of optical transmission measurements hence a package was developed enabling devices to be mounted with the epitaxial layers downwards, so that the path of light spilling over the sample surface would be blocked by the mount itself. Essentially, the slab waveguide has to overlap the edges of the mount

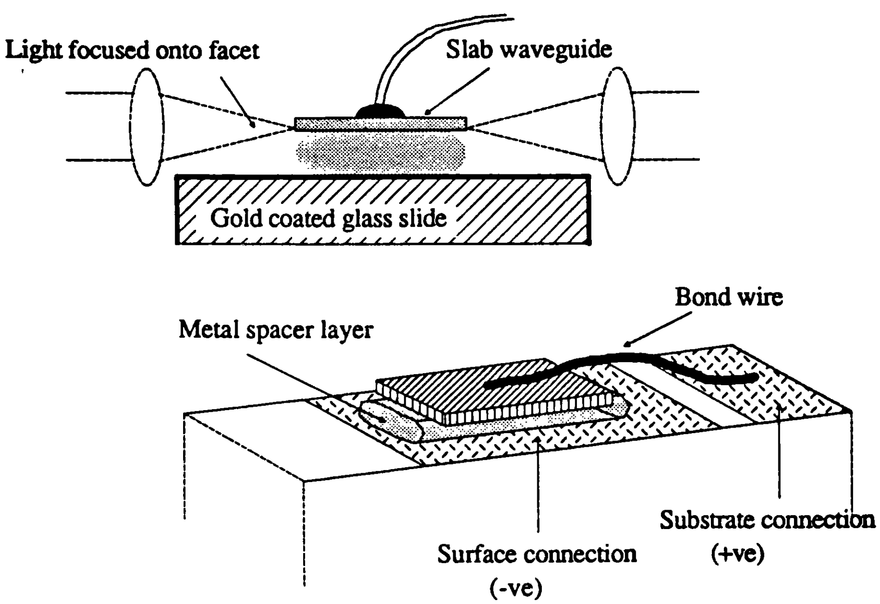

Figure 4.2.2 *Packaging of slab waveguides.*

to stop access to the core region becoming restricted. A small metal spacer, made from a flattened piece of gold plated wire, was mounted on the glass slide underneath the device. The spacer, sample and gold bond wire are all electrically connected with heat setting silver loaded epoxy and the glass slides are vacuum coated with gold tracks (in the manner described above for contact metallisations) to enable connection to the external circuit. This inverted mounting technique not only provided the necessary optical access to the waveguide core, but enabled all tweezer-handling of the samples from the substrate side, reducing damage to the facets, and consequently increasing bonding yields.

The slab waveguide devices are simply formed by cleaving the substrate in a manner similar to that used to form laser diodes. The disadvantage of this method is that good breakdown voltages are difficult to achieve, although the technique has in fact been used for most of the work described in this thesis. A technique most recently adopted for fabrication of slab waveguides is illustrated in figure 4.2.3. Here, a mesa etched photodiode has two of the mesa edges removed by cleaving, giving vast improvements in the breakdown voltages seen. Unfortunately, the sample then has to be mounted surface up leading to the problem of unguided light passing over the top of the sample. An adaptation of the optical system, described in the next section, has been used to overcome this problem.

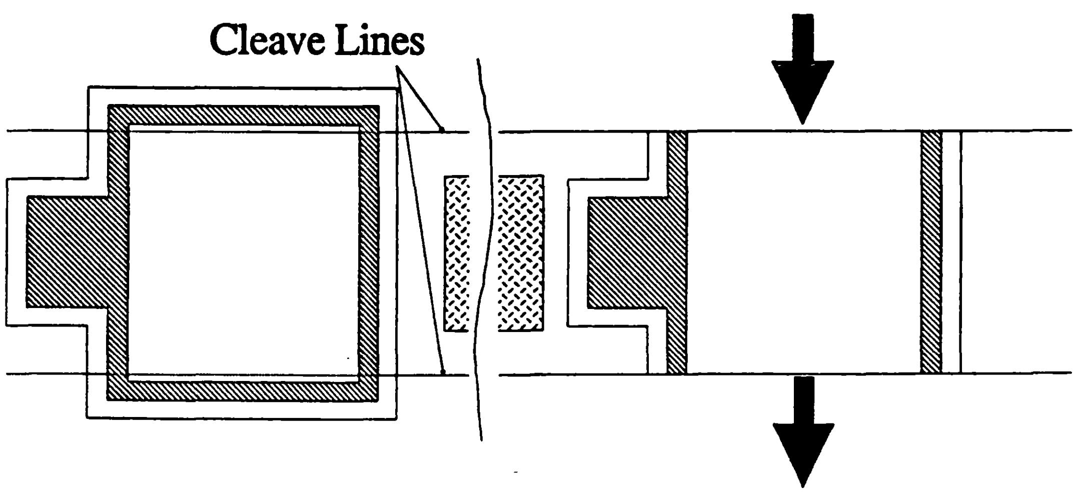

Figure 4.2.3 *Cleaving of mesa photodiodes to form high breakdown slab waveguides.*

4.3 Monochromator Measurement System

A monochromator system is used for the rapid assessment of the optical properties of fabricated photodiodes. Photocurrent spectra are taken and provide information about the optical absorption in the devices under test. The potential operation of a structure as a modulator can be rapidly addressed by studying the bias dependence of the photocurrent [Whitehead et al 1987].

The monochromator used is a Bentham M300 and the full assessment system is illustrated in figure 4.3.1. The wavelength at the monochromator output is determined by the movement of a grating which is driven by a stepper motor under the control of a BBC microcomputer [Abbott]. Also interfaced to the computer are a lock-in amplifier (EG&G 5104) for measuring the photocurrent, and an LCZ meter (Hewlett Packard 4277A) which is used as a programmable voltage source. The reference for the lock-in amplifier is provided by an optical chopper (Bentham 218) mounted between the source (Bentham 505) and the monochromator input as illustrated (figure 4.3.1). The programmable voltage source is used so that bias dependent spectra can be obtained with ease.

The photocurrent signal from the photodiode is converted to a voltage by connecting a resistor in series with the device. This also enables the required bias to be applied to the diode. The circuit configuration is illustrated in the inset of figure 4.3.1. The capacitances shown decouple the output from any DC bias and filter and smooth the input bias voltage.

For alignment of the photodiodes, an infra-red camera (Hitachi HV17TK) images the light reflected from the device. Manipulators are used to move the device until the window in the metallisation is illuminated. Photocurrent levels from single well devices are generally very low (nA) and careful adjustment of the monochromator slit widths, lock-in time constants and stabilising period between readings are required to obtain good results. The lock-in amplifiers successfully overcome the noise background which is due to electrical interference, leakage currents and ambient lighting.

The spectral resolution of the monochromator is specified as 0.5nm with slits widths of 50μm. This exceeds the ≈1nm resolution required in the experiments and allows a high output intensity enabling reduction of noise in the spectra. Crosstalk from higher orders of the diffraction grating is eliminated by

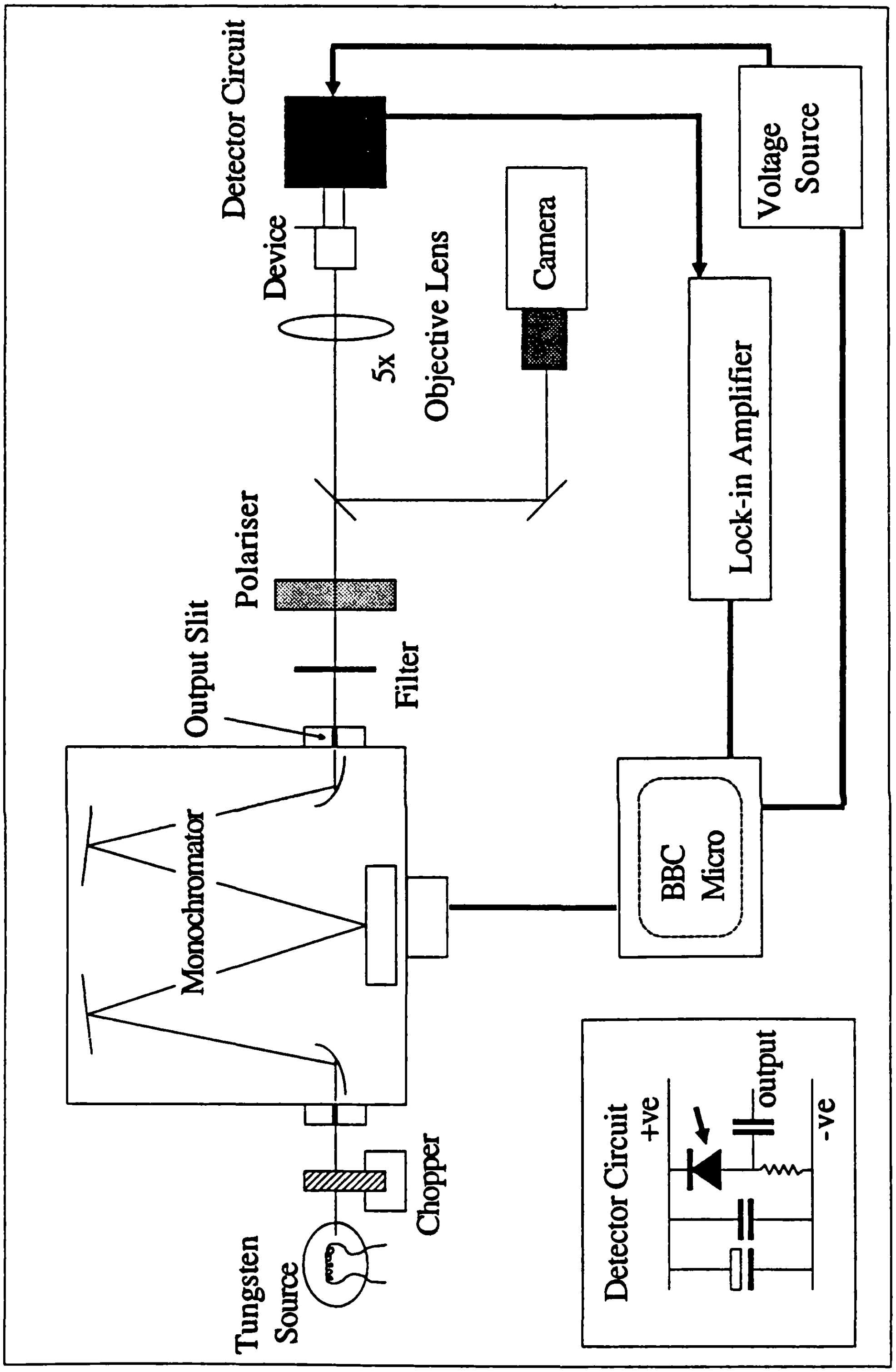

Figure 4.3.1 *Monochromator Measurement System*

filtering the monochromator output.

In addition to measurements of room temperature photocurrent, the monochromator is used in conjunction with a cryostat to measure photocurrent at liquid nitrogen temperatures. A photodiode, packaged in the usual manner, is mounted behind one of the cryostat windows, and the instrument replaces the usual sample holder. Current levels fall off considerably at low temperatures and extra amplification of the signals is required: for this purpose a 30 dB voltage amplifier (EG&G) is used.

4.4 Near Infrared Laser System

The slab waveguide devices are investigated using a continuous wave (CW) tunable laser system. Absorption spectra are obtained and the performance of devices as modulators can be assessed. This section describes the experimental apparatus, some of the basic techniques involved and the occurrence of Fabry Perot oscillations in the experimental spectra. Two further experimental arrangements which use the infrared dye laser are described: the first is an extension of the photocurrent measurements described above, and the second is optical pumping of the waveguide devices.

Transmission Measurements

The CW laser system and the experimental arrangement used is illustrated in figure 4.4.1. The tunable laser is a Coherent 599 Dye Laser which is pumped by a water cooled Argon Laser (Coherent I90-5). Styryl 9M dye (Lambdachrome) is used in the dye laser and this provides a useful output in the range 790-900 nm. The actual power used in the experiments is adjusted with a variable prism attenuator (Ealing) and is of the order of a few micro-Watts.

Tuning of the dye laser is achieved by rotating an intracavity birefringent plate which is driven by a stepper-motor. The stepper-motor is interfaced to a BBC microcomputer so that automated wavelength scanning is possible. Wavelength calibration for this arrangement is obtained by using an optical multichannel analyser monochromator system (EG&G OMA) to determine the output wavelength from which a calibration file is generated [Abbott].

The dye laser output power, which is typically of the order of 100mW, has a spectral dependence which is compensated for by use of the following

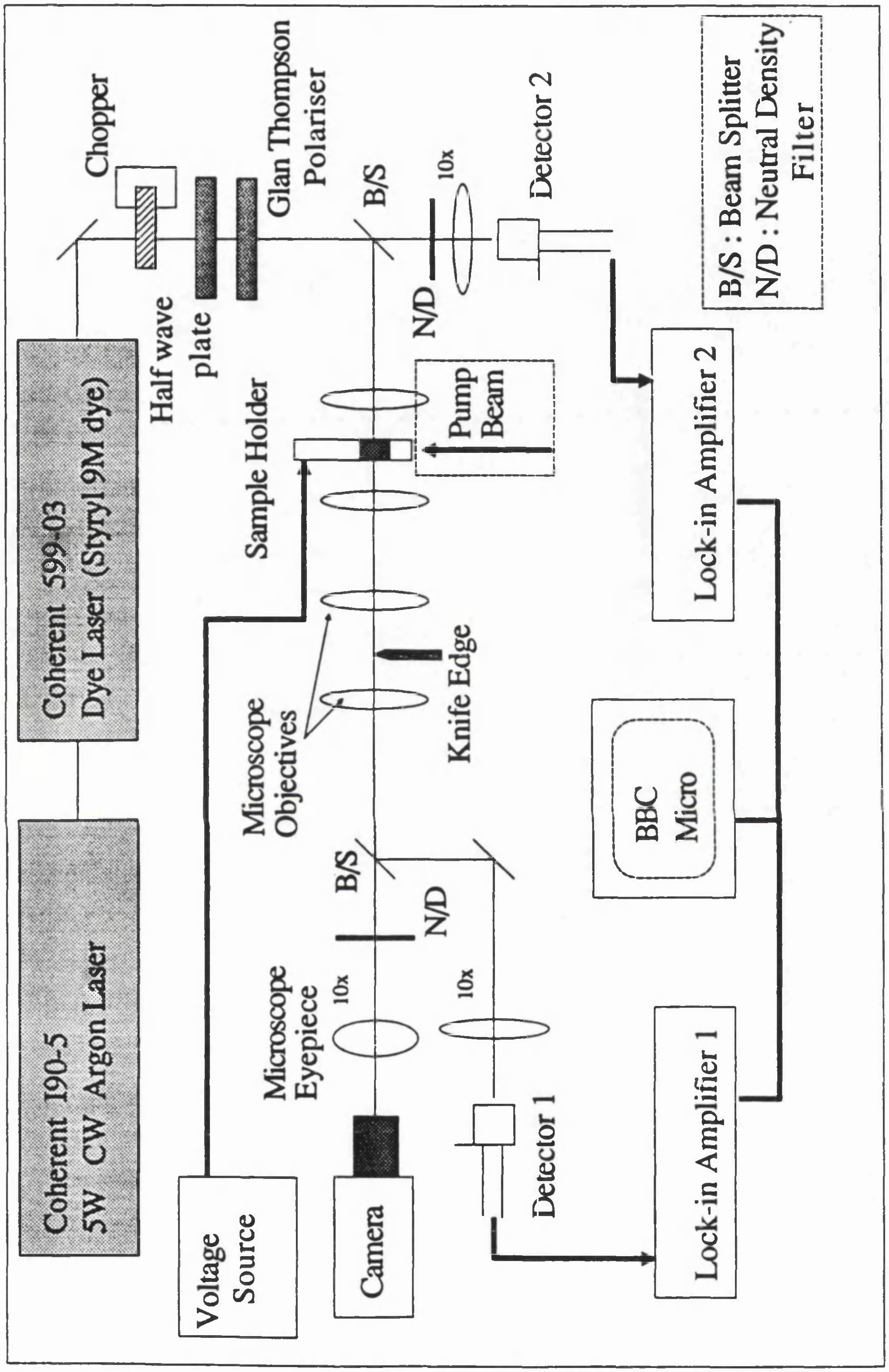

Figure 4.4.1 *Tunable Dye Laser Measurement System*

arrangement (figure 4.4.1). The transmitted and incident light are monitored by Si photodiodes 1 and 2 (RS BPX65) which are connected to separate lock-in amplifiers (EG&G 5104), referenced by an optical chopper (Bentham 218). The two lock-in amplifiers are interfaced the BBC microcomputer on which software has been developed [the author] to compensate for the power variations, whether spectrally or time dependent. The software essentially divides transmitted power by incident power and plots a transmission spectrum point by point as it scans the wavelength over a pre-determined range. Completed spectra are then written to disc for later analysis.

The output of the dye laser is *s* polarised and is determined by the birefringent tuning plate. With the vertical orientation of the sample, this polarisation is suitable for coupling to TE mode in the GaAs waveguides, but for TM mode the polarisation is rotated by the combination of a quarter wave plate (Ealing) and a high extinction ratio (50dB) Glan Thompson polarising prism (Melles Griot). In this arrangement, the quarter wave plate first produces elliptically polarised light and the Glan Thompson prism can then select any polarisation required.

The laser beam is end-fire-coupled into the waveguide under test by a 20x objective lens. Beam divergence has enlarged the beam to ≈4mm diameter at the focussing lens and typically a ≈2μm spot size is achieved. Piezo driven manipulators, providing focusing, vertical and lateral movements, are used for accurate placement of the waveguide at the focus of the incident beam. The output of the guide is recollimated using a 10x microscope objective and the resulting beam is split to one of the Si detectors and to a camera via a microscope eyepiece. The combination of eyepiece and objective are set to conform with a standard microscope length and the camera then images the waveguide output facet.

The initial alignment of a waveguide for analysis can prove difficult: obtaining coupling and detecting the output is a slow task due to the many degrees of freedom that the system has. To assist with this alignment, the device can be used as a photodiode and its position optimised for peak photocurrent. This technique usually provides rapid placement of the guide at the focus of the incident beam and the imaging can then be adjusted to observe the output facet.

The waveguide mount (or package) is fully described in section 4.2 and can take two forms. The first, and simplest to use, is the inverted structure which blocks any unguided light which commonly would spill over the top of the sample. A typical "clean" image of the output of the waveguide is illustrated in figure 4.4.2a. Without this inversion, the proximity of the guide to the surface of the sample means that stray light will appear in the image and at the detector, giving a false transmission spectrum. Figure 4.4.3b shows this stray light in a surface-up sample, but also to the right of the image is indicated a knife edge in the same focal plane. The implementation of this knife edge is indicated in figure 4.4.2 and is in fact in a second focal plane formed after the waveguide. The knife edge can be move laterally and successfully restores the image to that seen with an inverted structure. This enables the surface-up mount to be used and its advantage of higher breakdown voltages to be exploited.

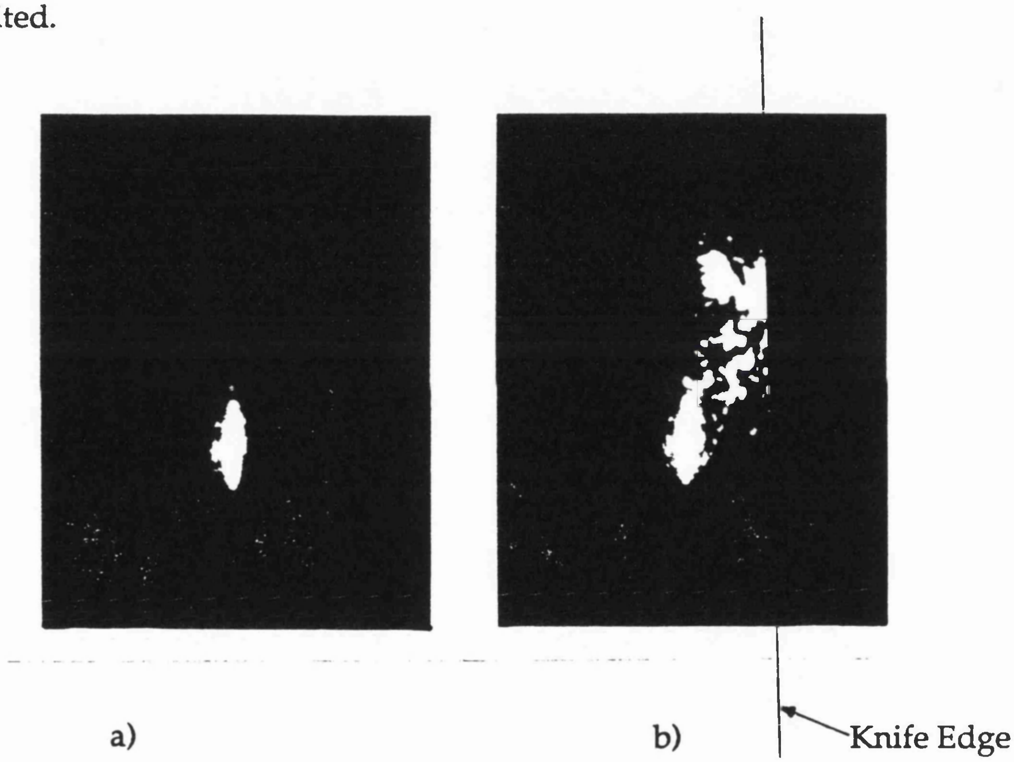

Figure 4.4.2 *Images of the output of the slab waveguide. a) Inverted mount technique b) Surface-up mount technique with focal plane knife edge in retracted position.*

Measurement of waveguide transmission is hampered, especially at low guide absorption, by Fabry-Perot cavity oscillations. The cavity is the waveguide and the reflectors are the cleaved semiconductor facets. There is essentially no difference between the waveguide structure of the fabricated QW-FEM and a Fabry-Perot Laser in this respect. The facet reflectivity for

GaAs is approximately 30% [Casey and Panish] producing large oscillations, especially at wavelengths which lie in the quantum well bandgap. These oscillations are illustrated in figure 4.4.3 for the low transmission region of a waveguide sample (MO733: see Chapter 5). The decreasing transmission to shorter wavelength is the effect of the quantum well absorption tail. The length (l) of the device can be reconciled with this data and the incident wavelength (λ) through the equation for Fabry-Perot peak separation ($\Delta\lambda$) in such a cavity:

$$\Delta\lambda = \lambda_{av}{}^2/2n_{eff}l$$

The device length was measured to 685±20μm and the averaged wavelength used was λ_{av}=839nm. For an estimated n_{eff} (modal index) for the waveguide of 3.46 [Casey and Panish] this gives a value for $\Delta\lambda$ of 1.48Å, close to the experimental value of 1.44Å.

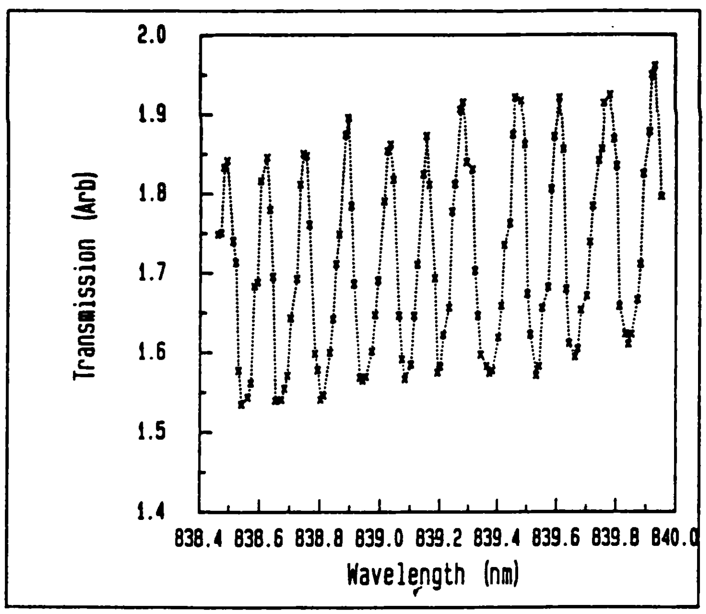

Figure 4.4.3 *Fabry-Perot oscillations in a bandgap transmission spectrum*

The Fabry-Perot effects are not desirable and can often extend into the absorbing regions at the excitonic features of the spectrum clouding the results. The ideal method for reducing the effect would be to deposit an anti-reflection coating (ARC) on one or both facets of the device. Many authors have succeeded in depositing accurate layers of such materials as SiO or SiN for the purpose of reducing modulator coupling losses, decreasing laser thresholds, or optimisation of external cavity lasers. For the work described here, no ARC was used due to the difficulties in accurate deposition and the limited number of fully fabricated devices produced. It was found that manipulation of the device during testing could often lead to suitably smooth spectra being compiled. The spectra can also be corrected after measurement with a smoothing routine and where this is used in this thesis the actual data points are indicated and a solid smoothed curve plotted between them. The routine simply averages, with a square weighting, over a variable number of points neighbouring the point which is being corrected. This cleans up the data but unfortunately may lead to slight broadening of the spectral features.

Photocurrent Measurements

Many of the epitaxial layer structures exhibit a nonuniformity of the optical properties, which will be discussed in greater detail in section 5.5. The scale of these nonuniformities is sufficiently small that the optical illumination from the monochromator tends to probe too large an area due to the difficulty associated with collimating the slit-like output beam. The use of a tightly focused spot assists in accurately determining the spectral characteristics; however, this is difficult to achieve with the monochromator due to an associated reduction in power level and the low absorption associated with a single quantum well. The use of the laser for this purpose reveals, in some cases, sharper data although over a restricted wavelength range. The laser set up is very similar to that used for transmission with the only differences being that the device under test replaces the output photodiode and the waveguide sample holder is empty. The software routine normalises the data to the laser spectral intensity by monitoring the input light in the usual manner.

Optical Pumping

One further experimental arrangement used with the laser system is the introduction of a pump beam onto the surface of a waveguide sample. The purpose of the experiment is to determine whether further saturation of the spectral features can be achieved in this way. The experimental results are discussed in section 5.6. The system illustrated in figure 4.4.1 indicates the position of the pump beam which is either supplied directly from the dye laser output or coupled by a fibre from a separate laser source. The waveguide device type used in this arrangement is the specially adapted cleaved photodiode (figure 4.3.3) and the pump beam is incident perpendicular to the sample surface through the photodiode window. The use of the knife edge in a second focal plane, as described above, is vital to this measurement due to the very large amounts of stray light which tend to saturate the output photodiode. In each case, the probe beam is chopped whilst the pump beam is uninterrupted so that the lock-in amplifier will reject any stray light that is collected.

4.5 Electrical Assessment Techniques

The electrical characteristics of a semiconductor device reveal useful information about the epitaxial layer structure and the quality of the fabrication. The devices discussed in this thesis are diodes which are invariably operated in reverse bias making current voltage (IV) and especially capacitance voltage (CV) important electrical assessment techniques. The following sections discuss the practical application of these techniques and some of the basic results inferred.

Current-Voltage Measurements

Current-Voltage (IV) measurements are an initial test for the functionality of the device as a diode. The measurement uses a commercial unit (Telequipment CT71, Tektronix 7CT1N plug-in) which sweeps voltage, measures current and displays current vs voltage as a continuous waveform. The devices can be assessed both before and after packaging. For packaged devices the curve tracer has a plug-in unit which receives the two or three pin headers used for mounting fabricated photodiodes. For testing of devices on wafers prior or during cleaving and bonding an electrical probe station is used. The probe station has tungsten needles for contacting the devices which are moved by micropositioners whilst viewed through a low power laboratory microscope. These needles are electrically connected by flying leads to the curve tracer.

The results obtained are essentially pass or fail due the reverse breakdown operation requirements. A low leakage current is needed, typically less than 100nA, at the desired breakdown voltage which is normally in the region of

6V for *p-n* devices and considerably greater for Schottky structures. High leakage currents and low breakdown voltages in the reverse bias characteristics indicate poor etched or cleaved surfaces. In general, a mesa etched surface has been found to produce the best characteristics whilst cleaved surfaces generally degrade the potential performance of the waveguide device. The *cleaved mesa* structure of figure 4.2.3 has been shown to provide a considerable improvement in breakdown voltage over a conventional waveguide device with all four edges formed by cleaving. With a good batch of mesa etched devices, sharp breakdown voltages could be seen to be very uniform across a wafer indicating that the processing had achieved the best results attainable from the epitaxial layer structure.

Capacitance Voltage Doping Profiles

Capacitance voltage measurements of semiconductor diodes are a routine technique for providing doping level information for the regions surrounding the junction [Blood]. The technique looks at the change of the device capacitance with reverse bias and derives the doping densities and associated distances from the junction. The capacitance measurements and voltage supply are obtained from a Hewlett Packard 4277A LCZ meter which is interfaced to a BBC microcomputer. The software written to drive the instrument [the author] plots the capacitance against voltage, doping against distance and voltage against distance to aid a full interpretation of the data.

As with the IV measurements, the devices can be assessed either before or after packaging. For packaged devices the LCZ meter has a plug-in unit which receives the photodiode headers. Stray capacitance associated with device packaging can be corrected for by insertion of a blank header and by offsetting the zero of the instrument accordingly. An adaptation of the probe station mentioned above provides a means of taking data without bonding the device to packages. Specially adapted probe arms have a coaxial cable fed direct to the probe needles to provide noise free measurements.

A simple experimental CV doping profile plot can be used to illustrate the measurement technique (figure 4.5.1). The structure used has a Schottky junction and clearly the plot indicates that a doping level of $\approx 7\times10^{14}\text{cm}^{-2}$ exists to a depth of 3.1μm, followed by a region of very high doping into which very little depletion can occur. The interpretation of CV data to produce this type of depth profile assumes an abrupt junction approximation [Sze p286] and

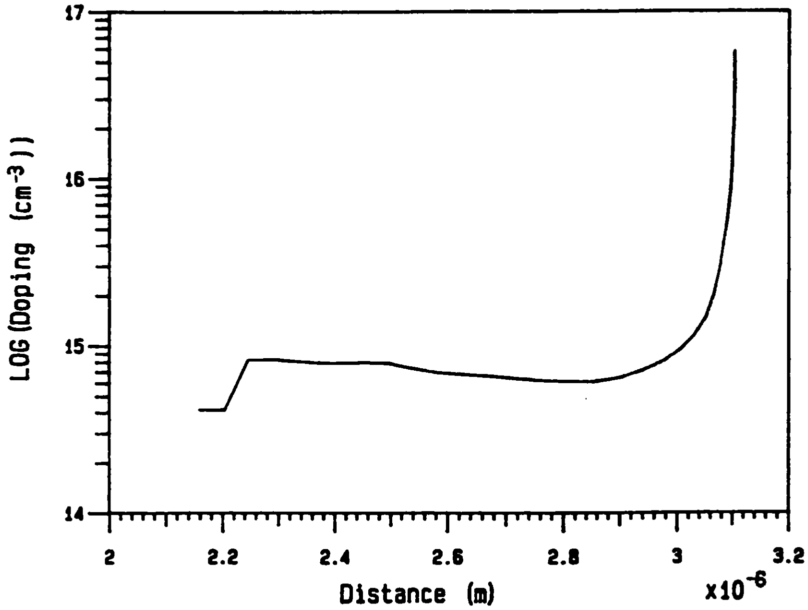

Figure 4.5.1 *Schottky junction doping profile (sample: MO685)*

accurate doping values are best obtained from one sided junctions such as the Schottky device illustrated here. A *p-n* junction structure with lightly doped *p* & *n* regions is more likely to give misleading results due to the depletion region lying to both sides of the junction. Some specific examples of these effects are highlighted in section 5.3 and their interpretation uses the extension of the *p-n* junction field model described in section 3.3. The results of this modelling show that distance and doping profiles have a large structural dependence for the lightly doped pn junctions used in this thesis, and that minute variations in experimental thickness or doping parameters can considerably influence the appearance of measured CV data.

In conclusion, the experimental methods described here detail both the device fabrication and the measurement techniques used for the assessment of the QW-FEM in this thesis. The subsequent chapter describes and analyses the results obtained by these methods and expands on the precise experimental techniques and their development where necessary.

Chapter 5

Experimental Study of QW-FEM Devices

5.1 Introduction

Introductory Remarks

The data presented in this chapter is for a series of epitaxial structures grown as a progressive optimisation and investigation of the properties of the QW-FEM device. The actual experimental details have been described in chapter 4 although these will be expanded upon where necessary. The device design tools, which are also used in some of the analysis performed here, were detailed in chapter 3. Little attempt is made to retain a chronological sequence to the work described in order to avoid repetition in the presentation. Nevertheless, it is instructive to outline the sequence of events to highlight the improvements in epitaxial growth, fabrication and measurements of the structures. Therefore, a brief chronology is given here, and this order retained through section 5.2 which illustrates the basic photocurrent measurements from each sample.

Chronology

The three basic types of QW-FEM device designs were discussed in section 3.3 and illustrated in figure 3.3.2, and the layer structures used in this series of experiments fit roughly into those descriptions. A chronological summary of the layers is given in Table 5.1.1 describing such details as the method of growth, well width, junction type and information regarding the selective doping. The main exception to the simple categories is the extension of some of the *p-n* structures to include a donor spike both above *and* below the quantum well. The complete *as-grown* layer structures for each sample are illustrated in appendix A, sections A1 to A10. The section which follows is a brief summary of the progression of the QW-FEM structures and does not attempt to give results but merely suggest the course which the research followed. Each item is expanded upon within this chapter.

Following through the sequence of table 5.1.1, the progression firstly investigates a series of well widths to optimise this parameter for the biased recovery of the excitonic feature. The transition from the initially conceived Schottky junction (section 3.3 and 3.4) to a *p-n* junction was also made to give improved electric field control in the region of the quantum well when MOCVD material is used. The position of the doping spike within the structure was then considered in order to assist in maximising the quantum well population and improving the unbiased quenched state. It was moved from below the well to above, and following that samples with twin spikes were used. The spacer thickness is also reduced, with the same goal of increased quenching in the unbiased state. The MBE grown samples supplement this work by providing a very low doped Schottky QW-FEM structure and an undoped (no donor spike) sample which acted as a control for the experimental procedures. Three of the layers are labelled as *FET layers* indicating that semi-insulating substrates have been used in conjunction with *p*-type blocking layers in the lower cladding region to enhance FET action. The FET layers and associated results will be discussed briefly in this chapter and again in chapter 7 in the context of monolithic integration.

Sample	Growth method	L_W Å	Jnc.	Spike	Spacer Å	Subst.	Comment
CPM459	MOCVD	75	*p-n*	b	100	n^+	
CPM460	MOCVD	100	Sch	b	100	n^+	
MV292	MOCVD	50	*p-n*	b	100	n^+	Peak Recovery
MV317	MOCVD	50	*p-n*	a	100	n^+	
CB1	MOCVD	50	*p-n*	a&b	100	n^+	Multi-moded
MO685	MBE	50	Sch	b	100	n^+	No N_s Control
MO733	MBE	50	Sch	-	-	n^+	Undoped
CB44	MOCVD	50	*p-n*	a&b	50	SI	FET layer
CB111	MOCVD	50	*p-n*	b	75	SI	FET layer
CB171	MOCVD	50	*p-n*	b	75	SI	FET layer

Table 5.1.1 *Sample Table. Layer Structures used in the experimental investigation of the QW-FEM. The categories under "spike" refer to the position of the donor region and correspond to: a=above the quantum well; b=below, with the top of sample defined as the surface. The letters "Sch" under junction type (Jnc) correspond to the use of a Schottky metallisation. The basic designs of the devices are illustrated in the design section (figure 3.3.2).*

As well as the chronology of layer structures there was also a continuous improvement in the measurement and analysis techniques used. Data recorded from each sample was updated during the development of the experimental methods described in chapter 4. An increasing comprehension of one problem in particular, that of wafer nonuniformity, led to optimisation of devices and measurement techniques to assist in extracting the data presented in this chapter. Variations of the optical and electrical characteristics on a <1cm scale was discovered in both the photocurrent and CV profiles of sample MV292. The properties of the wafer were mapped to find the area which had the potential for the best optical modulation. All wafers prior to, and following this discovery, were mapped in a similar fashion. A discussion of the origin of these problems is found in the next section. To assist with reducing the effects of the variations of the characteristics across a sample two steps had to be taken. In the case of the photocurrent measurements, spot size reduction led to improved linewidths with some samples. The use of the CW laser system for this purpose, rather than the monochromator, was made when the *spot size power dependence* became restrictive. For the waveguide devices, a reduction in guide length and careful selection of the area of the wafer eventually led to excellent transmission spectra which show agreement with the photocurrent measurements.

A second large contribution to the improvement of measurement procedures was the automation of the laser transmission measurement system (section 4.4) which proved vital to reduction in data noise levels. Spectral and temporal laser intensity variations necessitated a means of monitoring the incident power and using this parameter for normalisation of the transmitted intensity. Experimental random wavelength errors (±2Å) and systematic errors introduced by manual laser wavelength tuning were eliminated by installation of a stepper-motor and calibration system. This also served to decrease the measurement time, reducing the observed waveguide coupling drift. When gradually overcoming these problems, the data for each device was updated to provide improved spectral data presented in section 5.5.

5.2 Photocurrent Analysis

The experimental procedure for the initial analysis of layer structures was described in section 4.3 and involves spectral photocurrent measurements using a monochromator system. All of the initial measurements providing the rapid analysis of QW-FEM transverse samples have been performed using this system. At some points, a move to the use of the tunable dye laser system is indicated where the sample nonuniformities mentioned above became restrictive. The laser spot size is of the order of a 1-2μm diameter, whereas the the monochromator slit image illuminates the device over a 200μm stripe in order to achieve a noise free photocurrent level. This has the effect of sharpening the spectral features of some layers. There are three main sections to the development: the first is a well width study, the second looks at ways of increasing the quantum well carrier density, and the third turns to study layers suitable for FET operation. Further discussion of all of the data presented here appears in sections of this chapter regarding comparisons with device design and analysis of the performance achieved.

Effects of Quantum Well Width.

A series of three epitaxial structures were grown with different quantum well widths. The experimental results successfully highlight changes in both the quenched and unquenched states of the excitonic resonance as a function of the well width. The samples use were: CPM459, CPM460, MV292 which have 75Å, 100Å, 50Å nominal well widths respectively. The well widths are

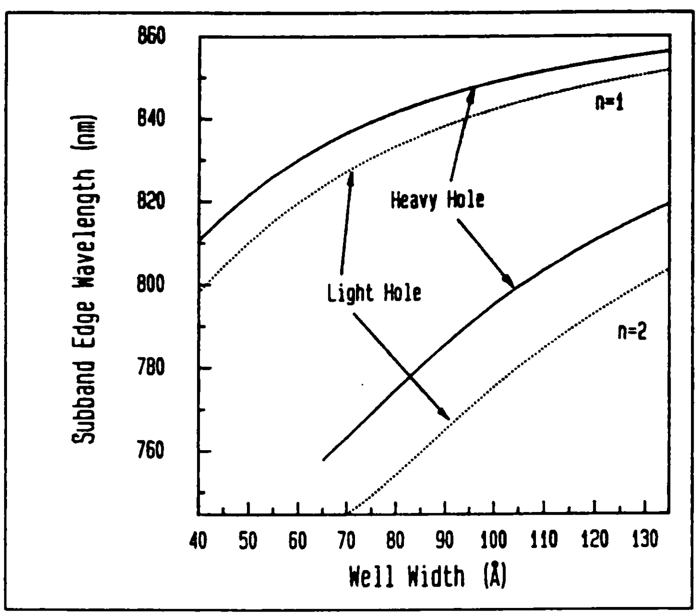

Figure 5.2.1 *Subband edge position calculated as a function of the well width. The N=1 and N=2 light and heavy hole curves are shown.*

described as nominal because they are the figures derived from the growth rates and confirmation of these values is not made by any means other than the arguments presented here. To aid interpretation of the data which follows, figure 5.2.1 illustrates the position of the N=1 and N=2 subband edges as a function of the well width. The spectral position of the exciton is related to this by subtracting the associated binding energy which, for the purpose of this discussion, can be taken as approximately 10 meV (≈6nm) in the unquenched state [Ekenberg and Altarelli]. This data is obtained using the zero field subband energy level calculations described in chapter 6.

Figures 5.2.2 a,b,c illustrate the photocurrent spectra for samples CPM459, CPM460, amd MV292 respectively. The photocurrent levels measured are smaller at at low bias due to a reduced quantum efficiency of the photodiodes. But for this fact, the photocurrent can be taken as a reasonable indication of the absorption in the device (section 5.4). The full layer structures are in Appendix A, sections A1, A2 and A3 respectively. The striking differences between the spectra are the increased changes in photocurrent found at the bandedge as the well width is decreased. This indicates that a greater modulation should be possible in a device with a narrow quantum well.

Sample CPM459 is a 75Å quantum well *p-n* junction structure and clearly shows two changes occurring in the spectra as bias is applied (figure 5.2.2a). The two regions have been assigned to particular transitions and are labelled in the figure. An initial change is seen at the N=2 subband edge and successive shifts of a feature at the N=1 subband edge are observed at higher biases. From figure 5.2.2, the anticipated wavelengths for the N=1 and N=2 excitons in an undoped 75Å quantum well are approximately 845nm and 780nm respectively. However, the features of the photocurrent spectra lie to longer wavelength indicating a greater than nominal thickness for the well. Both of these changes in the photocurrent spectra are thought to be due to recovery of broadened and Stark shifted excitonic resonances. The change of saturation with electric field seen at the N=2 subband indicates that large quantum well carrier densities are being achieved. This N=2 quenching effect is due to a combination of the N=1 subband population screening the N=2 excitons and also a considerable thermal electron population of the N=2 subband.

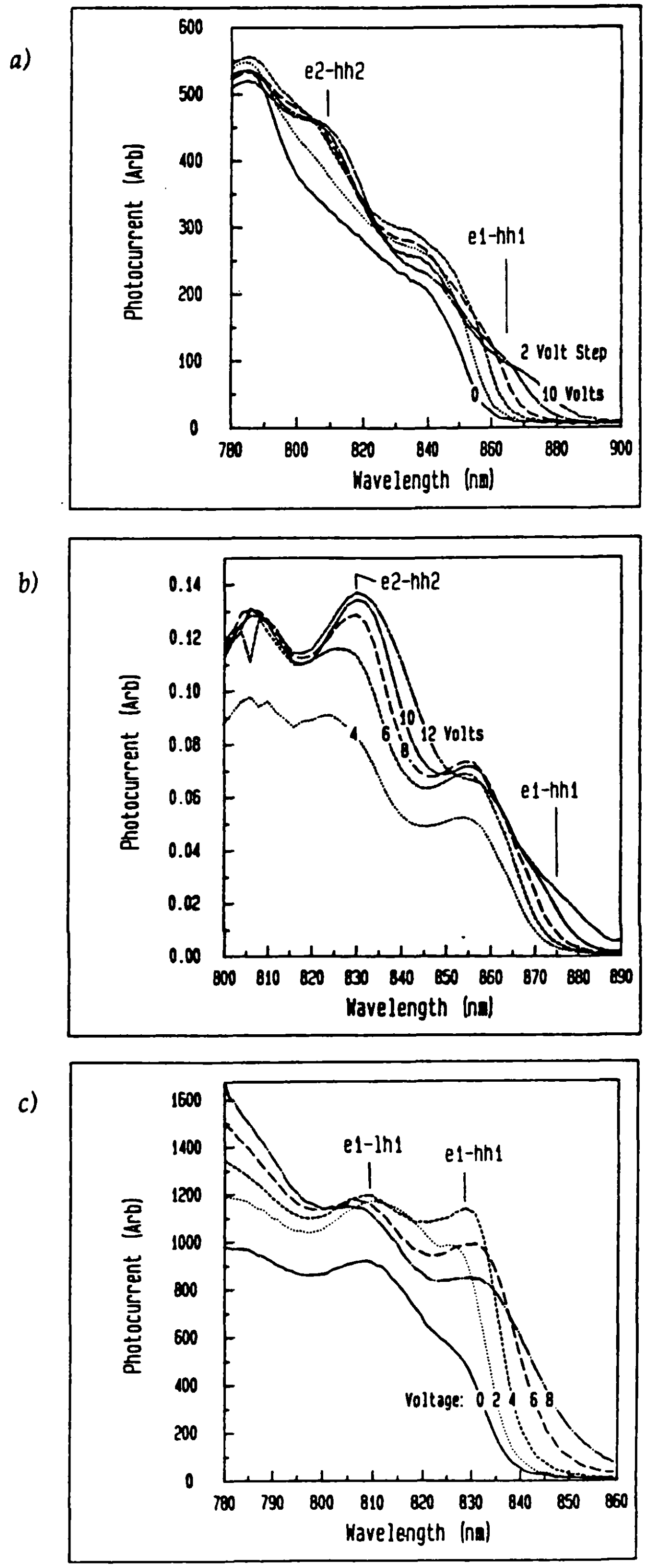

Figure 5.2.2 *Photocurrent spectra for sample: a) CPM459.[75Å] b) CPM460.[100Å] c) MV292.[50Å] Note a) and c) use the monochromator measurement system whilst b) uses the tunable laser system.*

Sample CPM460 is the 100Å well Schottky gate structure and, interestingly, shows its greatest absorption change at the position of the N=2 peak (figure 5.2.2b). The slow recovery and the weaker change of the photocurrent at the N=1 subband edge suggest that sufficient carrier control is not achieved before the breakdown of the device at ≈12V. A discussion of the electric field within this sample appears in the next section and illustrates this point. The position of the excitonic features in the spectrum, anticipated from figure 5.2.1, are approximately 805 and 855nm for the N=1 and N=2 respectively. This again implies that the nominal well width of 100Å is an underestimate.

The final sample in the well width sequence, MV292, illustrates the desired excitonic recovery effect with the use of a 50Å quantum well (figure 5.2.2c). The anticipated wavelength of the N=1 exciton in an undoped sample is approximately ≈ 827nm. Clearly, a large quenching of the exciton is seen at low bias and the greatest recovery is observed at a reverse bias of -4 volts. The effects observed at the N=2 subband in the wider well samples cannot be observed here as this energy level ceases to exist for $L_W \leq 65$Å (figure 5.2.1). To shorter wavelength the spectrum is simply dominated by the absorption tail of the barrier region which is $Al_xGa_{1-x}As$ with an aluminium mole fraction of 20%. This bandedge lies at approximately 740nm, but with the electric field broadening of the Franz-Keldysh effect [Pankove] it succeeds in introducing an absorption change at ≤790nm. This is compounded by the depletion region of the junction being predominantly AlGaAs which gives a longer absorption length by comparison with the quantum well, hence producing this significant photocurrent change at short wavelengths.

The recovered excitonic resonances found in the samples described above do not reproduce the peaks found in undoped material (section 1.2). The electric fields which are used to sweep the electron population from the quantum well reduce the excitonic oscillator strength and shift the features to longer wavelength. This is most notable in the wide well structures but is still marked in the 50Å sample. These effects are largely related to the quantum confined Stark effect produced by the applied field which instigates the recovery of the excitonic feature (section 2.2). It has been shown for MQW structures that the Stark shift is greatest in wider quantum wells for a given electric field [Stevens and Parry], but linked with this is a greater reduction in oscillator strength. The important factor for the QW-FEM is not the shift itself but the associated reduction in the oscillator strength of the excitonic resonance. The two are intimately linked through the greater separation, with field, of the bound *e-h* pair allowed by a wide quantum well. This gives a bigger shift in energy but a corresponding reduction in both the binding energy and the oscillator strength. For the QW-FEM, this simply means that with identical excitonic recovery fields, a narrower quantum well will increase the observed excitonic recovery. Consequently, the narrower 50Å well width was selected for all future samples. A further analysis of these photocurrent spectra is detailed in the next section where comparison of the experimental data and the designed behaviour is made.

The degree of excitonic recovery found with the move to a 50Å well width has a clear advantage for optical modulation over that of the wider well widths. However, the quenching of the excitonic resonance clearly remains incomplete in the spectra of the 50Å quantum well sample (MV292, figure 5.2.2c), as the feature can still be observed on the bandedge at zero bias. Further epitaxial structures were grown in an attempt to optimise the zero bias quenching.

Tailoring the Electron Population

The samples discussed in this section were designed to improve the zero bias quenching of the excitonic resonance. The obvious route is to increase the carrier population by modification of the doping spike and its position with respect to the quantum well. The third type of structure described in section 3.3 was designed with the aim of achieving higher carrier densities in the quantum well. Essentially, the idea is to ensure that at zero bias no electric field can exist across the quantum well by virtue of the depletion region of the controlling junction being blocked by the doping spike itself. This is simply achieved by moving the doping spike to lie between the junction and the quantum well. The samples in this category are MV317 and CB1 which have an inverted (doping spike above the quantum well) and a twin spike structure respectively. Both have *p-n* junction control of the population, and the additional doping spike in sample CB1 is designed to provide carriers from both sides of the quantum well. The photocurrent spectra for samples MV317 and CB1 are illustrated in figure 5.2.3a,b and the full layer structures are in appendix A sections A4 and A5 respectively.

a)

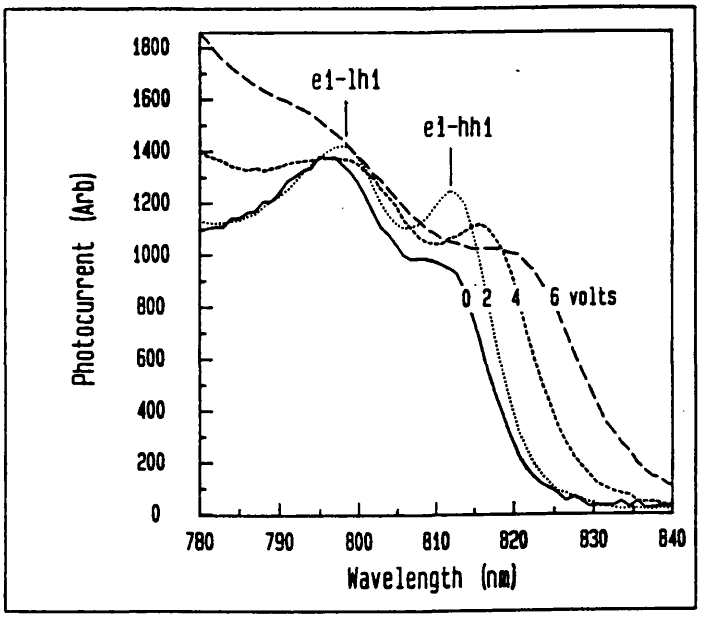

b)

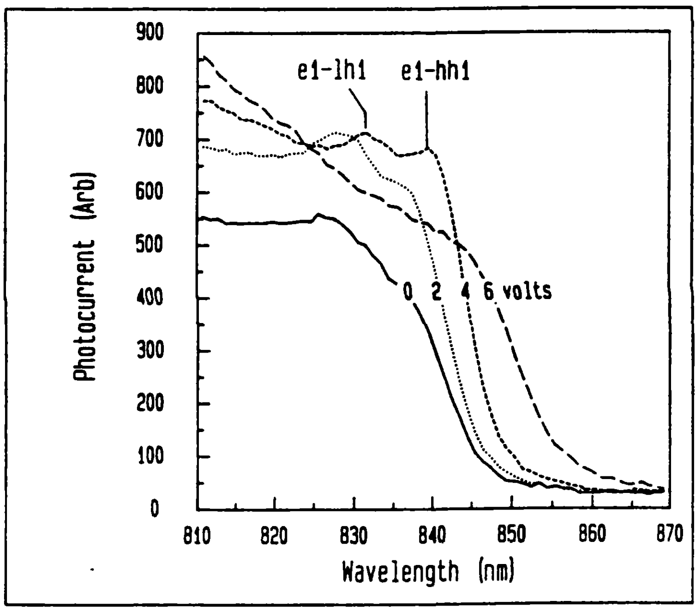

Figure 5.2.3 *Photocurrent Spectra for sample: a) MV317 [50Å well inverted spike structure], b)CB1 [50Å well twin spike structure]*

The first sample, MV317, shows only a modest zero bias quenching of the exciton and would suggest that the inverted structure has failed in the attempt to increase the saturation. A point to be noted from this spectrum is the position of the excitonic peak which lies to considerably shorter wavelength than the comparable sample, MV292 (figure 5.2.2c). This indicates a narrower well width which can be estimated to be smaller than 40Å from the data of figure 5.2.1. This sample consequently represents a further well width reduction, and perhaps confirms the increased difficulty associated with populating narrower wells. The bias dependence of the peak recovery shows very low voltage operation, and the similarity of this device to an enhancement mode structure suggested that forward bias operation may improve the saturation. This, unfortunately, could not be measured using photocurrent as the quantum efficiency as a detector falls to very low levels. Transmission measurements have to be introduced and these are reported in section 5.5, but in fact show only a slight improvement in quenching.

The photocurrent of sample CB1, figure 5.2.3b, shows the return of strong excitonic quenching and recovery. The spectral position of features in this data would indicate a well width of 60Å, slightly greater than that of MV292. The bias dependence of the recovery is remarkably similar to MV292 and the saturation of the exciton itself is equally good. However, at a glance, the modulation possible appears less due to the remaining absorption edge and this draws attention to the separation of the light and heavy hole peaks in the two samples. It is noted that there is a large variation in this separation and the misinterpretation of the transisitons is a possibility where a large separation occurs.

Further Epitaxial Structures

The five structures described in the two sections above illustrate the directions taken in an attempt to optimise the QW-FEM, and the photocurrent spectra indicate that considerable success has been achieved. The further analysis of these samples appears throughout this chapter, in sections considering anticipated and experimental performance both in terms of electrical design and waveguide modulation. The layers which followed are briefly described in table 5.1.1 and include two epitaxial layers grown by MBE: one to repeat the Schottky gated structure (CPM460), and a second as a control sample to illustrate the success of the MBE quantum well epitaxial growth. The layer numbers for these samples are MO685 and MO733, respectively. A further three samples were grown and these were designed to enhance the excitonic quenching whilst simultaneously providing the opportunity for FET operation. The layer numbers for these samples are CB44, CB111 and CB171.

The photocurrent spectra for the MBE Schottky sample MO685 shows a sharp bandedge with no residual excitonic features visible (figure 5.2.4). However, no control of the carrier density in the quantum well appears possible with this device. Transmission measurements also performed on the same structure confirm the shape of the bandedge and the lack of absorption control. Although the sample is deemed a failure for optical modulation, it is nevertheless interesting from the point of view of the analysis of the layer structures using the experimental procedures of chapter 4. A simple explanation for the problems encountered is found, and this is detailed in the next section where comparison of design and experimental results are made and the advantage of MBE growth for Schottky structures is highlighted.

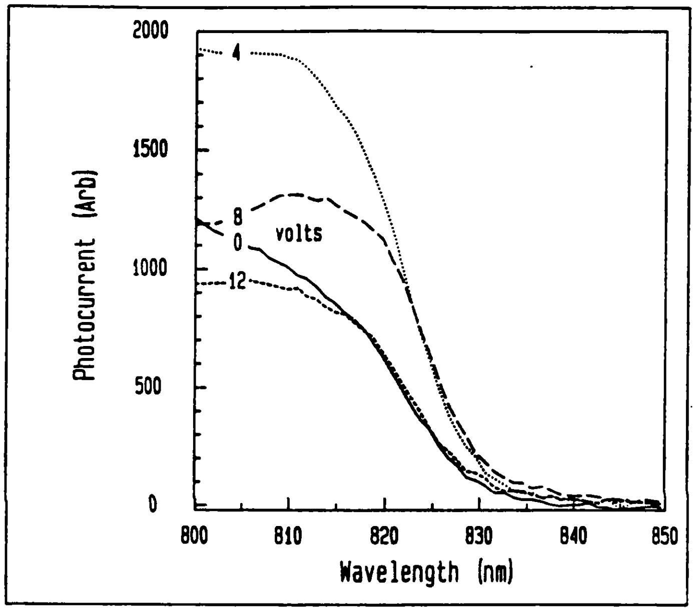

Figure 5.2.4 *Photocurrent Spectra for sample MO685.*

The further MBE sample, MO733, was grown as a control sample in the light of the failure of the modulation effect in sample MO685. The results illustrate the excellent quantum well growth available with this epitaxial technique and dispelled doubts about the results from sample MO685. Sample MO733 proved most useful in confirmation of the transmission measurement system and the excellent spectra for this sample appear in section 5.6, figure 5.6.1.

The FET structure is not a major departure from the layers described above. The difference lies in the use of undoped substrates to eliminate conduction paths other than that through the conduction channel itself (section 7.3). Also attempted, with the same layer structure modification, was the reduction in the spacer layer thickness to enhance the quantum well population (Table

5.1.1 and appendix A8, A9, A10). The photocurrent measurements on each of the FET layers showed only a broad bandedge illustrating that the quantum well had become highly doped due to the segregation of donor atoms, as described in chapter 3. Spacers of 75Å and 50Å and the return to single doping spike structures showed no signs of improving the absorption characteristics. The fabrication of devices from the FET structures is considerably more complex and the opportunity for mistakes in the fabrication sequence is high. Photocurrent measurements for the samples depend upon accurate contacting to the FET channel and experimental errors in the etch depths cannot be avoided. For this reason, the photocurrent spectra alone could not be used to dismiss the sample in terms of its functionality. However, waveguide transmission measurements were made on the samples which unfortunately confirmed the poor spectral characteristics. Nevertheless, some preliminary FET operation was achieved and results are illustrated along with a transmission spectrum in section ~~in section~~ 7.4.

5.3 Model Comparison

The validity of the electrical design, described in section 3.3, is established by a comparison of the theoretical predictions and experimental results. The voltage at which the exciton can be seen to reach full recovery is the clearest indication that the device is operating as predicted, whilst extending the electric field modelling to simulate capacitance-voltage (CV) data gives a further important comparison with measured doping profiles. The Stark shift found also provides vital information about the internal electric fields being developed. The most appropriate divisions for the comparison of experiment and theory are provided by the three QW-FEM categories of figure 3.3.2: Schottky junction, *p-n* junction, and inverted/double spike structures.

Schottky Junction Structures

The first Schottky structure grown (CPM460) had the disadvantage of having a wide quantum well, as described in the section above, but also contributory to the low recovery of the excitonic features (figure 5.2.1b) was the limiting strength of the electric field which could be applied across the quantum well. This limit is indicated experimentally by the breakdown voltage of the device and through the use of capacitance voltage profiles. The junction model (figure 5.3.1) demonstrates this clearly when used with the *as-grown* doping parameters (Appendix A1), of which the upper cladding region doping has the greatest effect.

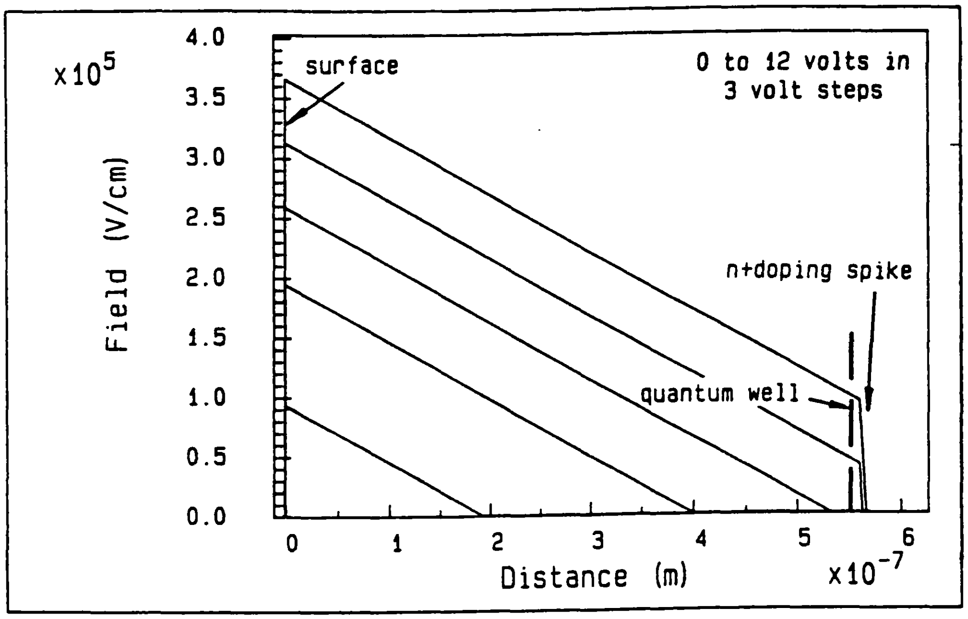

Figure 5.3.1 *Electric field plot for the Schottky structure, CPM460.*

The plot both shows the field which can be developed across the quantum well for a given bias and indicates the limiting value which is caused by the GaAs breakdown field ($\approx 4 \times 10^5$V/cm) being reached under the Schottky contact at the sample surface. As indicated, the highest achievable field at the quantum well is of the order of $\approx$100kVcm^{-1}, barely sufficient to give the required population control. Doping profiles for this sample, both measured and simulated, are illustrated in figure 5.3.2. Depletion to, but not through, the doping spike is indicated as the breakdown of the device is reached.

The CV trace for the MBE grown Schottky sample, MO685, was illustrated in section 4.5 (figure 4.5.1) and the photocurrent and electric field plots are illustrated in figure 5.2.4 and figure 5.3.3, respectively. The electric field control apparently available at the quantum well is seen to be vastly increased over that available in the MOCVD sample, due to the decrease in the undoped levels which act to reduce the field under the contact layer. This justifies the continued use of Schottky structures where MBE grown material is available. By studying the photocurrent spectra from this sample (figure 5.2.4), it is clear that unfortunately little change in the spectral shape of the bandedge is found, with the only major difference being a variation in the quantum efficiency of the device. A point to be noted here is that the bandedge shape indicates that donors are present and agrees with the hypothesis of a failure to control the carrier density in the quantum well, rather than destruction of the mechanism by donor segregation. The justification for this is that the later MOCVD layers which suffer from segregation show a very large broadening of the bandedge (figure 7.4.6) not exhibited with this sample. The explanation for the inability to influence the quantum well carrier population lies in careful interpretation of the CV data. The depth of the doping spike from the surface is approximately 0.56μm (Appendix A6), yet the experimental doping profile

a)

b)

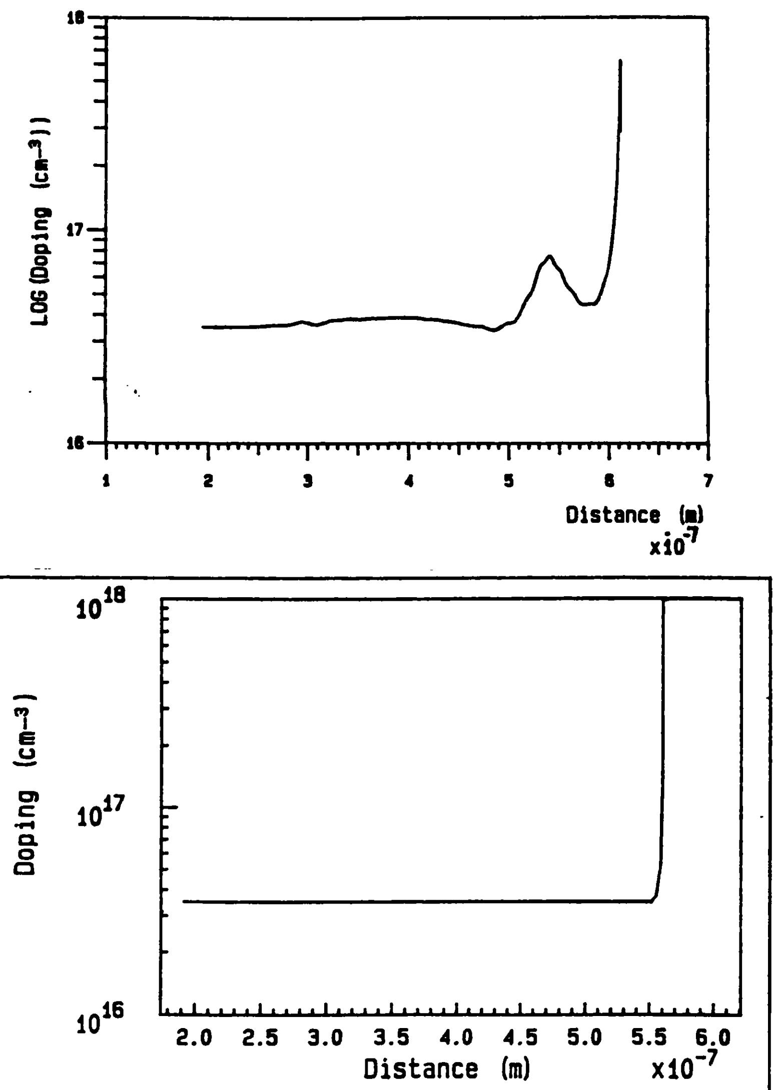

Figure 5.3.2 *Experimental (a) and simulated (b) CV doping profiles for CPM460.*

only indicates a highly doped region occurring at 3.1μm. A simulated doping profile confirms the depth to be 0.56μm rather than that of the measured data. However, it is the distance scale minima that are of interest, indicating 0.56μm in the simulated case and 2.2μm in the experimental case. Even if the doping spike was absent, the maximum zero bias depleted distance which could be anticipated is 1.1μm. In other words, the capacitance measured is greater than expected from an unbiased Schottky junction, or a junction potential of 3.5 volts (over three times that which can be anticipated) would be required to reconcile the experimental data. In fact, the answer lies in the background doping in the sample which is a *p*-type impurity common to MBE growth. This leads to the formation of two junctions within the sample, one formed at the surface with the Schottky metallisation, and a second between the lightly *p*-type epitaxial layers and the *n*-type substrate. This then gives to two built in potentials and twin depletion regions which gives rise to the larger than expected zero bias capacitance. The consequence of this is that the depletion regions meet at the doping spike and are unable to produce sufficient electric field to affect the emptying of the quantum well.

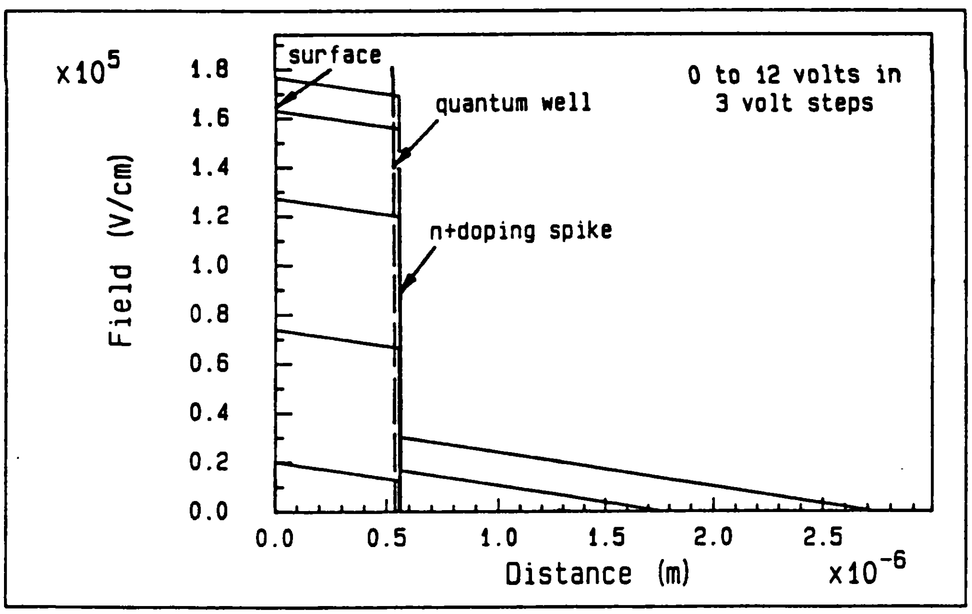

Figure 5.3.3 *Modelled electric field plot for sample MO685*

p-n Junction Structures

The second classification of QW-FEM is the *p-n* junction device. This structure avoids the difficulties of the MOCVD Schottky device associated with the high doping experienced in the the AlGaAs cladding regions. The use of the semiconductor-semiconductor junction enables a closer proximity to the quantum well and hence greater field control than that provided by the Schottky metallisation.

The agreement between theoretical electric field predictions and photocurrent spectra regarding the recovery of excitonic absorption is most clearly seen in the *p-n* junction sample MV292 (figure 5.2.2c). Onset of excitonic recovery is seen at 2V (reverse bias), both light and heavy hole peaks are clearly present at 4V, while at 6V the band edge has shifted by virtue of the Stark shift and the exdtonic recovery is fully complete. The theoretical curves for the field in the sample indicate that the recovery field of $\approx 10^5$V/cm (section 3.3) exists across the quantum well at a bias of 4V (figure 5.3.4), in good agreement with the experimental recovery voltage. This is summarised in table 5.3.1, along with data for sample CPM459.

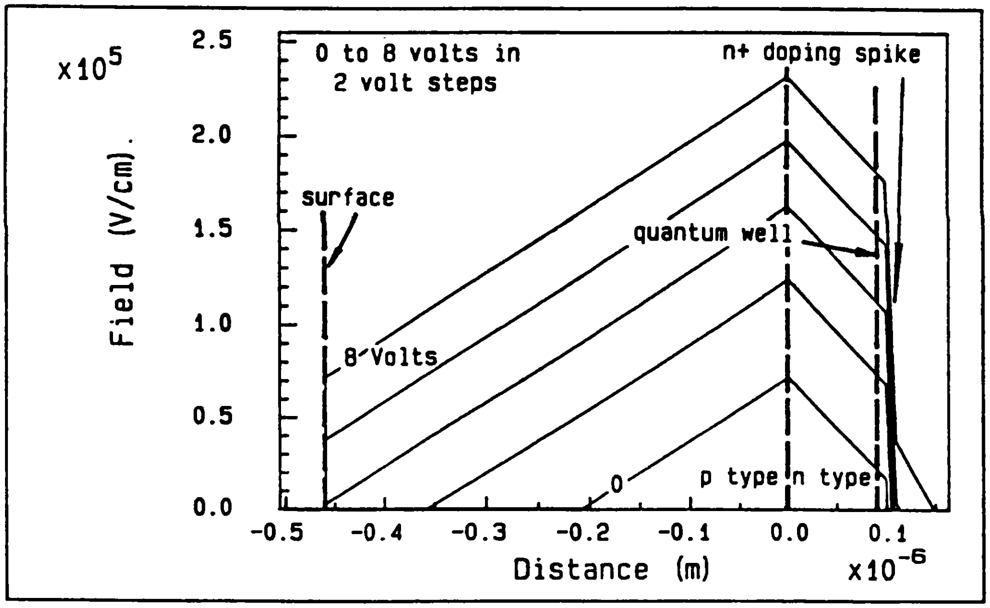

Figure 5.3.4 *Predicted electric field curves for sample MV292*

Evident in each of the spectra illustrated in the previous section is the combination of Stark shift with the recovery of the excitonic feature. As explained previously, this is brought about by the reverse bias operation of the device and the large electric fields used to sweep the electrons from the quantum well. The Stark shift is a known parameter and hence shifts of the excitonic peaks can be reconciled with the electric field plots: this provides a

Sample	Experimental: Recovery voltage	Theoretical: Electric field	Theoretical: Recovery voltage @ $1x10^5Vcm^{-1}$
MV292	4 volts	$1.1x10^5Vcm^{-1}$	3.5 volts
CPM459	≈6 volts	$1.3x10^5Vcm^{-1}$	4.2 volts

Table 5.3.1 *Comparison of experimental and modelled recovery biases and electric fields. The theoretical value of electric field is determined at the experimental recovery voltage. The theoretical recovery voltage corresponds to the anticipated recovery field of* $1x10^5Vcm^{-1}$.

further indication of the validity of the design approach. Figure 5.3.5 illustrates the Stark shift of excitonic resonances as a function of electric field and well width [Peter Stevens], giving values of around 2.5nm and 8nm at electric fields of $1x10^5$ and $1.8x10^5V/cm$ respectively for a 50Å quantum well. Measurements of this parameter from the MV292 photocurrent spectra (figure 5.2.2c) yield approximate values of 3±1nm and 7±1nm respectively for the field values above. The errors lie in determining the position of the zero bias exciton, however a check of the shift obtained between two high field values is also in reasonable agreement.

A similar analysis of the data for the 75Å well width sample, CPM459, shows that a bias of ≈5V is required to produce the exciton recovery field of approximately $10^5V/cm$ (Table 5.3.1). This is largely confirmed by the spectral data for the sample (figure 5.2.2a). However, the lack of an excitonic peak somewhat restricts the analysis that can be performed.

The doping profiles for these samples have been studied in detail to gather doping information and to confirm that the sample is functioning as anticipated. The interpretation of CV data becomes considerably more complex as *p-n* junctions are introduced, especially where both *p* and *n* type lightly doped regions exist. The measured CV data provides feedback to the electric field and simulated doping profile program so that accurate field values can be obtained.

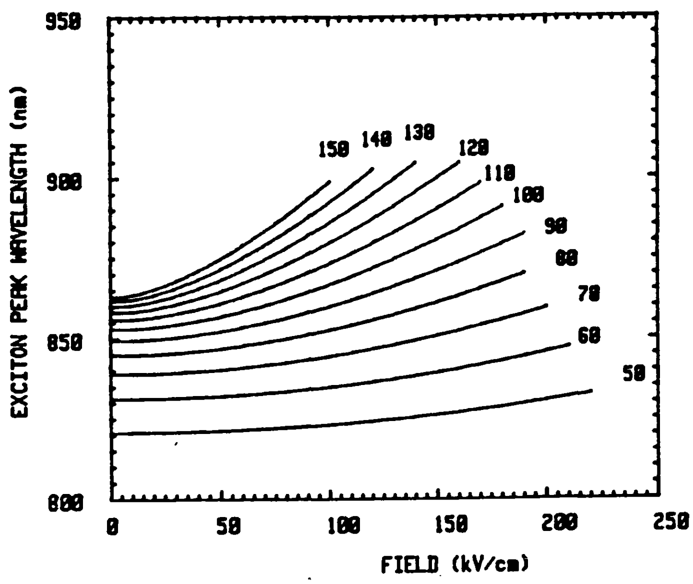

Figure 5.3.5 *Stark shift as a function of field for a variety of well widths [Peter Stevens]. The barrier used in this data is* $Al_{0.3}GaAs$ *as opposed to* $Al_{0.2}GaAs$ *used for the QW-FEM, nevertheless the shifts are expected to be in reasonable agreement although absolute values of wavelength should be discounted.*

The experimental and measured doping profiles for sample CPM459 are illustrated in figure 5.3.6 and clearly there is some agreement. However the experimental data shows a much wider doping spike than expected, although the voltage at which the spike appears agrees well with the modelled field and simulated CV plots. However, the distance scale is inconsistent and is shifted by approximately 0.15μm at all biases along the plot. This could be attributed to the presence of an unknown capacitance which adds to that of the device. To eliminate the experimental arrangement as a source of error in this respect, both packaged and unpackaged samples were used for CV measurements and found to be in agreement. A second possible source of error was the contact metallisation on the device which may have been producing a depletion region due to an unexpected potential barrier. This possibility was also entertained by measuring the CV profiles of a set of samples before and after a high temperature alloying cycle: no marked change was found. The third, and most likely, source of error is the method used to measure the capacitance value. A DC bias is applied to the device as required, and the meter (Hewlett

Packard LCZ) superimposes an AC signal and measures the out of phase component of the current flowing in the test device: from this the capacitance determined. It can be shown that this measurement is sensitive to any series resistance, essentially through an RC time constant [Blood]. A typical *problem-value* of resistance is of the order of 50Ω for the size of sample and measurement frequency used, and measured forward bias characteristics for the devices indicate values of this order. Unfortunately, this analysis would suggest a reduction in capacitance rather than the increase found. The problem is not apparent in other samples to the extent seen with CPM459 & MV292, and no conclusions have been reached about the source of error.

a)

b)

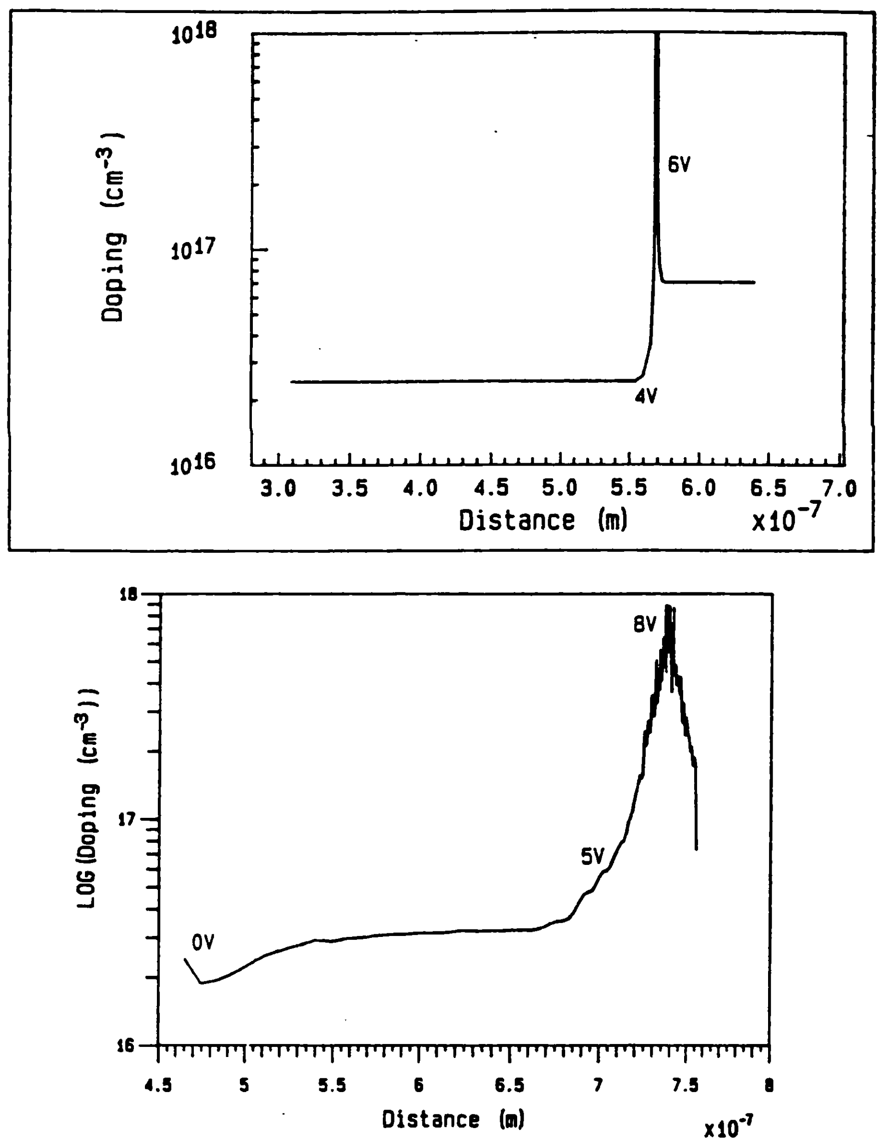

Figure 5.3.6 *Measured (a) and simulated (b) doping profiles for sample CPM459*

Capacitance voltage doping profiles for the sample MV292 (figure 5.3.7 a) clearly show a doping spike of a more reasonable width, although large discrepancies were found across the sample. The initial, simple interpretation of the collective CV data was that a variation in the doping spike existed across the wafer. However, photocurrent spectra partly contradicted these observations, as the highest degree of screening appeared to correspond to the areas of the sample for which CV measurements indicated the lowest doping spikes. This turns out to be an artefact in the CV measurement introduced by the variation of both the *p*-type doping and the doping spike across the wafer, and the scales of these variations are not as severe as initial interpretation of the CV data indicated. The doping spike can only appear in the CV profile if the *p*-type depletion region succeeds in extending to the ohmic contact at the surface of the sample. The width of this depletion region then becomes fixed and the application of further reverse bias can only deplete the *n*-type regions of the sample. If the n^+ doping spike is not fully depleted at this point it will appear in the doping trace. Figures 5.3.8a and 5.3.8b demonstrate this effect by modelling the expected doping profiles and compare with the experimental profiles of figure 5.3.7a,b respectively. In figure 5.3.8a (5.3.7a) the doping spike appears due to the *p*- type depletion region extending the surface. The converse is illustrated in figure 5.3.8a (5.3.7b) when an increase in *p*-type doping from $2x10^{16}$ to $3x10^{16}$ has been introduced.

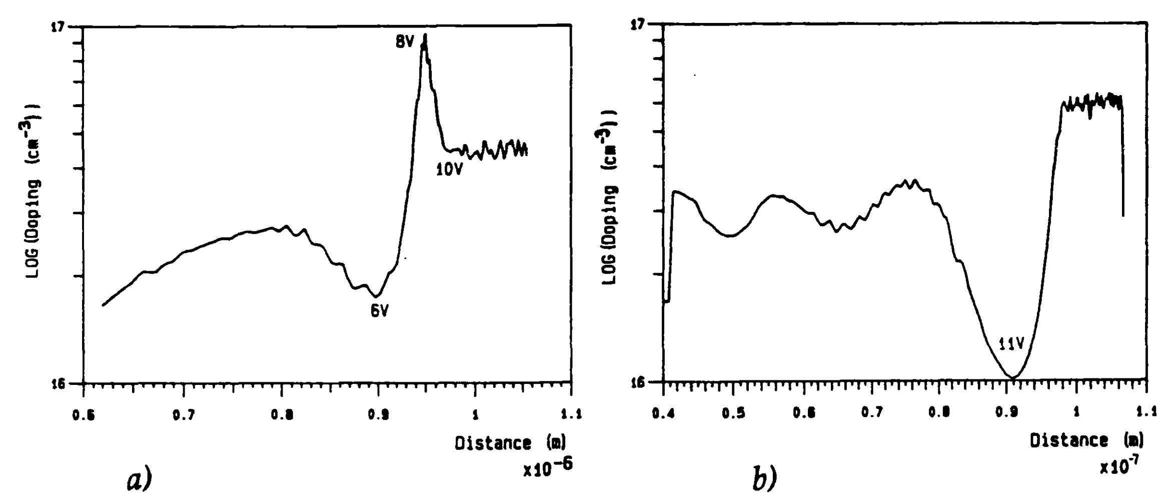

Figure 5.3.7 *Measured doping profiles for sample MV292. a) and b) correspond to two different areas of the wafer.*

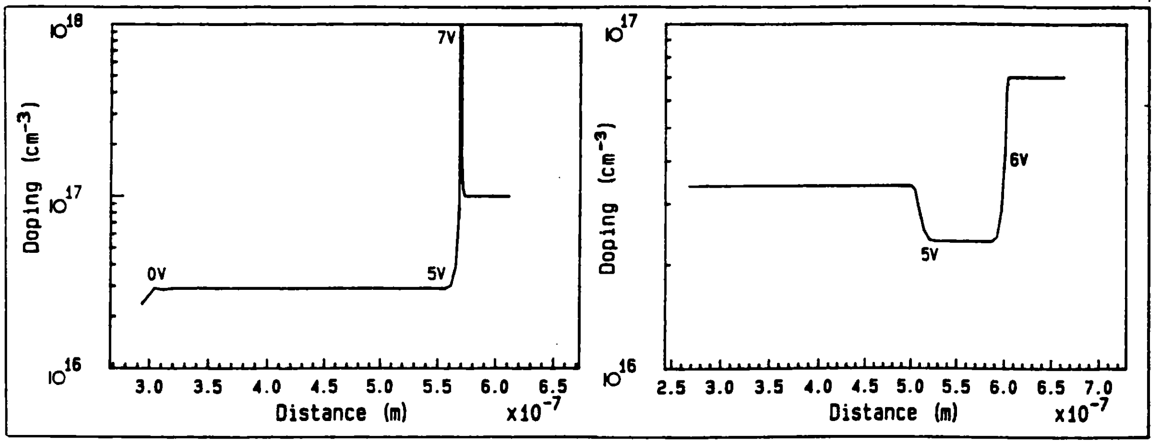

a) *b)*

Figure 5.3.8 *Simulated doping profiles for sample MV292. a) and b) correspond to marginally different doping levels in the p-type upper cladding layer.*

The nonuniformity of both the optical and electrical characteristics, which was highlighted by doping profiles and photocurrent measurements, has a marked effect on the performance of the devices. As a consequence, each wafer was mapped both optically and electrically to ensure that the best performance was found. Producing a picture of the characteristics in this way enabled the source of the problem to be highlighted and more rapid assessment of successive layers. The degree of quenching found in MV292, for example, can be seen to decrease rapidly across the wafer in the direction of the gas flow in the MOCVD reactor. This dependence would perhaps suggest the depletion of reactants such as the SiH_4 used to provide the donors of the doping spike. This has not been confirmed by any other means. The most alarming consequence of the variation in the quenching is that the size of the standard photodiode is sufficiently large to introduce spectral broadening if the spot size is not restricted (section 4.4). Similarly, the effects on waveguide transmission are catastrophic as the inhomogeneity of the characteristics along a typical interaction of the order of 0.5mm broadens the spectral features. This is described in section 5.5. The particular problem with sample MV292 is that the area of the sample which shows the greatest modulation of excitonic oscillator strength lies at the immediate front edge of the wafer (≤5mm) where fluctuations in all of the growth parameters can be expected.

Inverted and Twin Stripe Structures

The inverted and twin stripe structures are important in the development of greater carrier densities for improving excitonic saturation. As described earlier, the motivation for moving the doping spike was to ensure zero electric field across the quantum well when no external bias is applied to the device. The technique used to do this can best be seen by studying a specific structure. Sample MV317 has a single doping spike above the quantum well (Appendix A4) and the corresponding electric field profile is illustrated in figure 5.3.9. The zero bias electric field lines suggest that the doping spike thickness prevents depletion into the quantum well in the desired manner, however care must be taken with this interpretation. The quantum well is designed as a channel into which electrons fall and hence the doping spike is, in fact, "depleted" to some extent by the quantum well itself. Clearly, the simple model used becomes very restricted at this stage, especially since the sheet population of the well and the donor concentration of the doping spike are comparable. More precise design should incorporate a self consistent approach allowing for the redistribution of the carriers [Inoue et al 1985].

The quenching of the excitonic resonance is weak in MV317 and, as noted earlier, this may be due in part to the very narrow *as-grown* well width. This

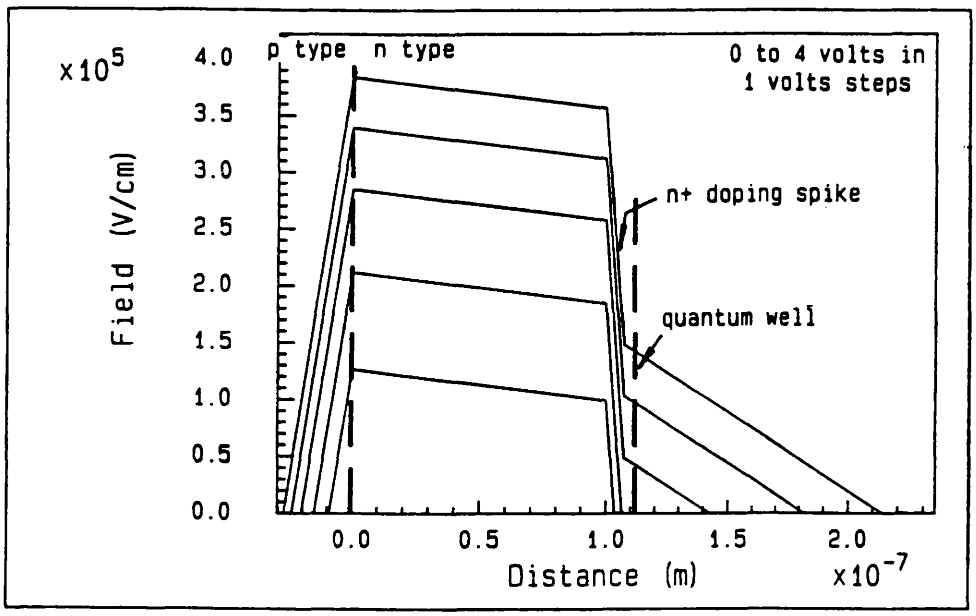

Figure 5.3.9 *Predicted electric field profile for sample MV317*

reduction in width pushes the N=1 energy level towards the top of the quantum well, reducing the offset with the barrier conduction band. Restriction of the quantum well population occurs due to the reduced confinement to the well through thermal and tunnelling effects. Nevertheless, the quenching effect *is* small and further analysis of the electrical properties of the device suggest that an electric field exists across the well at zero bias.

The doping profile distance scale for this sample indicates a depleted depth of over 0.2μm even at 1V forward bias, whereas the sample specification (Appendix A4) and the electric field profile plots indicate that half this value is expected. Offset in the distance scales of doping profiles have been noted with other samples. However, a second strong indication that an electric field exists across the quantum well at zero bias comes from the breakdown voltage of the devices. The breakdown field anticipated for GaAs ($4 \times 10^5 Vcm^{-1}$) and the predicted field developed in the sample (figure 5.3.9) indicates that a breakdown of voltage of only 5V is expected for the device. In fact, values of around 12V are achieved for mesa etched structures, indicating that the doping spike does not have the donor density expected and it has been effectively "depleted" in populating the quantum well. This confirms the conclusions drawn from the CV data, i.e. that a field exists across the quantum well at zero bias.

The twin spike structure of sample CB1 represents the most complex used in this thesis (Appendix A5). The introduction of a second spike gives the sample the advantage of zero field across the well at low bias, whilst the dual spikes act to supply a very large donor density. The electric field profile for this structure is illustrated in figure 5.3.10 and shows that fields from 0 to $2.3 \times 10^5 V/cm$ are developed at the well for a voltage swing from 0 to 4 volts. The design is restricted by the breakdown field of GaAs in a manner similar to the inverted structure above (MV317). The depletion of the first doping spike is vital to the control of the electron density in the quantum well, and consequently the spike must remain sufficiently narrow that the field at the junction must not exceed $4 \times 10^5 V/cm$ when the field at the well is approximately $2 \times 10^5 V/cm$. This criteria is quite restrictive, especially when growth tolerances must be accounted for in the design.

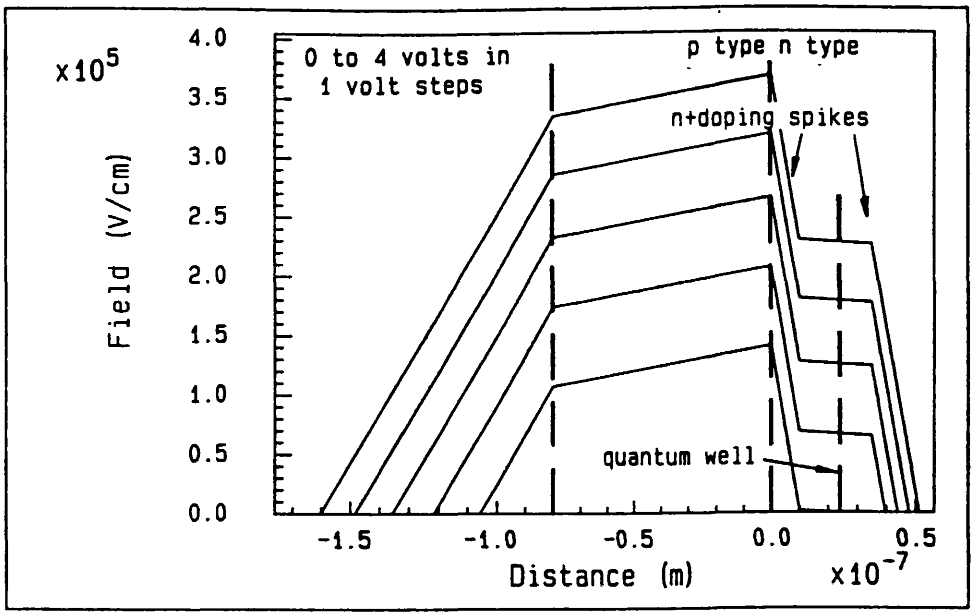

Figure 5.3.10 *Modelled electric field profiles for sample CB1*

Little can be derived from the doping profile of CB1 due to the continued depletion to both sides of the junction eliminating the peak from the plot in a manner similar to that described for MV292. Bias dependence of the spectral position of the excitonic peak, however, is notably greater than in MV292. This is both due to the wider quantum well having a larger Stark shift (figure 5.3.5) and the differences in the design of the junction, which lead to a greater field at the quantum well for a given bias in sample CB1. Also notable is a reduction in the initial Stark shift (0-2 volts) which perhaps indicates that an electric field initially exists across the quantum well. The excitonic quenching in this sample does not represent an improvement over that in MV292 and the high field Stark shifted spectra also broadens considerably more whilst rapidly losing oscillator strength due to the increased width.

The various attempts to increase the oscillator strength have proved relatively unsuccessful in the light of the early 50Å quantum well sample. The data from the twin spike sample, CB1, indicates that the limit to the quenching attainable may have been reached. This possibility is considered in the waveguide saturation and polarisation measurements of section 5.6.

5.4 Derivation of Absorption and Transmission Spectra

The photocurrent spectra for QW-FEM structures can be used to deduce the absorption in the quantum well giving useful comparison with values obtained in undoped MQW structures. These corrected spectra then give a clear indication of the anticipated waveguide transmission spectra (section 5.5) and modulation performance which can be expected (section 5.7). Also, through the Kramers-Kronig relationship, the refractive index variation associated with the absorption change can be found. This has a two fold use: firstly, the index change at the absorption modulation wavelength is obtained and gives an indication of the chirp-like spectral broadening which can be expected; secondly, the potential of the mechanism for phase modulation in an optical waveguide can be assessed. These will be compared with the equivalent parameters for MQW structures.

Calculation of Absorption from Photocurrent Data

The calculation required to transform photocurrent data and produce an absorption spectra involves the measurement of both the incident light intensity and the photocurrent at a point in the absorption spectrum. There are also several basic assumptions which must be made in order to justify the transformation and these are discussed here. Photocurrent I_{ph} can be related to the absorption (α) in the sample via the equation:

$$I_{ph}(V,\lambda) \quad = P_o\left(\frac{q\lambda}{hc}\right)(1-R)\,\eta(V)\,(1-e^{-\alpha l})$$

where P_o is the incident power, q the electronic charge, λ the wavelength of the incident light, h is Planck's constant and c is the velocity of light. The factor (1-R) accounts for the light reflected at the surface of the sample and the reflection coefficient for GaAs is taken as 30%. The term $(1-e^{-\alpha l})$, which includes both the absorption and the absorber length, l, can be approximated to αl for the case of a single quantum well, as the incident power is barely depleted by the absorption which takes place. The quantum efficiency, $\eta(V)$, is typically low at zero bias rapidly increasing to a fixed limit with applied field. Consequently, the low voltage spectra must be normalised to compensate for

a)

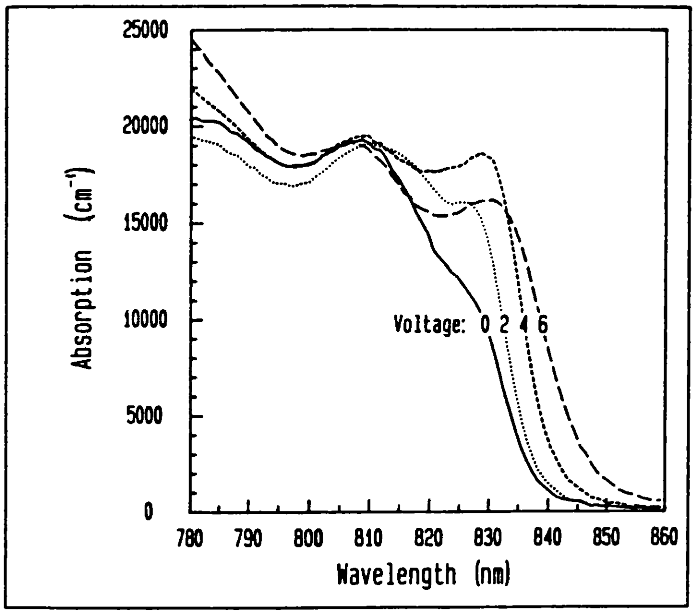

b)

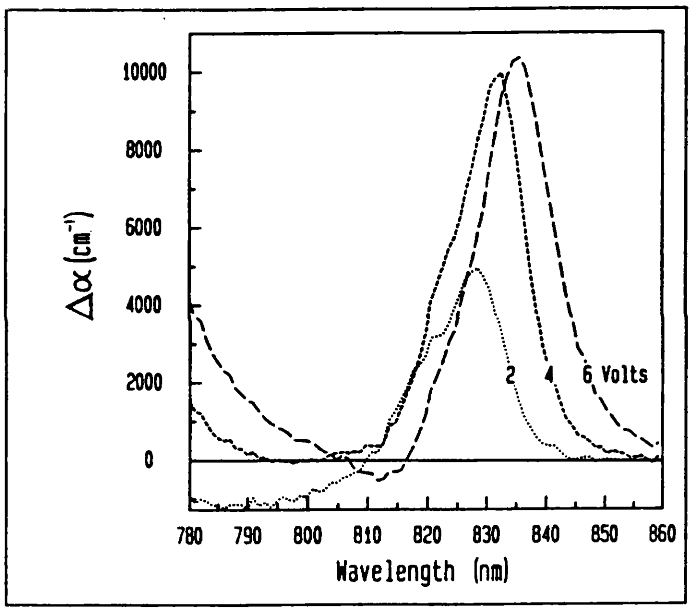

Figure 5.4.1 *a) Absorption spectra for sample MV292 derived by normalisation of photocurrent spectra. b) The change in absorption with bias as a function of wavelength calculated from part a).*

the reduced quantum efficiency and this is generally performed by finding a short wavelength point in the spectra where all the high quantum efficiency curves meet. It is assumed that the quantum efficiency is independent of wavelength and also that the maximum value is unity. This latter point is a reasonable assumption for the case of a single quantum well [Miller et al 1985].

The actual measurements require a careful calibration of laboratory instruments for determining the photocurrent and incident light levels. The experiment is performed with a calibrated power meter to measure light intensity (Coherent 212, Si head) and a lock-in amplifier to measure photocurrent (section 4.3). The power level measured with the meter must obviously be doubled due to the chopping of the incident beam. The lock-in amplifier was calibrated using a function generator to provide a known signal at the sample holder.

The normalisation of the photocurrent spectra for sample MV292 has been performed and the resulting absorption spectra are illustrated in figure 5.4.1a. Also illustrated are the *absorption change* spectra derived by simple subtraction of the 0V spectrum from the successive biased spectra (figure 5.4.1b). The absorption values which have been assigned agree well with MQW data of other authors. Data provided by Mark Whitehead for a 50Å quantum well (Chapter 6, figure 1.2.4) indicates a value of approximately 22,000cm^{-1} on the N=1 subband to the short wavelength side of the excitonic peaks. This region of the spectrum is the most appropriate for comparison as the excitonic features cannot be expected to correspond to those of an undoped sample (Section 5.2). The figure is in good agreement with the data presented here for sample MV292.

The absorption values, and specifically the absorption change ($\Delta\alpha$), lead directly to the calculation of the modulation available in an optimised device. A full analysis of this appears in section 5.7 where the absorption data is used to calculate realistic curves illustrating both modulation depths and insertion losses in a refined waveguide structure.

Refractive Index Modulation

The modulation of the refractive index follows hand-in-hand with the absorption change and can be related through the Kramers-Kronig relationship [Seraphin and Bottka].

$$\Delta n(\omega) = \frac{c}{\pi} \int_0^\infty \frac{\Delta\alpha(\omega')}{\omega'^2 - \omega^2} \, d\omega'$$

Where ω is the angular frequency of the incident radiation and the integral is performed over all values of frequency (ω'). The parameters n and α have their usual meaning of, respectively, refractive index and absorption. In practice the integral need only be performed in the region where the absorption change is significant. To simply integrate using a trapizoidal approximation the mathematical expression in terms of wavelength becomes:

$$\Delta n(\omega) = \frac{1}{2\pi^2} \sum_{i=1}^{n-1} \frac{\Delta\alpha(\lambda_n)}{(\lambda_n/\lambda_i)^2-1} + \frac{1}{2\pi^2} \sum_{i=n+1}^{m} \frac{\Delta\alpha(\lambda_n)}{(\lambda_n/\lambda_i)^2-1}$$

The summation is split into two halves to avoid the singularity which occurs when λn and λi are equal. This expression is then calculated for each point (1 to m)in a $\Delta\alpha$ spectrum. The Kramers-Kronig transform is computed for the absorption spectra of figure 5.4.1 and appears in figure 5.4.2. The refractive index relationship for GaAlAs was given in section 3.4, and roughly corresponds to n = 3.5 for $GaAl_{0.2}As$. Hence, the maximum modulation of the index obtained ($\Delta n/n$) is 1.1% of the index value.

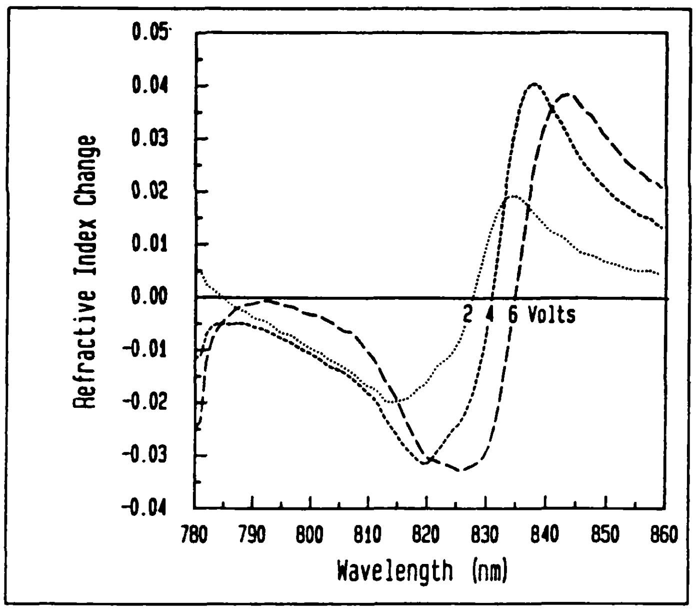

Figure 5.4.2 *Change in the refractive index as a function of wavelength and bias derived from the absorption data of figure 5.4.1*

For useful phase modulation the actual value of index change available is very much smaller. The reason is that a very high absorption change or modulator *contrast* is associated with the peak index change. For absorption modulation purposes it is important to *minimise* this refractive index change as it introduces a phase change which represents spectral broadening. Both of these situations will be discussed below, but first, for comparative purposes, it is useful to introduce a figure of merit indicating the ratio of refractive index and absorption effects. The parameter used is the *γ-factor** which is equivalent to the change in the refractive index divided by the change in the extinction coefficient and gives an indication of the "usefulness" of the mechanisms in both phase and absorption modulation cases. This can be expressed as:

$$\gamma = \Delta n \,/\, \Delta n'$$

where n and n' are the real and imaginary parts of the refractive index respectively. The imaginary part of the refractive index is identical to the extinction coefficient which is related to the absorption γ through the expression:

$$n' = \alpha\lambda/4\pi \quad \Rightarrow \quad \Delta n' \equiv \lambda\Delta\alpha/4\pi$$

$$\Rightarrow \quad \gamma = 4\pi\Delta n' \,/\, \lambda\Delta\alpha$$

This parameter is calculated as a continuous function of wavelength for sample MV292 and illustrated in figure 5.4.3a,b. The data is calculated for the 4 volt difference spectra of figure 5.4.2 and the position of the maximum absorption is indicated on the expanded scale plot.

The study of refractive index changes in quantum well material are of interest for producing highly efficient phase modulators. [Zucker et al 1988a, Bradley et al]. The peak index changes indicated in the Kramers-Kronig analysis above are typical of those reported for MQW devices and the spectral behaviour to long wavelength also shows a similar tail [Bradley et al, Zucker et al 1988b]. For pure phase modulation there should be no associated absorption changes, however it is the absorption which is producing the index change with this mechanism. The result is that the largest index changes cannot be used and "detuning" from the excitonic features must be employed to reduce the intensity modulation. The *γ-factor* is hence an important

**The symbol γ is used here, whereas many texts refer to this parameter as α. This is not used here to avoid confusion with optical absorption.*

parameter for determining the usefulness of the phase change in the light of a residual absorption modulation. The data of Zucker et al [1988a] indicates that the *γ-factor* exceeds 20 at a detuning to long wavelength from the excitonic peak of 40nm. The long wavelength values of the *γ-factor* reported here are subject to a systematic error due to the unavoidable truncation of the data in

a)

b)

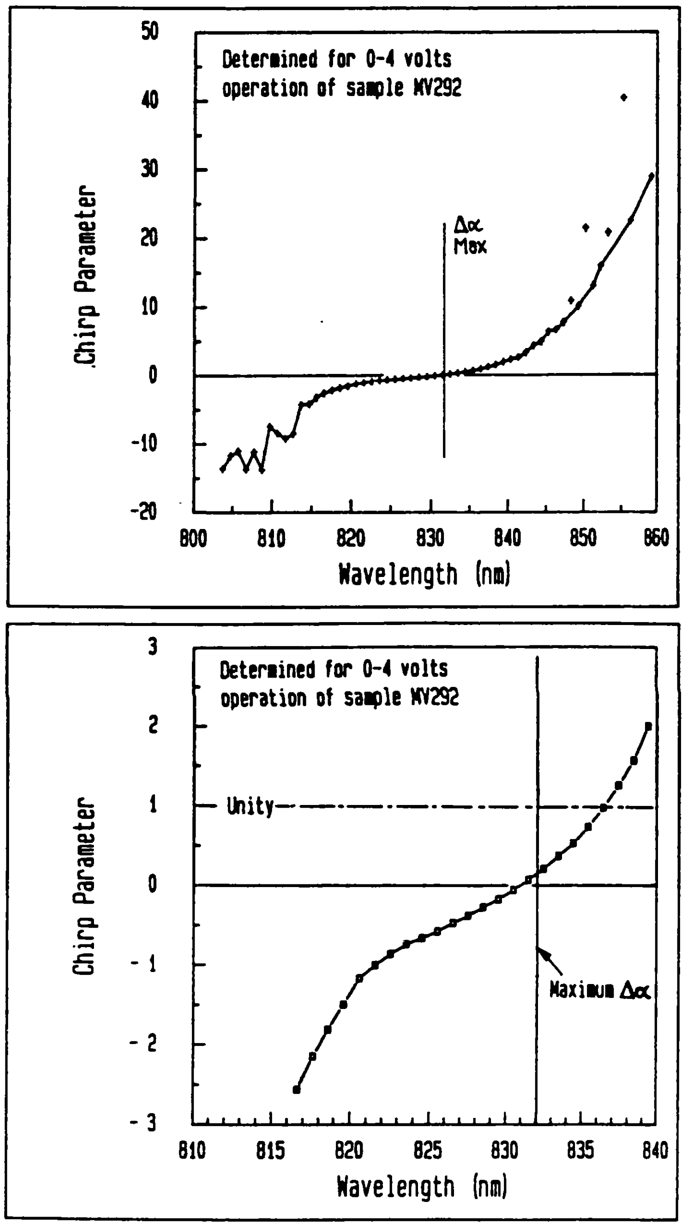

Figure 5.4.3 *Change in the γ-factor as a function of wavelength derived form the Δα data of figure 5.4.1b and the index data of figure 5.4.2. Part a) illustrates the full range of the parameter: the noise on the spectrum is due to the fluctuation around zero on the Δα spectrum. Part b) is an expanded plot illustrating the γ-factor at maximum absorption change.*

the Kramers-Kronig transform and a random error due to the noise component in the spectral data at low absorption levels. However, the data suggests values of the same order (figure 5.4.3a) and also very similar index changes, typically extrapolated to ≈0.01 at a similar detuning. The device of Zucker et al [1988a] gives a 90° phase shift in a 220μm long device with a γ-*factor* of 5, representing a 2.4dB intensity modulation. The argument here is not whether this is a useful phase modulating device, but that the QW-FEM shows no particular excellence in this respect. In addition, the QW-FEM has the overwhelming disadvantage of being restricted to a single well and, as a consequence, unless a moderate contrast can be tolerated there is no advantage over devices using carrier effects and/or the linear electro-optic effect for index changes [Mendoza-Alvarez et al].

The phase modulation associated with the absorption change is also an important parameter for a high speed quantum well absorption modulator, however in this case it is its reduction which is important. The phase shift which occurs acts to spectrally broaden the transmitted light. This is very similar to the effects seen in a directly modulated semiconductor laser [Linke 1984] where, essentially, a blue shift of the output is observed at switch-on and a red shift at switch-off. The occurrence of this introduces large power penalties and a limit to the transmission bandwidth of a single mode fibre system using a directly modulated laser, as discussed briefly in chapter 1 [Linke 1988]. External modulators can be introduced as a means of increasing system bandwidth by virtue of an anticipated smaller spectral broadening. The linewidth enhancement factor which describes the chirp of a directly modulated semiconductor laser [Koyama and Iga] is identical to the γ-factor introduced above for an external modulator. This enables direct comparison of laser chirp and the chirp-like behaviour of an intensity modulator.

Measurements of the refractive index change for MQW samples have appeared in the literature and values reported for the calculated chirp parameter. The work of Nagai et al clearly illustrates the source of the residual chirp by studying the $\Delta\alpha$ and Δn spectra. He finds that the point of zero absorption change gives a minima in the refractive index data, but unfortunately the converse is not exactly true and an index change *is* found at the wavelength of maximum $\Delta\alpha$. The index data in fact goes through a point of inflection at the $\Delta\alpha$ maxima but this does not coincide with the zero index change ordinate. The work of Nagai et al concludes that values obtained for γ are as low as 1.5. The chirp parameter for the QW-FEM is illustrated in the expanded scale plot in figure 5.4.3b and the values are considerably lower, of the order of 0.2 $\pm$0.1: the error indicated is in the measurement of the peak absorption change. The presence of an index change accompanying absorption modulation is again due to the displacement of the maximum $\Delta\alpha$ from the index change minima, however the situation here is slightly different. The shift of the spectral peaks in a MQW Stark shift modulator produces a large negative swing in the $\Delta\alpha$ spectrum adjacent to the more useful positive swing; this negative swing does not appear in the case of the QW-FEM due to the quenching, rather than shifting, of the excitonic features. This obviously has a considerable effect on the Δn spectrum and in fact produces the advantageous consequence of bringing the minimum index change into closer alignment with the maximum absorption change, hence reducing the chirp parameter. It is the symmetry of the $\Delta\alpha$ spectrum which is critical to the spectral position of the *γ-factor* zero and clearly the spectra of figure 5.4.1b show considerable success in this respect.

Chirp parameters for semiconductor lasers are related to carrier density effects rather than absorption changes and are fundamental to the operation as a consequence. Typical values reported recently range from $\gamma\approx4.6$ [Harder et al 1983] to 2.2 for bulk lasers [Kickuchi and Okoshi] and are around $\gamma\approx1.5$ for a quantum well laser [Ogasawara et al] (as interpreted by Koyama and Iga [1988]). This indicates that external modulation has considerable advantages in the reduction of spectral broadening. Dynamic measurements of the chirp produced by external modulators have been reported [Noda et al, Wood et al 1987] and values for the *γ-factor* of the order of unity have been found in both cases. The chirp-like behaviour is not related to the dynamics of the operation of the device in the manner seen in a laser diode [Linke 1984], and consequently the measured chirp must be influenced to a very large extent by the modulation signal. The dependence on rise times must play a large part in the reduction of observed degradation and hence comparison of dynamic measurements is difficult. Nevertheless, it is apparent that external modulation is an improvement over direct modulation of semiconductor lasers for long haul communications systems and that the QW-FEM may have a direct advantage in chirp reduction.

5.5 Experimental Waveguide Transmission

This section serves to illustrate the transmission spectra obtained from the best absorption quenching structures, MV292 and CB1. Modulation characteristics are presented but the predictions of the optimised performance in the light of the results obtained are deferred to section 5.7. The nonuniformity of the layer structures is discussed and the effects on the transmission spectra illustrated. Calculations of the transmission spectra are made for comparison and these use the absorption data calculated from the photocurrent in section 5.4. Further measurements of the transmission of other waveguide layers have been made and are described elsewhere in this thesis.

Initial waveguide measurements produced curves similar to those illustrated in figure 5.5.1a (MV292, sample I). The disappointing lack of the features visible in the photocurrent data is noticeable, although the general changes in the spectrum can be attributed to the excitonic quenching and Stark shift seen. Noise on the data, especially at high transmission, is attributable to Fabry-Perot cavity resonances. These are discussed in section 4.4, as is the smoothing which has been applied to give the solid curves illustrated. The spectra of figure 5.5.1b is for a sample (sample II) fabricated from the same wafer and, in fact, the pieces of the wafer used are less than 3mm apart. One marked difference in the devices is the length: Device I, 500μm; Device II, 330μm. Sample II can be seen to have a much higher transmission at short wavelengths as a consequence of the shorter guide length and a corresponding increase in Fabry-Perot cavity effects. However, this is not the full reason for the change in spectral characteristics: the second difference is the direction the light propagates with respect to the orientation of the cleave planes of the substrate. Clearly, a broadening process is in operation as the linewidths of the data are seen to increase with the device length. As described in section 5.2, this is brought about by a nonuniformity of the doping spike across the epitaxial structure. The effect is compounded by using samples from the front edge of the wafer where the excitonic quenching is highest and the layer uniformity is also greatest. Essentially, the quenching and peak position varies along the length of the guide as does the electric field across the quantum well, and the resultant data can be considered as a combination of many individual spectra. The diagram of the wafer usage (figure 5.5.2) illustrates which area each

a)

b)

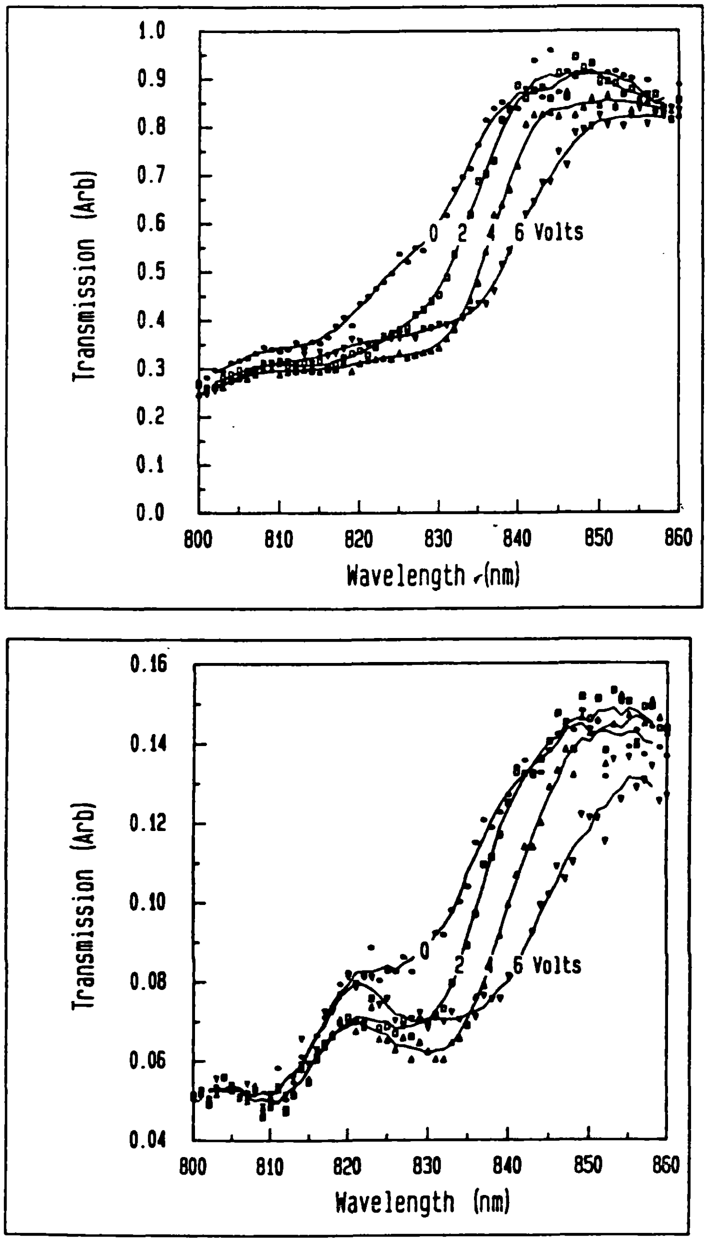

Figure 5.5.1 *Absorption spectra for sample MV292 a) 500μm device b)330μm device.*

sample came from. Also illustrated is the orientation in the MOCVD reactor and the corresponding optical and electrical nonuniformities. Within the scope of this simple analysis these dependences are all apparently related to the reactant flow direction. With this in mind sample II was chosen to have the waveguide propagation direction perpendicular to the reagent flow, and I believe that this has led to the improved characteristics seen.

For comparison the bias dependent transmission of a waveguide device can be predicted from the derived absorption spectra of section 5.4. The method is

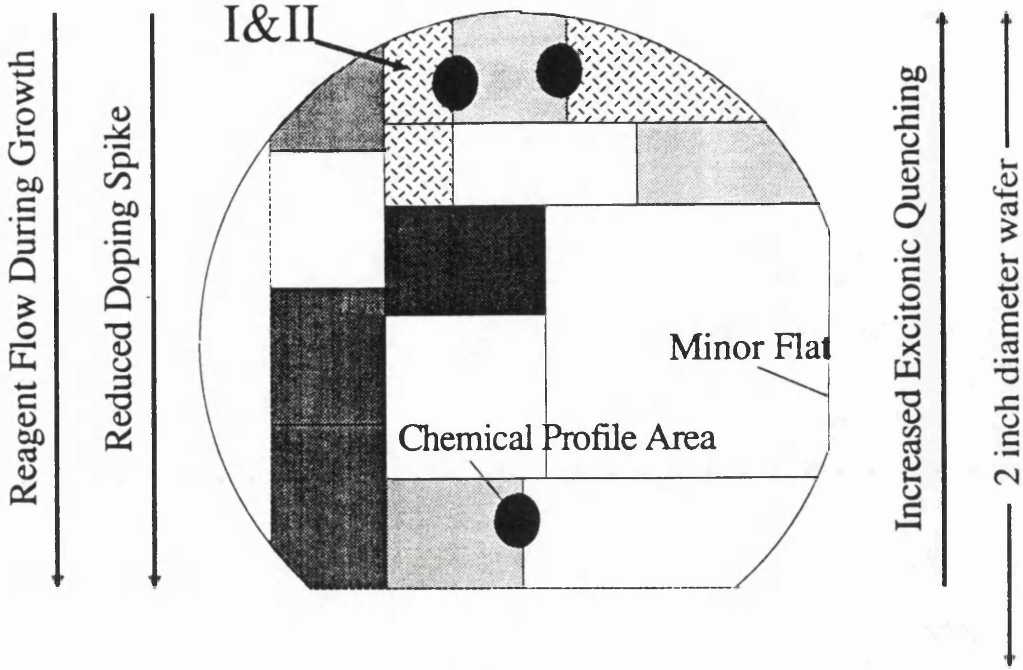

Figure 5.5.2 *Map of the MV292 wafer showing the orientation during growth, the position of sample I and II and the general trends in electrical and optical characteristics.*

a simple extension of the equations used for the calculation of modulation depth from published data (section 3.4). The normalised transmission is simply given by:

$$T/T_0 = \exp(-\alpha\Gamma l)$$

and this is applied to each point in the absorption spectrum. No additional absorption mechanisms are accounted for in these calculations: typically, propagation losses of the order of 0.2 dB/cm can be expected from the best GaAs waveguides [Inoue,H. et al 1985] and this represents a 1% reduction in the peak transmission found for a guide length of 300µm. An anticipated transmission spectra for sample MV292 is given in figure 5.5.3 and is modelled on the actual epitaxial structure and an experimental device length for sample II.The waveguide length (l) and overlap (Γ) parameters used are l=330µm, Γ=0.12%. The transmission spectra obtained is generally in good agreement with the experimental transmission data.

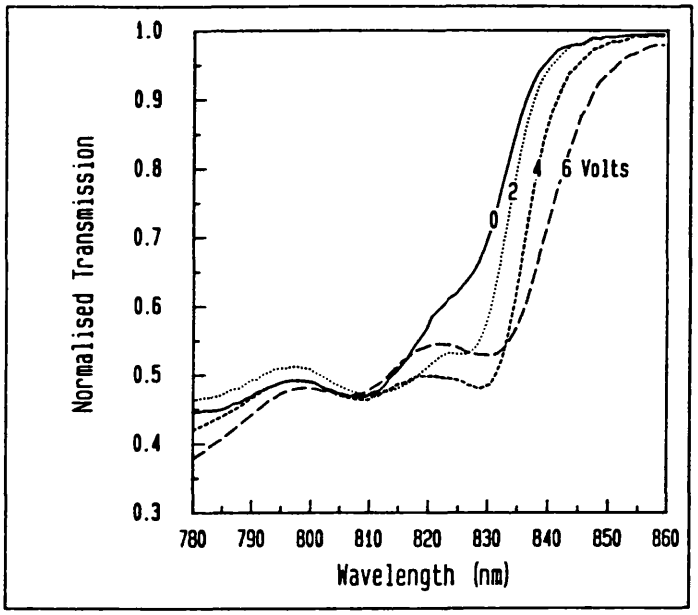

Figure 5.5.3 *Derived waveguide transmission spectra for samples MV292*

The transmission spectra for sample I and sample II, and the data derived from the photocurrent spectra, illustrate a continued improvement of characteristics as might be expected. The linewidths (half-width half-maximum) of sample I at a bias of 4 volts is greater than 10nm. Similar data for sample II and the derived transmission data show values of ≈9nm and 8nm respectively indicating that some residual broadening does exist. A further point to note is that the photocurrent data also exhibits broadening at higher biases (≥6V), presumably due to electric field inhomogeneities brought about by doping spike variations.

The waveguide ΔT spectra from sample MV292-II are shown in figure 5.5.4. The data shows that the device output intensity is varied by up to 34%. The greatest modulation depth (6V) is found to be 2dB while the insertion loss is 0.4dB. Both figures are calculated from the transmission spectra and insertion loss is internal and omits coupling losses. The device length is 330μm and the confinement factor of the 50Å quantum well is approximately Γ=0.12%. The modulation depth in the device is modest due to this low optical overlap with the quantum well and the non optimum length of the device. An increase of the device length to 1mm with the current degree of quenching and no additional broadening could achieve a contrast ratio of ≅6dB with an insertion loss of 1.4dB. The absorption in the quantum well at the excitonic peak (4V) is calculated using these figures and is found to be ≅21000cm^{-1} in good agreement with the absorption data derived form photocurrent measurements and the data of Mark Whitehead (figure 1.2.4). The corresponding change in absorption at the same wavelength is ≅5500cm^{-1}.

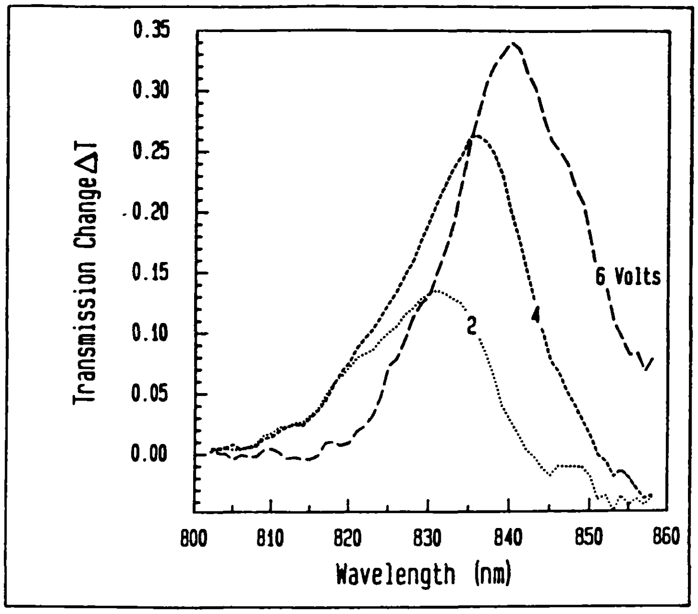

Figure 5.5.4 *Transmission change spectra calculated from the spectra of figure 5.5.1b*

Further transmission measurements have been performed using the sample CB1. The spectra are illustrated in figure 5.5.5 and it is clear that the data is of superior quality to that obtained from MV292. The uniformity is obviously considerably better as excitonic peaks are visible in the spectra of this very long (>1mm) waveguide. The device used in this assessment suffered from a low breakdown voltage, and consequently further bias could not be applied across the structure. However, without the need for a better device it is clear that some other spectral mechanism is at work. Observation of the near field pattern of the waveguide output facet during wavelength scanning showed an oscillation in the position of the image and the unexpected spectral feature at 850nm can be directly attributed to this effect. The guide appears to have a two moded operation and the modes are interfering at the output. It is also probable that this second mode has a greater attenuation due to a very much larger optical overlap with the metal applied to the surface of the device, or through coupling into the GaAs substrate. Attempts to launch the fundamental mode only, by use of a selection of lenses with different numerical apertures failed to have any major affect on this behaviour. The first order mode cut off for the standard waveguide design (section 3.4) lies at approximately 750nm, and consequently considerable deviations from the expected layer thicknesses or aluminium mole fractions of the AlGaAs layers must have occurred.

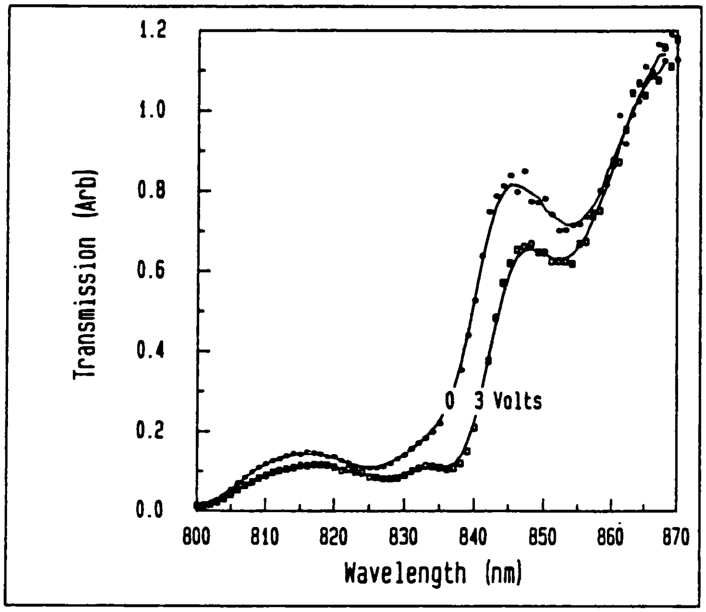

Figure 5.5.5 *Transmission spectra for sample CB1.*

5.6 Excitonic Quenching Performance Analysis

The current limitation to the device modulation depth, and to a greater extent the insertion loss, is evident in both the photocurrent and transmission spectra of the 50Å quantum well samples. The zero bias state, with the quantum well filled with carriers, does not produce a complete quenching of the excitonic resonance even in the case of MV292 (figure 5.2.2c) and CB1 (figure 5.2.3b). Attempts at further tailoring of the device designs have failed to produce the extra excitonic quenching required (section 5.3) and, as a consequence, a series of experiments were performed on the existing samples in an attempt to show that the desired results are feasible. Three methods were used to address the problem of incomplete excitonic saturation and these are discussed in detail in this section. The first of these experiments exploits a polarisation dependence of the excitonic absorption in a waveguide to show that the band edge feature is in fact the heavy hole exciton. The second experiment looks at the photocurrent in the structure at low temperatures in order to maintain a higher electron concentration in the quantum well. The third technique involves further carrier generation by the optical pumping of the structure. The conclusions are favourable and indicate that better modulator performance can be anticipated.

Investigation of Polarisation Effects

The launching of two different polarisations of light into the waveguide structures has been investigated. These polarisations correspond to the electric field vector ê, parallel and perpendicular to the plane of the quantum wells. Selection rules exist which imply that the heavy hole excitonic peak should not appear in the absorption spectrum of an undoped quantum well waveguide in the $\hat{e}_{\perp}$ case. These selection rules are due to the splitting of the light and heavy hole subbands and are derived at the zone centre (k=0) [Hensel and Feher]. The light and heavy holes have different spin states and the various allowed transitions can be calculated with their associated light polarisations [Weisbuch p51]. This polarisation vector describes the electric dipole motion and light must be emitted/absorbed perpendicular to this motion, from the classical picture of radiation from a dipole. The selection rules are derived from these facts and from studying the transitions: the light hole has strong and weak transitions with polarisation vectors perpendicular and parallel to the quantum well plane respectively, enabling absorption in both TM and TE polarisations; the heavy hole has only transitions with polarisation vectors in the plane of the well and hence TE propagating modes are not absorbed. The case for the transverse device is identical to that for TE mode in a waveguide with the transitions in the plane of the quantum well being allowed.

These selection rules have been confirmed in the work of Weiner et al [1985a,b] and are also an explanation of polarisation dependent gain found in quantum well laser diodes [Yamada et al]. The effect is demonstrated by experimental measurements on the undoped control sample MO733, which act as a confirmation of the experimental procedure. The two spectra, representing TE ($\hat{e}_{||}$) and TM ($\hat{e}_{\perp}$) modes in the guide, are illustrated in figure 5.6.1. Clearly the heavy hole excitonic peak is totally suppressed and the light hole peak oscillator strength is seen to increase as theory predicts [Hensel and Feher].

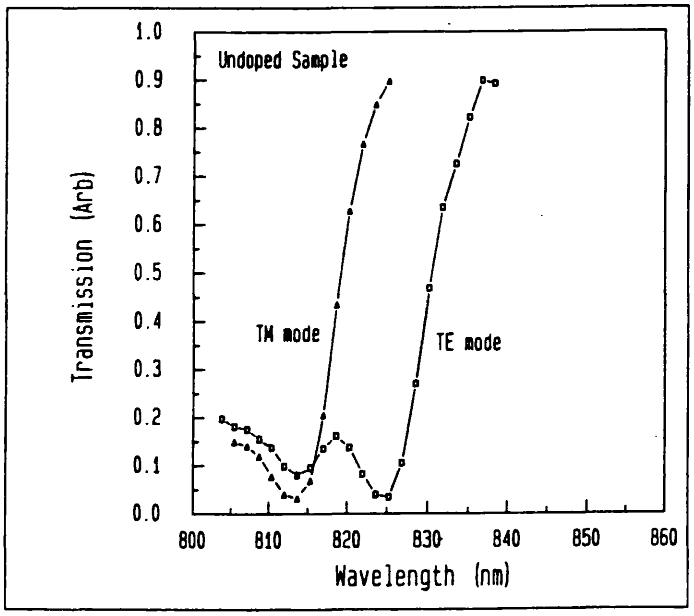

Figure 5.6.1 *TE and TM mode transmission spectra for sample MO733*

Measurements of the effects of polarisation on sample MV292 act to eliminate the heavy hole excitonic absorption and to reveal the renormalised subband edge expected in the quenched state. Figure 5.6.2a shows TE and TM modes at zero bias, illustrates the removal of the residual heavy hole spectral feature and shows a slight increase in the oscillator strength at the light hole. The residual absorption in the 830-850nm region has a constant slope and with the absence of heavy hole absorption constitutes a renormalised subband edge (section 2.2). As such, this is illustrating an achievable insertion loss for the modulator if this degree of heavy hole quenching can be attained. Similar measurements have been made at the excitonic recovery voltage and are illustrated in figure 5.6.2b. The heavy hole peak is seen to vanish as anticipated but the selection is not as clear cut as that seen in the undoped sample, MO733. The resulting linewidth is considerably broadened by comparison with the heavy hole peak and it is probable that residual heavy hole absorption exists. The reason for this apparent disagreement lies in the difference between the two samples rather than any experimental inconsistency: the possibility of impure polarisation selection has been eliminated through comparison with sample MO733 and cross checking with a second polariser.

a)

b)

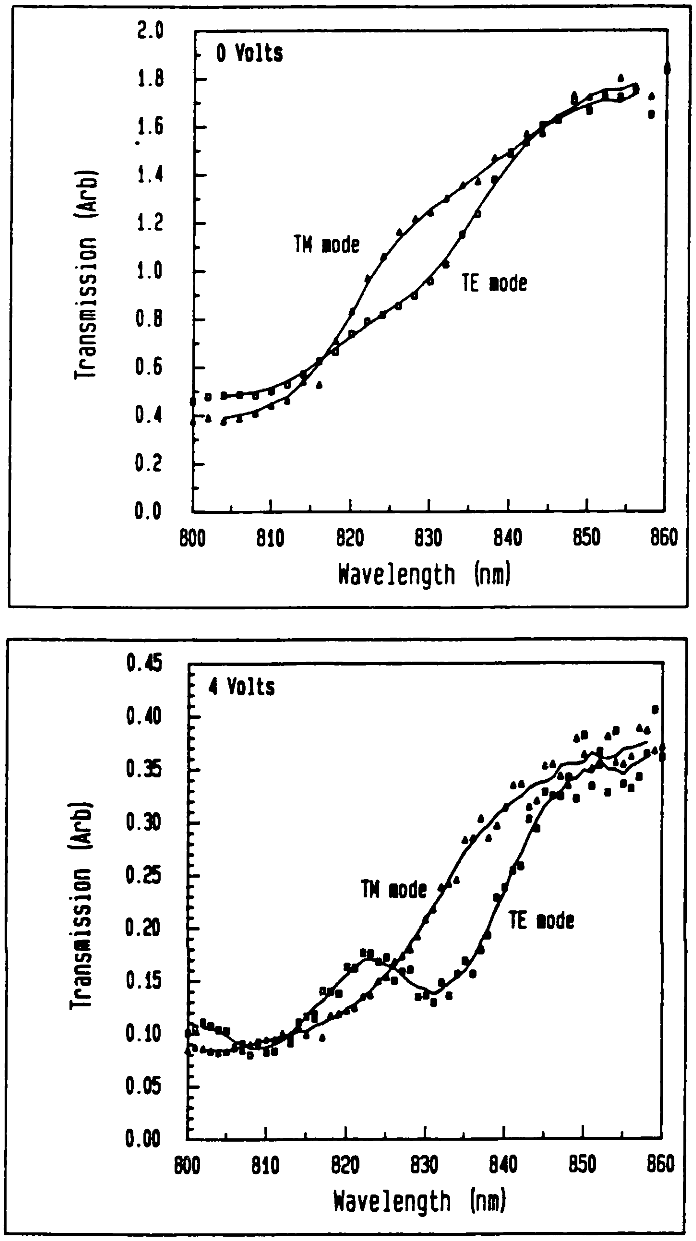

Figure 5.6.2 *TE and TM transmission modes for sample MV292 at a) 0 Volts and b) 4 Volts reverse bias*

The presence of a carrier population has been shown to mix the valence subbands and relax the selection rules for TE and TM polarisations [Sooryakumar et al] and this can account for the incomplete suppression of the heavy hole excitonic absorption. Sooryakumar et al describe polarisation dependent photoluminescence measurements from a modulation doped quantum well waveguide and concluded that completely mixed heavy and light character is observed for $k \approx 10^6 cm^{-1}$: this is estimated to correspond to an electron population of approximately $5x10^{12}cm^{-2}$. An investigation by Weiner et al 1985a, however, shows that optically nonlinear suppression of the light hole by TM propagating light does not break down the selection rules and no re-introduction of a heavy hole component is seen. Similar subband mixing effects might be expected with high electric fields across the quantum well [Miller,D.A.B et al 1985] (the appearance of forbidden transitions), although, in a separate paper, Weiner et al 1985b clearly shows that application of electric fields of up to $1.8x10^{5}cm^{-1}$ has little effect on the linewidth of the light hole during TM propagation in a quantum well waveguide.

There is obviously some doubt as to whether or not the selection rules are conserved in the case of the QW-FEM. The linewidths of the experimental data implies that some heavy hole character could exist for TM propagation in both biased and unbiased states. This casts doubt on conclusions drawn from the unbiased spectrum regarding the renormalisation of the subband edge. The heavy hole excitonic absorption may still be partly responsible for the absorption tail observed. Assuming that the maximum carrier density in the quantum well could be increased the $\hat{e}_{\perp}$ quenched spectra represents a worse case limit on the insertion loss that could be achieved.

Low Temperature Studies

A study of the QW-FEM photocurrent characteristics has been made at low temperature to increase the equilibrium thermal population of the quantum well, and to show that further excitonic saturation is possible at zero bias. A second effect is that a linewidth reduction of the excitonic features occurs increasing the excitonic recovery exhibited. These measurements are made using a photodiode fabricated from sample MV292 in an optical cryostat at a temperature of ≈80K (section 4.3).

The photocurrent data obtained is illustrated in figure 5.6.3a. The excitonic peak position, measured at a 4 volt bias, is seen to shift 43nm to shorter wavelength of its room temperature position (from 829nm to 786nm). The linewidths (HWHM) of the features are seen to improve dramatically with the recovered excitonic peak showing 4.4nm at 83K which compares with the 8nm observed at room temperature. The 1 volt photocurrent spectra has been magnified to illustrate the shape of the band edge which clearly shows no heavy hole excitonic contribution, suggesting that the quenching at low bias is vastly improved. The apparent absorption modulation at this temperature is clearly excellent. The bias dependence of excitonic recovery is also dramatically altered, with a stronger feature found at lower voltage. An important further observation is that the photocurrent falls with temperature and becomes undetectable at zero bias. This latter effect unfortunately throws doubt on any initial interpretation of the data due to the implications of carrier transport which are discussed below.

a)

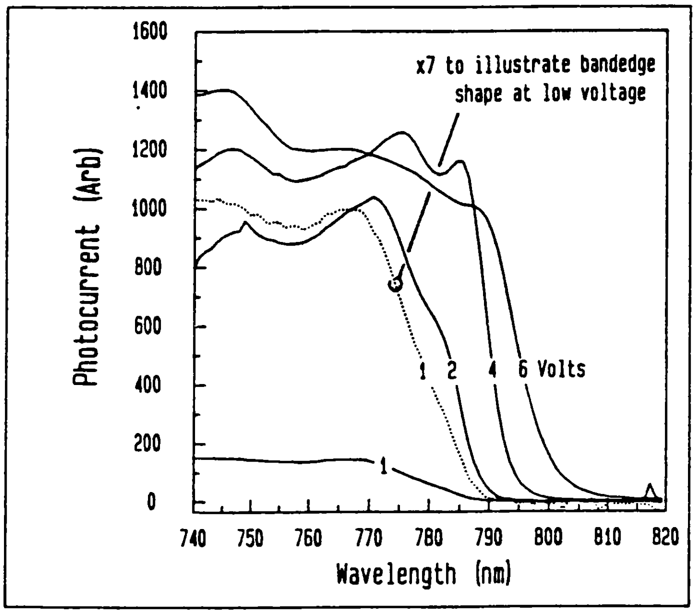

b)

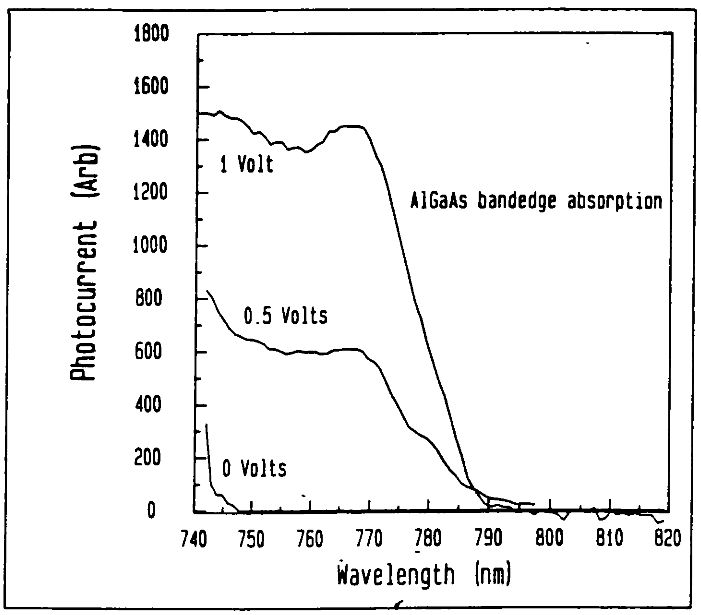

Figure 5.6.3 *Low temperature photocurrent spectra for sample MV292. a) illustrates the general changes seen in high field photocurrent data. b) show the "freeze out" of photocurrent at low biases.*

The increased occupation of the N=1 electron subband can be expected at low temperature through the change in the Fermi distribution which no longer extends into the continua above the well (section 6.2). The thermionic emission of carriers is reduced, as is the tunnelling probability. The zero contribution of heavy hole absorption to the photocurrent seems to agree with this, however the changes in the quantum efficiency of the device must be considered.

The observation of reduced photocurrent can be linked to the effects of thermionic emission. This is illustrated in the second series of spectra (figure 5.6.3b) where the low bias dependence of the photocurrent shows that the zero field quantum efficiency is effectively nil. The carriers introduced by photon absorption are unable to escape from the quantum well within their recombination lifetime and hence cannot create a measurable photocurrent. The zero volt photocurrent is found to be >30dB below that of the 2 volts spectrum. The only slight up-turn in quantum efficiency at ≈740nm is the absorption tail of the AlGaAs barrier material (section 5.2).

The changes in quantum efficiency are complex and only the basic points are expanded upon here. Both of the carriers created by photon absorption must escape to constitute a photocurrent in the external circuit. This implies that the lowering of quantum efficiency need only be attributed to the change in the transport properties of either the electron *or* hole. The heavy hole escape probability will dominate over that of the electron due to its large mass. An important point to note is that the escape probability must differ for the light and heavy holes due to their differing masses, and this leads to different quantum efficiencies for the light and heavy hole subbands. We could expect, therefore, that the apparent increased quenching of the heavy hole absorption is attributable to a decreased photocurrent quantum efficiency for the heavy hole subband. However, at room temperature, scattering of the light holes into the heavy hole subband occurs on a very short timescale so that the escape probability, and hence the quantum efficiency, is effectively equal for both. It is plausible that this is no longer true at low temperatures when kT becomes smaller than the separation of the hole subbands.

The low temperature data presented here suggests in principle that further excitonic quenching is possible with a higher electron density. The are two provisos. The first is that this population has been achieved at temperatures where thermal effects have been eliminated from the equation governing the equilibrium population of the quantum well. As such, there is no evidence that this population can be achieved by any means at room temperature in a quantum well of precisely this construction. The second point is that the removal of the heavy hole feature may in fact be a transport effect rather than a real quenching.

Optical Pumping for Excitonic Saturation

Another approach to increasing the carrier density in the quantum well is to simply exploit the optically nonlinear phenomena which formed the basis of the discussion of the QW-FEM modulation mechanism and design (section 2.2). However, the purpose here is simply to see if a larger carrier density can be created and thus assess the possibility of further quenching through the field effect mechanism.

The set-up for these experiments is described in section 4.4 and essentially enables a high power beam to illuminate the surface of the sample. The waveguides used are of the cleaved mesa variety and consequently have a window for this purpose. Two different sources were used for the pump illumination; the first from a separate tunable mode locked laser and the second simply split off from the unattenuated probe supply. The advantage to be gained from the former is the ability to pump at any wavelength whilst scanning the probe to compile a spectrum in the usual manner. The power used to illuminate the sample was approximately 30mW delivered in a 5ps pulse on a 13ns repetition rate. This failed to have any effect on the absorption in the sample (MV292). This is thought to be due to both the lifetime of the *e-h* plasma being a fraction of the mode-locked period, and the power density (@30Wcm^{-2}) being disappointingly low because of coupling losses involved in delivering the pump power via an optical fibre.

The second experimental arrangement used the same CW tunable dye laser as the probe and pump supply with the limitation that transmission spectra cannot be obtained, as a fixed pump wavelength is required. Power split from the unattenuated laser output was coupled onto the sample surface via a microscope objective lens. An incident power of 10mW corresponds to a power density of approximately 30Wcm^{-2}. Large attenuation of the probe supply was used to restrict power levels to ≈ 200nW and the beam was optically chopped to allow lock-in amplifiers to distinguish between pump and probe. The change in the transmitted power was measured as a function of the incident wavelength and pump power for zero applied bias. The sample used was MV292 and the optimum wavelength was found to be 830nm giving ~~and~~ the normalised transmission change (ΔT/T) vs pump power plotted in figure 5.6.4.

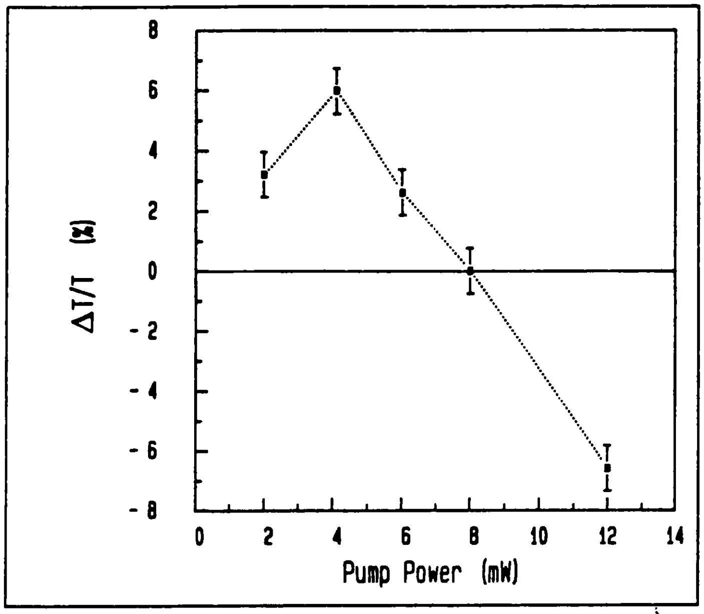

Figure 5.6.4 *Transmission Change as a function of the pump power. 10mW pump power correspond to an approximate power density of 30Wcm^{-2}*

The pump power density used is low compared to that of many authors [Lee, H.C et al]. However, the changes in saturation measured are also small. The further saturation is significant in terms of the improved excitonic quenching that it represents. The initial increase in transmission of up to 6% can be attributed to the further saturation of the excitonic feature, and indicates that greater population densities can be achieved in the quantum well subband. The dramatic fall in the transmission which follows as pump power is increased is thought to be due to self biasing of the device. An external resistance, with the photocurrent passing through it, will develop a voltage across itself and the modulator, giving rise to the normal bias dependent absorption characteristics. For alignment purposes, a curve tracer was used to measure photocurrent generated by the pump beam so that the incident power could be maximised.It was observed that a bias of up to 1 volt appeared on the curve tracer due to its internal resistance, hence during measurements the device was operated in short circuit. This enabled an increase in the saturation but a similar turn over in the transmitted intensity was seen in both short and open circuit cases. Photocurrent levels were typically of the order of 20μA which would suggest a series resistance of approximately 50kΩ if 1 Volt was to be developed across the device. The DC resistance of the device in forward bias was measured and found to be very high, probably due to the quality of the contacts and the epoxies used for bonding. However, a value of only 500Ω was found. The possibility of detector saturation was also entertained but stay pump power arriving at the detector was only of the order of 20μW, well below the saturation level.

To conclude, the features on the bandedge of the QW-FEM absorption spectra have been identified as residual excitonic absorption by the use of waveguide polarisation techniques and a lower limit to the degree of saturation proposed. The present samples have been shown to be capable of further diminishing this feature in two separate experiments. Low temperature photocurrent data shows a complete suppression of the residual heavy hole feature which probably indicates total quenching of the exciton, notwithstanding the selective quantum efficiency effects described. Optical saturation, exploiting nonlinear behaviour, has shown that further quenching is apparent at room temperature. This data collectively implies that greater excitonic saturation, giving a greater optical modulation, is possible if the carrier population can be increased.

5.7 Optimisation of Device Performance

Optimisation Scheme

An optimisation of the QW-FEM can be envisaged through the re-design of the optical waveguide. With the use of the *p-n* junction being favoured, rather than the Schottky barrier, the assymmetric waveguide design becomes redundant and the quantum well can be buried deeper into the epitaxial structure. From the discussion of the waveguide design in section 3.3 the parameter suitable for optimisation is the overlap of the optical field with the quantum well, Γ_{well}. Calculations of this parameter for a symmetric waveguide, performed using the model described in section 3.3, are illustrated in figure 5.7.1. The waveguide core considered in this data has the usual x=20% mole fraction $Al_xGa_{1-x}As$ composition and each curve on the graph indicates a different core width. The aluminium composition in the cladding region is swept and the plots indicate that Γ_{well} can easily reach 2.5% by the use of narrow core regions. The data is for a 50Å quantum well and the overlap for other well widths is easily derived as the relationship is approximately linear. Two factors affect the true availability and usefulness of the values indicated. Firstly, the use of high aluminium mole fractions is undesirable due to the stability of the material and the levels of unintentional doping found with MOCVD growth (see Section 3.2). Secondly, the use of very narrow cores is undesirable due to the consequential introduction of high coupling losses and the decrease in saturation intensity. The latter of these two problems is of greatest concern here.

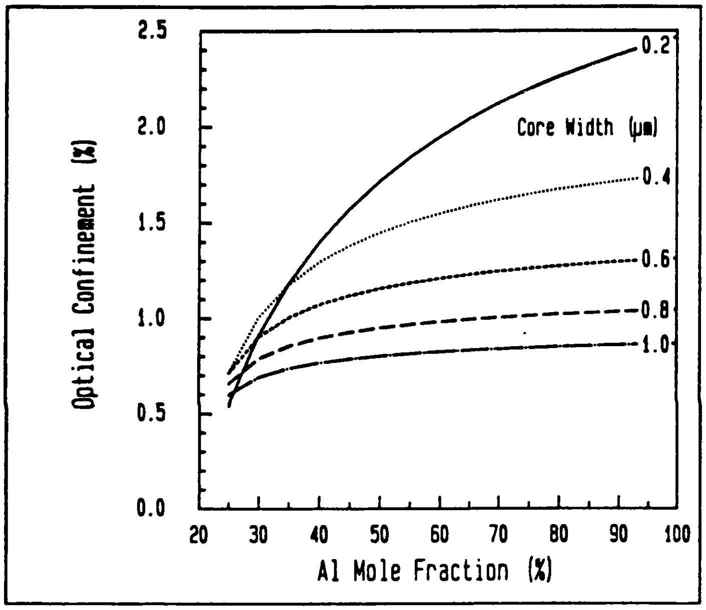

Figure 5.7.1 *The confinement waveguide optical field in a 50Å quantum well*

Narrow core widths typically increase coupling losses due to the diffraction limited beam waist of incident light from an objective lens [Hecht and Zajac]. At 850nm the best value that can be attained is approximately 1µm and in reality this is likely to be increased to 1.3µm with a standard laboratory lens [Ealing]. The confinement curves representing cores of 0.2 and 0.4µm are thus dismissed for this work, with the possible exception of use within a Photonic Integrated Circuit. In that case, light rarely, or indeed may never, need to leave the waveguide if the multifunctionality of the structure is exploited. This is covered in detail in chapter 7.

The second point regarding narrow core widths is the reduction in saturation threshold due to the increased intensity within the waveguide (or, specifically, within the quantum well). Saturation of the modulation mechanism was discussed in section 5.6 and since the relationship is proportional to Γ_{well} we can easily deduce new power thresholds. With these considerations taken into account, the compromised use of a 0.6µm core width and $Al_{0.45}GaAs$ nevertheless retains a respectable Γ_{well} of 1.1% ,which is nearly a ten fold increase over that of the previous design.

Extrapolated Performance Figures

Having arrived at this value of 1.1% for Γ_{well} we can study the experimental absorption characteristics of the QW-FEM and that of published data (Sakaki et al), and thus calculate the performance for the optimised device. Absorption data is extracted from the waveguide transmission measurements (figure 5.5.1b), the normalised photocurrent spectra (figure 5.4.1a) and the published excitonic quenching data of Sakaki et al. The performance data is presented as a graph of waveguide contrast ratio and insertion loss as a function of the device length (figure 5.7.2). The absorption in a waveguide is simply given by

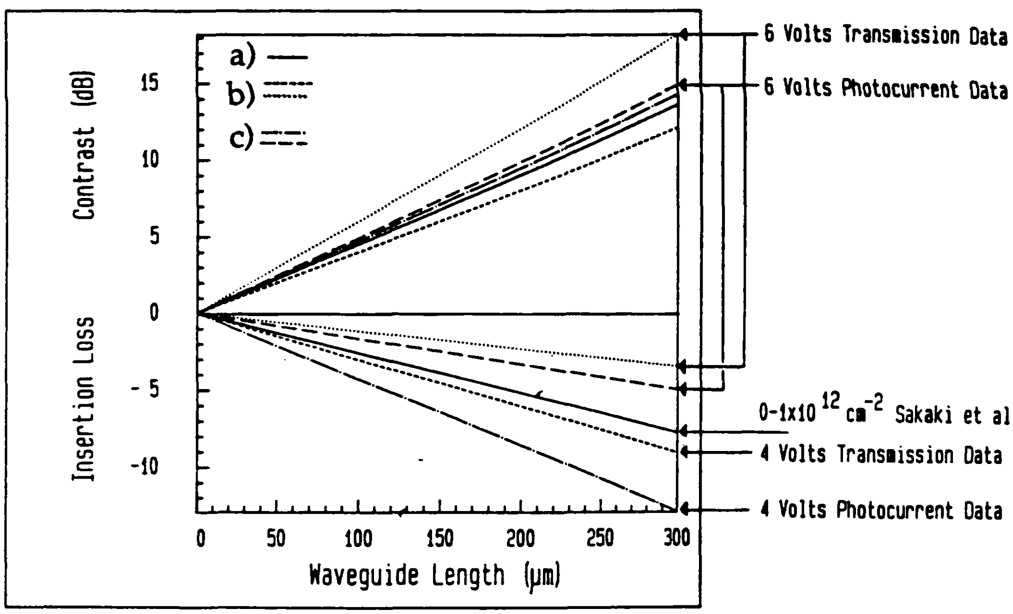

Figure 5.7.2 *Contrast ratios and insertion loss plotted as a function of device length. Curves represent: a) data of Sakaki et al (figure2.2.1); b) sample MV292 @ 4V and 6V bias c) absorption calculated from photocurrent data of MV292 @ 4V and 6V bias*

function with an exponential dependence on absorption change (section 3.4), and consequently a plot in decibels is a series of straight lines as given by the equation:

$$\text{Contrast (dB)} = \text{Log}_{10}\{\exp(\Gamma\Delta\alpha l)\} = 4.34\Gamma\Delta\alpha l$$

A similar expression is used for the derivation of the insertion loss which, for the purposes of this comparison, excludes coupling and reflection losses. Clearly, the best modulation comes from the experimental transmission data measured at 6 volts for MV292. A 10dB contrast requires a 165μm device length and has an associated 1.9dB insertion loss. The data calculated from photocurrent spectra is in reasonable agreement, indicating that the 10dB contrast point requires a 200μm interaction length and gives a 3.3dB insertion loss. We can conclude that high modulation depths are available with the *p-n* junction structures and that the insertion losses derived from experimental data in this manner are currently at acceptable levels when a 10dB modulation is considered. The optimisation proposed here simply makes the most of the available experimental data, and does not account for the fact that the insertion losses of the QW-FEM can be improved upon by increasing the zero field quenching as described in section 5.6.

5.8 Conclusions

Evidence has been found for the quenching and recovery of excitonic absorption in structures designed as QW-FEMs. Measurements indicate that the efficient sweeping of carriers from the quantum well subband is most readily achieved by *p-n* junction control of the applied electric field due to the limitations introduced by the optical waveguide. A study of the dependence of QW-FEM performance upon the well width shows that a narrow quantum well (50Å) provides greatest excitonic oscillator strength recovery under applied field conditions.

A comparison between the experimental IV and CV measurements and the theoretical predictions of an electric field profile model aids interpretation of performance of device layer structures. This leads to an understanding of the field conditions within the device and enables the resultant Stark effect, and its consequences for excitonic recovery, to be reconciled. The agreement between the theory and experiment underlines the usefulness of this simple approach to the device design. In measuring both the electrical and optical characteristics of the devices, a nonuniformity was found across the surface of the semiconductor wafers. Once discovered, an analysis of the trends led to successful identification of the high performance areas of the wafers and the minimisation of the degrading effects on device operation.

Experimental transformation of the photocurrent spectra to give absorption values enables the absorption change spectra to be derived, and from these the related refractive index change can be determined. The symmetrical shape of the absorption-change and refractive-index-change spectra leads to a very low chirp parameter which is highly desirable for modulation in long haul optical communications systems.

An experimental analysis of the performance of the modulation mechanism highlights, by several means, that full quenching of the excitonic resonances is not being achieved. However, the same work shows that further quenching is possible if higher electron densities can be provided. Alternative designs of the QW-FEM structure were used in an attempt to optimise the zero bias quantum well population but no further improvement in quenching was gained.

Waveguide transmission measurements succeed in reproducing the excitonic quenching and recovery exhibited in the photocurrent spectra of transverse devices, and also confirm the values of absorption coefficient assigned by reconciling photocurrent and incident power levels. The waveguide measurements also, unfortunately, act to highlight the difficulties with sample nonuniformity found by electrical and photocurrent wafer mapping. Long waveguides cannot be used as a consequence of the inhomogeneities along their length and hence full modulator performance cannot be measured experimentally. This, however, is not fundamental to the design of the device nor to the epitaxial growth process and consequently the predicted performance is experimentally achievable.

A scheme of modulator optimisation, using the experimental waveguide data and a proposed reconfiguration of the waveguide, shows that large modulation depths are available in the QW-FEM with low insertion loss penalties. A 10dB modulation depth with a 1.9dB insertion loss is predicted. Further improvements to optical modulation are anticipated by increasing the carrier density in the quantum well, hence reducing the residual excitonic absorption and improving the insertion loss.

Chapter 6

Modelling of the Performance of Excitonic Quenching Modulators

6.1 Introduction

The work described in this chapter sets out to model the optical modulation performance of the QW-FEM by considering the simple case of two limiting absorption states of the device. A zero field exciton quenched condition and a biased recovered exciton state are used and their corresponding absorption spectra calculated. The derived absorption changes are used, in conjunction with a model of the optical waveguide, to predict the optimum device performance, and comparisons with experimental data are made.

The selective doping of quantum well material to give an electron or hole population in a quantum well subband is an interesting theoretical problem and there have been several publications regarding the resultant effects. Bastard [1986] has studied the electron wavefunctions in a modulation doped quantum well using a variational approach, taking into account the band bending effects of an electron population and determining the energy levels as a function of the well width. Similar calculations of the electronic states in a quantum well have been performed by Inoue et al [1985] using a self consistent technique, and the results have been successfully applied to the voltage dependence of conduction found in a selectively doped heterostructure FET.

The binding energy and oscillator strength dependence on the quantum well population has been studied by Kleinman. He takes into account a single carrier type (electron *or* hole) population and shows that electron densities of approximately $2\times10^{11}cm^{-2}$ are sufficient to reduce the excitonic oscillator strength in a 50Å well to $1/10^{th}$ of its zero population value. The data extracted from the work by Kleinman is illustrated in section 6.3, figure 6.3.1. Perhaps the most comprehensive calculation is that of Sanders and Chang which determines the electronic levels, the binding energies and oscillator strengths for the excitons, and then moves on to derive a full absorption spectra. The absorption spectra are then compared with low temperature absorption and luminescence data, and experimental agreement is found.

Recent work by Chemla et al [1988] is more closely related to the QW-FEM and is based on a study of the absorption change seen under the gate of a SDHFET which was originally performed in 1987 [Chemla et al 1987]. This work follows the route of self consistently solving the single particle states of the quantum well with a population of electrons distorting the bands. Bandgap renormalisation effects are then taken into account and finally a term related to the occupation of the subbands is added. The appearance of excitonic effects in the spectra is ignored. This model is applied to low temperature (10K) experimental data by fitting the shape of the bandedge to transmission *change* ($\Delta T/T$) data. The fitting parameters used are the Fermi level and the effective temperature of the electrons, which is determined to be 50K. Heating of the carriers above this temperature is observed as the population is increased due to the current flow observed in the enhancement mode of operation (section 3.3).

None of these models specifically set out to describe the change in absorption which may be anticipated at the bandedge in a device operating using the excitonic quenching mechanism. The full solution of this problem is of considerable complexity. However, to quantify device operating limits a considerably simpler approach can be taken. The simplest goal of such a model is the determination of a contrast value and an insertion loss, due to residual absorption at the modulation wavelength (section 5.7). The former can be obtained by use of a quantum confined Stark shift model of a quantum well while the latter can be achieved through calculation of the subband absorption in the complete absence of the excitonic features. Considerable work has already been reported which follows these two distinct approaches. The QCSS modelling was mentioned in section 1.2 and the subband edge modelling has been used ~~in~~ predominantly in determining gain spectra of quantum well lasers diodes, rather than for modelling of absorption. The subband calculations performed here are drawn from laser models but also resemble the work of Chemla et al [1988] which was briefly described above.

6.2 Description of the Model

Basic Assumptions Used in the Model

The two most basic assumptions used in this model of device behaviour are:

1. *The zero bias state represents the flat band condition (zero field across the quantum well) and corresponds to the maximum carrier density in the quantum well.*

2. *The high field state implies zero carrier density in the quantum well and the field value is determined by the manner described and confirmed in chapters 4 & 5*

This simplifies the modelling, enabling well established techniques to be used for determining the absorption spectra. The zero field high population state has many similarities to laser gain calculations through the equations for transition probabilities, while the high field zero population state corresponds to quantum confined Stark shift (QCSS) of the subband and excitonic energies. The former is the bulk of the work described in this chapter whilst the latter comes directly from a model developed by Peter Stevens.

Following the calculation of absorption spectra which correspond to the two states of the QW-FEM, the modelling is continued by firstly deriving the absorption change $\Delta\alpha$. Secondly, the optical waveguide model, described in chapter 3, is extended to give a comprehensive indication of the achievable optical overlap with the quantum well. Finally, for a given value of this overlap parameter, a range of modulation depths is defined and the corresponding insertion losses are evaluated.

The Quenched State Model

Expressions for the carrier dependent subband absorption in a quantum well can be derived from the starting point of the standard equation for the transition probability between two states [Casey and Panish]. This has been performed by Stevens and Mukai and the resulting expression is used in this work. The absorption changes are due to the occupation of states in the quantum well and hence the electron quasi-Fermi level is the most important parameter. This must be calculated as a summation of the contributions from each subband state [Asada et al 1984]. The subband energy levels are calculated in the envelope function approximation [Bastard and Brum] and account for the differing effective masses in the well and barrier regions through use of an expression for the wavefunction continuity at the interface [Blood et al]. Bandgap renormalisation, based upon the observed Many Body calculations of Kleinman and Miller, is included in the equation for the absorption. At this stage, a step-like (section 1.2) absorption spectra is obtained. The broadening mechanisms must be accounted for, and again the work draws from that of quantum well laser calculations. Carrier-carrier scattering and well width fluctuations are the dominant mechanism and a expression for these effects is convolved with the absorption spectra. Both bandgap renormalisation and bandedge broadening are vital to the understanding of the QW-FEM insertion loss.

Subband Energy Levels

Evaluation of the subband energy levels involves solving the Schrödinger equation in the envelope function approximation. This gives subband energies levels equal to those in the one dimensional finite quantum well, which is formed by the bandedge discontinuities [Bastard and Brum]. The assumption of the flat band condition in the quantum well enables this simplification, without which a self consistent solution of the Schrödinger and Poisson equations would have to be employed [Inoue et al 1985]. This assumption is reasonable for the populated quantum well and especially in the case of the twin spike structures (section 3.3,5.3) [Livescu et al].

The differing effective masses for the electrons in the well (m_w^*) and barrier (m_b^*) are taken into account using the derivative expression:

$$\frac{1}{m_w^*}\cdot\frac{dF_w}{dz} = \frac{1}{m_b^*}\cdot\frac{dF_b}{dz}$$

which specifies the condition for the continuity of the envelope function, F, across the well/barrier interface [Blood et al]. The discrete energy level E_n for a well width L_w and barrier height ΔE are then given by the expression:

$$\left\{\frac{m_w^*}{m_b^*}\cdot\frac{\Delta E - E_n}{E_n}\right\}^{1/2} = \begin{matrix}\tan\\ -\cot\end{matrix}\left\{\left[\frac{m_w^* E_n}{2}\right]^{1/2}\frac{2\pi L_z}{h^2}\right\}\begin{matrix}\text{n odd}\\ \text{n even}\end{matrix} \qquad (1)$$

where h is Planck's constant and m^* is the effective mass for the confined electron or hole. The bandedge discontinuity ΔE is determined from the band offset ratio and the respective bandgaps for the well and barrier layers. These parameters are given in table 6.2.1 along with the effective masses and their associated aluminium mole fraction behaviour. The data used in chapter 5, figure 5.2.1, illustrating the subband gap energies for the well width range 40-150Å, is extracted from these calculations at this point. Using the simple expression:

$$E_{cv}^n = E_g + E_{el}^n + E_{hh}^n$$

the values of the inter-subband transition energies, E_{cv}^n, can be determined, where E_{el} is the conduction subband energy level series and E_{hh} is a similar series for the valence subband. E_g is the well material bandgap. An identical expression exists for the light hole energy levels. For the 50Å quantum well with 20% aluminium mole fraction in the barriers only an N=1 transition for the electron exists. The N=2 transition appears at a well width of ≈65Å. These calculations are performed using an IBM PC in the Pascal language.

Parameter	Value	Reference
$Al_xGa_{1-x}As$ Bandgap		
E_g	1.4247 + 1.247x	Casey and Panish
Band offset ratio	65:35	Duggan et al
Effective Mass		
m_e^*	0.0667 + 0.0835x	Miller,R.C et al
m_{lh}^*	0.094 + 0.066x	Miller,R.C et al
m_{hh}^*	0.34 + 0.412x	Miller,R.C et al

Table 6.2.1 *Values of bandgap and effective mass parameters for the AlGaAs material system and their sources. The mole fraction of aluminium in the barrier layers is labelled x.*

Subband Fermi Level

Having obtained values for the subband energies and transitions, the Fermi level in the quantum well is required in order to calculate the distribution of the states available for absorption. In the standard configuration of the computer program a range of sheet electron densities is used and the quasi-Fermi level in the conduction subbands is calculated. The values of sheet carrier density are N_{2D} = 1, 2, 5, 10, 20, 50, 100 $\times 10^{10}cm^{-2}$

The equilibrium quasi-Fermi level in the conduction subbands is related to the sheet carrier density, N_{2D}, via the expression [Zielinski et al 1987]:

$$N_{2D} \equiv \frac{4\pi m_e^* kT}{h^2 L_w} \sum_n \ln\left[1+\exp\left(\frac{E_{fc}-E_{el}^n}{kT}\right)\right] \qquad (2)$$

which is a summation of the contributions to the Fermi level from each band.

The constant k is Boltzmann's constant and E_f is the conduction band Fermi level. A numerical approach is used to solve the equation. Two initial estimates for the Fermi level are chosen and the contributions from each subband evaluated and summed to give two values of the electron density. A better Fermi level approximation can then be derived and the sequence repeated to home in on the correct value. The figure below (figure 6.2.1) shows a continuous plot of the Fermi level dependence on carrier density with the contributions from successive subbands indicated.

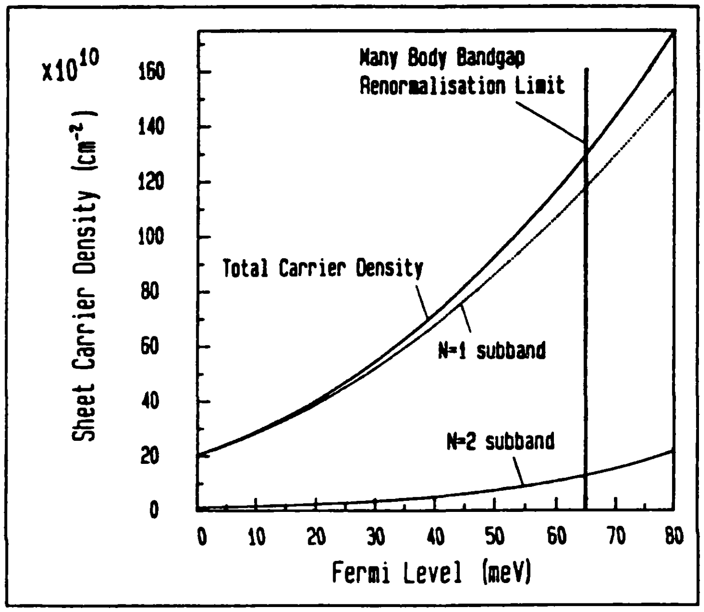

Figure 6.2.1 *Quasi-Fermi level in the conduction band as a function of electron density for a 100Å quantum well. The contributions from each subband are indicated. The N=1 and N=2 subband energies are 27.7 and 106meV respectively. The limit to the accuracy of the many body renormalisation is indicated as a 10% occupancy of the higher subband.*

Bandgap Renormalisation

A product of the filling of the subband states is to cause a change in the effective bandgap of the quantum well. The mechanism which predominates is a many body renormalisation (MBR) causing bandgap narrowing. The rigid shift of the subbands which is obtained was described in section 2.2 and the importance of this effect for the insertion loss of the QW-FEM was highlighted. To recap, the renormalised and broadened subband edge in the exciton quenched condition is expected to shift to longer wavelength, and hence produce an absorption contribution at the wavelength of the recovered exciton. This will constitute the limit to the absorption change between the two states of the device. The effect is well documented and the dependence on the carrier density has been calculated and experimentally confirmed [Kleinman and Miller] and is typical of other published work [Tomita and Suzuki]. The numerical expression:

$$-\Delta E_g = 2.2\text{x}10^{-3}\, N_{2D}^{3.2}$$

is used where energy and density are in units of meV and cm^{-2} respectively. A correction is applied for the use of different well widths and this is also extracted from the data of Kleinman and Miller.

The limit to the application of this model is the point at which a sizeable fraction of the quantum well carrier population begins to occupy higher order subbands. The Fermi level in successive subbands for a 100Å quantum well is shown in figure 6.2.1. Typically, the limit to the model is a density of approximately $2\text{x}10^{12}cm^{-2}$ [Kleinman and Miller] for this well width and constitutes the commencement of occupation of the N=2 subband. The bandgap renormalisation is related to the carrier density in the N=1 subband and a valid assumption would be to extend beyond these limits by considering only the N=1 occupation. The carrier densities used in this work are kept below this limit which has been reassessed to take into account narrower quantum wells. A 10% occupation of the continuum states above a 50Å quantum well can be estimated from the Fermi function to correspond to a sheet carrier density of $\approx 1.2\text{x}10^{12}$. The second bandgap renormalisation effect described in section 2.2, the Burstein-Moss shift, is implicit in the Fermi functions included in the absorption calculations which follow.

Ideal Unbroadened Absorption Spectrum

The subband absorption in quantum well material is calculated assuming both subband- and k-selection rules. The expression used is that of Stevens and Mukai and is a summation over allowed subband transitions for both light and heavy holes:

$$\alpha(E) = \sum_{lh,hh}\sum_{subbands} \frac{2q^2 m_r^2\,|M_{QW}|^2}{\varepsilon_0 m_0^2 c h n_{in} E L_w}\,[f(E_c)-f(E_v)]\; H(E-E_{cv}^{\;n}) \qquad (3)$$

In the above equation q is the electronic charge, m_r^* is the reduced mass, M_{QW} is the matrix element, ε_0 is the dielectric constant, m_0 is the electron mass, c is the speed of light, h is Planck's constant, n_{in} is the refractive index, E is the photon energy and L_w is the well width. The functions $f(E_c)$ and $f(E_v)$ are the conduction and valence band quasi-Fermi functions. The Heavyside step function, H, represents the cut-off in absorption when the photon energy, E, lies below that of the n^{th} subband transition energy.

Of these parameters, three need further explanation. The reduced mass is simply given by the expression:

$$m_r^* = m_{el}^* m_{hh}^* / m_{el}^* + m_{hh}^*$$

with a similar expression for the light hole. The electron Fermi-function is given by the usual expression:

$$f_c(E_c) \quad = \frac{1}{1+(\exp(E_c-E_f)/kT)}$$

and there is a similar equation for the hole Fermi function which is defined as the probability of finding an *electron*, and hence can be set to unity where only an electron population exists. The *k*-selection rules are implemented in the Fermi function through the relationship:

$$E_c-E_{el}^n = (E_{ph}-E_{cv}^n)\, m_r^* / m_{el}^*$$

where E_c is a proportion of the photon energy falling in the conduction band. The band gap renormalisation described above is introduced into this equation via the expression:

$$E_{cv}^n = E_g - \Delta E_g + E_{el}^n + E_{hh}^n$$

and also affects the absorption cut-off in the Heavyside function.

The absorption equation above (equation 3) is derived from the Einstein relations which hold true for any material [Casey and Panish]. The differences between various materials are contained in the transition probabilities which are evaluated from quantum mechanics and are given by the square of the transition matrix element. This is dependent upon photon energy, polarisation and whether the transition is for a light or heavy hole interaction. The matrix elements used in this work are:

$$|M_{QW}^{hh}|^2 = 1/4(3 + 3(E_{el}^{n})^2/E_c)\ |M_b|^2$$

$$|M_{QW}^{lh}|^2 = 1/4(5 - 3(E_{el}^{n})^2/E_c)\ |M_b|^2$$

for TE mode propagation [Asada et al 1984]. $|M_b|^2$ is the average matrix element for the Bloch states of the well material and is derived by Casey and Panish.

The summation of the absorption over all the light and heavy hole subbands in equation 3 is restricted to the N=1 levels in this work as it is the absorption edge at the bandgap which is of most interest. Figure 6.2.2 illustrates the unbroadened absorption spectra obtained at this stage with the sheet carrier swept over a series of values of N_{2D} and the hole Fermi function set to unity. The effect of the bandgap renormalisation is clearly visible at the bandedge. The carrier densities used in this data are typical of those cited in section 2.3 and range from $1x10^{10}cm^{-2}$ to $1x10^{12}cm^{-2}$ in the data presented here.

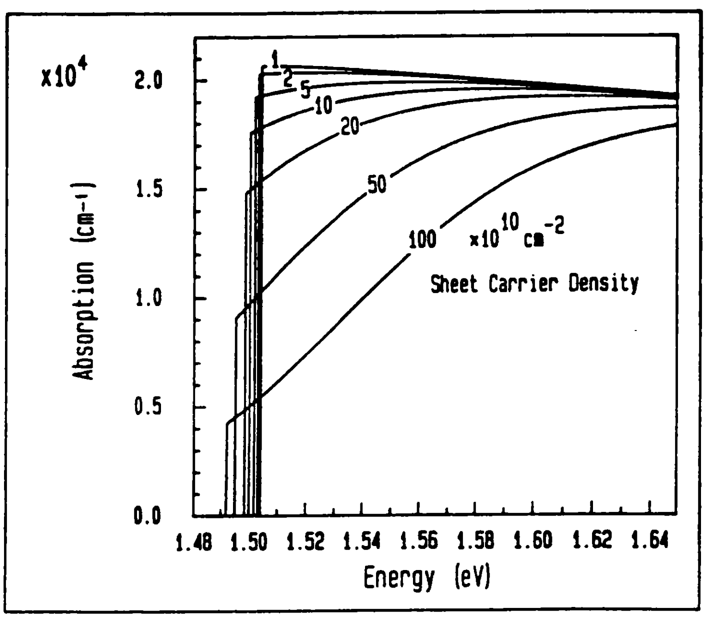

Figure 6.2.2 *Unbroadened absorption spectra as a function of carrier density for a 50Å quantum well. The barrier composition is $Al_{0.2}GaAs$.*

Broadening of the Absorption Spectrum

The abrupt and step-like bandedge predicted in the theory above, and illustrated for the N=1 subband (figure 6.2.2), is not seen in reality as it is broadened by several mechanisms. The broadening arises from the processes of well width fluctuations and scattering by phonon and carrier-carrier interactions.

The well width fluctuation broadening is proportional to the rate of change of the subband energies with well width. Fluctuations of the order of a monolayer become of greater significance at narrow well widths. The effect of well width fluctuation broadening is compounded by the increased change in energy with well width in the narrow well width regime. The full width half maximum of the broadening, Γ_{FWHM}, is related through an expression given by Juang et al,

$$\Gamma_{FWHM} = \partial E_{cv}{}^{1}(L_w)/\partial L_w \bullet 2.35\ \delta L_w$$

where the factor 2.35 is a correction for the RMS fluctuation of the well width. The differential energy/well width values are calculated from the data in figure 5.2.1. These values, and the final broadening figures, are listed in table 6.2.2 for 50, 75 and 100Å well widths. A well width fluctuation of one monolayer (2.83Å) is assumed for the data in the table.

The second broadening mechanism is that of carrier-carrier and phonon-carrier interactions which are intra-band relaxation effects [Kucharska and Robbins]. These relaxations are characterised by a time constant which relates directly to a linewidth through the uncertainty principle. Such effects are generally studied for the calculations of gain spectra in quantum well lasers, and the work of Asada et al [1988] describes calculations of the scattering probability of the electrons and holes, illustrating the carrier-carrier and phonon-carrier broadening as a function of the well width. Similar data is calculated by Kucharska and Robbins, although reduced levels of broadening are found. The latter work considers only scattering events in the conduction band which may be the more suitable case for this work in the light of the purely electron population. Due to this uncertainty involved in the use of this broadening mechanism, a variation of the broadening parameter is used and the results are discussed below. For this reason the data of Asada et al [1988] is tabulated (table 6.2.2) as it represents an upper limit to the broadening which might be encountered.

Well Width Å	$\partial E_{cv}^{1}(L_w)/\partial L_w$ meV/Å	Γ_{wwb} meV	Γ_{ccs} meV	Γ_{tot} meV
50	0.845	11.6	12	16.5
75	0.435	5.91	17	19.9
100	0.232	3.17	21	22.5

Table 6.2.2 *Broadening parameters as a function of the well width. In the well width fluctuation broadening* δL_w *is taken as one monolayer (2.83Å). The carrier-carrier scattering is taken from the data of Asada et al [1988].*

Both of these broadening mechanisms are homogeneous, but to include them the ideal absorption spectrum has been convoluted with a Gaussian profile. The choice of Gaussian and Lorentzian profiles for this purpose is discussed by Yamanishi and Lee and the conclusion reached is that a combination of the two is actually required. The Lorenztian profile is frequently noted to be inconsistent with experimental results as it has too long a tail for accurate fitting of theoretical and experimental profiles. This is due to the inherent weak convergence of the Lorentzian function, whereas the Gaussian function, on the other hand, has a stronger convergence. Since the interest here lies in the absorption tails of bandedges, the Gaussian profile is used for both the well width fluctuation and carrier-carrier/phonon broadening mechanisms. The two linewidths Γ_{wwb} and Γ_{ccs} are simply combined by taking the root of the sum of the squares, to give the width of the Gaussian function used for convolution.

There is an uncertainty in the broadening parameter which is convoluted with the spectra of figure 6.2.2. The well width fluctuations are generally considered to be of the order of one monolayer [Stevens et al, Miller,D.A.B et al 1985], and the intra-band scattering mechanisms, although applicable in this case, do not have firm values as described above. For this reason, to illustrate the range of the effect that broadening has on the absorption spectra, three values of the broadening factor have been used in the preliminary calculations. The resultant spectra for populations of $1x10^{10}cm^{-2}$ and $1x10^{12}cm^{-2}$ are illustrated in figure 6.2.3. These correspond to Γ_{wwb}, Γ_{ccs} plus Γ_{wwb}, and $2\Gamma_{ccs}$ plus Γ_{wwb}. The data is switched to a wavelength axis from an energy axis so that comparison with experimental data can be made.

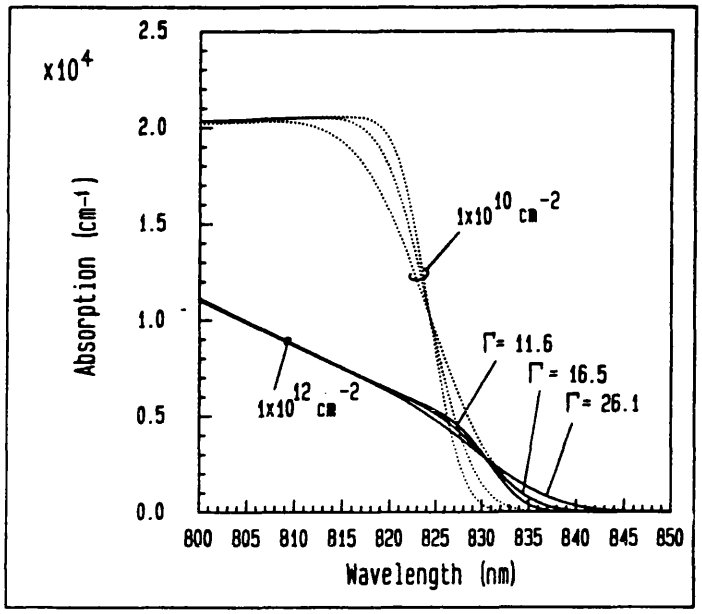

Figure 6.2.3 *Subband absorption spectra for high and low carrier densities as indicated. The sets of three curves correspond to three different broadening factors as described in the text.*

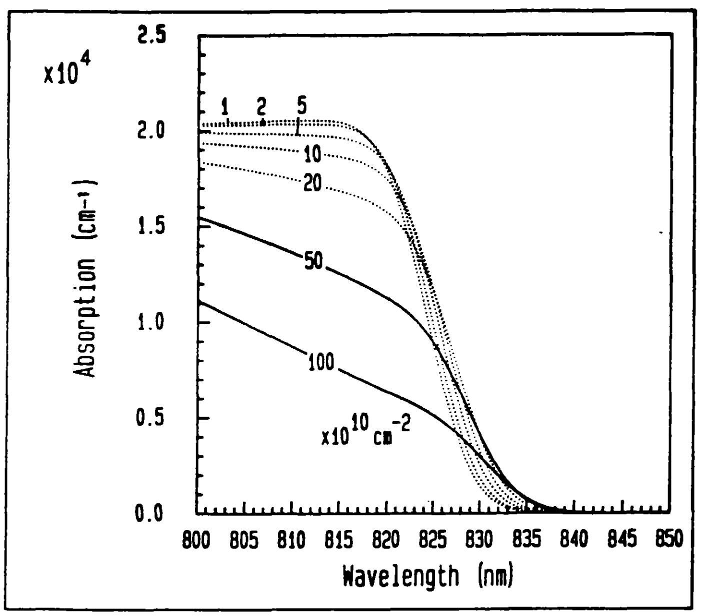

Figure 6.2.4 *Broadened absorption spectra for a 50Å quantum well, taking into account both well width fluctuations and carrier-carrier/phonon mechanisms. The broadening used is Γ=16.5 meV.*

The broadening parameter is seen to have a marked effect on the shape of the spectrum. However, the error that this can introduce in terms of modulator insertion loss is small, as the comparison with the recovered state spectra shows in the discussion below. The curves of figure 6.2.4. serve to illustrate the bandedge as a function of carrier density. The data is that of figure 6.2.2 convoluted with a Gaussian broadening of 16.5meV.

The Recovered State Model

The absorption spectra for the recovered state of the excitonic resonance is simply considered as a high field case for a undoped quantum well structure. This assumes zero carrier density in the quantum well at the electric field where maximum excitonic recovery is found. This enables a less rigorous treatment than that embarked upon by Chemla et al [1988] and a model of the QCSS in quantum well structures can simply be applied.

The calculated quantum confined Stark shift absorption spectra used in this thesis were provided by Peter Stevens. When modelling this effect, the solutions of the Schrödinger equation are no longer as simple as for the zero field case, and the energy levels are most readily determined by a tunnelling resonance calculation [Miller, D.A.B et al 1985]. The model uses the envelope

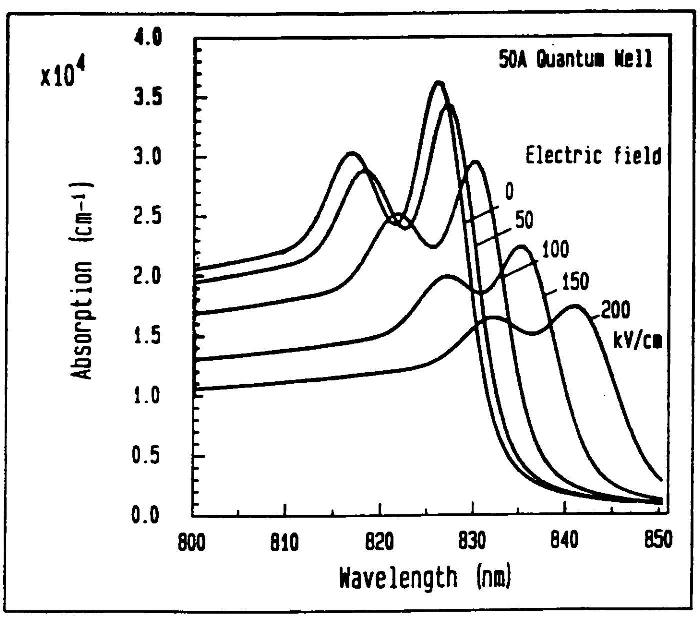

Figure 6.2.5 *Electric field dependent absorption using the quantum confined Stark shift. The data was calculated for a 50Å quantum well by Peter Stevens.*

function approximation and considers the tunnelling probability through a quantum well lying between two barriers of finite thickness and height as a function of incident electron energy. The probability reaches a maximum when this energy equals that of one of the confined levels. This model gives excellent agreement with experimental QCSS data [Stevens et al]. However, the narrow well widths and low barrier height of the QW-FEM approach the limits of its applicability and some experimental inconsistency exists. This is outlined in the next section and a comparison with experimental QCSS data is made.

The calculated electric field dependent absorption spectra in a 50Å GaAs quantum well with x=20% aluminium mole fraction in the $Al_xGa_{1-x}As$ cladding regions are illustrated in figure 6.2.5 for electric fields of 0, 50, 100 and 150 kV/cm.

6.3 Derived Spectra and Discussion

Modelling Parameters

The calculations of the subband absorption, described in the previous section, constitute a preliminary investigation of the quenched excitonic state of the QW-FEM. To investigate the performance limits of the QW-FEM the subband spectra must be compared with the absorption in the recovered exciton state. To do this, several further parameters must be investigated. These are the values of the electron population (N_{2D}) at which the exciton oscillator strength can be expected to collapse, the achievable population of the quantum well, the electric field across the quantum well in the recovered state, and the absolute value of the absorption.

A theoretical study of the effects of a single carrier type population in a quantum well has been performed by Kleinman. The work determines both the exciton oscillator strength and binding energy as a function of the sheet electron population. A summary of these results is shown in figure 6.3.1 and the data has been extrapolated to cover L_w=50Å. This illustrates that even at quite high populations some excitonic behaviour remains. Nevertheless, it is clear that the exciton oscillator strength is < $1/10^{th}$ of its zero population value for carrier densities of approximately $5x10^{11}cm^{-2}$ in a 50Å quantum well. The experimental exciton quenching data of Chemla et al 1988 and Sakaki et al verify the theoretical electron concentrations of Kleinman for quantum wells of $L_W \approx 100Å$. Here, the assumption made that a density of greater than $5x10^{11}cm^{-2}$ is needed for the contribution of excitonic absorption to be ignored.

The actual value of N_{2D} that can be achieved in a quantum well by selective doping puts an upper limit on the quenching of the exciton. Values of sheet

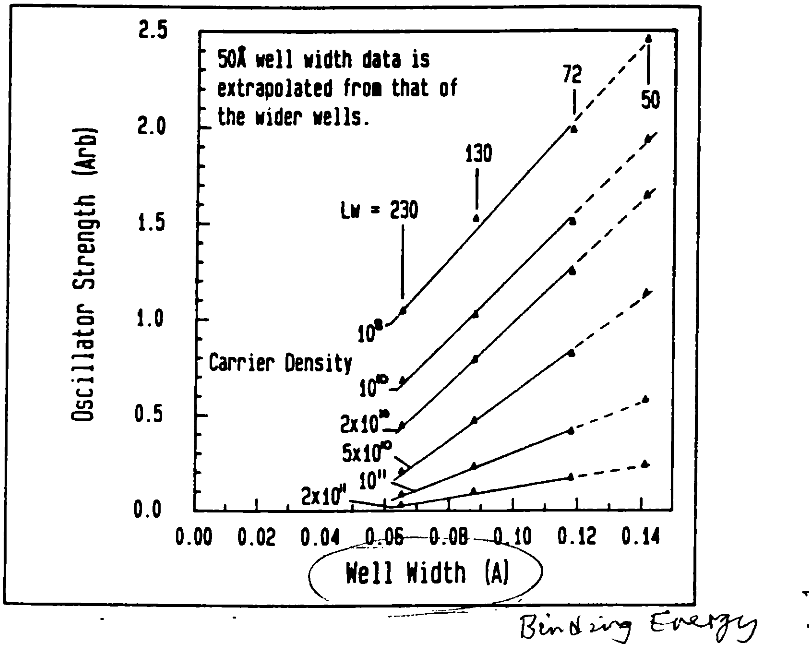

Figure 6.3.1 *Oscillator strength as a function of the sheet carrier density in a 50Å quantum well (after Kleinman).*

densities of up to $2.3x10^{12}cm^{-2}$ have been achieved in selectively doped quantum well by Powell et al and $2x10^{12}cm^{-2}$ by Inoue et al [1984] in SDHFETs. In the former case, the barrier aluminium mole fraction was 45% and the well width 90Å, whilst in the later these values are 30% and 300Å respectively. The QW-FEM has $Al_{0.2}GaAs$ barriers to assist in forming an optical waveguide and the well width is 50Å and as a consequence values as high as this cannot be expected. Room temperature Fermi level calculations similar to figure 6.2.1 suggest that at densities of $1x10^{12}cm^{-2}$ the population of the continuum states above the quantum well becomes significant (4%), and this must represent the limit to the carrier density that can be achieved in the subband. There is only one confined state in the 50Å quantum well (figure 5.2.1) and the continuum states are simply approximated by including an extra level at the energy of the bandedge discontinuity.

The electric field across the quantum well associated with full recovery of the exciton is important for use of the QCSS model. A field of 1×10^5V/m is used in the light of the experimental and modelled data detailed in sections 3.3 and 5.3 of this thesis.

The calculated value of the absorption in the quantum well subbands is typically lower than that observed experimentally. There is a correction to subband absorption commonly used in models of the spectra of undoped quantum wells. This is the Sommerfeld enhancement factor which is a correlation enhancement introduced by electron-hole Coulomb interaction of the exciton [Shinada and Sugano]. The functional form is a slowly increasing absorption which reaches a maximum at the subband edge. The absence of excitonic effects in the quenched state spectrum suggests that this factor should be ignored, which it is in this work. However, this then presents a difficulty in comparison of the *quenched* and *recovered* state models. The effect can be seen in figures 6.2.4 and 6.2.5. In the former case, the absorption in the subband is seen to have the reciprocal energy dependence of equation 6.2.3, whereas in the latter case the Sommerfeld factor is included and the absorption is seen to fall at an enhanced rate. The consequence of this is that a point in the spectrum must be chosen where agreement between the subband absorption levels of the two sets of spectra can be assigned. The most obvious point to perform this correction is immediately to higher energy of the light hole excitonic feature. In doing this a factor of 5/4 is introduced to scale the absorption calculations for a 50Å quantum well, and is used throughout this work.

Modelled Spectral Behaviour

With the parameters described above it is possible to make a comparison of the quenched and recovered states of the absorption spectra. Figure 6.3.2 illustrates such a comparison for a carrier density of 1×10^{12}cm^{-2} in the quenched state. Clearly, as anticipated, the renormalised subband edge is seen to be the limit to modulation at the wavelength of the recovered excitonic peak. The broadening used in this data is 16.5 meV (FWHM), although a comparison of this plot and those of figure 6.2.3 shows that only a small error in the value of $\Delta\alpha$ would result for the Γ_{tot} variations indicated. The value of $\Delta\alpha$ is 27000, whilst the residual value of α is 3500.

The QCSS data shows a discrepancy in the absorption level of the subband

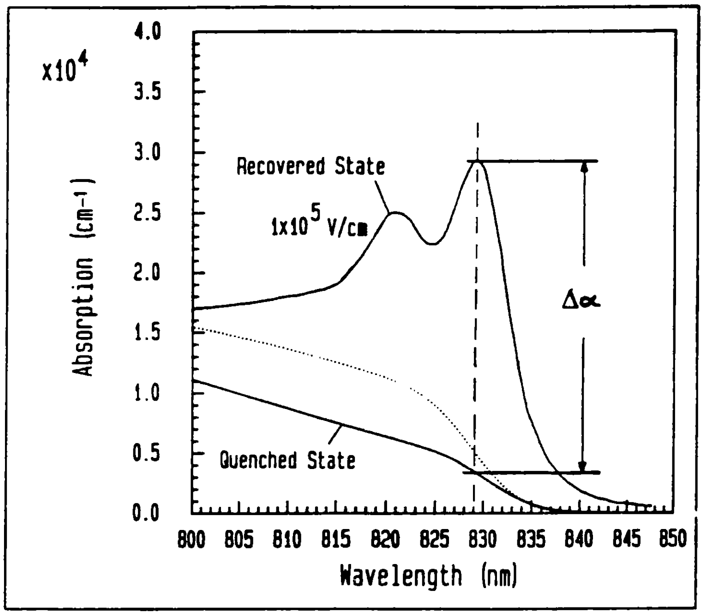

Figure 6.3.2 *The calculated broadened subband and QCSS absorption for the QW-FEM. The solid lines are for $N_{2D}=1x10^{12}Vcm^{-2}$ in the quenched state and a field of $1x10^5cm^{-1}$ in the biased state. The dotted curve corresponds to a density of $5x10^{11}cm^{-1}$. The well width is 50Å and the barriers are $Al_{0.2}GaAs$.*

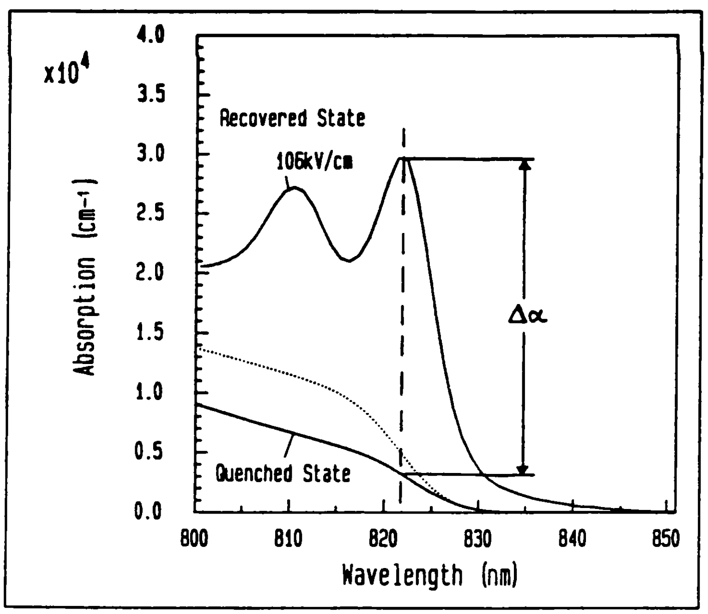

Figure 6.3.3 *The calculated broadened subband and experimental QCSS absorption. The solid lines are for $N_{2D}=1x10^{12}cm^{-2}$ in the quenched state and a field of $1x10^5Vcm^{-1}$ in the biased state. The dotted curve corresponds to a density of $5x10^{11}cm^{-1}$. The well width is 47Å and the barriers are $Al_{0.3}GaAs$.*

at high electric fields. It is seen to reduce more rapidly with applied field than expected from experimental considerations. This is primarily due to a difficulty in calculating the forbidden transitions in narrow, low barrier quantum wells. For this reason, a set of experimental QCSS data [Mark Whitehead] is introduced, and used to form a second description of the twin states of the QW-FEM. This latter set of data has a well width of 47Å, as determined by comparison with the tunnelling resonance calculation, however the barrier height is larger due to the aluminium mole fraction of the AlGaAs barriers which is increased from 20% to 30%. The second calculation of the subband absorption and the associated QCSS data is illustrated in figure 6.3.3. The stability of the subband absorption coefficient with bias is visible in a plot of the same data for a series of biases (figure 1.2.4). The comparable modelled spectra are those of figure 6.2.5 (note the change in barrier height).

The modelling parameters allow a comparison with the experimental data of sample MV292 (figure 5.1.2c). The most notable difference is the recovered excitonic peak, which is seen to be considerably better resolved in the QCSS experimental and modelled data. A comparison of the linewidths of the recovered exciton shows half-width half-maxima of 5.5nm and 8nm for the QCSS and QW-FEM data respectively. If this extra broadening were to be accounted for in the QCSS data, a better fit to experiment might be obtained. The origin of this extra broadening is not understood, and could be due to larger than expected well width fluctuations, or, more probably, an effect of donor atoms in the quantum well causing mini-fields in the plane of the epitaxial layers. Electric fields applied in this direction were shown by Miller D.A.B. et al [1985] to considerably broaden the excitonic peaks. A second difference between the modelled and experimental data of the QW-FEM is the subband edge itself. Obviously the saturation of absorption is stronger, but this saturation also extends to shorter wavelength than found experimentally. This compares well with the date of Chemla et al 1988, but is inconsistent with the QW-FEM experimental spectra. The discrepancy lies with the light hole peak, which, contrary to expectation [Kleinman], remains unquenched.

Waveguide Modulator Performance

The QW-FEM performance analysis of chapter 5 can be invoked at this point to give an insight into the optimum QW-FEM modulation performance possible. The contrast and insertion loss curves are calculated in the manner described in section 5.7 using the maximum value of $\Delta\alpha$ and the corresponding quenched state residual absorption at the same wavelength. The contrast and insertion loss are plotted as a function of device length in figure 6.3.4 and are calculated for a 0.6μm core width with a quantum well overlap of $\Gamma = 1.1\%$. Experimental data is also included for comparison, and is the 0-4 volts data of sample MV292 as this corresponds most closely to the modelled situation.

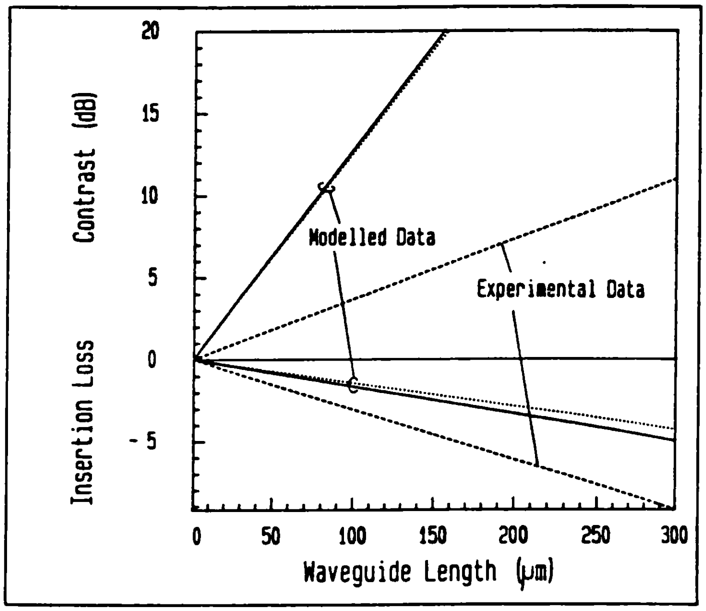

Figure 6.3.4 *Contrast ratio and insertion loss modelled for waveguides of the design in section 5.7. The data is for the two sets of modelled $\Delta\alpha$ changes and the 0-4 volts data of sample MV292 (figure 5.7.2)*

The figures for waveguide modulation and insertion loss illustrated above predict excellent performance of the QW-FEM. However, the results obtained are probably optimistic due to the approach used in the modelling, and serve mainly to give a useful upper limit on the performance which can be achieved. The high contrast ratio values are predominantly due to the use of QCSS data in the recovered state, as experimentally the excitonic features are not seen to make such a strong recovery. The carrier density assumed may also result in some residual excitonic absorption which has not been accounted for here, although the contribution is thought to be small (figure 6.3.1). With the contrast ratio aside, and using the QCSS data purely in its capacity of indicating the modulation wavelength, a value for the internal insertion loss/unit length can be determined, which is considered to be fundamental to the operation of the QW-FEM. Typically the minimum loss per unit length, calculated using the modelled subband data, is 1.5db/100µm and is due to the subband renormalisation and broadening effects.

6.4 Conclusions

This chapter has described a preliminary study of a simple technique to model the operation of the QW-FEM. The approach used concentrates on producing subband absorption spectra for the quenched state of the device. The calculations consider the influence of the Fermi level in the quantum well upon the absorption, taking into account bandgap renormalisation and broadening effects. The absorption data obtained is used in conjunction with modelled and experimental QCSS spectra to determine the absorption changes and contrast values for the QW-FEM, within the optimised design of section 5.7. By virtue of the two state modelling approach these values represent an upper boundary to the performance which can be achieved. The modelling also confirms that the absorption of the renormalised subband edge constitutes the limit to QW-FEM operation.

Chapter 7

Monolithic Integration and Optoelectronic Integrated Circuits: an Assessment of QW-FEM Potential

7.1 Introduction to Optoelectronic Integrated Circuits

The concept of an Opto-Electronic Integrated Circuit (OEIC) is the combination of both photonic devices and electronic circuitry on the same chip to perform a function which would be implemented through the interconnection of discrete components [Lee.C.P. et al]. This is thought to be the only approach by which one can fabricate, for example, extremely high bandwidth optical transmitters or very high sensitivity optical receivers. To date, these two particular functions are performed with greatest success through the discrete approach [Krakowski et al, Gimlet et al] in spite of many successful attempts at monolithic integration [Soda et al, Harder et al 1988]. Nevertheless, it is obvious that to perform more complex functions and eventually achieve the highest bandwidths, sophisticated monolithic approaches are the natural progression. The OEIC also introduces the possibility of new functions unlikely to be feasible through the combination of discrete devices. Such functions as optoelectronic gating [Wakao et al, Crawford et al] and wavelength demultiplexing [Larsson et al] can be produced with otherwise unachievable ease via monolithic integration. A study of future systems requirements is needed to understand the role of the OEIC and the performance that is required or, indeed, can be tolerated from such chips in view of the reductions in complexity and cost that they represent.

In this chapter, I will outline the requirements of OEICs by describing four classifications of optical systems which can benefit from their introduction. There are a limited number of approaches to OEIC design and they are driven by the fabrication and, predominantly, by the growth technologies of III-V compounds. I will briefly describe these different approaches, their merits, and current and future limitations. The design of the QW-FEM will then be described in this context and some preliminary data showing the versatility of the device will be discussed. Finally, I will describe the possible end products of using the QW-FEM structure in an monolithic circuit and the advantages brought about by moving to the use of the InP material system in preference to the current GaAs based materials.

7.2 The Requirement for OEICs

Introduction: Research Goals for OEICs

There are varied opinions on the initial role that OEICs will fulfill but the future goals of increased electronic complexity are recognised [Forrest, Kao, Hayashi]. The application to high speed long haul digital communications in the form of monolithic transmitters, receivers and repeaters is the aim of many laboratories but should not necessarily be the driving force for OEIC research. The future for the OEIC lies more in the implementation of the local area network (LAN) or the optical interconnect due to potential demand and the mass production of the well designed chip. The specification for the monolithic circuits for LANs at first glance do not differ enormously from those of long haul systems, but the emphasis shift towards a mass market and the performance criteria, expanded upon below, are increasingly being allowed to bias the course of research work.

Sub-division of OEIC types

To look more closely at the design requirements the OEIC "market" can be divided into four categories: 1) *Optical Interconnects* where two or more nodes are connected with either a high bandwidth optical path or a high density parallel optical network. Typically, this architecture is envisaged as a chip to chip, backplane, or mainframe to mainframe interconnect. 2) *Communications Networks* such as local area networks (LANs). Here, moderate bandwidths and moderate data rates are required for the communication between computer terminals or the optical implementation of local telephone networks. 3) *Long Haul Communications Systems* with optical transmission using low loss fibres and the minimum number of repeaters. These systems require very high bit rates and excellent receiver sensitivity to cut installation and operating costs. 4) *Optical Computing* represents a fundamentally different systems architecture exploiting the parallel connectivity of multiple light paths. This is often envisaged with free space light propagation and active elements perpendicular to the incident light beams. These elements would switch intensity, position or phase of the transmitted beam. Nevertheless, the requirements for this type of OEIC are remarkably similar to the earlier categories.

Comparison of System Demands

Transmitters and receivers, for converting electrical impulses to optical impulses and vice-versa, form the basis of these systems yet even such basic building blocks have enormously varied specifications. High modulation bandwidth is obviously of the utmost importance to both the long haul fibre system and the optical interconnect where data rate is the driving force. The design of monolithic FET driven lasers, for example [Suzaki et al], has the advantage of reduced circuit parasitics due to "monolithic wiring" rather than inductive bond wires and capacitive bond pads. This gives the potential for increasing the available bandwidth. The LAN has a more modest bandwidth requirement as the high bit rates, used in long haul systems to reduce running costs, are not necessarily needed. Optical computing architectures derive large bandwidth from their parallelism and consequently the bandwidth of each element need not be high in the first instance.

Packing density is a second important parameter subdividing OEIC design. The parallelism of optical computing architectures requires that sources or detectors form an array of particularly high density. This close packing of devices is echoed in the design of the optical interconnect where many parallel optical paths are required to exist. The packing density of components for LANs is of a lesser importance but must meet the requirements of the local exchange where data is to be routed, whereas the long haul communication system is characterised by very few devices at large distances apart.

Receiver sensitivity is a parameter which also serves to subdivide the system types. The short transmission distances of the optical interconnect and optical computing applications allows both to use low sensitivity receivers giving an increased choice in the designs of detector which can be used. The LAN has a longer transmission length and a moderate requirement whilst the the long haul system needs the most sensitive receivers possible. Typical long haul receivers use a PIN or avalanche detectors and a low noise FET amplifier for sensitivity and bandwidth [Gimlet et al].

Transmitters and receivers are the input and output of the OEIC but elaborate optoelectronic functions may also be a requirement. The handling of a bidirectional link [M.Wale et al 1986] in a LAN, for example, would require a complex OEIC. The functions of detection, modulation, optical switching and optical amplification would be combined using a waveguide geometry with associated control and driving electronics. Similar circuit complexity arises for optical interconnects [Crow]. The architecture of optical computing technologies are by nature complex high density arrays of modulators or surface emitting lasers and detectors. Addressing of the elements in these arrays as density increases is the most important task for the OEIC electronic components. One dimensional arrays would exist in optical interconnection architectures and, although simpler than the 2D case, the task is not trivial, especially since larger bandwidth is a requirement.

A further thought on complexity lies in the question, *Does the complexity of the OEIC lie with the optics or the electronics?* The question simplifies the decision of which route to follow in fabrication of an OEIC by making the maturity of the electronics or optics an important parameter. This has led much of the recent material systems development expanded upon in the discussion below. Typically, chip to chip interconnect would be developed using, for example, existing Si VLSI with optics added whereas laser drivers require development of transistors compatible with III-V′ optoelectronic materials.

The arguments described here are summarised in the table below (Table 7.2.1): the emphasis shift when comparing long haul communications with other systems is very noticeable. Current research is weighted towards long haul systems OEICs, which is not only the smallest end of the market, but is also clearly peculiar to the market as a whole. Complexity and density are gradually being approached [Wada 1989, Crow, Nakano et al] and will be the back-bone of future OEIC development.

System	Bandwidth	Density	Sensitivity	Complexity
Interconnect	•••	•••	•	•••
LAN	••	••	••	•••
Long Haul	•••	•	•••	•
Optical Computing	•	•••	•	••

Table 7.2.1 *System demands on OEIC design*

Comments on Performance

The success of OEIC chips hinges on the performance required from the individual components. *Independently optimised* devices represent the largest headache. Photonic and electronic devices are seen to be reaching excellent levels of performance, but the combination of the two produces trade-offs. Fabrication difficulty is increased when independently optimised devices are to be combined. Techniques such as selective area epitaxy and the growth of opposing types of semiconductor on one another have to be introduced to produce, for example, high bandwidth FETs or MQW modulators in combination with single frequency DFB lasers [Kasahara et al, Kawamura et al]. This often leads to an "artistic" and expensive solution which has a role, but it is questionable whether this should be the driving force of OEIC design. If ultimate bandwidth or single frequency laser operation is not required, then relatively simple structures requiring single stage epitaxy may suffice. Design of OEICs, rather than a combination of independently optimised devices, is an approach most suited to development of chips for LANs, as simple and more readily achievable techniques can be used.

Another question to be addressed is how far should integration be taken. The discrete hybrid packaging approach which OEICs are designed to supercede is labour intensive and its automation is difficult. Monolithic integration, even in a simple form, represents a step towards cheaper components. With many of the envisaged applications however, painstaking optical alignment of one or more fibres and bonding of the chip to input/output and supply lines is still required. Could two chips, perhaps OEICs in themselves, be optically or electronically coupled at this stage with a considerable saving in integration complexity? One example of this form of integration is a 600MHz bandwidth 4x4 optical switch [Wada 1988] assembled from four channel receive and transmit OEICs and a GaAs switch IC. The problem of the fibre coupling can been addressed by the use of *micro*-machining of semiconductor substrates [Reid et al] and self alignment of fibres [Wale et al 1989], but without this kind of technology the reduction of the "packaging bottleneck" and consequently the full advantage of the OEIC cannot be realised.

Conclusions

It should eventually prove less expensive and more compatible with mass production to combine electronic circuits with lasers, detectors and other photonic functions using monolithic integration rather than interconnect them by positioning and wiring in a hybrid fashion. The monolithic circuits produced in this way will be more compact enabling the requirement for high density systems to be realised. Ruggedness and reliability will also be improved. Moreover, the reduction in size will lead to reduced parasitics due to the shorter monolithic wiring and consequently this approach will fulfill the demand for higher frequency optoelectronics.

7.3 Engineering Approaches to OEIC Fabrication

Overview

The engineering problem associated with the OEIC is the conflict of requirements of the optical and electronic functions. Generally, the optical components are larger in area and greater in depth than the electronic devices to be formed around them. They also generally require highly doped regions of semiconductor above and below the optically active region, whereas the tendency with electronic devices is to use careful selective doping and semi-insulating substrates. Careful avoidance of cross-talk between devices is also necessary where, for example, the active region of a transistor absorbs light at the optical frequency. The discussion here will concern the integration approaches linked with the semiconductor aspects of OEIC engineering.

Monolithic Integration Techniques

The two basic approaches to monolithic integration can be classified as vertical and horizontal integration and generally these represent single and multiple epitaxial growth stages respectively.

The vertical approach essentially combines the electrical and photonic functions by epitaxial growth of one device on top of the other. The buried device can then be revealed by simply etching through the upper structure down to the necessary layer [Yust et al] (figure 7.3.1). The draw back of this approach is that it produces large amounts of surface relief which limits the feature size of the most common lithographic techniques. This compromises the once buried component which, unfortunately, is generally required to be the transistor due to the isolation afforded by an underlying semi-insulating substrate. An increase in feature size represents a decrease in bandwidth, reducing the advantage of this monolithic approach. However, many state of the art FETs now use gates written by an electron beam which is a

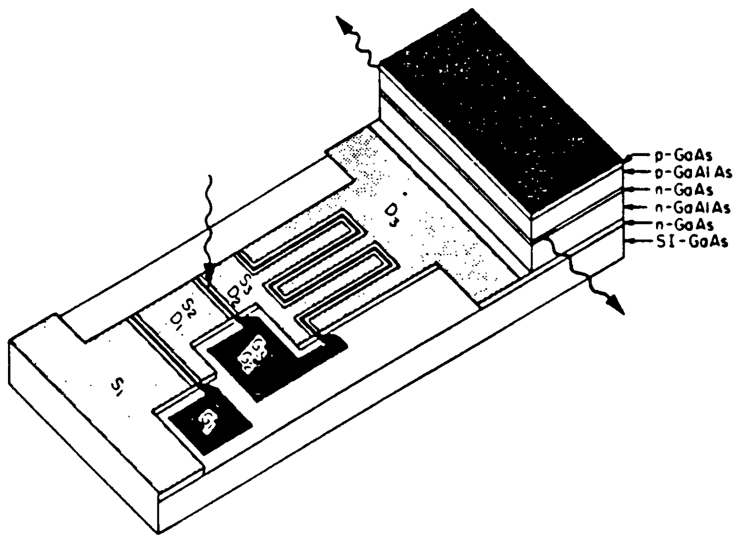

Figure 7.3.1 *Monolithically integrated repeater using the vertical integration approach (after Yust et al)*

lithographic process which does lend itself to overcoming the problems with non-planarity. The recent development of PINFET receiver [Spear et al] using single stage epitaxity and a recessed substrate successfully overcomes the planarity problem: a FET structure is buried under a PIN photodiode which is later removed by etching in the non-recessed regions leading to low-surface-relief-integration. A further drawback of vertical integration is the thickness of the structures which can rapidly become prohibitive for epitaxial growth techniques, especially that of MBE which has a low growth rate. Nevertheless, the simplicity of a single growth stage approach is an overwhelming advantage.

Horizontal integration on the other hand relies on the secondary growth of islands of semiconductor material which form the second function on the monolithic chip. Even though the majority of optical devices are several times deeper than most electronic devices, planarity is commonly achieved through the use of trenched substrates (in a manner not dissimilar to that described above). The epitaxial growth of a laser structure for example would lie in an etched groove neighbouring an FET driver circuit [Nakano et al] (figure7.3.2). This method has improved flexibility over single stage epitaxity in that more complex structures can be handled. The key to this work is the removal of unwanted semiconductor formed on top of the first epitaxial layers during the

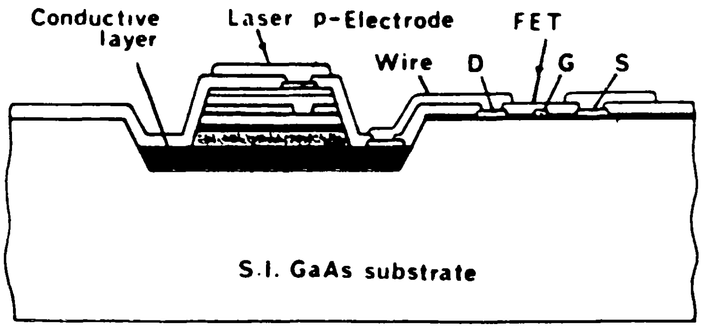

Figure 7.3.2 *Monolithic integrated laser driver and monitor using two stage epitaxy and trenched substrate (after Nakano et al)*

second growth stage. If compatible with the structure, this can be removed by etching after a lithographic step, but the technique has the limitation that the lithography is inaccurate and, as a consequence, selective area epitaxy is under development [Kamon et al]. "Selectivity" is often obtained using a glassy dielectric layer deposited over the primary device to inhibit nucleation during growth. Efficient removal of both this glassy layer, and any polycrystaline semiconductor deposits which form on it, is the critical step in this approach. A drawback of horizontal integration is that the electronic circuitry becomes separated from the photonic device due to the islands of each type of structure: this may be undesirable when performance is considered.

Contrary to the "conflict of requirements" of the two functions of the OEIC mentioned earlier in this section, it is sometimes possible to conceive of a structure which has an intrinsic duality. This fits into the category of vertical integration as described above but has the important difference that one device is combined with the other through common epitaxial layers rather than the two being separately optimised and physically distinct, vertically. This not only represents a reduction both of the complexity of the structure and the demands on the epitaxial growth, but also improved planarity can be expected. The performance of the devices is likely to be compromised, but the added simplicity and single stage epitaxy is the desirable feature. Katz et al have developed a monolithic heterojunction bipolar transistor and heterostructure laser by this route using a compatible structure and selective ion implantation during processing. More recently, Wada et al have investigated a planar implanted MQW structure which successfully provides Laser, Detector and FET functions. The QW-FEM falls into this category of device structure and this will be expanded upon in the next section.

Material Systems Constraints

There are two predominant lattice matched material systems currently considered for OEICs and these were developed for discrete optoelectronic devices. The materials have one very important factor in common, that of a direct bandgap, which gives the necessary optical properties for operation of lasers, detectors etc. These material systems exist by virtue of being lattice matched to readily producible substrates, typically GaAs and InP. The least complicated of these two systems is GaAs in combination with the lattice matched ternary alloy $Ga_{1-x}Al_xAs$. The mole fraction x, and consequently the bandgap, can be varied from 0 to 1 with continuous match to the GaAs lattice parameter. A more complicated, yet more versatile system, is that of InP/ $In_{1-y}Ga_yAs$/ $In_{1-z}Al_zAs$. Here, the lattice match of the ternary alloys to the binary, InP, is not "automatic" and is only achieved for one value of the mole faction (y=0.47, z=0.48). This is a major disadvantage compared to the GaAs/GaAlAs system and consequently two quarternary alloys, GaAlInAs and InGaAsP have been developed. These give an increased flexibility as the continuous bandgap and lattice match range exhibited by GaAs/AlGaAs is imitated. The epitaxial growth of quarternaries is however much more complex to achieve, but has the advantage that the OEIC designer gains considerably greater material and structural choice.

For the OEIC a choice must be made between these materials. There are three main parameters on which this should be based.

1. *Optical Wavelength* The development of the InP based materials for optoelectronic components fulfills the requirements of long haul fibre transmission systems. Optical fibres typically have their lowest loss and dispersion characteristics at a wavelength of 1.55μm. This "Fibre Window" can be exploited by the bandgaps, and hence emission frequencies, of the

quarternary alloys InGaAsP and GaAlInAs which are lattice matched to InP substrates. For any other optical system, probably with the *inclusion* of LANs, GaAs based material will suffice giving operation at a less attractive fibre window (850nm) but with the advantage of epitaxial simplicity.

2. *Optical Transparency* There is a two fold importance in this parameter. Firstly, transverse devices such as photodetectors or transmission modulators often require optical access to the active region through the substrate. Secondly, the integration of photonic and electronic devices may lead to cross-talk between the two functions due to optical absorption. The relationship of the bandgap of the alloys to that of the substrate is of prime importance here. Taking the most common operating wavelengths, InP is transparent at the desired 1.55μm whereas GaAs absorbs at the required 850nm. Lattice matched alloy layers grown on InP have narrower bandgaps whilst the converse is true for GaAs. A consequence for GaAs MQW modulators, for example, is that the substrate must be windowed for transmission [Wood et al 1984] whereas the InP does not present a problem [Guy et al]. In the case of GaAs FETs or HBTs integrated with detectors, the transistor itself is unfortunately capable of detecting stray light. However, a basic InP FET is not capable of absorbing light at 1.55μm and for this wavelength detectors must be fabricated with the narrower bandgap InGaAs ternary. These examples highlight simple problems, but more sophisticated devices which use much heteroepitaxy need careful engineering to avoid cross-talk in *both* GaAs and InP structures.

3. *Carrier Mobilities* The carrier mobilities of the III-V materials are greater than that of Silicon, hence the potential for higher speed devices exists. Recent advances in SDHFETs [Brown et al] have been brought about by exploiting the highest mobilities using materials such as InGaAs for the conduction channels. These appear to be at least a factor of two improvement over those of GaAs channels [Powell et al]. This advantage is also echoed in exploiting InP for HBTs and in the saturation characteristics of high speed detectors [Farley et al].

Lattice matched material systems provide a comprehensive range of alternatives for OEICs, but recently there has been much interest in the development of lattice mismatched growth. The lattice match of semiconductors is important for crystalinity but by the use of strained layers it is possible to grow mismatched semiconductors of usable quality on one another. Development of such processes is designed to enable combination of mature device technologies. GaAs grown on silicon substrates for the combination of optical devices with VLSI circuits [Fischer et al] should lead to the implementation of *inter-* or *intra-* chip interconnects. Silicon itself has limited optical properties due to an indirect bandgap, giving this unfortunate need for secondary optical material growth, but also perhaps has an advantage in the elimination of the possible photonic-electronic cross-talk problems discussed in #2 above. Silicon transistors have excellent performance, with recent reports of operation of 1/128 dividers at 12.5GHz [Chen,T.Z et al]. This, linked with complexity and maturity considerations, makes their use in specific OEICs applications very attractive. In a similar manner, InP strained growth on GaAs [Hodson et al] and vice versa [Suzuki et al] leads to lasers and FETs or detectors and FETs being integrated with use of well established device designs. These techniques present a rapid approach to the development of the more sophisticated OEICs.

Advanced Processing Techniques

At this point it is interesting to introduce new processing techniques specific to the fabrication of OEICs. Many important techniques already exist by virtue of the independent development of both discrete optoelectronic devices and III-V ICs. As pointed out previously, the most important processing tool, that of lithography, would benefit from flexibility to cope with non-planarity of semiconductor surfaces. This is being developed as a matter of course for GaAs MESFET design in the form of E-beam written gate electrodes. Similarly, the vital ion implantation process has been fine-tuned in the fabrication of III-V transistors of various types.

Processing techniques specific to OEICs relate more to the optical functions therein. Arguably, the most important of all is the development of a variety of laser facet internal to a chip. Discrete lasers are fabricated by cleaving the substrate to give good reflectors at *both* ends of the cavity. Monolithic external-modulator/ laser combinations, for example, must have facets internal to the chip structure. These can be achieved in three ways; the first, and probably least desirable, is the process of micro-cleaving [Nobuhara et al] which involves chemically under-cutting a region of semiconductor which is then physically cleaved to give a facet. The second process used involves Reactive Ion Etching (RIE) or Ion Beam Milling (IBM) to cut a vertical trench on the semiconductor. This is the most frequently used method, although it does suffer from reduced reflectivities and scattering losses, it has the advantage of electrical isolation of active and passive waveguide regions. The third technique uses a Distributed Bragg Reflector (DBR) as the "second facet" eliminating the *(optical)* need for a cleaved or etched facet. A stunning example of this work is the implementation of a Y-guided surface emitting laser with a total of 90 DBR gratings and gain regions [Carlson et al]. One of the more functionally complex photonic integrated circuits to date combines the techniques of DBRs and IBM etched facets in a triple laser source for wavelength division multiplexed communication systems [Koren et al 1989]. The chip consists of three lasers with DBR sections and RIE facets, a passive waveguide combiner, and an optical amplifier section. In the context of semiconductor growth, the fabrication of this device is not trivial and requires two stage epitaxy with an intermediate recessing step.

Further processing techniques specific to OEIC fabrication include disordering of semiconductor material to tailor the absorption at the bandgap. Two examples of this work are the fabrication of passive waveguides from the same epitaxial layer as a quantum well laser [Werner et al] and the construction of integrated quantum well low loss phase modulators [Ribot et al]. Both use the disordering to shift the quantum well levels to higher energy reducing insertion losses at the operating wavelength of the unmodified quantum well structure.

To move further away from the complexities of the growth technologies it is refreshing to see very simple extensions of existing III-V technology giving good OEIC performance. The two examples cited here answer, to some extent, the questions posed in the previous section: Is it possible to avoid the attempted combination of *independently optimised* devices; how far should monolithic integration be taken?

Complex GaAs MESFET circuits have had optical interfaces incorporated by the development of the simple Metal-Semiconductor-Metal (MSM) detector [Lee,W.S. et al]. This detector uses semi-insulating substrate material and interdigitated Schottky contact fingers and has the advantage of requiring little or no deviation from standard FET integrated circuit processing. The responsivity of the detector is roughly halved by virtue of the metallisations over the sample surface but is still a very usable 0.4A/W. The largest circuit published [Crow] has over 8000 elements and consists of four optical receivers with clock recovery and demultiplexer circuitry and has GHz performance.

This same MESFET-MSMs technology has also led to high speed (5.2GHz) low complexity detector chips [Harder et al 1988].

A very successful integration technique, neither strictly in the category of monolithic integration nor hybrid technology, is that of flip-chip bonding [Sussmann et al]. Combination of two device types, such as FETs and PIN detectors, involves the bonding together of two chips using "solder bumps". Typically, the detector is inverted and attached to the FET circuit. The most successful work to date has produced a twin PINFET detector for coherent communications with successful operation at 7GHz [Wada et al]. The PIN detectors in this case have the added advantage of a cleverly lensed substrate reducing the effort involved in fibre alignment. Flip-Chip structures reduce considerably the parasitics introduced by hybrid fabrication and at present represent performance between that of hybrid and OEIC approaches.

7.4 The QW-FEM for Optoelectronic Integration

Versatility of the QW-FEM Structure

The concept of a QW-FEM OEIC falls into the category of a vertically integrated structure using the approach of layer compatibility. The meat of the structure is the quantum well and to perform the task of optical modulation this is buried in the core of a heterostructure waveguide (see chapter 3 for full details). The mechanism which provides the optical modulation is also compatible with the control of a two dimensional electron gas used in heterostructure FETs. These selectively doped heterostructure FETs (SDHFET) have excellent transconductance figures which is a great advantage for receiver sensitivity, high modulation bandwidth and high current capability. As well as operation of the structure as both an FET and optical waveguide modulator, there are several other functions which the device can perform. The most obvious is that in the reverse biased state the waveguide modulator structure will act as a high efficiency detector. The bandwidth of this detector is limited by the capacitance in a similar manner to the modulator (section 3.1), although the possibility of using the two dimensional gas in a high speed lateral detector does exist [Chen,C.Y et al]. In forward bias the structure provides the possibility of both lasing and optical amplification. The merits of the modulator form the bulk of this thesis and it is the other compatible functions which are discussed here.

The most attractive of these features of the QW-FEM structure is the potential for FET operation. There have been many reports of the progress of the SDHFET in recent years in both GaAs and InP based material systems. The current state-of-the-art performance, with regard to bandwidth, is a ≈130GHz f_t microwave HEMT fabricated with AlInAs/InGaAs heterostructures and having a 0.1μm gate length [Mishra et al]. Similar performance has been

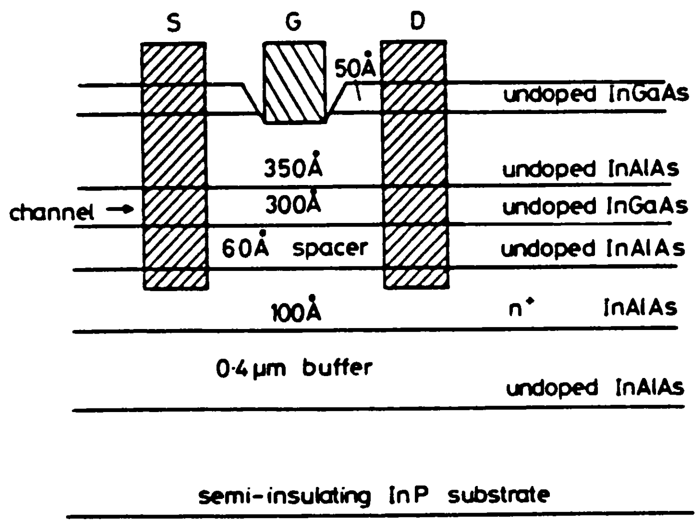

Figure 7.4.1 *Cross-section of a typical SDHFET (After Seo et al)*

obtained with a pseudomorphic $Al_{0.3}GaAs/In_{0.25}GaAs$ MODFET [Nguyen et al]. A typical SDHFET cross-section is illustrated in figure 7.4.1 [Seo et al]. More important is to realise the improvements and advantages over the conventional GaAs MEtal Semiconductor FET (MESFET). The trans-conductance is typically $100mSmm^{-1}$ for a MESFET and over $1000mSmm^{-1}$ for a SDHFET. These figures need clarifying somewhat as state of the art structures are being reported with very short gate lengths and need to be scaled accordingly. Implementation of similar gate lengths would leave perhaps a factor of three advantage in peak transconductance for the use of a two dimensional electron gas [Wang and Feng]. The transconductance in a selectively doped structure is also obtained at much lower current levels than in a conventional MESFET.

These FET transconductance figures are related to both the mobility and the carrier density in the conduction channel. The mobility figure is vital for gate transit times and hence bandwidth, whilst the channel carrier density determines the current handling capability. The sensitivity of PINFET receivers is also closely related to the same parameter. At high bit rates the sensitivity decreases with a 3/2 power dependence due to the FET channel noise [Wada 1988]. Sensitivity is regained by minimising the ratio of the square of the total (gate and detector) capacitance and the transconductance. The optimisation argument for the PINFET, with the use of the SDHFET, leads to the ~~the~~ PIN detector being the limiting component.

Fabrication Techniques and Multifunctionality Trade-offs

There are several points regarding the use of all of the functions proposed above. The over-riding advantage is obvious: a single epitaxial growth is used followed by a series of well established processing steps. The disadvantages are connected with the compromises brought about by increased "parasitics" that each device may have as a consequence of the forced non-optimum design. These trade-offs are outlined below and discussed in the context of possible scenarios for the OEIC function.

To outline the simplicity of the fabrication of the FET-modulator combination a cross-section of these two devices is illustrated in the figure below (figure 7.4.2). The modulator is shown as a strip loaded structure with the necessary

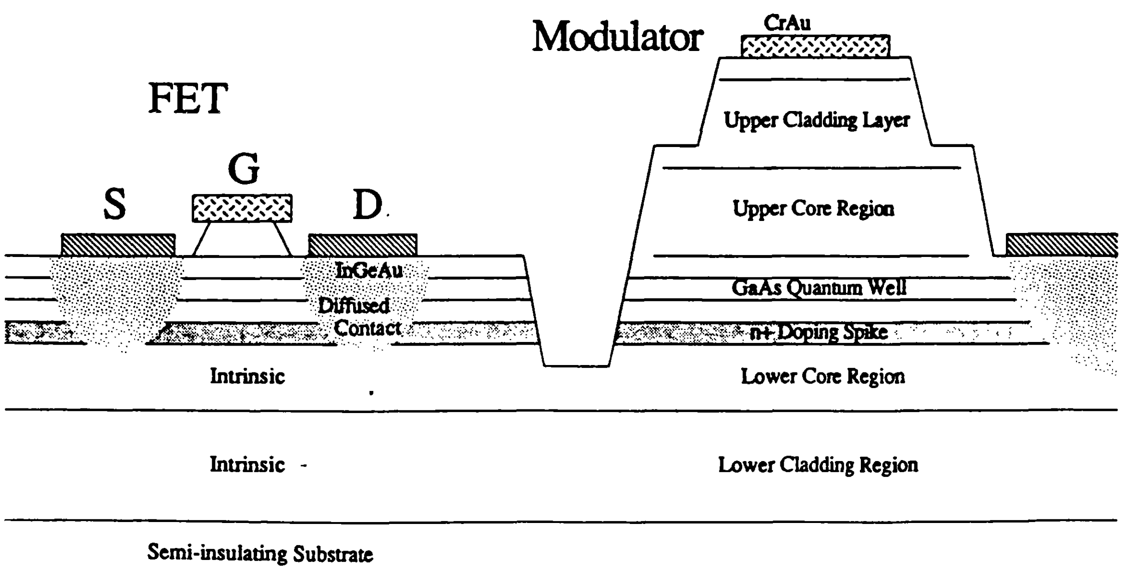

Figure 7.4.2 *Cross-section of monolithic modulator/FET combination*

electrical isolation of *p-* and *n-type* layers provided by means of a second mesa. Guiding losses and the device capacitance are kept to a minimum with this technique. The epitaxial layers for the depletion mode FET lie in the waveguide core and to give a good "non-conducting" state the layer structure indicates a semi-insulating substrate with the lower (cladding) epitaxial layers formed of intrinsic material. The fabrication of a high bandwidth FET requires the stripping of the upper cladding region and part of the core region of the waveguide to reveal the layer directly above the quantum well conduction channel. Fine line lithography can then be used to delineate the gate. The gate length would be compromised if the upper layers were not removed, by virtue of the depth of the structure and available processing techniques. Contacting to the FET channel can be achieved with diffused contacts, typically InGeAu, which are alloyed into the semiconductor surface forming a doped region down to the level of the quantum well. The gate electrode is a Schottky contact which replaces the *p-type* layer used to form a junction in the modulator itself. The provision of electrical isolation between the devices involves etching a trench either down to the undoped lower core region or to the substrate level if necessary.

The disadvantages of the FET operation, as compared with an optimised discrete SDHFET, are linked with the quantum well conduction channel width. The conclusions of the experimental modulator investigation (chapter 5) indicated that a narrow well width would lead to the highest modulation efficiency due to the excitonic peak recovery. A converse trend is reported for the FET operation [Sakaki et al] for reasons of decreased interfacial scattering effects improving carrier mobilities, and giving an improved overall transconductance. Nevertheless, good FET operation should be possible with a well width reduced from the optimum value as recently very high mobilities have been reported in a 90Å GaAs quantum well selectively doped structure [Powell et al].

The fabrication of a laser or optical amplifier from the QW-FEM structure is a departure from the more conventional construction. The semi-insulating layers lying below the FET, which serve to improve gate source leakage, leave the structure without the usual *p-i-n* configuration. Perhaps most suitable in this case would be the implementation of a lateral-injection laser structure [Wada et al]. The fabrication of a lateral device (figure 7.4.3a) involves producing *p-type* and *n-type* regions by the use of implantation or diffusion which then also act to disorder the semiconductor and reduce refractive index to either side of the proposed gain region . The drawback generally found is the inability to simultaneously provide good lateral optical confinement and vertical current confinement, hence producing undesirably high threshold currents, even with the advantage of quantum well operation. Nevertheless, a quantum well lateral injection laser has been reported with a 27mA threshold [Wada 1988].

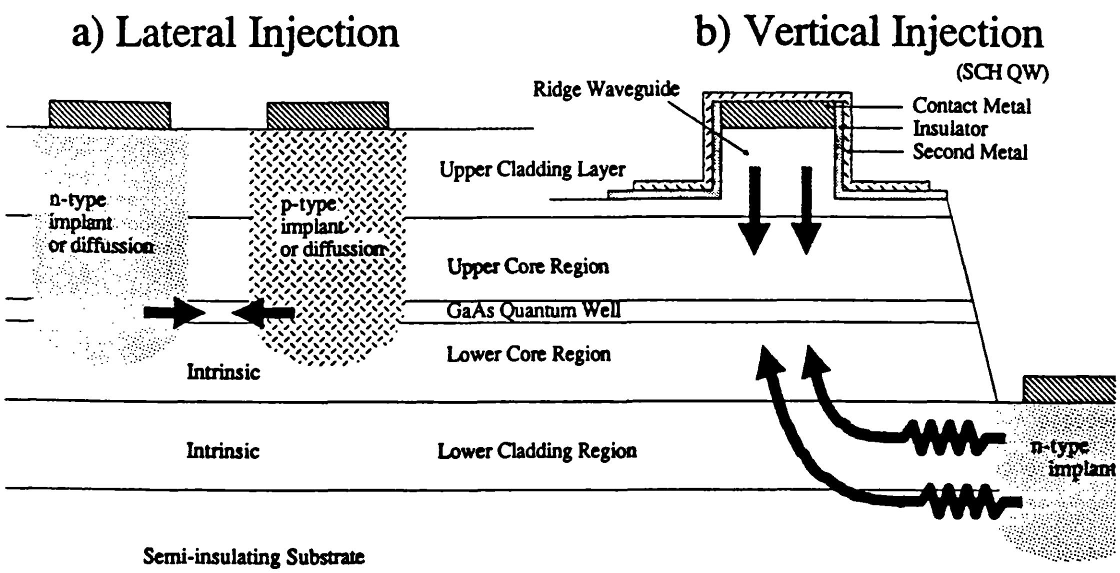

Figure 7.4.3 *a) Lateral laser design (after Wada et al) b) Vertical laser with series series resistance highlighted.*

Semiconductor laser research is striving, on the OEIC front, to reduce the lasing threshold current and hence reduce power consumption and the associated thermal dissipation and driver circuit difficulties. The lowest thresholds reported for quantum well laser diodes are below 2mA [Sugimoto et al], a value unlikely to be obtained with the QW-FEM structure in a lateral configuration. A vertical laser diode is more desirable, due to the lateral optical confinement available through ridge waveguiding and the low leakage vertical current path which leads to the low threshold exhibited in GRIN-SCH-LDs [Tsang 1981]. Unfortunately, the low *n-type* doping would produce a large series resistance, as indicated in figure 7.4.3b, and an imbalance of the injected carrier ratio, causing a decrease in the bandwidth and an increase in the threshold current. It may be possible to use a deep implant of donors to partially overcome both problems, with any lack of bandwidth being recovered by implementation of external modulation.

As a further point on trade-offs, the optimisation of the QW-FEM described in the previously (section 5.7) led to the suggested use of a narrow waveguide core for optimum modulation and reduced device length. Coupling efficiency is compromised and consequently the external insertion loss of the waveguide is increased. This provides reduced efficiency for modulator, detector and amplifier configurations, however the implementation of even a simple "optical circuit" with any combination of *modulator-laser-detector-optical amplifier* eliminates this coupling problem within the chip itself.

The monolithic combination of laser and modulator using the QW-FEM is one attractive and less complicated possibility. The goal of such an external modulator design is the high bandwidth of the signal which can be achieved and the reduction of the chirp parameter to levels below that of directly modulated semiconductor lasers (see section 5.4). The advantage of the QW-FEM implementation over an MQW structure is the desirable low chirp values observed (figure 5.4.3b). Further comparisons between the use of MQW and QW-FEM structures are made later in this section. However, a second parameter, that of modulator saturation, is a concern which should not be overlooked. Optical nonlinearities in MQW structures have been shown to have low thresholds for saturation onset, typically of around 500Wcm^{-2} [Lee,H.C. et al]. The power density in the core of a waveguide approaches 20 times this value, yet modulator saturation effects are not apparent: an experimental study by Wakita et al shows that there was no degradation in on/off ratio with incident powers of up to 11mW. In this case, the power density in the waveguide core was estimated to be in excess of 20kW/cm^{-2}. Experimental investigations by other authors [Wiener et al 1985a] do succeed in saturating the absorption in waveguides at moderate power densities but do not study the effects of bias on the spectra. The spectral study of optical nonlinearities in the literature have been performed exclusively in unbiased samples, where the population of the quantum well subbands is limited by the recombination rate (section 2.3) [Miller et al 1982]. The decay mechanism of this population changes with bias as the escape time from the well falls below the recombination time. This is illustrated in the quantum efficiency of photocurrent spectra (section 5.4) which is only seen to approach unity [Miller et al 1985] at fields of approximately 10kVcm^{-2}, showing an increase in the escape probability above that of recombination. The *biased absorbing* mode of operation of quantum well modulator is an advantage in this respect as saturation threshold will be lifted due to the change in the population decay mechanism. The use of single quantum wells may also have an advantage over MQW structures due to the transport mechanism through multiple wells which involves recapture after escape [Larsson et al].

The data of figure 7.4.4 is an illustration of the effect of high power densities on sample MV292. This preliminary investigation shows little change in the spectra with an estimated power of 0.5mW coupled into the guide. The peak intensity is of the order of 20kWcm^{-2}. However the waveguide in this case is the standard slab guide (section 4.4) and hence lateral spread of the optical mode reduces this by at least a factor of twenty at the output (30-40μm output stripe). This reduces the information which can be gained from such an experiment.

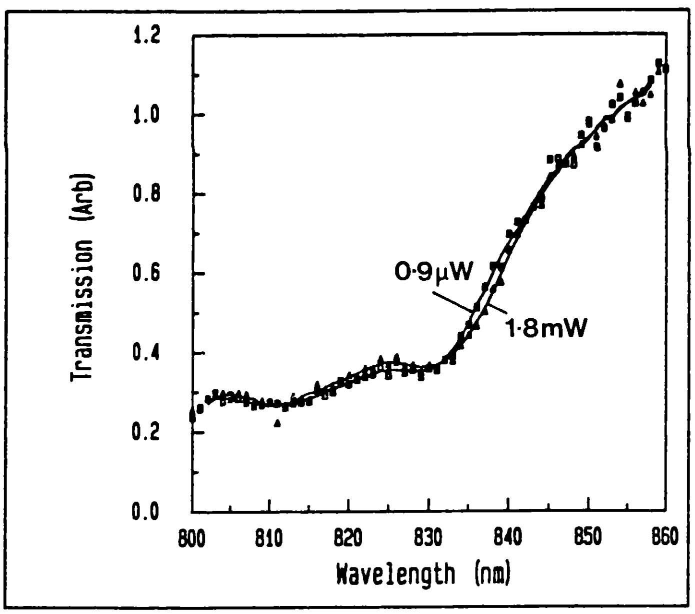

Figure 7.4.4 *Transmission spectra at high (1.8mW) and low (0.9μW) incident power levels in sample MV292. A total coupling loss of approximately 5.6dB is estimated. A reverse bias of 4V is applied to the device.*

Finally, the implementation of a photo-detector from the QW-FEM structure can be envisaged as simply a modulator used under reverse bias so that a high quantum efficiency absorbing state is achieved. The device bandwidth would be limited by the capacitance/ unit length of the structure, which is equal to that of the modulator, although at a small sacrifice of sensitivity the bandwidth can be tailored by using a shorter detection length. A second detector configuration, proposed by Chen,C.Y et al uses the two dimensional electron gas to produce fast response times. The device requires no bias, due to the photoconductive mode of operation, and consequently has a low noise figure compared with shot noise caused by leakage currents in reverse biased detectors. Rise times as short as 30ps have been reported in a 800μm device.

Results of FET fabrication

The operation of the device as a FET has been confirmed with two of the series of layer structures. The specification is illustrated along with the device cross section in figure 7.4.5a. The lowest available *n*-type doping level ($\cong 10^{16}$) in "undoped" regions represents considerable conductivity when compared to that of the quantum well and a *p*-type region had to be introduced below the

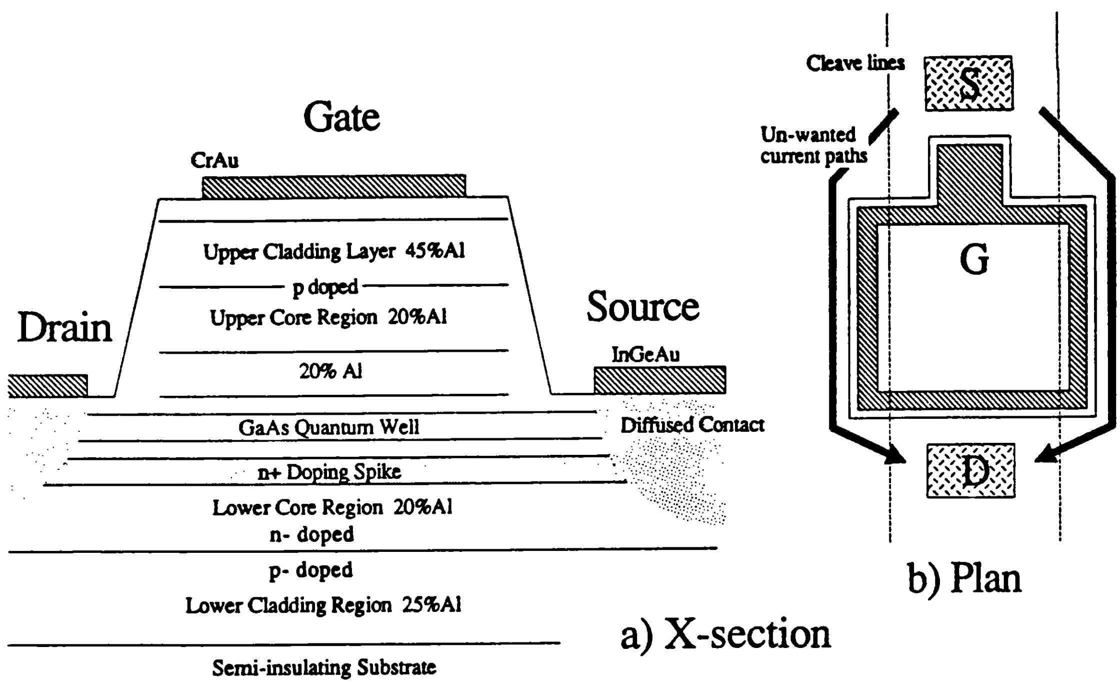

Figure 7.4.5 *a) Layer structure and cross-section of FET based on QW-FEM design b) Plan view of a fabricated test FET indicating cleaving to remove leakage paths*

well to block this conduction path and enable the desired FET operation to be possible. These structures were also grown on semi-insulating substrates for the same reason as well as the availability of inter-device isolation. The test devices are fabricated in the manner used for photodiodes (chapter 2.2) with additional InGeAu diffused contacts added to provide the source and drain connections to the conduction channel (figure 7.4.5b). The upper *p-type* layers are not removed as proposed previously but instead the device is operated as a junction FET for simplicity. Additional ungated conduction paths exist to either side of the etched mesa which lies between source and drain: these are removed by cleaving as illustrated giving a notable performance increase. The FET characteristics for the two epitaxial layer structures are shown in figure 7.4.6a,b. Conductivity is low as indicated by values on the current axes and the voltage for maximum pinch off is large at ≈5V due to the *p-n* junction operation: however this agrees well with the QW-FEM excitonic recovery voltage anticipated for the device. *Unfortunately,* none of the FET layers show the optical properties observed in the earlier QW-FEM samples and it is doubtful that the operation is due to manipulation of a two dimensional electron gas as intended. The optical photocurrent and transmission spectra for sample CB111 are illustrated in figure 7.4.7a,b. Clearly, an absorption

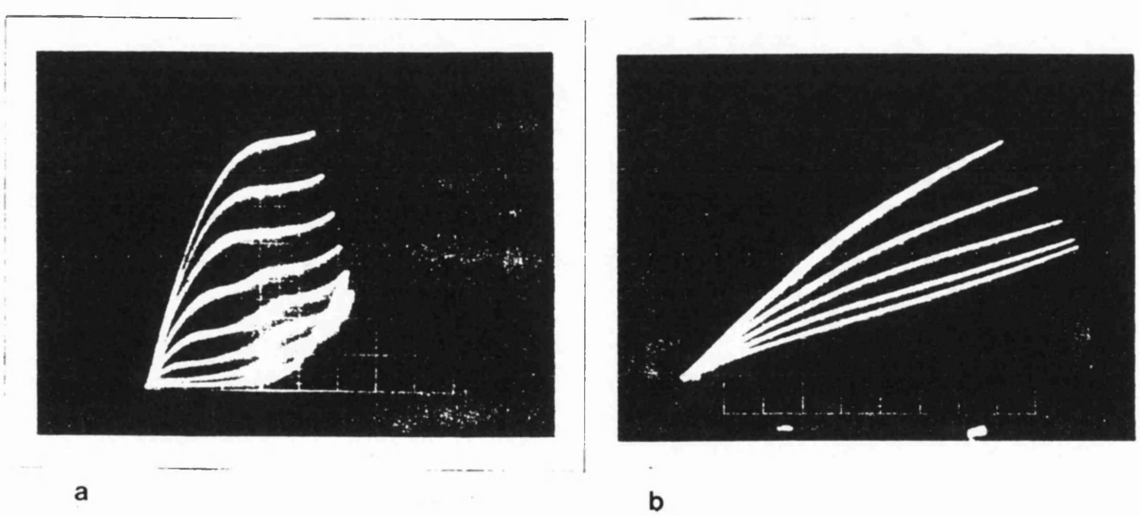

Figure 7.4.6 *FET I_d-V_{sd} characteristics. The vertical current scale is 200μA/div and the horizontal voltage scale is 2V/div. The gate voltage step is 1V. a) CB111, b) CB171*

change is found at the bandedge although the anticipated excitonic recovery is absent. The absorption tail continues to considerably longer wavelength than that of any of the previous QW-FEM layers.

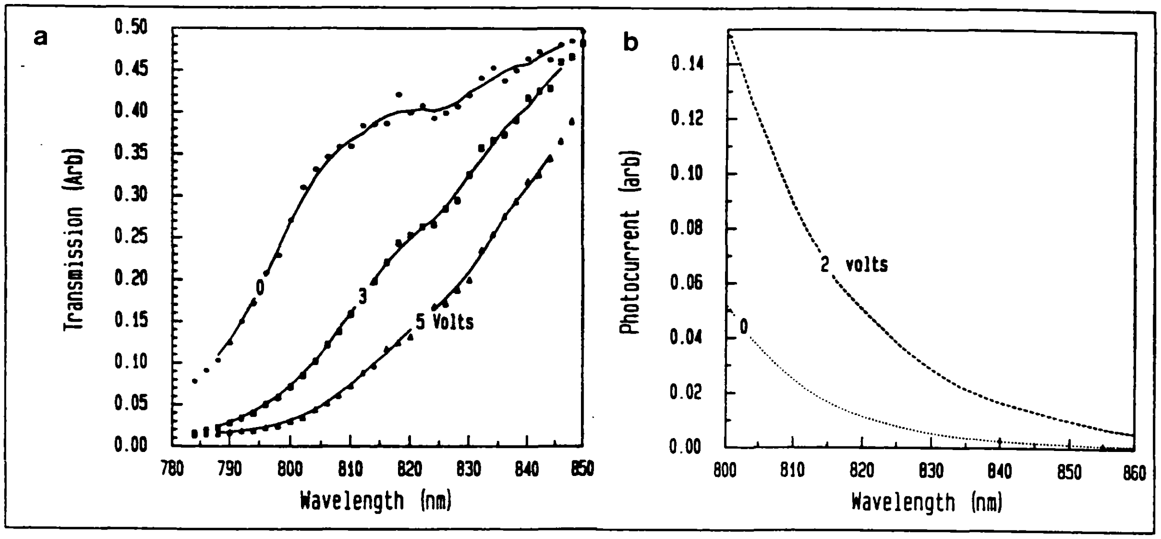

Figure 7.4.7a,b *a) Transmission and b) photocurrent spectra for sample CB111.*

Advantages of the InP Material System for the QW-FEM

A more suitable approach to the monolithic integration of this device would be the use of the InP based material system. The advantages are numerous and the more obvious, such as increased mobility for the FET operation, have been pointed out previously. The additional advantages are related specifically to the device function and to the OEIC fabrication process.

The fabrication of FETs from the QW-FEM structure would be made easier by inclusion of an etch stop layer directly above the quantum well. This would typically be a layer of GaAs in the present material system to give a suitable Al mole fraction variation at the desired interface for differential wet or dry etch rates to exist. The GaAs layer could then also be used to provide a high quality Schottky contact not available with an AlGaAs surface. This layer would have the undesirable consequence of introducing an additional GaAs layer to the waveguide core region with disastrous absorptive properties extending to longer wavelength than spectral features of the quantum well itself. If the structure was fabricated using the InP based material system with an InGaAs quantum well the additional ternary alloy AlInAs could be introduced as both an etch stop layer and Schottky contact layer (figure 7.4.8). This structure would then produce a FET identical to many SDHFETs

[Seo et al] and the AlInAs layer, having similar bandgap to InP, would have no undesirable optical consequences. The advantages gained in moving to the more complex InP/InGaAs/InAlAs material system is apparent in this light, and combined with the increased electron mobility afforded, the case is strong. However, as argued previously, the use of the long wavelength material systems is not necessarily advantageous for all optical technologies.

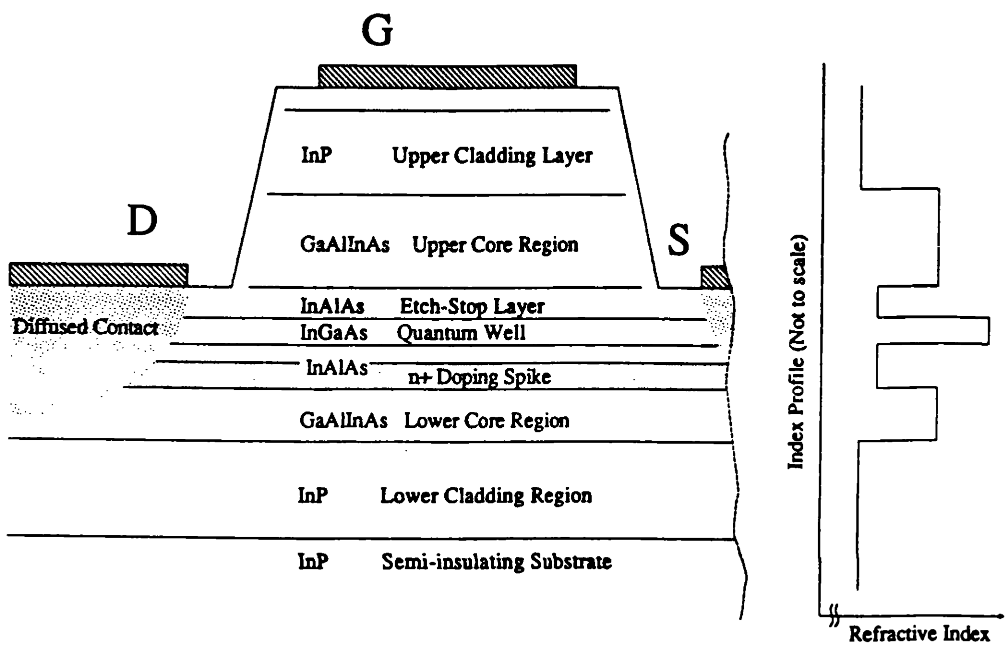

Figure 7.4.8 *A possible long wavelength implementation of the QW-FEM structure. The index profile is also shown to the right*

Comparison of QW-FEM OEICs with the MQW Approach

Comparison must be made at this point with a closely related approach to OEIC fabrication which has a similar integration goal. The argument here is based around the most common modulation mechanism in use in III-V materials, the quantum confined Stark shift. The development of this type of modulator has been discussed in general terms in chapter 1 and the arguments here are a direct comparison of integration aspects with those of the QW-FEM.

The coupling losses to the QW-FEM waveguide modulator are limited by the narrow core design which would be implemented to increase the optical field overlap with the single quantum well (section 5.7). The tighter optical confinement gives greatest modulation depth and allows short device lengths. On the negative side, the saturation intensity of the modulator is decreased for the exact same reason (section 7.4, above) along with the bandwidth of the device, which is degraded due to increased capacitance. The advantage that a MQW modulator has in these respects is the use of several quantum wells enabling "dilution" of the waveguide optical intensity without loss of the modulation performance. Essentially, the waveguide core can be widened and more quantum wells used to retrieve the required modulation depth. This improves the coupling losses and could increase the saturation intensity by up to a factor of 10. As mentioned earlier saturation intensity in excess of 11mW has been observed by Wakita et al in an MQW modulator with 10 quantum wells which represents a useful power for most optical systems. For example, a long haul optical communications system operating at high bandwidth and using narrow linewidth laser is limited by the input power which can be used. This is due to the onset of Stimulated Brillouin Scattering which can occur at threshold values as low as 10mW and causes a depletion of the system input power [Aoki et al].

The waveguide core width relationship to the modulation bandwidth is connected with the doping profile in the device. Typically, the core is undoped with *p-* and *n-type* doping in the cladding regions. A waveguide MQW modulator may have up to 1μm of intrinsic region whilst the QW-FEM would typically have approximately 0.6μm and would also suffer from a longer device length leading to a factor of two decrease in bandwidth. Neither of these comparisons consider the integration argument which in fact may lead to similar performance for the two modulator types. A laser fabricated from MQW material has an optimum number of wells which is typically of the order of 4 and also has a narrow core to provide low thresholds and single mode operation. This has implications for the integrated laser/modulator which must use the same structure for both devices and, consequently, the optimised parameters of the MQW modulator must be compromised and the QW-FEM structure becomes more attractive as a consequence.

The operating wavelength of a quantum well laser diode lies to the low energy side of the heavy-hole excitonic resonance due to carrier induced bandgap renormalisation effects [Kleinman and Miller]. This makes the fabrication of a Stark-shift MQW integrated laser modulator a reasonable task, as the quantum confined Stark shift moves the excitonic resonance to lower energy (section 1.2). Unfortunately, there is still residual absorption at the lasing wavelength which is generally only separated from the heavy hole peak by approximately 15nm [Tsang 1987]: this is comparable with the typical 5nm half-width half-maximum of the excitonic absorption peak [Stevens et al] and leads to a residual absorption of approximately 10%. The QW-FEM may be more suited to this integration technique on the grounds of reduced absorption at the lasing wavelength due to the zero bias quenching of the heavy-hole peak. An approach for overcoming this problem in MQW structures is the use of disordering as mentioned in the previous section. This enables the shift of the operating wavelength of the modulator to a shorter wavelength reducing the residual absorption [Ribot et al].

If MQW devices were to be grown on semi-insulating substrates the removal of the epitaxial layers which form the modulators would reveal a site for the fabrication of conventional GaAs FETs (notwithstanding the disadvantages of vertical integration and surface relief outlined earlier). These FETs do not have the outstanding properties, such as the bandwidth seen in heterostructure FETs, but at the same time we must consider the capacitance limited bandwidth of the modulator itself. A typical modulator bandwidth of 20GHz was suggested in Section 3.3 and this figure is not beyond the scope of simple GaAs FETs. The problems encountered are more likely to be associated with the inability to drive low impedance loads such as lasers and detectors due to the lower transconductance of MESFETs.

7.5 Conclusions

The implementation of monolithic integrated circuits, with electronic and optoelectronic components, to form OEICs has major advantages for the majority of tasks performed within current and future communications systems. The complexity of fabrication, and the corresponding expense incurred, can be reduced with the introduction of multifunctionality built into the fabric of the device design. This may not produce the ultimate in performance for the most demanding applications, but it reaches the goals of many systems which rely on high complexity, density, and bandwidth, but require a low cost and mass production capability.

The QW-FEM is an excellent candidate for OEIC fabrication due to the many applications of the structure which include such devices as modulators, FETs, detectors, lasers and optical amplifiers. The competition is from the more established MQW modulator. These alternatives each have their advantages as described above, and to invoke the QW-FEM solution the emphasis must lie with a need for the excellent high performance SDHFET devices which are available.

Conclusions

This thesis has reported the development of a novel GaAs quantum well optical waveguide modulator. The device uses an alternative mechanism to the more usual quantum confined Stark shift (QCSS), which provides an increase in the potential for monolithic integration. Optical modulation is achieved by quenching the excitonic absorption through provision of an electron population in the quantum well. The control of this electron population, and hence the absorption, operates in an identical manner to a SDHFET. Increased flexibility in integrated monolithic design is introduced primarily by this duality of the FET and modulator mechanism. This new device has been named the quantum well *field effect* modulator (QW-FEM).

The QW-FEM has been experimentally investigated both by means of optical transmission and photocurrent measurements. Evidence has been found for the desired excitonic quenching mechanism and absorption modulation in an optical waveguide is observed. The dependence of the quenching mechanism on well width has been experimentally investigated and confirms that narrow quantum wells produce greater excitonic absorption control. Different semiconductor junctions have also been examined, and the use of a *p-n* junction has been found preferable to a Schottky barrier due to the restrictions on epitaxial growth imposed by a waveguide geometry. The design of the QW-FEM structure has been implemented using a simple model of the junction electric field. This enables the operating voltage to be tailored and excellent agreement between theory and experiment is demonstrated.

Studies of absorption spectra derived from photocurrent data have revealed that the absorption modulation mechanism intrinsically has a lower chirp parameter than the corresponding QCSS of MQW devices. This is an attractive quality for long haul optical communications applications. Drawbacks of the fundamental single quantum well design of the QW-FEM have been discussed in terms of the saturation powers and the bandwidth. Typically both will be reduced in comparison with an optimised MQW device, similarly the insertion loss will be increased. However these disadvantages are reduced when considering structures for monolithic integration of devices.

Nonuniformities in the layer structures have limited the experimental modulation depth available through the restriction to short waveguides. The greatest modulation attained was 2dB. However the observed transmission spectra yield values for the absorption coefficient in the waveguide and from this it is possible to extrapolate to the performance of an optimised structure. The absorption changes, and residual absorption levels found, constitute a 10dB modulation in a 160μm waveguide with a 1.9dB internal insertion loss. The required layer uniformities are not fundamental to the design of the QW-FEM, and are not limited by the technique of epitaxial growth, hence the predictions of modulation depth are meaningful.

An experimental analysis of the performance of the modulation mechanism has used polarisation and optical saturation effects in a waveguide, and low temperature photocurrent studies. These reveal that a greater excitonic quenching should be possible, leading to a reduction in the experimental values of insertion loss. The limit to the modulation depth in a QW-FEM is theoretically determined to be due to the residual absorption of a broadened and shifted subband edge. The carrier population in the quantum well, which acts to quench the excitonic resonance, has the secondary effect of introducing a renormalisation of the subband gap. This, combined with broadening due to well width fluctuations and carrier scattering interactions, leads to an absorption contribution at the spectral position of optimum modulation. This undesirable effect was quantified by using expressions for absorption and bandfilling taken from calculations of laser gain characteristics. The modelling also predicts an upper limit for the modulation achievable in the QW-FEM by introduction of quantum confined Stark shift data of undoped MQW samples to represent the biased recovered excitonic state.

The functionality of the device extends beyond optical modulation and the experimentally observed FET operation. The absorption in the biased state acts as a detector, whilst both laser and optical amplification functions should also be possible. A study of the goals of optoelectronic integrated circuits (OEICs) has illustrated that the flexibility and performance the QW-FEM is ideal for monolithic integration. Such a device structure uld enable the mass production of low cost communications components for implementation of local area and long haul networks. It is expected that there is also a future need for switching components in the form of photonic integrated circuits, a role for which the QW-FEM is suited. A study of the proposed implementation of QW-FEM devices for OEICs has illustrated the simplicity of possible fabrication schemes.

Publications List

C.Tombling, M.M.Stallard, J.S.Roberts *Observation of Absorption Modulation in a Single Quantum Well Exciton Screening Device* 14th European Conference on Optical Communication ECOC 1988.

C.Tombling, M.M.Stallard, J.S.Roberts. *A Study of Waveguide Modulation by Excitonic Screening* IEE Colloquium, Heterojunction and Quantum Well Devices: Physics and Applications, October 1988.

C.Tombling, M.M.Stallard, J.S.Roberts *Modulation of Excitonic Quenching in a Selectively Doped Single Quantum Well* IEEE/OSA Topical Meeting on Quantum Wells for Optics and Optoelectronics, Salt Lake City, Utah, USA March 1-3, 1989.

C.Tombling, M.M.Stallard, J.S.Roberts *Quenching of the Excitonic Resonance in a Waveguide Quantum Well Field Effect Modulator* Submitted to Semiconductor Science and Technology.

J.H.Abeles, W.K.Chan, A.Kastalsky, J.P.Harbison, L.T.Florez and R.Bhat *Guided-Wave GaAs/AlGaAs FET Optical Modulator Based on Free-Carrier-Induced Bleaching* EL 23 (24) 1987 pp1302-1304.

M.D.Abbott *Software for the Monochromator and Laser Stepper Drive Facilities Developed For Use at UCL.*

S.Adachi *GaAs AlAs and $Al_xGa_{1-x}As$: Material parameters for use in research and device applications* JAP 58 (3) 1985

G.P.Agrawal and N.K.Dutta *Long Wavelength Semiconductor Lasers* Von Nostrand Rienhold, 1986.

Y.Aoki, K.Tajima, I.Mito *Input Power Limits of Single Mode Optical Fibres due to Stimulated Brillouin Scattering in Optical Communication Systems* JLT 6 (5) 1988 pp710-718.

Y.Arakawa, A.Larsson, J.Paslaski and A.Yariv *Active Q-Switching in a GaAs/AlGaAs Multiquantum Well Laser with an Intracavity Monolithic Loss Modulator* APL 48 (9) 1986 pp561-563.

M.Asada, A.Kameyama and Y.Suematsu *Gain and Intervalence Band Absorption in Quantum Well Lasers* IEEE JQE QE-20 (7) 1984 pp745-753.

M.Asada, S.Hausser, E.Zielinski and M.Pilkuhn *Intraband Relaxation Time in Quantum Well Lasers due to Carrier Carrier Scattering* Int. Quantum Electron. Conf. Tokyo, TuP44 1988 p419. See also M.Asada *Intraband Relaxation Time in Quantum Well Lasers* JQE to be published.

I.Bar-Joseph, J.M.Kuo, C.Klingshirn, G.Livescu, T.Y.Chang, D.A.B.Miller and D.S.Chemla *Absorption Spectroscopy of the Continuous Transition From Low to High Electron Density in a Single Modulation-Doped InGaAs Quantum Well* PRL 59 (12) 1987 pp1357-1361.

G.Bastard *Energy Levels in Semiconductor Quantum Wells* Surface Science 170 1986 pp426-437.

G.Bastard and J.A.Brum *Electronic States in Semiconductor Heterostructures* IEEE JQE QE-22 (9) 1986 pp1625-1644.

G.E.W.Bauer and T.Ando *Theory of Band Gap Renormalisation in Modulation-doped Quantum Wells* J.Phys.C: Solid State Phys 19 1986 pp1537-1551.

P.Blood *Capacitance-Voltage Profiling and the Characterisation of III-V Semiconductors Using Electrolyte Barriers.* Semicon Sci Technol. 1 1986 pp7-27.

P.Blood, S.Colak and A.I.Kucharska *Influence of Broadening and High-Injection Effects on GaAs-AlGaAs Quantum Well Lasers* IEEE JQE 24 (8) 1988 pp1593-1604.

N.Bouadma, J.Riou, A.Kampfer *Low Threshold GaAs/AlGaAs BH Lasers With Ion Beam-Etched-Mirrors* EL 21 (13) 1985 pp566-568.

G.D.Boyd, J.E.Bowers, C.E.Soccolich, D.A.B.Miller, D.S.Chemla, L.M.F.Chirovsky, A.C.Gossard and J.H.English *5.5 GHz Multiple Quantum Well Reflection Modulator* EL 25 (9) 1989 pp558-560.

Piero Bradley *Waveguide Optical Modulators in AlGaAs GaAs Multiple Quantum Well Material* Doctoral Thesis 1990, Department of Electronic and Electrical Engineering, University College London.

P.J.Bradley, M.Whitehead, G.Parry, P.Mistry and J.S.Roberts *Effect of Device Length and Background Doping on the Relative Magnitudes of Phase and Amplitude Modulation in GaAs/AlGaAs pin Multiple Quantum Well Waveguide Modulators* Applied Optics 28 (8) 1989 pp1560-1564.

A.S.Brown, U.K.Mishra, J.A.Henige and M.J.Delaney *The Impact of Epitaxial Layer Design and Quality on GaInAs/AlInAs High Electron-Mobility Transistor Performance* J.VacSciTech B6 (2) 1988.

J.A.Brum, J.Orgonasi, G.Bastard, C.Delalande, M.Voos, G.Weimann and W.Schlapp *Optical Properties of One-side Modulation-doped Quantum Wells* Surface Science 196 1988 pp512-517.

M.W.Carlson, G.A.Evans, S.K.Liew, C.J.Kaiser *Grating Surface Emitting Diode Arrays for Optical Communications* Proc.(5) Optical Fibre Communications Conference 1989 p9.

H.C.Casey Jr and M.B.Panish *Heterostructure Lasers Part A.* Academic Press 1978.

D.S.Chemla, I.Bar-Joseph, J.M.Kuo, T.Y.Chang, C.Klingshirn, G.Livescu and D.A.B.Miller. *Modulation of Absorption in Field Effect Quantum Well Structures* JQE 24 (8) 1988 pp1664-1676.

D.S.Chemla, I.Bar-Joseph, C.Klingshirn, D.A.B.Miller, J.M.Kuo and T.Y.Chang *Optical Reading of Field-effect Transistors by Phase-space Quenching in a Single InGaAs Quantum Well Conducting Channel* APL. 50 (10) 1987 pp585-587.

D.S.Chemla and D.A.B.Miller *Room-temperature Excitonic Nonlinear-optical Effects in Semiconductor Quantum-Well Structures* J.Opt.Soc.Am.B Vol 2 (7) 1985 pp1155-1173.

D.S.Chemla, D.A.B.Miller, P.W.Smith, A.C.Gossard and W.Weigmann *Room Temperature Excitonic Nonlinear Absorption and Refraction in GaAs/AlGaAs Multiple Quantum Well Structures* IEEE JQE 20 (3) 1984 pp265-275.

D.S.Chemla, T.C.Damen, D.A.B.Miller, A.C.Gossard and W.Wiegmann *Electroabsorption by Stark Effect on Room-Temperature Excitons in GaAs/GaAlAs Multiple Quantum Well Structures* APL 42 (10) pp864-866. 1983

G.K.Chang, W.P.Hong, J.L.Gimlett, R.Bhat, C.K.Nguyen *High-Performance Monolithic Dual-MSM Photodetector for Long-Wavelength Coherent Receivers* EL 25 (16) 1989 pp1021-1022.

C.Y.Chen, A.Y.Choo, C.G.Bethea and P.A.Garbinski *Bias-free Selectively Doped* $Al_xGa_{1-x}As$*-GaAs Picosecond Photodetectors* APL 41 (3) 1982 pp282-284.

T.Z.Chen, K.Y.Toh, J.D Cressler, J.Warnock, P.F.Lu, D.D.Tang, G.P.Li, C.T.Chuang and T.H.Ning *A Submicrometer High-Performance Bipolar Technology* IEEE EDL 10 (8) 1989 pp364-366.

D.Cotter and K.I.White. *Picosecond Pulse Generation and Detection in the Wavelength Range 1200-1600nm*. Optics Communications, 49.(3) (1983) pp205-209.

D.Crawford, G.W.Taylor, P.A.Kiely, P.Cooke, A.Isabelle, T.Y.Chang, B.Tell, M.S.Lebby, K.Brown-Goebeler and J.G.Simmons *An Inversion Channel Technology for Optoelectronic Integration* Proc.(2) 14th European Conference on Optical Communications (ECOC) 1988 pp211-214.

J.D.Crow *Optoelectronic Integrated Circuits for High Speed Computer Networks* Proc.(5) Optical Fibre Communications Conference 1989 pp83-84.

C.Delalande, J.Orgonasi, J.A.Brum, G.Bastard and M.Voos *Optical Studies of a GaAs Quantum Well Based Field-Effect Transistor* APL 51 (26) 1987 pp1346-1348.

R.Dingle, W.Wiegmann, and C.Henry *Quantum States of Confined Carriers in Very Thin* $Al_xGa_{1-x}As$ *- GaAs -* $Al_xGa_{1-x}As$ *Heterostructures* Pys Rev Lett 33 (14) 1974 pp827-830.

D.Dolfi, M.Nazarathy, R.L.Jungerman *40GHz Electro-optic Modulator with a 7.5V Drive Voltage* EL. 24 (9) 1984 pp528-529.

G.Duggan, H.I.Ralph and K.J.Moore *Reappraisal of the band-edge discontinuities at the* $Al_xGa_{1-x}As$*-GaAs Heterojunction* Phys Rev B 32 (12) 1985 pp8395-8397.

U.Ekenberg and M. Altarelli *Exciton Binding Energy in a Quantum Well with Inclusion of Valence-band Coupling and Nonparabolicity* Physical Review B, Vol 35 (14) 1987 pp7585-7595.

C.W.Farley, M.F.Chang, P.M.Asbeck, N.H.Sheng, R.Pierson, G.J.Sullivan, K.C.Wang, R.B.Nubling *High Speed (f_t=78GHz) AlInAs/GaInAs Single Heterojunction HBT* EL 25 (13) 1989 pp846-847.

R.Fischer, T.Henderson, J.Klem, W.Kopp, C.K.Peng, H.Morkoç, J.Detry and S.C.Blackstone *Monolithic Integration of GaAs/AlGaAs Modultion-Doped Field-Effect Transistors and N-Metal-Oxide-Semiconductor Silicon Circuits* APL 47 (9) 1985 pp983-985.

P.M.Frijlink, J.P.Andre and M.Erman *Metal-Organic Vapour-Phase Epitaxy of Multilayer Structures With III-V Semiconductors* Philips Tech.Rev. 43 (5/6) 1987 pp118-132.

S.R.Forest *Optoelectronic Integrated Circuits* Proc IEEE, Vol 75, (11) 1987 pp1488-1497.

J.L.Gimlet *A New Low Noise 16GHz PIN/HEMT Optical Receiver* Proc.(2) 14th European Conference on Optical Communications (ECOC) 1988 pp13-16.

C.H.Gnauck, J.E.Bowers and J.C.Campbell * *Gbit/s Transmission Over 30km of Optical Fibre* EL 22 (11) 1986 pp600-602.

J.W.Goodman, F.I.Leonberger, S.Y.Kung and R.A.Athale *Optical Interconnections for VLSI Systems* IEEE Trans Cons Elect. 34 (1988) pp116-35

A.C.Gossard *Growth of Microstructures by Molecular Beam Epitaxy* IEEE JQE Vol QE-22 (9) 1986 pp1649-1655.

D.R.P.Guy, L.L.Taylor, D.D.Besgrove, N.Apsley and S.J.Bass *High Contrast Ratio Electro-Absorptive InGaAs-InP Quantum Well Modulator EL 24 (19) 1988 pp1234-1235*

C.Harder, K.Vahala and A.Yariv *Measurement of the Linewidth Enhancement Factor α of Semiconductor Lasers* APL Vol 42 (4) 1983 pp328-330.

C.Harder, B.v.Zeghbroeck, H.Meier, W.Patrick and P.Vettiger *5.2GHz Bandwidth Monolithic GaAs Optoelectronic Receiver* EDL 9 (4) 1988 pp171-173

H.Haug and S.Schmitt-Rink *Basic Mechanisms of the Nonlinearities of Semiconductors Near the Band Edge* J.Opt.Soc.Am.B. Vol 2 (7) 1985 pp1135-1142.

I.Hayashi *Research Aiming for Future Optoelectronic Integration: The Optoelectronics Joint Research Laboratory* IEE Proc 133J (3) 1986 pp237-244.

E.Hecht and A.Zajac *Optics* Addison-Wesley 1974.

J.C.Hensel and G.Feher *Cyclotron Resonance Experiments in Uniaxially Stressed Silicon: Valence Band Inverse Mass Parameters and Deformation Potentials* Physical Review 129 (3) 1963 pp1041-1063.

P.D.Hodson, R.H.Wallis, J.I.Davies *Low Leakage InGaAs Photodiodes Grown on GaAs Substrates Using a Graded Strained-Layer SuperLattice* EL 23 (6) 1987 pp273-275.

D.Huang, H.Y.Chu, Y.C.Chang, R.Houdre and H.Morkoc *Excitonic Absorption in Modulation-Doped GaAs/$Al_xGa_{1-x}As$ Quantum Wells* Phys.Rev.B 38 (2) 1988 pp1246-1250.

H.Inoue, K.Hiruma, K,Ishida, T.Asai and H,Matsumara. *Low Loss GaAs Optical Waveguides* JLT 3 1985 pp1270-1276.

K.Inoue and H.Sakaki *A New Highly-Conductive (AlGa)As/GaAs/(AlGa)As Selectively-Doped Double-Heterojunction Field-Effect Transistor (SD-DH-FET)* JJAP Vol 23 (2) 1984 ppL61-L63.

K.Inoue, H.Sakaki and J.Yoshino *MBE Growth and Properties of AlGaAs/GaAs/AlGaAs Selectively-Doped Double-Heterojunction Structures with Very High Conductivity* HJAP.23 (10) 1984 ppL767- L769.

K.Inoue, H.Sakaki, J.Yoshino and T.Hotta *Self-consistent Calculation of Electronic States in AlGaAs/GaAs/AlGaAs Selectively Doped Double-heterojunction Systems Under Electric Fields* JAP Vol 58 1985 pp4277-4281.

F.Y.Juang, J.Singh, P.K.Bhattacharya, K.Bajema and R.Merlin *Field Dependent Linewidths and Photoluminescence Energies in GaAs-AlGaAs Multiquantum Well Modulators* APL 48 (19) 1986 pp1246-1248.

K.Kamon, S.Takagishi and H.Mori *Selective embedded growth of AlGaAs by low pressure organometallic vapour phase epitaxy* Jpn JAP 25 1986 ppL10-L12.

C.K.Kao *10^{12} bit/s Optoelectronics Technology* IEE Proc 133J (3) 1986 pp230-236.

K.Kasahara, A.Suzuki, S,Fujita, Y,Inomoto, T.Terakado and M.Shikada *InGaAsP/InP Long Wavelength Transmitter and Receiver OEICs forHigh Speed Optical Transmission Systems* 12th European Conference on Optical Fibre Communications 1986 pp119-122.

A.Kastalsky, J.H.Abeles and R.F.Leheny *Novel Optoelectronic Single Quantum Well Devices Based on Electron Bleaching of Exciton Absorption* APL.50 (9) 1987, pp.708-710.

J.Katz, N.Bar-Chaim, P.C.Chen, S.Margalit, I.Ury, D.Wilt, M.Yust and A.Yariv *Monolithic Integration of GaAs/AlGaAs Bipolar Transistor and Heterstructure Laser* APL 37 (2) 1980 pp211-213.

Y.Kawamura, K.Wakita, Y.Itaya, Y.Yoshikuni and H.Asahi *Monolithic Integration of InGaAsP/InP DFB Lasers and InGaAs/InAlAs MQW Optical Modulators* EL 22 (5) 1986 pp242-243.

K.Kikuchi and T.Okoshi *FM- and AM-Noise Spectra of 1.3μm InGaAsP DFB Lasers in 0.3 GHz Range and Determination of their Linewidth Enhancement Factor* ∝ EL Vol 20 (25/26) 1984 pp1044-1045.

C.Kittel *Introduction to Solid State Physics* 5th Edition, J.Wiley and Sons, New York.

D.A.Kleinman *Theory of Excitons in Semiconductor Quantum Wells Containing Degenerate Electrons or Holes* Physical Review B, Vol 32 (6) 1985 pp3766-3771.

D.A.Kleinman and R.C.Miller *Band-gap Renormalisation in Semiconductor Quantum Wells Containing Carriers* Physical Review B, Vol 32 (4) 1985 pp2266-2272.

W.H.Knox, R.L.Fork, M.C.Downer, D.A.B.Miller, D.S.Chemla and C.V.Shank *Femtosecond Dynamics of Resonantly Excited Excitons in Room-Temperature GaAs Quantum Wells* PRL 54 (12) 1985 pp1306-1309.

U.Koren, T.L.Koch, B.I.Miller, G.Eisenstein and R.H.Bosworth *Wavelength Division Multiplexing Light Source with Integrated Quantum Well Tunable Lasers and Optical Amplifiers* APL 54 (21) 1989 pp2056-2058.

U.Koren, B.I.Miller, T.L.Koch, G.Eisenstein, R.S.Tucker, I.Bar-Joseph and D.S.Chemla *Low-Loss InGaAs/InP Multiple Quantum Well Optical Electroabsorption Waveguide Modulator* APL 51 (15) 1987 pp1132-1134.

F.Koyama and K.Iga *Frequency Chirping in External Modulators* JLT 6 (1) 1988 pp87-93.

F.Koyama and K.Iga *Frequency Chirping of External Modulation and its Reduction* EL Vol 21 (23) 1985 pp1065-1066.

M.Krakowski, D.Rondi, A.Talneau, Y.Combemale, G,Chevalier, F.Deborgies, P.Maillot, P.Richin, R.Blondeau, L.D'Auria and B.de.Gremoux *Ultra-Low-Threshold, High Bandwidth, Very-Low-Noise Operation of 1.52μm GaInAsP/InP DFB Buried Ridge Structure Laser Diodes Entirely Grown By MOCVD* JQE, Vol 25 (6) 1989 pp1348.

A.Kucharska, D.Robbins *Lifetime Broadening in GaAs-AlGaAs Quantum Well Lasers* JQE to be published.

A.Larsson, P.Andrekson, S.Eng, A.Yariv *Tunable Superlattice p-i-n Photodetectors: Characteristics, Theory and Applications* JQE 24 (5) 1988 pp787-801

C.P.Lee, S.Margalit, I.Ury and A.Yariv *Integration of an Injection Laser with a Gunn Oscillator on a Semi-insulating GaAs Substrate* APL 32 pp806-807.

W.S.Lee, G.R.Adams, J.Mun and J.Smith *Monolithic GaAs Photoreceiver for High Speed Signal Processing Applications* EL.22 (2) 1986 pp147-148.

H.C.Lee, A.Hariz, P.D.Dapkus, A.Kost, M.Kawase and E.Garmire *Nonlinear absorption in AlGaAs/GaAs Multiple Quantum Well Structures Grown by Metalorganic Chemical Vapour Deposition* APL. 50 (17) 1987 pp1182-1184.

J.H.Leheny, W.K.Chan, A.Kastalsky, J.P.Harbison, L.T.Florez and R.Bhat *Guided-Wave GaAs/AlGaAs FET Optical Modulator Based on Free-Carrier-Induced Bleaching* EL. 23 (24) 1987 pp1302-1304.

R.A.Linke *Transient Chirping in Single-Frequency Lasers: Lightwaves Systems Consequences* EL. 20 (11) 1984 pp472-474.

R.A.Linke *Ultra High Speed Digital Transmission Systems* Proc ECOC 1987 pp126-131.

G.Livescu, D.A.B.Miller, D.S.Chemla, M.Ramaswamy, T.Y.Chang, N.Sauer, A.C.Gossard and J.H.English *Free Carrier and Many-Body Effects in Absorption Spectra of Modulatio-Doped Quantum Wells* IEEE JQE 24 (8) 1988 pp1677-1689.

J.G.Mendoza-Alvarez, R.H.Yan and L.A.Coldren *Contribution of the band-filling Effect to the Effective Refractive-index Change in Double-heterostructure GaAs/AlGaAs Phase Modulators* JAP Vol 62 (11) 1987 pp4548-4553.

M.H.Meynadier, J.Orgonasi, C.Delalande, J.A.Brum, G.Bastard, M.Voos, G.Weimann and W.Schlapp *Spectroscopy of a High-mobility GaAs-$Ga_{1-x}Al_xAs$ One-side-modulation-doped Quantum Well* Physical Review B Vol 34 (4) 1986 pp2482-2485.

D.A.B.Miller, D.S.Chemla, D.J.Eilenberger, P.W.Smith, A.C.Gossard and W.T.Tsang *Large Room-Temperature Optical Nonlinearity in GaAs/$Ga_{1-x}Al_xAs$ Multiple Quantum Well Structures* APL 41 (8) 1982 pp679-681.

D.A.B.Miller, D.S.Chemla, T.C.Damen, A.C.Gossard, W.Wiegmann, T.H.Wood, C.A.Burrus *Electric Field Dependence of Optical Absorption Near the Band Gap of Quantum Well Structures* Pyhs Rev B 32 (2) 1985 pp1043-1059.

R.C.Miller, D.A.Kleinman, O.Munteanu and W.T.Tsang *New Transitions in the Photoluminescence of GaAs Quantum Wells* APL 39 (1) 1981 pp1-3.

R.C.Miller, D.A.Kleinman, A.C.Gossard *Energy-gap Discontinuities and Effetive Masses for GaAs-AlGaAs Quantum Wells* Phys Rev B 29 (12) pp7085-7087.

U.K.Mishra, A.S.Brown, S.E.Rosenbraum, C.E.Hooper, M.W.Pierce, M.J.Delaney, S.Vaughin and K.White *Microwave Performance of AlInAs-GaInAs HEMTs with 0.2 and 0.1μm Gate Length* IEEE EDL, Vol 9 (12) 1988 pp647-649.

T.Miyazawa, T.Kagawa, H.Iwamura, O.Mikami and M.Naganuma *Two-Wavelength Demultiplexing p-i-n GaAs/AlAs Photodetector using Partially Disordered Multiple Quantum Well Structures* APL Vol 55 (9) 1989 pp828-829.

H.Morkoç, T.J.Drummond, R.E.Thorne and W.Kopp *Mobility Enhancement in Inverted AlGaAs/GaAs Modulation Doped Structures and its Dependance on Donor-Electron Separation* Jpn JAP 20 (12) ppL913-916

H.Nagai, M.Yamanishi, Y.Kan and I.Suemune *Field-induced Modulations of Refractive Index and Absorption Coefficient in a GaAs/AlGaAs Quantum Well Structure* EL 22 (17) 1986 pp888-889.

H.Nakano, S.Yamanshita, T.P.Tanaka, M.Hiroa and M.Maeda *Monolithic Integration of Laser Diodes, Photomonitors, and Laser Monitoring Circuits on a Semi-Insulating GaAs* JLT Vol LT4 (6) 1986 pp574-582.

D.F.Nelson, R.C.Miller, C.W.Tu and S.K.Sputz *Exciton Binding Energies from an Envelope-function Analysis of Data on Narrow Quantum Wells of Integral Monolayer Widths in* $Al_{0.4}Ga_{0.6}As/GaAs$ Physical Review B Vol 36 (15) 1987 pp8063-8071.

Y.Noda, M.Suzuki, Y.Kushiro and S.Akiba *High-Speed Electroabsorption Modulator with Strip-Loaded GaInAsP Planar Waveguide* JLT Vol LT-4 (10) 1986 pp1445-1453.

L.D.Nguyen, D.C.Radulescu, P.J.Tasker, W.J.Schaff and L.F.Eastman *0.2μm Gate Length Atomic-Planar Doped Pseudomorphic* $Al_{0.3}Ga_{0.7}As/\ In_{0.25}Ga_{0.75}As$ *MODFETs with* f_T *over 120GHz* IEEE EDL Vol 9 (8) 1988 pp374-376.

H.Nobuhara, O.Wada, T.Fujii *GRIN-SCH Laser Photodiode Array by Improved Microcleaved Facet Process* EL21 (17) 1985 pp718-719.

N.Ogasawara, R.Ito and R.Morita *Linewidth Enhancement Factor in GaAs/AlGaAs Multiple Quantum Well Lasers* Jap.JAP 24 1985 ppL519-L521.

J.I.Pankove *Optical Processes in Semiconductors* Dover Publications Inc. New York 1975.

A.L.Powell, J.S.Roberts, P.I.Rockett, T.J.Foster and L.Eaves *Modulation-Doped (AlGa)As/GaAs Quantum Well Structure With High Electron Sheet Density* EL 25 (17) 1989 pp1147-1148.

M.Razeghi, F.Omnes, M.Defour and P.Maurel *High-Quality GaInAs/InP Heterostructures Grown by Low Pressure Metalorganic Chemical Vapour Deposition on Silicon Subsrtates* APL Vol 52 (3) 1988 pp209-211.

D.C.J.Reid, R.Carpenter and B.T.Debney *Sixteen Channel Single Mode WDM Component* Proc.(1) 15th European Conference on Optical Communications (ECOC) 1989 pp29-32.

H.Ribot, K.W.Lee, R.J.Simes, R.H.Yan and L.A.Coldren *Disordering of GaAs/AlGaAs Multiple Quantum Well Structures by Thermal Annealing for Monolithic Integration of Laser and Phase Modulator* APL 55 (7) 1989 pp672-674.

A.Rivers *Unpublished data on the alloying of semiconductor contacts*

J.S.Roberts, M.A.Pate, P.Mistry, J.P.R.David, R.B.Franks, M.Whitehead and G.Parry *MOVPE Grown MQW pin Diodes For Electro-Optic Modulators and Photodiodes With Enhanced ElectronIonistaion Coefficient* Journal of Crystal Growth (93) 1988 pp877-884.

H.Sakaki *Physical Limits of Heterostructure Field-Effect Transistors and Possibilities of Novel Quantum Field-Effect Devices* IEEE JQE Vol 22 (9) 1986 pp1845-1852.

H.Sakaki, H.Yoshimura and T.Matsusue *Carrier Concentration Dependent Absorption Spectra of Modulation Doped n-AIGaAs/GaAs Quantum Wells and performance Analysis of Optical Modulators and Switches Using Carrier Induced Bleaching (CIB) and Refractive Index Changing* JJAP. 26.(7) 1987 ppL1104-L1106.

G.D.Sanders and Yia-Chung Chang *Theory of Photoabsorption in Modulation Doped Semiconductor Quantum Wells* Phys Rev B 35 (3) 1987 pp1300-1315.

S.Schmitt-Rink, D.S.Chemla and D.A.B.Miller *Theory of Transient Excitonic Optical Nonlinearities in Semiconductor Quantum-Well Structures* Phys.Rev.B32.(10) 1985 pp6601-6609.

K.S.Seo, P.K.Bhattacharya and K.R.Gleason *DC and Microwave Characteristics of an $In_{0.53}Ga_{0.47}As/In_{0.52}Al_{0.48}As$ Modulation-Doped Quasi-Misfet* EL 23 (6) 1987 pp259-260.

B.O.Seraphin and N.Bottka *Franz-Keldysh Effect of the Refractive Index in Semiconductors* Phys. Rev. Vol 139 (2A) 1965 ppA560-A565.

J.Seymour *Electronic Devices and Components* 1981 Pitman.

J.Shibata and T.Kajiwara *Recent Progress and Advanced Technology of InGaAsP/InP OEICs for Lightwave Systems, Lasers, Detectors and HBTs* Proc.(1) 14th European Conference on Optical Communications (ECOC) 1988 pp17-20.

M.Shinada and S.Sugano *Interband Optical Transitions in Extremely Anisotropic Semiconductors. I. Bound and Unbound Exciton Absorption* J Phs Soc Jpn 21 (10) 1966 pp1936-1946.

M.S.Skolnick, P.R.Tapster, S.J.Bass, A.D.Pitt, N.Apsley and S.P.Aldred *Investigation of InGaAs-InP Quantum Wells By Optical Spectroscopy* Semicond.Sci.Technol.1 1986 pp29-40.

H.Soda, K.Nkai and H.Ishikawa *Frequency Response of an Optical Intensity Modulator Monolithically Integrated with a DFB Laser* Proc.(1) 14th European Conference on Optical Communications (ECOC) 1988 pp227-230.

G.J.Sonek, J.M.Ballantine, Y.J.Chen, G.M.Carter, S.W.Brown, E.S.Koteles and P.Salerno *Dielectic Properties of GaAs/AlGaAs Multiple Quantum Well Waveguides* JQE Vol QE-22 (7) 1986 pp1015-1018.

R.Sooryakumar, D.S.Chemla, A.Pinczuk, A.Gossard, W.Weigmann and L.J.Sham *Direct Observation of Band-mixing in GaAs-*$(Al_xGa_{1-x})As$ *Quantum Heterostructures* J.Vac.Sci.Technol B2 (3) 1984 pp349-350.

D.A.H.Spear, P.J.G.Dawe, G.R.Antell, W.S.Lee and S.W.Bland *New Fabrication Technology for Long-Wavelength Receiver* OEICs EL 25 (2) 1989 pp156-157.

F.Stern *Dispersion of the Index of Refraction Near the Absorption Edge of Semi-Conductors* Phys Rev Vol 133 (6A) 1964 ppA1653-A1664.

Peter Stevens *Modelling, Assessment and Applications of Multiple Quantum Well Optical Absorption Modulators* Doctoral Thesis 1990, Department of Electronic and Electrical Engineering, University College London.

P.Stevens, M.Whitehead, G.Parry and K.Woodbridge *Computer Modelling of the Field Dependent Absorption Spectrum of Multiple Quantum Well Material* JQE 24 (10) 1988 pp2007-2014

P.Stevens and G.Parry *Limits to Normal Incidence Electroabsorption Modulation in GaAs/(GaAl)As Multiple Quantum Well Devices* JLT 7 (7) 1989 pp1101-1108.

P.J.Stevens, T.Mukai *Predicted Performance of Quantum Well GaAs/(GaAl)As Optical Amplifiers* JQE to be published.

M.Sugimoto, N.Hamao, N.Takado, K.Asakwa and T.Yuasa *Very Low Threshold AlGaAs/GaAs Quantum Well Lasers Fabricated by Self Aligned Impurity Induced Disordering* Jpn JAP 28 (6) ppL1013-1015.

R.S.Sussmann, R.M.Ash, A.J.Moseley and R.C.Goodfellow *Ultra-Low Capacitance Flip-Chip-Bonded GaInAs PIN Photodetector for Long-Wavelength High-Data-Rate Fibre-Optic Systems* EL 21 (6ish) 1985 pp593-594.

T.Suzaki, S.Fujita, Y.Infomoto, T.Terakado, K.Kasahara, K.Asano, T.Torikai, T.Itoh, M.Shikada, A.Suzuki *1.2 Gbit/s, 52.5km Optical Fibre Transmission Experiment Using OEICs on GaAs-on-InP Heterstructure* EL 24 (20) 1988 pp1283-1284.

A.Suzuki, T.Itoh, T.Terakado, K.Kasahara, K.Asano, Y.Inomoto, H.Ishihara, T.Torikai and S.Fujita *Long Wavelength PINFET Receiver OEIC on a GaAs-on-InP Heterostructure* EL 23 (18) 1987 pp954-955.

S.M.Sze *Physics of Semiconductor Devices 2nd edition* 1981 Wiley.

K.Tai, J.Hegarty and W.T.Tang *Nonlinear Spectroscopy of InGaAs/InP Multiple Quantum Wells* APL. 51 (2) 1984 pp86-88.

S.Tarucha, H.Kobayashi, Y.Horikoshi and H.Okamoto *Carrier Induced Gap Shrinkage in Current-Injection GaAs/AlGaAs MQW Heterostructures* JJAP 23.(7) 1984 pp874-878.

S.Tarucha, H.Iwamura, T.Saku and H.Okamoto *Waveguide-Type Optical Modulator of GaAs Quantum Well Double Heterostructures Using Electric Field Effect on Exciton Absorption* JJAP 24 (6) 1985 ppL442-L444.

S.Tarucha and H.Okamoto *Monolithic Integration of a Laser Diode and an Optical Waveguide Modulator Having a GaAs/AlGaAs Quantum Well Double Heterostructure* APL. 48 (1) 1986 pp1-3.

G.H.B.Thompson *Semiconductor Lasers* Wiley, London 1978.

A.Tomita and A.Suzuki *Carrier Induced Wavelength Shifts for Quantum Well Laser Diodes* JQE 23 (7) 1987 pp1155-1159

W.T.Tsang *Quantum Confinement Heterostructure Semiconductor Lasers* Semiconductors and Semimetals, Volume 24 Editor, R.Dingle (Accademic Press) p441. 1987

W.T.Tsang *Extremely Low Threshold (AlGa)As Modified Multiple Quantum Well Heterostructure Lasers Grown by Molecular Beam Epitaxy.* APL 39 1981 pp786-788. see also W.T.Tsang *Heterostructure Semiconductor Lasers Prepared by Molecular Beam Epitaxy* JQE 20 (10) 1984 pp1119-1132.

O.Wada *Optoelectronic Integration Based on GaAs Material* Optical & Quantum Elec. 20 1988 pp441-474.

O.Wada *Advances in III-V Semiconductor Optoelectronic Integration* Proc.(2) 15th European Conference on Optical Communications (ECOC) 1989 pp114-120.

O.Wada, A.Furuya and M.Makiuchi *Planar Compatible OEIC's Based on Multiquantum Well Structures* PTL 1 (1) 1989 pp16-18.

K.Wakao, T.Sanada, K.Kondo and S.Yamakoshi *Giga-bit Operation of InGaAsP/InP Optical Gate Integrated with Optical Amplifier* Proc.(1) 15th European Conference on Optical Communications (ECOC) 1989 pp244-247.

K.Wakita, Y.Kawamura, M.Nakao and H.Asahi *Long Wavelength Waveguide Multiple Quantum Well Optical Modulators* JQE 23 (12) 1987 pp2210-2215.

M.J.Wale, P.J.Duthie, I.Bennion *The Design of Bidirectional FibreOptic Links Using Reflective Modualtion Techniques* Proc Eur. Conf. Opt. Comm. pp149-152 1986.

M.J.Wale, C.Edge, F.A.Randle and D.J.Pedder *A New Self-Aligned Technique for the Assembly of Integrated Optical Devices with Optical Fibre and Electrical Interfaces.* Proc.(1) 15th European Conference on Optical Communications (ECOC) 1989 pp368-371.

R.G.Walker *High Speed Electrooptic Modulation in GaAs/GaAlAs Waveguide Devices* JLT 5 (10) 1987 pp1444-1453.

G.W.Wang and M.Feng *Quarter-Micrometer Gate Ion-Implanted GaAs MESFETs with an* f_t *of 126 GHz* IEEE EDL Vol 10 (8) 1989 pp386-388.

J.S.Weiner, D.S.Chemla, D.A.B.Miller, H.A.Haus, A.C.Gossard, W.Wiegmann and C.A.Burrus *Highly Anisotropic Optical Properties of Single Quantum Well Waveguides* APL 47 (7) 1985a pp664-667.

J.S.Weiner, D.A.B.Miller, D.S.Chemla, T.C.Damen, C.A.Burrus, T.H.Wood, A.C.Gossard and W. Weigmann *Strong Polarisation-Sensitive Electroabsorption in GaAs/AlGaAs Quantum Well Waveguides* APL 47 (11) 1985b pp1148-1150.

J.S.Weiner, D.B.Pearson, D.A.B.Miller, D.S.Chemla, D.Sivco and A.Y.Cho *Nonlinear Spectroscopy of InGaAs/InAlAs Multiple Quantum Well Structures* APL 49 (9) 1986 pp531-533.

J.Werner, E.Kapon, N.G.Stoffel, E.Colas, S.A.Schwarz, C.L.Schwartz and N.Andreadakis *Integrated External Cavity GaAs/AlGaAs Lasers Using Selective Quantum Well Disordering* APL 55 (6) 1989 pp540-542.

Mark Whitehead *Optimization of Normal-Incidence GaAs-AlGaAs Multiple Quantum Well Optical Modulators* Doctoral Thesis 1990, Department of Electronic and Electrical Engineering, University College London.

M.Whitehead, P.Stevens, A.Rivers, G.Parry, J.S.Roberts, P.Mistry, M.Pate and G.Hill *Effects of Well Width on the Characteristics of GaAs/AlGaAs Multiple Quantum Well Electroabsorption Modulators* APL 53 (11) 1988 pp956-958.

M.Whitehead, A.Rivers, G.Parry, J.S.Roberts and C.Button *A Low Voltage Multiple Quantum Well Reflection Modulator with >100:1 On:Off Ratio* EL 25 (15) 1989 pp984-985.

M.Whitehead, A.Rivers, G.Parry, J.S.Roberts, P.Mistry, P.Li Kam Wa and M.A.Pate *Electric Field Effects in Quantum Well Devices and their Applications in Digital Optics* IEE Colloquium on "Optical Techniques for Information Processing", 25.11.87.

C.Weisbuch *Semiconductor and Semimetals* Volume 24. Editor, R.Dingle. Accademic Press 1987.

T.H.Wood, C.A.Burrus, D.A.B.Miller, D.S.Chemla, T.C.Damen, A.C.Gossard and W.Weigmann *High Speed Optical Modulation with GaAs/AlGaAs in a p-i-n Diode Structure* APL 44 (16) 1984 pp16-18.

T.H.Wood, C.A.Burrus, R.S.Tucker, J.S.Weiner, D.A.B.Miller, D.S.Chemla, T.C.Damen, A.C.Gossard and W.Weigmann *100 ps Waveguide Multiple Quantum Well (MQW) Optical Modulator with 10:1 on/off Ratio* EL 21 (16) 1985 pp693-694.

T.H.Wood, R.Tkach and A.Chraplyvy *Observation of Large Quadratic Electro-optic Effect in GaAa/AlGaAs Multiple Quantum Wells* APL 50 (13) 1987 pp798-800.

T.H.Wood, E.C.Carr, C.A.Burrus, B.I.Miller and U.Koren *Large Electroabsorption Effect in GaInAs/InP Multiple Quantum Well (MQW) Optical Modulator Grown by OMVPE* EL 24 (14) 1988 pp840-841.

M.Yamada, S.Ogita, M.Yamagishi, K.Tabata, N.Nakaya, M.Asada, Y.Suematsu *Polaisation Dependent Gain in GaAs-AlGaAs Multi-Quantum Well Lasers: Theory and Experiment* APL 45 (4) 1984 pp324-325.

M.Yamanishi and Y.Lee *Phase Dampings of Optical Dipole Moments and Gain Spectra in Semiconductor Lasers* JQE 23 (4) 1987 pp367-370.

A.Yariv *In the Beginning of Integrated Optoelectronic Integrated Circuits* IEEE Trans ED 31 (11) 1984 pp1656-1661.

M.Yust, N.Bar-Chaim, S.H.Izadpanah, S.Margalit, I.Ury, D.Wilt and A.Yariv *A Monolithically Integrated Optical Receiver* APL 35 (10) 1979 pp795-797.

L.D.Zhu, B.Z.Zheng, Z.Y.Xu, J.Z.Xu and G.A.B.Feak *Optical Gain in GaAs/GaAlAs Graded-Index Separate-Confinement Single-Quantum-Well Heterostructures* JQE, Vol 25 (6) 1989 pp1171-1178.

E.Zielinski, H.Schweizer, S.Hausser, R.Stuber, M.Pilkuhn, G.Weimann *Systematics of Laser Operation in GaAs/AlGaAs Multiquantum Well Heterostructures* JQE 23 (6) 1987 pp969-975.

J.E.Zucker, T.L.Hendrickson and C.A.Burrus *Low-Voltage Phase Modulation in GaAs/AlGaAs Quantum Well Optical Waveguides* EL Vol 24 (2) 1988a pp112-113.

J.E.Zucker, T.L.Hendrickson and C.A.Burrus *Electro-Optic Phase Modulation in GaAs/AlGaAs Quantum Well Waveguides* APL Vol 52 (12) 1988b pp945-947.

Reference Key for Periodical Abbreviations

APL	Applied Physics Letters
EDL	Electronics Device Letters
EL	Electronics Letters
JAP	Journal of Applied Physics
JJAP	Japanese Journl of Applied Physics
JLT	Journal of Lightwave Technology
JQE	Journal of Quantum Electronics
PRL	Physical Review Letters
J.Opt.Soc.Am	Journal of the Optical Society of America
J.Phys.Soc.Jpn	Journal of the Physical Society of Japan
J.Vac.Sci.Tech	Journal of Vacuum Science Technology
Trans.ED	IEEE Transactions on Electronic Devices

Appendix A

The ten sections to this appendix are the *as-grown* parameters for the epitaxial layer structures discussed in chapters 5 and 7 of this thesis.

Appendix A1. Sample CPM459 *MOCVD Sheffield University*

100 Å GaAs Cap
0.45 um $GaAl_{0.45}As$ p type $3x10^{16}$
800 Å $GaAl_{0.2}As$ n type $6x10^{16}$
75Å GaAs
100 Å $GaAl_{0.2}As$
100 Å $GaAl_{0.2}As$ n+ 10^{18}
1.05 um $GaAl_{0.2}As$ n type $7x10^{16}$
1.5 um $GaAl_{0.25}As$ n type $1x10^{17}$
n+ GaAs buffer layer and n+ Substrate

Appendix A2. Sample CPM460 *MOCVD Sheffield University*

100 Å GaAs Cap
0.45 um $GaAl_{0.45}As$ n type $8x10^{16}$
800 Å $GaAl_{0.2}As$ n type $6x10^{16}$
100Å GaAs
100 Å $GaAl_{0.2}As$
100 Å $GaAl_{0.2}As$ n+ 10^{18}
1.05 um $GaAl_{0.2}As$ n type $6x10^{16}$
1.5 um $GaAl_{0.25}As$ n type $1x10^{17}$
n+ GaAs buffer layer and n+ Substrate

Appendix A3. Sample MV292 *MOCVD Sheffield University*

100 Å GaAs Cap
0.45 um $GaAl_{0.45}As$ p type $3x10^{16}$
800 Å $GaAl_{0.2}As$ n type $4x10^{16}$
50Å GaAs
100 Å $GaAl_{0.2}As$
100 Å $GaAl_{0.2}As$ n+ 10^{18}
1.05 um $GaAl_{0.2}As$ n type $7x10^{16}$
1.5 um $GaAl_{0.25}As$ n type $1x10^{17}$
n+ GaAs buffer layer and n+ Substrate

Appendix A4. Sample MV317 *MOCVD Sheffield University*

100 Å GaAs Cap
0.45 um $GaAl_{0.45}As$ p type $1x10^{18}$
0.1 um $GaAl_{0.2}As$ n type $1x10^{16}$
75 Å $GaAl_{0.2}As$ n+ $2x10^{18}$
50 Å $GaAl_{0.2}As$
50 Å GaAs
50 Å $GaAl_{0.2}As$
1.05 um $GaAl_{0.2}As$ n type $1x10^{17}$
1.5 um $GaAl_{0.25}As$ n type $1x10^{17}$
n+ GaAs buffer layer and n+ Substrate

Appendix A5. Sample CB1 *MOCVD Sheffield University*

100 Å GaAs Cap
0.45 um $GaAl_{0.45}As$ p type $3x10^{17}$
800Å $GaAl_{0.2}As$ p type $3x10^{17}$
100 Å $GaAl_{0.2}As$ n+ 10^{18}
100 Å $GaAl_{0.2}As$
50Å GaAs
100 Å $GaAl_{0.2}As$
100 Å $GaAl_{0.2}As$ n+ 10^{18}
1.05 um $GaAl_{0.2}As$ n type
1.5 um $GaAl_{0.25}As$ n type
n+ GaAs buffer layer and n+ Substrate

Appendix A6. Sample MO685 *MBE Amoco Research Center*

100 Å GaAs Cap
0.45 um $GaAl_{0.45}As$ undoped
800 Å $GaAl_{0.2}As$ undoped
50Å GaAs undoped
100 Å $GaAl_{0.2}As$ undoped
100 Å $GaAl_{0.2}As$ n+ 10^{18}
1.05 um $GaAl_{0.2}As$ undoped
1.5 um $GaAl_{0.25}As$ undoped
n+ GaAs buffer layer and n+ Substrate

Appendix A7. Sample MO733 *MBE Amoco Rsearch Center*

100 Å GaAs Cap
0.45 um $GaAl_{0.45}$ As undoped
800 Å $GaAl_{0.2}$ As undoped
50Å GaAs undoped
100 Å $GaAl_{0.2}$ As undoped
100 Å $GaAl_{0.2}$ As undoped
1.05 um $GaAl_{0.2}$ As undoped
1.5 um $GaAl_{0.25}$ As undoped
n+ GaAs buffer layer and n+ Substrate

Appendix A8. Sample CB44 *MOCVD Sheffield University*

100 Å GaAs Cap
0.45 um $GaAl_{0.45}$ As p type $3x10^{17}$
0.5um $GaAl_{0.2}$ As p type $3x10^{17}$
0.1um $GaAl_{0.2}$ As p type $3x10^{16}$
150 Å $GaAl_{0.2}$ As n+ 10^{18}
50 Å $GaAl_{0.2}$ As
50Å GaAs
50 Å $GaAl_{0.2}$ As
200 Å $GaAl_{0.2}$ As n+ 10^{18}
0.5 um $GaAl_{0.2}$ As n type $1x10^{16}$
1.5 um $GaAl_{0.25}$ As p type $1x10^{17}$
p GaAs buffer layer and SI Substrate

Appendix A9. Sample CB111 *MOCVD Sheffield University*

100 Å GaAs Cap
0.45 um $GaAl_{0.45}As$ p type $3x10^{17}$
0.5um $GaAl_{0.2}As$ p type $3x10^{17}$
0.1um $GaAl_{0.2}As$ n type $3x10^{16}$
200 Å $GaAl_{0.2}As$
50Å GaAs
75 Å $GaAl_{0.2}As$
200 Å $GaAl_{0.2}As$ n+ 10^{18}
0.5 um $GaAl_{0.2}As$ n type $1x10^{16}$
1.5 um $GaAl_{0.25}As$ p type $1x10^{17}$
p GaAs buffer layer and SI Substrate

Appendix A10. Sample CB171 *MOCVD Sheffield University*

100 Å GaAs Cap
0.45 um $GaAl_{0.45}As$ p type $3x10^{17}$
0.5um $GaAl_{0.2}As$ p type $3x10^{16}$
0.1um $GaAl_{0.2}As$ n type $3x10^{16}$
200 Å $GaAl_{0.2}As$
50Å GaAs
75 Å $GaAl_{0.2}As$
150 Å $GaAl_{0.2}As$ n+ 10^{18}
0.5 um $GaAl_{0.2}As$ n type $1x10^{16}$
1.5 um $GaAl_{0.25}As$ p type $1x10^{17}$
p GaAs buffer layer and SI Substrate

fin